Design of recharge and abstraction well systems in heterogeneous aquifers

Modeling and experimental studies

Jan H. van Lopik

205 UTRECHT STUDIES IN EARTH SCIENCES

Design of recharge and abstraction well systems in heterogeneous aquifers: modeling and experimental studies

Jan H. van Lopik

Reading committee:
Prof. dr. V. Cnudde
Prof. dr. P. Dietrich
Prof. dr. E.O. Holzbecher
Dr. G.J. Houben
Prof. dr. ir. T.N. Olsthoorn

Examination committee:
Dr. ir. J.M. Bloemendal
Prof. dr. P. Dietrich
Prof. dr. E.O. Holzbecher
Dr. G.J. Houben
Prof. dr. ir. T.N. Olsthoorn
Dr. ir. F.J. Vermolen

ISBN:	978-90-6266-566-2
Title:	Design of recharge and abstraction well systems in heterogeneous aquifers: modeling and experimental studies
NUR code:	934
NUR description:	Hydrologie
Number of pages:	290
Cover lay-out:	Margot Stoete, Utrecht University
Printed by:	Ipskamp Printing

Design of recharge and abstraction well systems in heterogeneous aquifers: modeling and experimental studies

Ontwerp van infiltratie- en onttrekkingsputsystemen in heterogene grondwaterpakketten: modelleer- en experimenteel onderzoek

(met een samenvatting in het Nederlands)

Proefschrift

ter verkrijging van de graad van doctor aan de
Universiteit Utrecht
op gezag van de
rector magnificus, prof. dr. H.R.B.M. Kummeling,
ingevolge het besluit van het college voor promoties
in het openbaar te verdedigen op
maandag 20 januari 2020 des middags te 4.15 uur

door

Jan Hendrik van Lopik

geboren op 7 december 1988
te Leidschendam

Promotor:
Prof. dr. R.J. Schotting

Promotor:
Dr. A. Raoof
Dr. N. Hartog

This thesis was accomplished with financial support from the Technology Foundation STW, the technological branch of the Netherlands Organisation of Scientific Research, NWO, and the Dutch ministry of Economic Affairs under contract no. 13263, entitled Fast, High Volume Infiltration.

Acknowledgements

Many people have supported me during the writing of my PhD thesis.

At first, I wish to thank my supervisor Ruud Schotting. He introduced me in the world of hydrogeology with his upbeat enthusiastic courses during my Bachelors and Masters at the Utrecht University. This was the essential starting point eventually leading to this PhD. I am very grateful for his trust in me. He encouraged me to work freely, gave me the opportunity to give different lectures and field excursions, as well as to work with and to supervise bachelor and master students.

I wish to thank my co-supervisors Amir Raoof and Niels Hartog. The latter, I am very grateful for his help in the last year to finalize my PhD thesis. It also did recall the good internship memories which were the reason to dive into scientific research.

I wish to thank my paranymphs, Thomas Sweijen and Gilian Schout. Thomas provided me with fruitful comments on dewatering related research, while Gilian was always available to help at the field site. I also wish to thank all my friends, officemates, the group members and the visitors I have met during my time in the Environmental Hydrogeology group. Special thanks for the group secretaries Annuska Exel and Margreet Evertman, who were always available for any questions or help.

I am sincerely grateful to Willem Jan Zaadnoordijk for supporting me with the numerical simulations of HT-ATES systems and to Georg J. Houben for commenting on the papers on non-linear flow behaviour and well hydraulics. I also wish to thank the students Roy Snoeijers and Teun van Dooren for their efforts during labexperiments.

I am very grateful to the directors from the dewatering companies of O2DIT: Martin Bouten, Guido van Tongeren, Theo van Velzen and Thijs de Vet. Despite their busy schedule of running their own dewatering companies, they were always available for questions and help at any time. I wish to thank Thijs de Vet and the drilling operator Sjaak van Lanen for all their efforts in the early stage of my PhD by arranging the fieldwork in Mönchengladbach and guiding me into the world of construction dewatering and well completion. I wish to thank Peter de Vet for constructing and fine-tuning the laboratory set-up for the non-linear flow experiments. For all fieldwork issues at the Utrecht Science Park, such as the construction of different recharge designs, leaking pipelines, a not working generator, oil spills due to a failed attempt to steal the generator, and own clumsiness, Theo van Velzen always picked up his phone to help me out (weekend, evening, football match, doesn't matter). I wish to thank Guido van Tongeren for sharing useful construction dewatering data and for his valuable advice and support throughout the PhD research. I like to thank Martin Bouten for the nice meetings in Nijmegen and for the placement of the tracer test wells at the Utrecht Science Park. I thank the O2DIT directors, late Kees Snaterse and Willem van Starkenburg, for their

efforts, Frans Glorie for taking care of the logistical and economical part of the field experiment at the Utrecht Science Park, Fugro GeoServices for the hydrogeological site investigation, Bearnd Hylkema for providing and constructing the required materials to perform the bromide tracer test, Jon Burgmeijer from Inventec for installation of the optic fiber cable, Martin Bloemendal from KWR for providing the DTS unit, Irene Fransen from Hoogheemraadschap De Stichtse Rijnlanden and Hans de Jong from Vastgoed en Campus Utrecht University for their time and for allowing me to perform the tracer tests at the Utrecht Science Park. Also special thanks to all drilling operators, dewatering company employees, cone penetration test operators who have helped constructing the field set-up. It was fun to work with you and I am very grateful to all of you, because you have learned me in practice what I never could have learned in the academic world.

Finally, I am very grateful to my parents and brothers, who kept me company in the field and supported me by helping out with the hydraulic head measurements and groundwater sampling during the long fieldwork days in the field and for checking and correcting my manuscripts. Above all, I am very grateful to Louza for her daily moral support, her infinite patience, the encouraging words to keep me going, the plenty visits to the field to help me and cheer me up with nice picnics and her company, and for helping me out in the lab, while conducting a nice research together. I am really lucky to have you in my life.

Contents

Chapter 1

Introduction

For centuries, water wells have been used to access groundwater in the subsurface for recharge or production purposes (Kasenow 2010). One of the world's oldest water wells is found in Cyprus, dating from the Stone Age around 10,500 years ago (Peltenburg et al. 2000). Today, years of ongoing civilization and improvement in well technology have provided us with a huge range of possibilities to abstract groundwater and recharge water into the subsurface using well systems. Especially during the last decades, the use of wells for abstraction, recharge and storage of water in the subsurface is increased for a wide variety of applications. Besides common groundwater abstraction for drinking water supply or irrigation purposes (Kasenow 2010; Houben 2015a), water wells are used for dewatering of groundwater at mining and construction sites (Powers et al. 2007), groundwater remediation (Khan et al. 2004), production of geothermal energy (Bertani 2016), as well as for recharge, storage and recovery of fresh water resources (Bouwer 2002; Pyne 2005) and thermal energy in the subsurface (Bloemendal et al. 2018; Fleuchaus et al. 2018). For each well application, the well completion costs, the energy costs during well operation, the well development costs, its total operational time span and its hydraulic and environmental impact should be taken into account to obtain the ideal design for the entire well system, as well as for each individual well (Discroll 1986; Kasenow 2010; Houben 2015a).

For some water well applications the hydraulic impact needs to be limited to a given depth or portion of the aquifer in order to optimize the entire efficiency of the well system (see Fig. 1.1). For such cases, partially-penetrating wells (PPWs) screened in the desired portion of the aquifer instead of fully-penetrating wells (FPWs) or wells that screen a large portion of the aquifer are beneficial. The selection of a proper design for such PPW systems requires thorough understanding of the hydraulic characteristics of the subsurface and the well hydraulics of the PPW itself (Barker and Herbert 1992, Hemker 2000; Bakker 2001; Tügel et al. 2016). The present thesis focusses at the processes and conditions of recharge and abstraction well systems in heterogeneous aquifers. Moreover, the optimization of such well systems by using PPWs in heterogeneous aquifers is investigated. This is done for construction dewatering schemes with artificial recharge PPWs and high-temperature aquifer thermal energy storage (HT-ATES) systems.

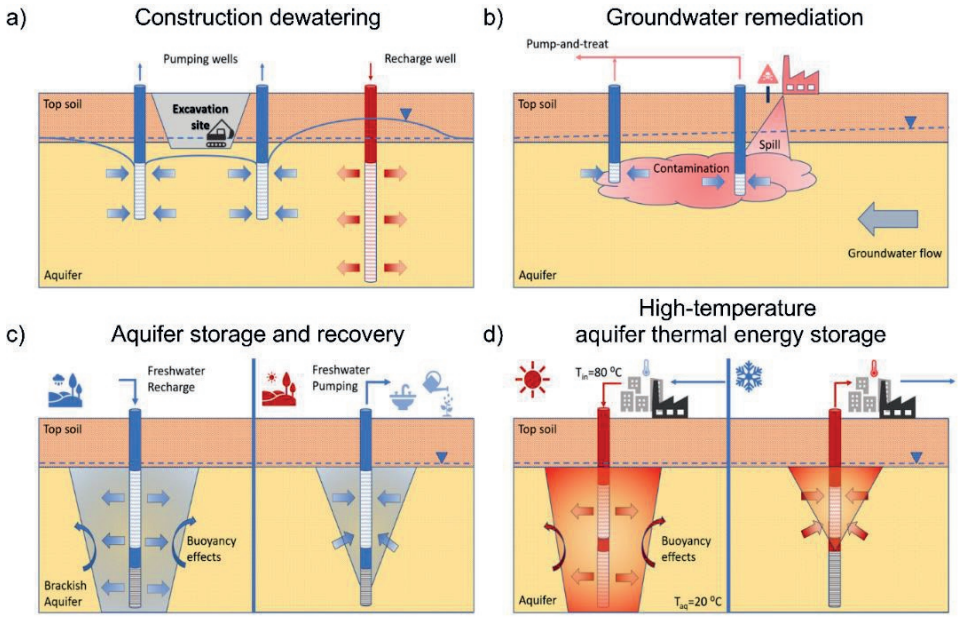

Fig. 1.1 Examples of water well applications with PPWs: **a)** dewatering at construction or mining sites, **b)** groundwater remediation by pump-and-treat, **c)** managing freshwater resources in brackish aquifers by the use of aquifer storage and recharge (ASR) and **d)** high-temperature aquifer thermal energy storage (HT-ATES).

1.1 Basics of groundwater flow

Common water wells are screened in aquifers, in which water can be easily produced or injected. Literally, aquifer means a water (*aqua*) bearing (*ferre*) unit. These water-bearing units consist of various geological formations, such as unconsolidated sand or gravel, as well as, consolidated sandstone, limestone, breccia or fractured rock (Bear 2007; Kasenow 2010). In nature, different kinds of aquifer exist. **Unconfined aquifers** are partly-saturated water bearing beds with a free groundwater table or phreatic surface. **Confined aquifers** are completely saturated water bearing beds confined by two impermeable layers. An aquifer that is overlain and/or underlain by semipermeable strata which are capable of transporting groundwater from (discharge) or to (recharge) the aquifer is called a **semi-confined or leaky aquifer**. Geological semi-confining units such as clays, peat, loam or shales, that are not useable for production or injection of water due to a low permeability are defined as *aquitard*s.

Groundwater flow in aquifers is described by Darcy's law, the well-known proportional relationship between the hydraulic gradient, dh/dl and the specific discharge in the l-direction q_l [m/s] through a porous medium (Darcy 1856):

$$q_l = \frac{Q_l}{A} = -K_l \frac{dh}{dl} \quad (1.1)$$

where K_l [m/s] is the hydraulic conductivity of the porous medium in the *l*-direction, A [m^2] is the cross-sectional area perpendicular to the *l*-direction and Q_l [m^3/s] is the volumetric discharge in the *l*-direction.

The empirical linear relationship of Darcy is only applicable for a specific flow regime. For most groundwater flow problems Eq. 1.1 suffices, but at high flow velocities the relationship between the hydraulic gradient (*dh/dl*) and specific discharge (q) is non-linear. To determine if groundwater is in the Darcy regime, the Reynolds number is used as an indicator:

$$Re = \frac{\rho d_{50} q_l}{\mu} \quad (1.2)$$

where ρ is the fluid density [kg/m^3], d_{50} [m] is the median grain size of the porous medium and μ [kg/(m s)] is the dynamic viscosity. Critical Reynolds numbers for non-linear flow behavior are ranging between 1 and 15 (e.g. Bear 1988; Comiti et al. 2000; Hassanizadeh and Gray 1987; Ma and Ruth 1993). The non-linear deviation from Darcy's law due to increased flow resistance at higher flow velocities is described by various equations in the literature (Forchheimer 1901; Izbash 1931).

1.1.1 Aquifer heterogeneity and anisotropy

In hydrogeology, aquifers are classified by means of their homogeneity and isotropy. A homogeneous aquifer consists of similar material over the entire thickness of the aquifer, while an isotropic aquifer has similar properties (identical hydraulic conductivities) in all directions from any point in the aquifer (Kazenow 2010). Using these criteria, three major classification types for unconsolidated aquifers can be distinguished in hydrogeology:

1) A ***homogenous, isotropic aquifer*** consists of rounded material which is uniformly distributed throughout the aquifer. As a consequence, the horizontal hydraulic conductivity $K_{x,y}$ is equal to the vertical hydraulic conductivity K_z, which is a practical assumption for quantification in analytical solutions and numerical modelling. However, such aquifers are rarely found in nature.
2) A ***homogenous, anisotropic aquifer*** also consists of material which is uniformly distributed throughout the aquifer. However, during the formation of the porous stratum by the deposition and compaction of angular, elongated

material a higher horizontal hydraulic conductivitiy $K_{x,y}$ than the vertical hydraulic conductivity K_z is obtained.

3) In nature, ***heterogeneous, anisotropic aquifers*** are the norm. Material is not uniformly distributed throughout the aquifer due to variation in sedimentation and existence of geological structures within the aquifer. Hence, aquifers are sedimentological heterogeneous, with each having its hydraulic properties for the present sedimentary strata within the aquifer (Bear 2007; Kazenow 2010).

In practice, due to a lack of reliable sedimentological field data, hydrogeologists simplify heterogeneous, anisotropic aquifers for groundwater models and analytical solutions. This can be done by using one equivalent homogeneous hydraulic property for the entire aquifer, or by dividing the aquifer in different homogeneous composite zones with each a given average hydraulic property.

A common example is homogenisation of multi-layered heterogeneous aquifer systems. Deposits in a stratified alluvial plain with different heterogenous-layered sediments, each having a different thickness and hydraulic conductivity, can be translated into a bulk hydraulic conductivity. Hence, an equivalent bulk anisotropy for the entire aquifer can be defined by the overall horizontal and vertical hydraulic conductivities of the different layers with various thicknesses H_i (Bear 2007; Kasenow 2010). The average horizontal hydraulic conductivity $K_{h,av}$ over the entire aquifer thickness H_{tot} (Fig. 1.2) is calculated by:

$$K_{h,av} = \frac{\sum K_{h,i} H_i}{H_{tot}} \tag{1.3}$$

The average horizontal hydraulic conductivity $K_{z,av}$ for the entire aquifer thickness is calculated by:

$$K_{z,av} = \frac{H_{tot}}{\sum \frac{H_i}{K_{z,i}}} \tag{1.4}$$

The use of Eq. 1.3 and 1.4 is an scaling tool for quantification of heterogeneous-layered aquifers to ***equivalent homogenous anisotropic aquifers*** in analytical solutions or numerical models. Commonly, in nature, anisotropy ratios ($K_{h,av}/K_{v,av}$) for such stratified alluvial aquifers range between 2 and 10 (Kasenow 2010) and are usually used as a rule of thumb in hydrogeology. However, for stratified aquifers with thin silt, clay, peat or loam layers anisotropy ratios can be a factor of ten higher.

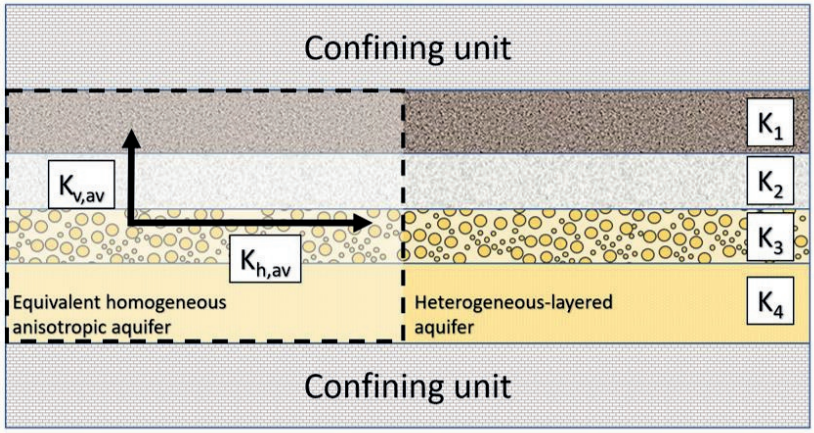

Fig. 1.2 Heterogeneous-layered aquifer with various hydraulic properties for the different bed layers (1-4) and its equivalent homogeneous anisotropic counterpart.

1.1.2 Predicting groundwater flow near wells

Both analytical solutions and numerical simulations are used as reliable tools to predict spatial and temporal head distributions during recharge or discharge in a water well (Kasenow 2010; Yeh and Chang 2013). Analytical solutions are still widely used as a reliable tool for predictions of the head distribution around a well and for estimation of the bulk hydraulic property of the aquifer using aquifer tests (Yeh and Chang 2013).

The simplest analytical formulations for well problems are based on the Dupuit-Forchheimer assumption, which postulates that groundwater flow is solely in the lateral direction and all vertical flow components can be disregarded. Hence, radial-symmetric flow conditions can be assumed and the area A in Eq. 1.1, perpendicular to the radial flow direction, can be expressed as the surface of a cylinder. One of the earliest analytical solutions described steady-state groundwater flow near abstraction or recharge wells in a fully confined homogeneous aquifer (Thiem 1870; Thiem 1906):

$$s = h_2 - h_1 = \frac{Q}{2\pi KH} \ln\left(\frac{r_2}{r_1}\right) \tag{1.5}$$

where s [m] is the drawdown, Q [m^3/s] is the volumetric well discharge/recharge, H [m] is the aquifer thickness and r_1 and r_2 [m] are the radial distances.

Since Thiem (1870) and Theis (1935) (for unsteady-state well flow conditions) have provided their classical works for groundwater flow to wells in confined aquifers, many analytical solutions have been postulated in the literature (e.g. De Glee 1930; Hantush 1964; Yeh and Chang 2013). In the vicinity of PPWs the vertical flow component close

to the well screen is significant and therefore, the Dupuit-Forchheimer assumption does not hold. The extent of the vertical flow component around the well depends on the characteristics of the aquifer (thickness, hydraulic conductivity, heterogeneity) and the well screen length. In literature analytical and more complex semi-analytical solutions for partially-penetrating wells (PPW) have been introduced to estimate the head distribution and the flow patterns around such PPWs in homogeneous and heterogeneous aquifers (Hantush 1964; Maas 1987; Haitjema and Kraemer 1988; Hemker 2000; Bakker 2001). However, in practice, many well-hydraulic problems often need to deal with complex boundary conditions, geometries and heterogeneity in the aquifer and require numerical approaches (Yeh and Chang 2013).

1.2 Soil and hydrogeology characterization

For optimal construction of efficient recharge or discharge well systems a reliable hydrogeological site investigation is important. However, in practice, obtaining a detailed overview of the spatial variability of hydraulic conductivity in aquifers is a challenging and costly procedure (Butler 2005). Therefore, the costs of obtaining soil and hydrogeological data in a hydrogeological site investigation should always be balanced with the possible risks, pitfalls, and potential extra costs of insufficient hydrogeological knowledge during the planning, construction and operation of well systems. Commonly, predictive groundwater models or analytical solutions are based on bulk parameters obtained from interpolation of field data, the most reasonable assumption of such parameters if no soil data is present, or stochastic approaches.

Since Thiem (1870) and Theis (1935), the Dupuit-Forchheimer assumption of solely lateral groundwater flow behaviour near wells and the use of an equivalent homogenous aquifer with one average hydraulic conductivity have widely shown its merits in the planning and construction of well systems (Powers et al. 2007; Kasenow 2010; Houben 2015a). However, for the design of many well systems the spatial variability of hydraulic conductivity in heterogeneous aquifers is key. More particularly, PPWs that only screen a small portion of heterogeneous aquifers need to account for anisotropy or vertical variability of the hydraulic conductivity (e.g. Maas 1987; Hemker 2000; Tügel et al. 2016). Also wells placed in alluvial plain deposits with a significant horizontal anisotropy ($K_x \neq K_y$) need to account for aquifer heterogeneity (e.g. Mathias and Butler 2007; Gianni et al. 2019). Aquifer heterogeneity is also important for predicting the preferential flow paths during heat or solute transport, as well as for predicting buoyancy-driven flow patterns (e.g. Buscheck et al. 1983; Zheng and Gorelick 2003; Simmons et al. 2001; Sommer et al. 2013; Ferguson 2007; Hidalgo et al. 2009; Seibert et al. 2014).

Today, many tools are available to obtain the in-situ hydraulic conductivities of the soil (Butler 2005). Classical methods that are used to obtain the hydraulic characteristics of the aquifer are the analytical or numerical analysis of aquifer tests, such as constant rate, constant head, recovery and slug tests (Bouwer and Rice 1976; Kruseman and De Ridder 1991; Butler and Healey 1998; Yeh and Chang 2013), analysis of tracer tests (Ptak et al. 2004; Anderson 2005) or the soil permeameter lab test on soil samples (Chapuis et al. 2005; Godoy et al. 2018). These tests enable the derivation of the in-situ hydraulic conductivity of the aquifer at different scales. For example, aquifer tests using fully penetrating wells provide an estimate of a bulk hydraulic conductivity over a large radial extent in the aquifer. Vertical variability in hydraulic conductivity can be obtained with borehole flowmeters, as well as partially-penetrating slug-tests, or packer tests which determine the local hydraulic conductivity K based on the hydraulic conductivity of the screened layer and the over- and underlying layers (Molz and Young 1993; Butler et al. 1994; Zlotnik 1994; Hyder et al. 1994; Zlotnik and Zurbuchen 2003; Sakata et al. 2015). Recently, direct pushed based technologies, such as the direct-push permeameter, direct-push injection logger and hydraulic profiling tool are available, which allow for detailed logging of the vertical variability in (relative) permeability (Butler et al. 2007; Dietrich et al. 2008; Köber et al. 2009).

Besides measuring the actual hydraulic conductivity of the soil, the hydraulic conductivity can also be estimated. Grain size distributions are used for estimation of the hydraulic conductivity with empirical relationships (Carrier 2003; Chapuis et al. 2005; Vienken and Dietrich 2011). Other methods, such as borehole logs, as well as cone penetrating test (CPT) are relatively cheap methods that can be used to determine the soil characteristics (e.g. Powers et al. 2007; Robertson 1990) and provide a rough picture of the local hydraulic characteristics (e.g. Oosterbaan and Nijland 1994). These methods are useful to interpolate or extrapolate sedimentological strata in the aquifer and correlate these with available measured hydraulic conductivities to obtain a better three-dimensional overview of hydraulic characteristics in the aquifer based on soil characteristics.

1.3 Water well applications

In many water well applications, PPWs are used to optimize the design of the well system. By screening PPWs at given depth in the aquifer, the entire efficiency of the water well system can be significantly improved. In this section, several water well applications that can potentially benefit from such procedure are described.

1.3.1 Construction dewatering and artificial recharge

The construction of building foundations and infrastructure require excavations (e.g. Tan and Wang, 2013; Fang et al. 2016). Hence, in areas with shallow groundwater levels, or for deep excavation pits, construction dewatering is used for lowering the groundwater table inside the excavation pit (Powers et al. 2007; Cashman and Preene 2013; Pujades et al. 2014). A wide variety of dewatering wells is suggested for different types of excavations, such as well-points, deep-wells, ejector systems and horizontal drains (Somerville 1986; Powers et al. 2007; Cashman and Preene 2013).

For dewatering purposes at excavations, PPWs are often used to target the upper portion of the aquifer in order to lower the hydraulic head (Fig. 1.1a). The oldest dewatering systems (around 1920 (Powers et al. 2007)) consisted of several well-points screened in the upper part of the aquifer. Using a vacuum pump, the groundwater level can be lowered by a couple of meters (Fig. 1.3). Still, for a shallow excavation, as well as for a trench dewatering, vacuum dewatering with well-points is the most common method of dewatering. For short term dewatering this is a reliable cost-efficient method, since well-points are quick, easy and cheap to install. In order to obtain an optimal well-design of a vacuum well-point dewatering system, the heterogeneity of the soil should be taken into account (Somerville 1986; Powers et al. 2007). Failure of such dewatering systems can occur by due to a poor soil characterization scheme (Shaqour and Hasan 2008). For heterogenous-layered soils with distinct alternating of more permeable sand/gravel layers with finer silts or clays, a close well-point spacing (wells at 2 meter distance) or longer well screens (shallow-wells) may be necessary to ensure the desired groundwater lowering throughout the entire strata section (Somerville 1986; Powers et al. 2007).

Fig. 1.3 Construction dewatering in practice: groundwater lowering at an excavation site by using a vacuum well-point system.

For deeper excavations in urban areas or prolonged dewatering, deep wells are used (Powers et al. 2007). In general, the installation of such wells is more expensive, but their well efficiency is much higher. Submersible pumps inside deep wells are used to pump water. Hence, the drawdowns that are obtained with such wells are much higher as compared to well-points systems with vacuum pumps. Selection of the well configuration (e.g. well screen depth, screen interval and well diameter) of deep wells depends on the aquifer characteristics, the extent of the excavation site and the required drawdown. For example, in high-permeability aquifers large submersible pumps and large diameter wells are required to obtain sufficient drawdown (Powers et al. 2007).

During dewatering procedures artificial recharge could be required to avoid risks of soil settlement due to lowered groundwater levels (Roy and Robinson 2009; Zheng et al. 2018; Zeng et al. 2019), or to reduce the hydrogeological and environmental impact of the dewatering (Preene and Brassington 2003; Cashman and Preene 2013) (Fig. 1.1a). Therefore, in the Netherlands, discharging groundwater for the larger dewatering projects into surface waters, such as ditches, rivers, is not allowed and groundwater has to be recharged into the same aquifer (SIKB 2017ab). Coastal areas encounter the risk of salinization during dewatering (Mas-Pla et al. 2013). Therefore, the dewatering companies have to take into account the fresh-salt water interface during dewatering in the Netherlands (e.g. SIKB 2017b). Commonly, artificial recharge wells are completed with wells screening a large portion of the aquifer (screen lengths larger than 10 m) (Fig. 1.1a). However, in the last decade Dutch and German dewatering companies started to use PPWs (so-called FHVI-wells) screened in deeper portions of the aquifer which allow

injection at larger well heads and volumetric flow rates, as well as a more targeted hydraulic impact in the deeper portion of the aquifer.

Besides the requirement of artificial recharge during construction dewatering, a lack of natural recharge by increased surface-runoff of rainwater in urban areas can result in significant lowering of the groundwater table, severe deterioration of groundwater quality, as well as increased risks of surface flooding (e.g. Niemczynowicz 1999; Weng 2001; Ragab et al. 2003). To overcome such problems, planning of efficient urban drainage systems is essential (Zischg et al. 2019). For example, the decoupling of stormwater run-off from sewage systems can be done by artificial recharge wells (Bouwer 2002).

The selection of the well design is essential in order to obtain an energy-efficient combined dewatering and artificial recharge system for a specific construction site. Ideally, one should base the selection of optimal well set-up dimensions on detailed knowledge about the hydrogeology, the natural groundwater flow in the specific area, the influence of other surrounding wells, as well as on the potential risk of well clogging (Powers et al. 2007; Cashman and Preene 2013). Incomplete characterization of the site hydrogeology complicates the prediction of the hydraulic impact of the entire dewatering system and therefore, may result in a poor quality of the well-system design (Shaqour and Hasan 2008; Jurado et al. 2012). However, in practice drilling companies base their well design on their own drilling experiences in the field and the conventional approaches for dewatering design. Often, lack of knowledge about the local hydrogeology, as well as of the implications of the used well geometry result in non-optimal well designs for a specific field site.

1.3.2 Soil contamination and remediation

Soil contamination by pollutants, such as volatile organic compounds, non-aqueous phase liquids, hydrocarbons, heavy metals and pesticides, occurs due to leakage or accidents at industry and storage facilities, as well as due to spills during transport (Khan et al. 2004; Powers et al. 2007). In the last decades, the impact of such contaminations in the subsurface on human health and environment has been recognized. Hence, the management and remediation of contaminated soils are nowadays stimulated and regulated by governments and industries, and have to be conducted by remediation experts (Khan et al. 2004; Powers et al. 2007). Usually, construction dewatering at contaminated sites combines the aimed groundwater level lowering at the excavation site with groundwater remediation, or plume control to minimize the environmental impact during dewatering (Powers et al. 2007).

In groundwater remediation, one of the most common methods to clean contaminated aquifers is the use of pump-and-treat (Gorelick et al. 1984; Bear and Sun

1998; Bayer et al. 2002; Khan et al. 2004; Powers et al. 2007). In general, abstraction PPWs for groundwater remediation are used to recover contaminants from the most contaminated areas of the aquifer (Fig. 1.1b). Different techniques have been applied, such as vacuum point wells, deep wells, as well as horizontally drilled wells or drains. Remediation of light nonaqueous phase liquids in the subsurface floating on the top of groundwater table requires wells screened in the upper part of the aquifer. For example, the use a well point system, which is easy and cheap to install, allows for a significant number of abstraction points and effective recovery of the contaminants (Powers et al. 2007). PPWs have to be screened at the lower part of the aquifer if the contaminant is a dense non-aqueous phase liquid (DNAPL).

After treatment, the cleaned water can be discharged into surface water or sewage systems, or can be recharged into the aquifer. More innovative remediation methods actively mobilize pollutants by a combined system of infiltration and pumping wells. The in-situ flushing of the contaminated soil by the infiltration of the treated abstraction water actively mobilizes the pollutants in contaminant plume between the two well sites towards the abstraction site (Otterpohl 2002; Khan et al. 2004). The infiltration of the treated abstraction water can be combined with the use of surfactants to enhance mobilization of hydrophobic pollutants (e.g. Juhasz et al. 2003). One needs to ensure that the hydraulic impact of the in-situ soil flushing is controlled at the remediated site in order to avoid transport of contaminants outside the treated area. Hence, good hydrogeology characterization, thorough investigation of the extent of the contamination plume and planning of the well design are required for the groundwater remediation techniques (Johnston et al. 2002; Khan et al. 2004; Rivett et al. 2006; Guo and Brusseau 2017).

1.3.3 Buoyancy-driven flow in aquifer storage and recovery (ASR) systems

In the last decades, the global growth of human population has drastically increased the use of fresh groundwater resources for irrigation, drinking water and industrial production (Jackson et al. 2001). Besides the intensified exploration of drinking and irrigation water, the stresses on fresh groundwater resources are also increased due to the ongoing climate change. In arid and semi-arid environments, severe deterioration of groundwater quality and the salinization of groundwaters by increasing periods of drought and the over-exploration of groundwater by agriculture have a huge impact on fresh groundwater reservoirs. In coastal regions, sea level rise combined with extensive groundwater abstraction also threatens freshwater reservoirs by salinization (Mas-Pla et al. 2013; Werner et al. 2013). In order to secure freshwater supply, better management

of the well placement and pumping rates is required (Cheng et al. 2000; Park and Aral 2004).

Aquifer storage and recharge (ASR) systems (Pyne 2005; Maliva and Missimer 2010) have become a successfully applied method to manage and store freshwater resources in the subsurface. ASR systems combine the use of artificial recharge when a surplus of freshwater is available and the pumping of water from the subsurface during excess of freshwater resources. In practice, successful implementation of ASR systems for the storage of freshwater in brackish aquifers is defined by the recovery efficiency of the freshwater. For an optimal well design one needs to take into account the potential mixing of freshwater with ambient brackish or saline groundwater due to background flow, as well as buoyancy-driven flow. The density contrast between recharged freshwater by ASR and ambient brackish water results in accumulation of freshwater in the upper part of the aquifer during the injection and storage stage (Pyne 2005; Ward et al. 2009).

The use of PPWs is suggested for optimal design of ASR systems (Maliva and Missimer 2010). Injection of freshwater in the lower parts of the aquifer during the recharge stage, combined with abstraction in the upper parts of the aquifer during the production stage can limit the negative buoyancy-effects on the recovery efficiency of the ASR-system (Fig. 1.1c). Zuurbier et al. (2014) have extended this principle to improve the recovery efficiency of their small-scale ASR system by using multiple PPWs. This resulted in successful stabilization of the freshwater volume in the brackish aquifer and reduced mixing caused by the buoyancy contrast. Hence, a three times higher recovery efficiency was obtained compared to an equivalent scenario that uses a fully-penetrating well.

1.3.4 Buoyancy-driven flow in aquifer thermal energy storage (ATES)

Recently, the use of the subsurface to store thermal energy for heating or cooling purposes of buildings has drastically increased (e.g. Paksoy et al. 2000; Sanner et al. 2003; Vanhoudt et al. 2011). Especially in moderate climates, aquifer thermal energy storage (ATES) systems are widely used (Dickinson et al. 2009; Yang et al. 2010; Kranz and Frick 2013; Bloemendal et al. 2018; Fleuchaus et al. 2018). The principle of seasonal ATES is the use of the subsurface to overcome the temporal mismatch of heat surplus and heat demand. Surplus of heat is stored in the aquifer during the summer months, while thermal energy is recovered from the aquifer to fulfil the heat demand during the colder winter months.

Currently, the majority of ATES systems have limited temperature differences (ΔT<15 °C) between the ambient groundwater on the one hand, and the injected warm and cold water on the other hand. The number of high temperature aquifer thermal energy storage (HT-ATES) systems is still limited, although the storage of water with higher temperatures (e.g. >70°C) increases both the energy storage capacity and overall energy efficiency (e.g. Kabus and Seibt 2000; Sanner et al. 2005; Réveillère et al. 2013).

Pilot studies in the field (Palmer et al. 1992; Molz et al. 1979; 1983ab), as well as numerical studies (Buscheck et al. 1983; Schout et al. 2014), have shown that the recovery efficiencies of HT-ATES systems are much lower compared to the typical low- to mid-range ATES systems. This is due to enhanced buoyancy-driven flow caused by the larger temperature contrasts between injected water and ambient groundwater. The studies of Molz et al. (1983ab) and Buscheck et al. (1983) showed that heterogeneous-layering in the aquifer has an impact on free convection during HT-ATES, and thus recovery efficiency. Therefore, the application of HT-ATES in heterogeneous aquifers requires proper characterization of the hydrogeology to predict actual recovery efficiencies. Similar to the use of PPWs to improve the recovery efficiency of ASR-systems (Maliva and Missimer 2010; Zuurbier et al. 2014), HT-ATES systems can be improved with PPWs to minimize the effects of buoyancy-driven flow on thermal recovery efficiencies (Molz et al. 1983a; Buscheck et al. 1983) (see Fig. 1.1d).

1.4 Well hydraulics

For every well application, the selection of the optimal well-type is essential to optimize the energy efficiency of the entire system. Thorough understanding of the well hydraulics is required to minimize head losses during the pumping or recharge of water in the subsurface (Houben 2015ab). Selecting the optimal well-design for a specific well application is always a trade-off between the overall costs of well completion and development, the optimal well hydraulics of the well itself, the hydraulic impact of the well system on its surroundings, as well as the required operational life-span of the well (Powers et al. 2007; Kasenow 2010; Houben 2015ab). For example, water wells for drinking water supply are operational for decades and hence, the use of expensive well completion methods (e.g. the use of large diameter wells, fully-penetrating wells, as well as controlled and precise drilling techniques) could highly reduce the overall energy costs during well operation (Houben 2015b). However, as described above, for some well applications a targeted hydraulic impact in the aquifer is required (see Fig. 1.1). Such wells could range from multiple-PPWs ASR of HT-ATES systems that need to be operational for decades, to dewatering wells with an operational time of several weeks. To make the right choice while balancing the interests of well completion and

development costs, the overall energy costs during well operation, as well as the hydraulic impact during operation, the knowledge on well hydraulics is essential.

1.4.1 Individual components of well loss

Ideally, most of the head losses during groundwater abstraction or injection occurs in the aquifer (Fig. 1.4). Besides the head loss in the aquifer itself, additional components of head loss determine the well efficiency (e.g. Discroll 1986; Barker and Herbert 1992; Bear 2007; Houben 2015ab). During pumping, turbulent flow in the well interior (well casing and screen), as well as through the screen slots cause additional head loss (Houben 2015b). Outside the well screen, additional head loss occurs in the gravel pack and in the skin layer at the borehole wall (Fig. 1.4). Moreover, additional head loss occurs due to partial penetration of the well in the aquifer or the occurrence of a seepage face in unconfined aquifers (Discroll 1986; Barker and Herbert 1992; Chenaf and Chapuis 2007; Kasenow 2010; Houben 2015ab). Starting from the classical work of Thiem (1870), most well hydraulic studies assume uniform influx over the entire length of the well screen. However, in reality this is only the case for homogeneous aquifers. Besides aquifer heterogeneity, also partial penetration of the well and the location of the submersible pump inside abstraction wells influences the rates of volumetric inflow per unit length of the well (e.g. Ruud and Kabala 1997; VonHofe and Helweg 1998; Houben and Hauschild 2011; Tügel et al. 2016; Zhu and Wen 2019). During well operation, clogging of abstraction and injection wells can cause additional head losses (e.g. Houben 2003; De Zwart 2007; Powers et al. 2007; Houben et al. 2018).

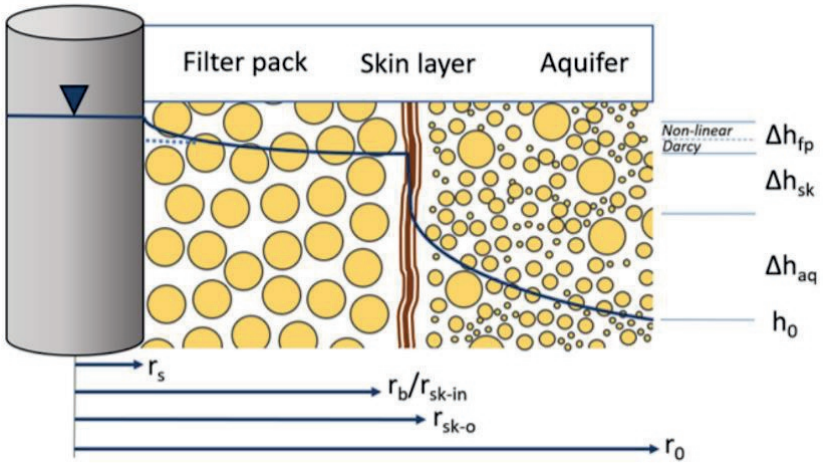

Fig. 1.4 Individual components of well loss in an artificial recharge well.

1.4.2 Well installation and completion

A wide variety of drilling methods is available for the installation of water wells. Each method has its advantages and disadvantages (Powers et al. 2007). In construction dewatering, drilling methods that are quick, easy to handle and cheap are widely used in practice for water wells that need to be operative for a relatively short period. Popular drilling techniques are manual jetting and mechanical uncased hole-drilling by straight flush (Fig. 1.5a) and reversed-circulation rotary drilling (Fig. 1.5b) (Powers et al. 2007). Due to excessive drilling fluid losses and unstable borehole conditions for uncased drilling techniques, drilling through gravel or pebble deposits might require cased borehole drilling techniques, such as sonic, dual rotary or cable tool drilling (see Fig. 1.5c). Moreover, water wells that need to be operative for longer periods might benefit from the time consuming and expensive well completion with cased borehole drilling techniques. For example, the use of drilling fluids to stabilize the borehole wall during uncased drilling techniques (Fig 1.5a-b) causes formation of a low permeability skin layer at the borehole wall, while such skin formation is significantly reduced for cable tool drilled wells (Timmer et al. 2003).

1.4.3 Straight flush rotary and well completion of PPWs

In the Netherlands and Germany, dewatering companies use quick and cheap straight-flush rotary drilling for well completion of artificial recharge PPWs without a filter pack (so-called fast, high volume infiltration (FHVI) wells) in high permeability strata in the aquifer. A skilled drilling operator uses his straight-flush drilling rig to indicate high-permeable layers in an aquifer. During straight-flush rotary, water is pumped down the drill-pipe of the drilling rig to flush out the debris (Fig. 1.5a). The velocity of the flush in the borehole annulus must be sufficient to lift the debris. Large quantities of the flushed water pumped down the drill-pipe are infiltrating into the surrounding soil during this drilling method (Powers et al. 2007). Drilling through high-permeability layers in the aquifer causes significant loss of flushed water volume into the surrounding soil and reduces the velocity of the flush in the borehole annulus. Hence, sometimes a higher flush-velocity must be used at depth if the flush in the borehole annulus is insufficient to lift the debris towards the surface. A large sudden reduction in debris flush outflow at the surface is a good indication of a high permeable layer in the aquifer and can be used by drilling operator to place the PPW at the desired depth in the aquifer. In general, such depths correspond well with high-permeability layers from CPT, borehole logs and in-situ soil data.

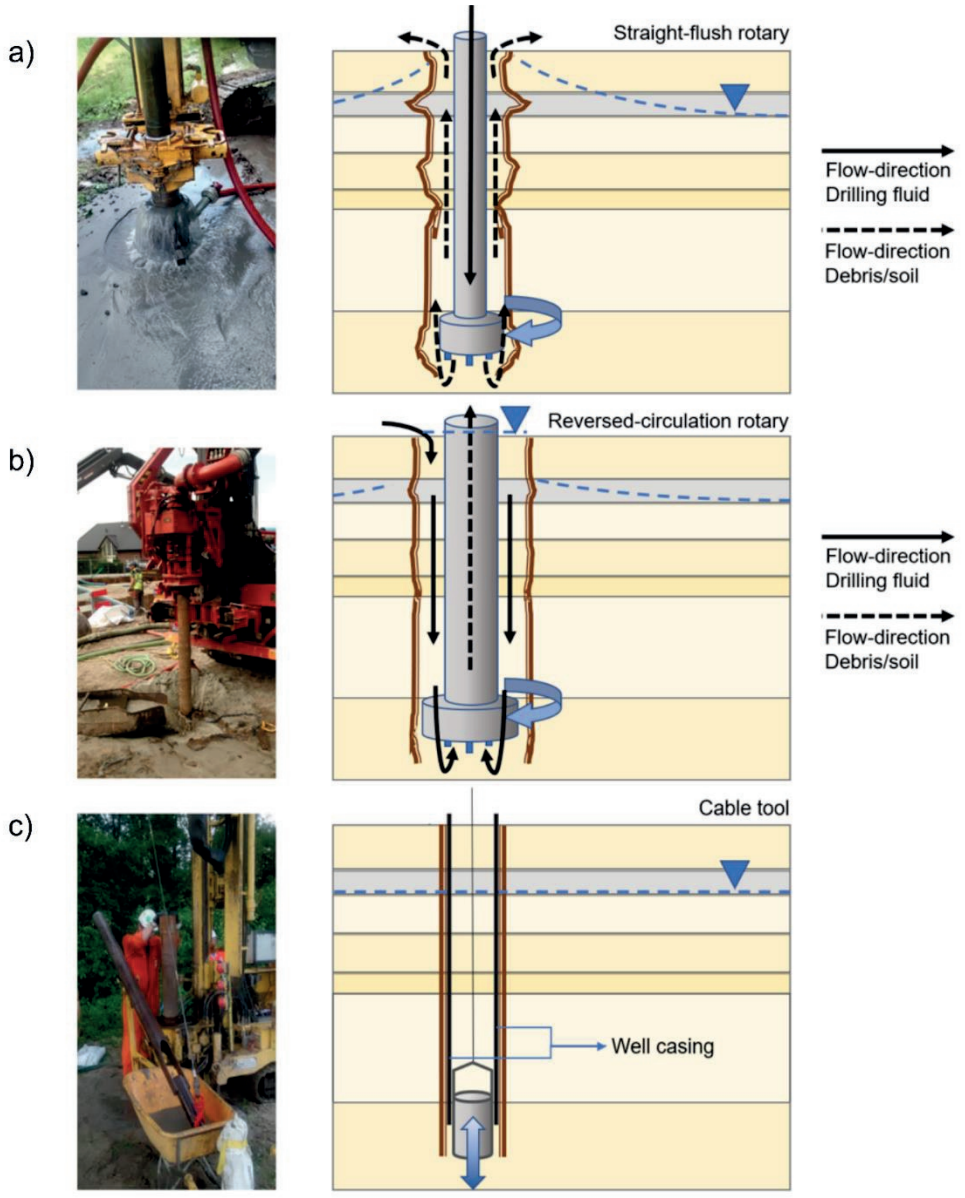

Fig. 1.5 Examples of widely used drilling methods for water well placement in construction dewatering. The schematic overview show the flow-directions in the borehole and drilling rod for uncased drilling with **a)** straight-flush rotary and **b)** reversed-circulation rotary. For reversed-circulation rotary, drilling fluid/debris is commonly discharged to a settling tank/container and re-used as drilling fluid. **c)** Cable tool drilling is an example of a cased drilling method.

1.4.4 Near well-hydraulics in filter pack and aquifer

Most water wells are drilled with a larger borehole diameter than the actual well diameter, allowing to pack the annulus around the well screen with filter sand or gravel. Such sands and gravels usually consists of rounded, uniformly graded granular material (Discroll 1986; Powers et al. 2007; Houben et al. 2015ab). Filter packs are installed to fulfil two different tasks. On the one hand, the filter pack has to ensure that the fines are retained in the aquifer so it will not be pumped into the well screen (e.a. the selected filter sand or gravel need to be sufficiently fine to do so). Sand pumping could cause severe pump damage and sedimentation in the well screen (Discroll 1986; Powers et al. 2007; Houben 2015a). On the other hand, the selection of a coarser filter pack material allows for easy removal of natural fines and mud cake from the borehole wall during well development and rehabilitation. Moreover, replacing aquifer material by coarser, more permeable filter sand or gravel allows for favourable hydraulic properties around the well screen during abstraction or production.

As a consequence, most drilling and well completion handbooks refer to the grain size of the aquifer material in order to select a proper filter pack. Usually, proper filter sand or gravel has an average grain size 4-6 times larger than of the well graded aquifer material (Discroll 1986; Roscoe Moss Company 1990). Powers et al. (2007) even suggest the use of average grain sizes up to 8 times larger, if the aquifer material is very well graded in order to allow for easy removal of natural fines during well development. For well completion of water wells in highly-stratified aquifers, the selection of the filter pack is restricted to the finest stratum. However, the highest abstraction or injection rates occur in the coarser strata of the aquifer and selection of the filter pack based on the finest strata (e.g. silt layers) reduces the these rates significantly. Using PPWs in the relative coarse strata might allow for coarse filter packs (Powers et al. 2007). Houben (2015a) refers to “gravel pack angst” of drilling companies to ensure non-sand pumping wells for costumers by save selection of finer filter packs during well completion. Some studies have investigated the hydraulic properties of different filter pack types and their effect on well efficiency (e.g. Kim 2014).

In practice, only a limited amount of water wells is installed without filter pack. This method of well completion is applicable if a naturally-developed pack can be created by removing fines from well graded material that contains amounts of very coarse sand, gravel or pebbles (Roscoe Moss Company 1990). Drilling with a larger borehole diameter than the installed well diameter causes a collapsed zone of aquifer material with higher hydraulic conductivity. Commonly, well completion without filter pack is often done in construction dewatering and allows for quick installation of water wells. This principle is also used for FHVI wells that are used for artificial recharge.

The hydraulic properties of the filter packs, as well as of the naturally-developed packs (collapsed aquifer zones) are key in order to understand the well hydraulics around wells. Due to high flow velocities (Re>10) by converging or diverging flowlines in the filter pack of respectively abstraction and recharge wells, head loss due to non-linear flow behaviour occurs (Engelund 1953; Basak 1978; Houben 2015b) (see Fig. 1.4). Ideally, the additional head loss due to non-linear flow behaviour in the aquifer, the filter pack, as well as in the naturally-developed pack should be limited. It is believed that non-linear flow behaviour promotes enhanced well incrustation and mobilisation of fines (Houben 2015a). The effect of non-linear flow behaviour in near well-hydraulics is investigated for various aquifer and well types (Sen 1989; Mathias and Todmann 2010; Wen et al. 2011; Mijic et al. 2013; Wen et al. 2013; Zhu and Wen 2019).

1.5 Outline of this thesis

The present thesis provides insight in the processes, conditions and optimization of individual water wells and well systems. Particularly, this thesis focusses on the optimization of two different well-systems in various aquifer systems. At first, the design optimization of construction dewatering systems with partially-penetrating recharge wells is investigated. Finally, the design optimization of seasonal high-temperature aquifer thermal energy storage (HT-ATES) systems that encounter significant heat loss and low thermal recovery efficiencies by buoyancy-driven flow during operation is investigated. This is done in five major parts:

- Design optimization of combined construction dewatering and artificial recharge systems. In **Chapter 2** we investigate the advantage of using PPWs instead of FPWs for artificial recharge near dewatering sites considering different target aquifers with various hydraulic characteristics. This is done by numerical simulation of various simplified pumping-recharge dewatering schemes, as well as by analysis of an experimental recharge test with a PPW in a heterogenous-layered semi-confined aquifer.
- Experimental studies on non-linear flow behaviour in various uniformly-graded sands and gravels (filter sands) in **Chapter 3**, as well as, in natural deposit sands and gravels in **Chapter 4** (aquifer material).
- Investigation of well hydraulics of typical water wells used in construction dewatering. In **Chapter 5** we investigate the implication of various well completion methods, well clogging in different filter pack types, as well as the well-efficiency of PPWs in heterogenous-layered aquifers. For this analysis the hydraulic properties of the sand and gravel tested in Chapter 3 and 4 are used.
- Solute and heat tracer experiments in a heterogeneous aquifer. In **Chapter 6** we experimentally investigate the flow and transport behaviour in the aquifer during injection in an artificial recharge PPW.
- Increasing the thermal recovery efficiency by design improvement of HT-ATES systems. In **Chapter 7** the use of a salinity contrast for density-difference compensation during injection and storage stage is investigated. In **Chapter 8** the use of multiple PPWs during injection and abstraction stage is investigated for various aquifer characteristics.

Chapter 2

Taking advantage of aquifer heterogeneity in designing construction dewatering systems with partially-penetrating recharge wells

Abstract

During construction dewatering, artificial recharge with wells might be required to discharge pumped groundwater. Preferably, artificial recharge wells are placed as close as possible to the construction site to limit the aboveground space for the dewatering infrastructure and the transport costs. However, the hydraulic impact on the dewatering site due to artificial recharge should be small to reduce the overall pumping costs. The present study shows that the use of recharge partially-penetrating wells (PPWs) in heterogeneous aquifers screened at depth minimize the hydraulic impact at the dewatering site. Sensitivity analysis show that a PPW (screened at 20 mbgl in a 25 m thick aquifer can be installed much closer to the dewatering site than a fully-penetrating well (FPW). For example, to obtain a required drawdown of 2.4 m within a radius of 10 meters from the abstraction site in a high-permeability aquifer (K=73 m/d) for combined abstraction and recharge at a rate of Q=250 m^3/h, PPWs can be installed at 20 m distance, while FPWs need to be installed at a distance of 41 m. Experimental recharge tests in the field were conducted in a heterogeneous layered semi-confined aquifer using a cheap and quickly installed naturally-developed recharge PPW screened in a relatively high permeable layer of 300 m/d and a FPW installed with a more expensive well completion method. Accounting for the vertical variability of hydraulic conductivity by good soil characterization is required for the PPW with limited screen length to predict near-well hydraulics accurately.

Submitted as: Van Lopik, J.H., Hartog, N., & Schotting, R.J. Taking advantage of aquifer heterogeneity in designing construction dewatering systems with partially-penetrating recharge wells. *Hydrogeology Journal*.

2.1 Introduction

In the last decades, the use of underground space in urban areas is drastically increased for the construction of building foundations and infrastructure (e.g. Tan and Wang 2013; Fang et al. 2016). In areas with shallow groundwater levels, or in deep excavation pits construction dewatering is widely used for lowering groundwater table inside the excavation pit (Power et al. 2007; Cashman and Preene 2013; Pujades et al. 2014). In general, dewatering procedures affect the design, the construction procedures, and overall costs of the construction project. Hence, dewatering systems should be carefully designed using the knowledge of the soil characteristics, hydraulic properties and construction dimensions for a specific field site (Galeati and Gambolati 1988; Wang et al. 2002; Power et al. 2007). Poor characterization of the subsurface in the design stage of dewatering systems can result in significant failure of the system and a drastic effect on the safety of the construction works, as well as increase the project costs by highly overdimensioning the entire dewatering system (Power et al. 2007; Jurado et al. 2012; Cashman and Preene 2013).

Discharge options of the pumped groundwater vary depending on the project scale and duration, as well as the hydraulic and environmental impact. Water can be discharged in sewerage systems, surface waters and in the subsurface by artificial recharge. Artificial recharge is done in the same dewatered aquifer, or in other target aquifers. In many countries, governing and environmental laws could largely restrict the amount of recharge options in surface waters for dewatering designs (Powers et al. 2007; Preene and Brassington 2007). For example, dewatered water can contain suspended solids (e.g. precipitated iron oxides) which are highly visible and potentially harmful to aquatic flora and fauna. Potential petroleum and contaminant residues in the aquifer from leakage and spill events are a potential risk to the environment and require extensive, costly treatment if they are abstracted during dewatering, while the mobilization of such contaminants in the aquifer during dewatering have to be avoided (e.g. Preene and Brassington 2007). Often, the pumped groundwater from the construction site must be recharged in the same aquifer close to the construction site to minimize the overall hydraulic and environmental impact (Cashman and Preene 2013).

To obtain an optimal dewatering design, it is key to reduce both the hydraulic impact on shallow groundwater levels outside the dewatered excavation site, as well as the hydraulic impact due to artificial recharge. For example, the old city centres of Copenhagen and Amsterdam are built on weak soils and have a strict ban on groundwater table lowering to limit the potential damage of the wooden foundation of old buildings (Cashman and Preene 2013). Especially for large dewatered groundwater volumes at deep excavation sites, the hydraulic impact outside the excavation pit and the risk on

settlement by groundwater lowering is large (e.g. Forth 2004; Roy and Robinson 2009; Pujades et al. 2017). A popular method to reduce the hydraulic impact of the dewatering project and prevent large groundwater influx rates into the excavation site is the use sealing curtains, such as sheet piling, diaphragm/slurry walls and soil grouting that penetrate partially into the pumped aquifer (Wang et al. 2013; Pujades et al. 2014, Wu et al. 2017). Consequently, the pumping-induced drawdown and settlement outside the excavation pit are reduced. However, vertical sealing curtains become cost-prohibitive for smaller shallow open or trench excavations where stable sides around the construction site can be attained throughout the entire construction operation to minimize the construction costs.

In addition, to mitigate groundwater lowering outside the dewatered site artificial recharge by infiltration wells is used in the same aquifer to prevent ground settlement outside the excavation (Zhang et al. 2017; Zeng et al. 2019). However, the shallow groundwater level rise due to artificial recharge should be taken into account to exclude potential damaging effects on surrounding underground buildings structures and infrastructure.

The negative hydraulic impact of artificial recharge near the excavation site on groundwater table lowering during dewatering is key for dewatering design. Higher pumping costs due to increased groundwater influx from the artificial recharge site into the dewatered excavation site need to be taken into account. In practice, the artificial recharge wells screen large parts of the aquifer to maximize recharge efficiency and minimize the rate of clogging over time (Powers et al. 2007). For planning and predicting the hydraulic impact of small dewatering projects, two-dimensional analytical solutions or numerical models usually suffice since groundwater flow is strictly in the lateral direction in the entire aquifer while using such artificial recharge wells (Fig. 2.1a). (e.g. Phien-wej et al. 1998; Powers et al. 2007; Zheng et al. 2019). The disadvantage of using fully-penetrating wells (FPWs) for artificial recharge is that the hydraulic impact on shallow groundwater levels is relatively high. Hence, artificial recharge wells are ideally installed downstream of the extraction site at considerable distance such that the pumping and infrastructure costs are at an optimum. (Powers et al. 2007; Cashman and Preene 2013). Particularly, in urbanized areas the available space at surface level is also a limiting factor in obtaining an optimal location for the artificial recharge.

The placement of partially-penetrating wells (PPWs) in deeper parts of the aquifer can be beneficial compared to FPWs due to reduced hydraulic impact in the upper part of the aquifer (Fig. 2.1b). The use of recharge wells that are only partly screened over the aquifer thickness, results in a hydraulic gradient over depth and, therefore, a significant vertical flow component in the vicinity of the well (e.g. Barker and Herbert 1992; Houben 2015a). In addition, anisotropy (lower vertical permeability) of aquifers

result in preferential lateral flow paths at depth and hampers flow in the vertical direction. Consequently, reduced head rise at shallow groundwater levels can be obtained with artificial recharge by PPWs in deeper portions of the aquifer compared to equivalent recharge with FPWs, allowing for closer placement of artificial PPWs to the dewatering site compared to FPWs (Fig. 2.1).

In dewatering projects, dewatering PPWs screened in the upper part of the aquifer are commonly used to target the hydraulic impact and reduce the shallow groundwater levels at a minimum of pumping costs (Powers et al. 2007). Dewatering systems for small excavation sites use well point systems at shallow aquifer depths, mostly in combination of diesel-powered pumps to obtain the desired groundwater table lowering. For deep excavation sites and larger pumped groundwater volumes, deep-wells with submersible pumps are used at targeted depth (Powers et al. 2007; Cashmann and Preene 2013). Wang et al. (2013) and Wu et al. (2017) show that the use of partial penetrating pumping wells embedded by sealing curtains can change the lateral flow to optimize the dewatering design. Jin et al. (2015) suggest the use of a vertical circulation well to minimize the hydraulic impact at shallow subsurface levels during dewatering.

However, to our knowledge, the use of artificial recharge PPWs to target the hydraulic impact to an aquifer depth with favourable hydraulic characteristics during construction dewatering is rarely done in practice. Therefore, in the present study, the potential use of recharge PPWs with limited screen lengths (1 m) instead of FPWs are tested experimentally and numerically for optimization of construction dewatering designs. At first, the potential of artificial recharge with PPWs is tested numerically with a simplified modelling scheme considering one abstraction well (dewatering) and one artificial recharge well (Fig. 2.1). A sensitivity analysis was performed to calculate the hydraulic impact at shallow groundwater level. This was done for:

1) Different PPW and FPW configurations assuming different horizontal distances between abstraction and recharge well, as well as different recharge depths for the PPW in a homogeneous anisotropic target aquifer.
2) Different aquifer characteristics of the target aquifer (e.g. aquifer thickness, unconfined/confined and anisotropy).
3) Scenarios that consider heterogeneous layering in the target aquifer by accounting for vertical variability in the hydraulic conductivity instead of assuming one equivalent homogeneous anisotropic aquifer.

The efficiency and potential of artificial recharge with a PPW with limited filter length was tested experimentally in a layered heterogeneous sandy with constant recharge rate tests. Similarly, constant recharge rate tests on a FPW that screened the entire depth of this target aquifer were performed. The spatial three-dimensional hydraulic head distribution of the PPW was measured and compared with the FPW. The importance of selecting the optimal screen depth of a PPW based on the aquifer heterogeneity is taken into account to minimize the required well head during recharge. The impact on the near-well hydraulic heads with the PPW in the heterogenous layered target aquifer was compared to an hypothetical homogeneous aquifer by numerical simulations.

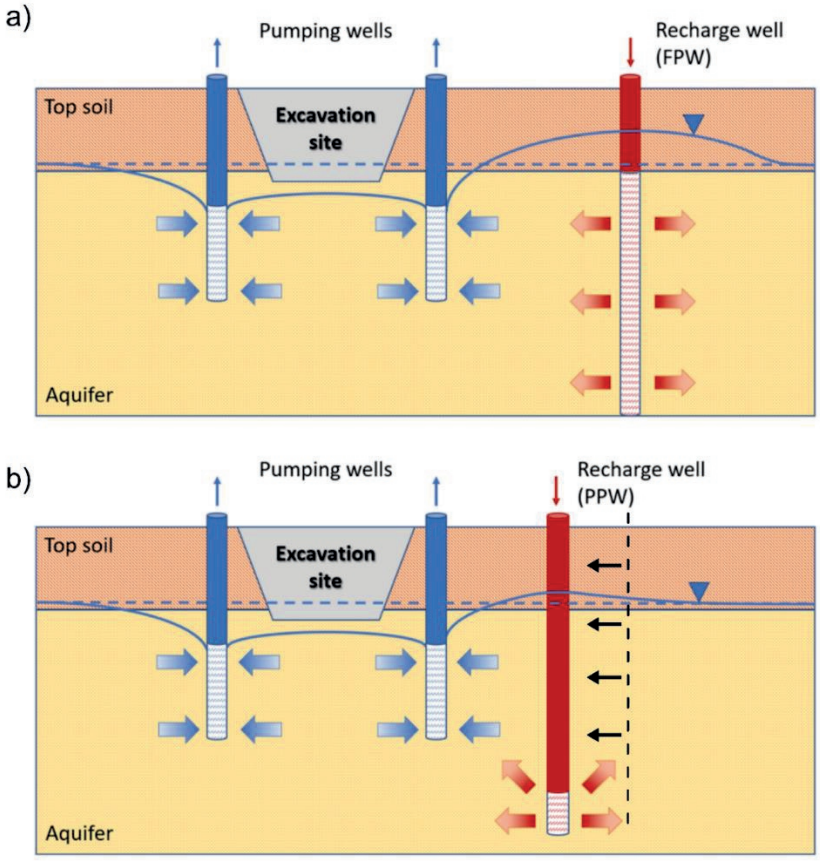

Fig. 2.1 Schematic overview of construction dewatering with **a)** a fully-penetrating well (FPW) and **b)** a partially-penetrating well (PPW). Considering no background groundwater flow, the initial groundwater table prior to the dewatering is given by the dashed line. The groundwater table during combined pumping and artificial recharge is given by the solid line.

2.2 Theory

In general, the Dupuit-Forchheimer assumption can be used for wells that screen a large part of an unconfined aquifer (Bear 2007). This assumption postulates that flow towards and from a well is lateral, and all vertical flow components are ignored. Multiple classical analytical solutions for stationary flow from and towards wells are determined (e.g. for a confined aquifer by Thiem (1870), and a semi-confined aquifer by De Glee (1930) and Hantush and Jacob (1955). The De Glee-Jacob-Hantush equation is:

$$\Delta h(r) = \frac{Q_{in}}{2\pi KH} \mathrm{K}_0 \left(\frac{r}{L}\right) \tag{2.1}$$

where Δh [m] is the hydraulic head increase, Q_{in} [m^3/d] is the constant injection rate, K [m/d] is the horizontal overall conductivity of the aquifer, H [m] is the aquifer thickness, r [m] is the radial distance and L [m] is the leakage factor, which is defined as:

$$L = \sqrt{kHc} \tag{2.2}$$

where c [d] is the vertical resistance of the aquitard. The analytical De Glee-Jacob-Hantush equation (Eq. 2.1) is used to predict the FPW constant recharge rate test in the semi-confined aquifer at the field site. This is done to provide good estimates of the over overall horizontal hydraulic conductivity of the target aquifer at the field site.

In the vicinity of PPWs the vertical flow components close to the well screen are significant and, therefore the Dupuit-Forchheimer assumption does not hold. Hence, Eq. 2.1 cannot be used for analysis of the constant recharge rate tests with the PPWs (e.g. Tügel et al. 2016). The extent of the vertical flow component around the well depends on the characteristics of the aquifer (thickness, hydraulic conductivity, heterogeneity) and the well screen length.

2.3 Field test on recharge wells

2.3.1 Site and soil description

The fieldwork area is located near Rheindahlen (Fig. 2.2), about 10 km southwest of Mönchengladbach (Germany). The recharge tests were conducted prior to a dewatering project for the construction of an underground influx channel for discharge of rainwater from the urban area of Mönchengladbach to a rainwater retention basin.

The top soil consists of loam and loess deposits (Gell & Partner GbR 2009). Based on multiple small ramming drilling samples up to a depth of 8 mbgl the hydraulic conductivity of the top is in the range of 0.1 to 0.4 m/d. At the field site location, these deposits extend to a depth of approximately 5 m. The aquifer at the field site location is 20 meter thick with its bottom at approximately 25 mbgl. The aquifer consists of Pleistocene river terrace sediments of the Rhine river. The aquifer increases in thickness in northeast direction with its bottom at 20 mbgl (15 m thickness) in the southwest of the area, and at 30 mbgl (25 m thickness) in the northeast of the area (Gell & Partner GbR 2009).

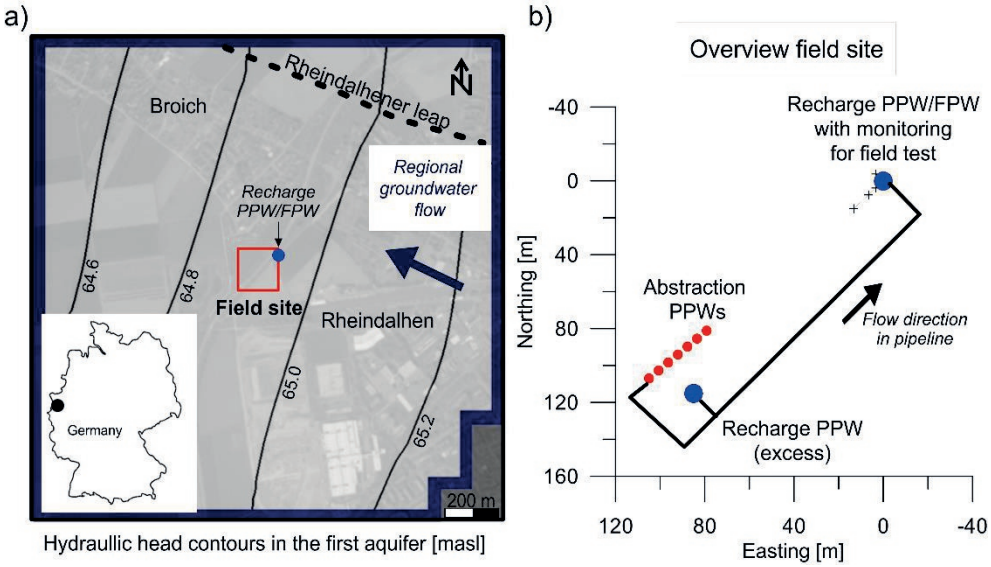

Fig. 2.2 a) The field area with the hydraulic head contours (meter above sea level, masl), and the regional groundwater flow direction. In the centre, the test site is shown with the exact well location fo the recharge PPW/FPW. **b)** Schematic plan view of the recharge test site with the location of the used abstraction and recharge PPWs, as well as the monitoring wells.

Soil samples were taken over the entire aquifer depth (up to 25 mbgl) at the recharge well location with a sampling interval of 0.5 m (Fig. 2.3). The hydraulic conductivity was estimated from the grainsize, d_{50} using the Kozeny-Carman relation:

$$K = \frac{g\rho}{\mu}\frac{d_{50}^2}{180}\frac{n^3}{(1-n)^2} \tag{2.3}$$

where ρ [kg/m^3] is the fluid density, μ [kg/(m s)] is the dynamic viscosity, g [m/s^2] is the gravity acceleration constant, d_{50} [m] is the median grain size of the porous medium and n [-] is the porosity. An average porosity of 0.32 is assumed. The estimated hydraulic conductivity over depth is shown in Fig 2.3c. According the soil data, the average hydraulic conductivity of the aquifer is 73 m/d. However, the target aquifer is very heterogeneous ranging from sandy fine/medium gravel layers with estimated hydraulic conductivities up to 480 m/d up to silty fine sand with estimated hydraulic conductivities around 1 m/d. Heterogeneous layering of the aquifer (pan-cake model) can be assumed based on borelogs in the near-well vicinity of the PPW/FPW test site. The target aquifer is underlain by confining unit of Pliocene clay of the Reuver formation of approximately 3-5 m thick with a hydraulic conductivity smaller than $9 \cdot 10^{-4}$ m/d. The top of this confining unit is considered as the base of our model.

The study area is located at the Venloer graben of the Lower Rhine Graben system. northeast from the study area, the Rheindalhener leap extents into the Quaternary river terrace sediments of the target aquifer, resulting in a clear geological offset with Miocene marine fine sands (K~1m/d) starting at a depth of approximately 7 mbgl at the northern part of the leap (Gell & Partner GbR 2009). The groundwater flow is in the northwest direction (see Fig. 2.2).

2.3.2 Arrangement of the recharge and observation wells

The layout of the abstraction and recharge wells used for the recharge tests is shown in Fig. 2.2b. A vacuum dewatering system was used to pump groundwater from a set of abstraction PPWs, screened at a depth of 6-8 mbgl, to the recharge well at the test site. Excess groundwater was recharged on PPW (excess), which is screened at 19.5-20.5 mbgl (Fig. 2.2b). The tested recharge PPW and FPW, as well as the observation points are placed at a distance of approximately 110 m from the abstraction PPWs (Fig. 2.2b) to minimize the hydraulic impact due to abstraction. For this field experiment, first a recharge PPW was installed and tested. Subsequently, this recharge PPW was replaced by a recharge FPW.

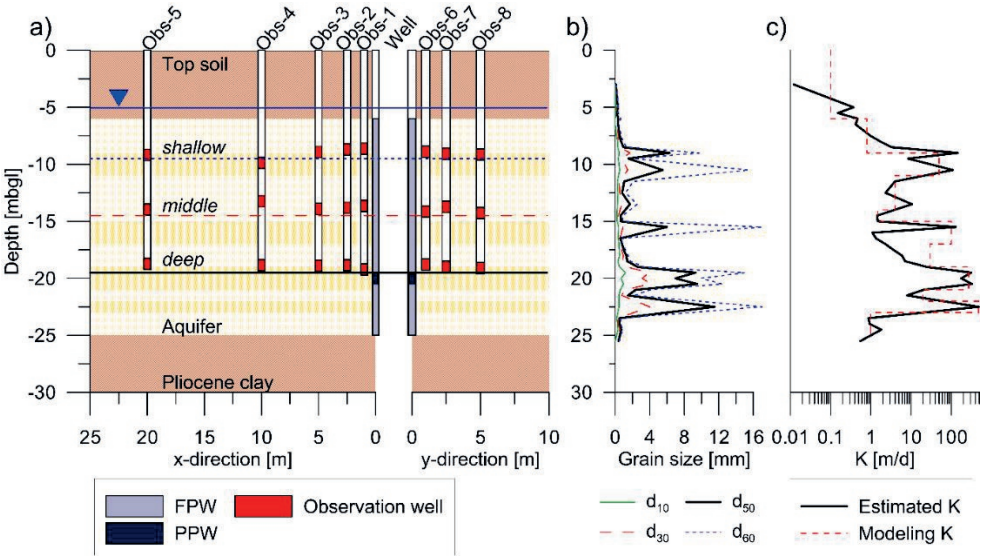

Fig. 2.3 a) Cross-section of the soil in the x- and y-direction, where the observation wells 1-5 are alligned in the x-direction, while 6-8 are alligned in the y-direction (see Fig. 2.2b). The solid black (*deep*), dashed red (*middle*) and dashed blue (*shallow*) lines indicate the monitoring depths in the aquifer at 9.5, 14.5 and 18.5 respectively. **b)** The determined grain sizes d_{10}, d_{30}, d_{50} and d_{60} of the soil samples by sieve analysis. **c)** The hydraulic conductivity over depth estimated by Kozeny-Carman, as well as the hydraulic conductivity used for the numerical model.

Installation of the recharge PPW

Initially, a borehole was drilled using straight-flush rotary. The naturally-developed PPW (⌀110 mm) without a filter pack was installed in the target aquifer with its filter screen in the high-permeable gravel layer at 19.5-20.5 mbgl (see Fig. 2.3). The PPW was drilled with straight-flush rotary. Prior to these recharge tests, an airlift pump is used to increase the well efficiency of the PPW. Initially, the performance of the PPW was quite bad, resulting in relative low discharge rates (up to only 15 m^3/h). Airlifting was applied for approximately one hour, resulting in an increased well performance (enabling discharge rates up to 25 m^3/h). Constant recharge rates in the recharge PPW (Fig. 2.3) were applied at approximately, 23, 19.5 and 14 m^3/h for Cases 1.P, 2.P and 3.P respectively (see Appendix A).

Installation of the recharge FPW

Subsequently, the PPW was pulled and replaced by FPW in the target aquifer. At the same location a borehole (⌀300 mm) was drilled using reversed-circulation rotary. A conventional infiltration well (⌀250 mm) with filter pack (1.0-1.6 mm) screened between 5 and 25 (mbgl) was placed. A bentonite clay plug was used for the upper 5 m screened in the top soil. Several recharge tests at constant recharge rates of 32.3 m^3/h (Case 1.F) and 16.7 m^3/h (2.F) were conducted on the FPW.

Monitoring configuration

In order to measure the hydraulic impact around the infiltration wells, eight boreholes were drilled with in each borehole a set of three monitoring wells with one meter screen length. The monitoring depths were at shallow (9.5 mbgl), middle (14.5 mbgl) and deep (19.5 mbgl) aquifer depths (Fig. 2.3a). Observation wells 1-5 were placed from southwest to northeast and observation wells 6-8 are placed from southeast to northwest (Fig. 2.2b). During each infiltration test the hydraulic head was monitored with pressure transducers (model 14 Mini-diver DI501, Schlumberger) with a measurement accuracy of 0.5 cmH2O. Manual hydraulic head measurements were done to check the diver data during the infiltration tests.

2.4 Modeling set-up

2.4.1 Numerical sensitivity analysis on the efficiency of recharge PPW

The three-dimensional steady-state groundwater flow in the simplified construction dewatering scheme is simulated with the groundwater model MODFLOW-2000 (Harbaugh et al. 2000). The groundwater flow is solved using the Preconditioned Conjugate Gradient 2 (PCG2) solver. The model domain is 1.5 by 1.5 km. A semi-confined aquifer of 20 meter thickness is assumed overlain by a 6 meter thick confining unit (hydraulic conductivity of 0.1 m/d). No background groundwater flow is considered. Simplified dewatering systems with one abstraction well in the top of the semi-confined aquifer and PPWs/FPWs at various recharge depths (Δz) and distances (Δx) from the abstraction well were tested numerically in the centre of the model domain (see Fig. 2.4). The screen length of the abstraction PPW is 3 m and screens between 6.5-9.5 mbgl, while the length of the artificial recharge PPW is 1 m and screens at various depths with the center of the well screen at depth (Δz). For this model a refined lateral and vertical discretization (Δx, Δy and Δz=0.1 m) was used in the vicinity of the wells to allow for steep hydraulic gradients in the zone of recharge and abstraction, with increasing grid sizes towards the model boundary (up to Δx and Δy of 100 m and Δz of 1 m).

Equal volumetric abstraction and recharge rates ($10<Q<50$ m^3/h) are used to model combined abstraction for dewatering and artificial recharge. The drawdown s is calculated at shallow aquifer depth (6.25 m) to account for the hydraulic impact due to recharge with the different recharge well configurations (see Fig. 2.4). The ratio λ between calculated drawdown (s) and the volumetric abstraction/recharge rate is determined:

$$\lambda = s/Q \tag{2.4}$$

where λ [h/m^2] is the relative drawdown. The relative drawdown is calculated for assessment of the sensitivity analysis and for scaling to required drawdowns for realistic volumetric abstraction/recharge rate in dewatering systems.

The model parameters used for the different cases of the sensitivity analysis are listed in Table 2.1. First, a detailed overview is given to analyze the effect on the drawdown in the upper portion of the aquifer using recharge PPWs in a homogeneous anisotropic semi-confined aquifer (based on the hydraulic characteristics of the field site aquifer (see section 2.3.1 '*Site and soil description*'). Case 1.1-4 were simulated to show the effect of varying the distance (Δx) between the pumping well and PPW at the given recharge depths ($10<\Delta z<25$ mbgl).

Besides the dimensional aspect of the dewatering design with artificial recharge PPWs (Case 1.1-4), the hydraulic impact while using an artificial recharge PPW at Δx=20 and Δz=20 m instead of a FPW in different kinds of aquifers is analyzed. This is done for an unconfined aquifer (Case 2), a fully confined aquifer (Case 3), a thinner and thicker aquifer thickness (Case 4-5), an aquifer with a higher and lower hydraulic conductivity (Case 6-7) (Table 2.1). In addition, the effect of overall aquifer anisotropy on the dewatering-recharge system is tested (see Case 8-9).

		Top soil				**Aquifer**	
		K_H [m/d]	**K_v [m/d]**	**$H_{aq.}$ [m]**	**a (K_H/K_V)**	**K_H [m/d]**	**K_v [m/d]**
Case 1	***Ref. scenario***	0.1	0.1	20	10	72.7	7.27
Case 2	***Uncon. Aq.***	***72.7***	***7.27***	20	10	72.7	7.27
Case 3	***Con. Aq.***	**-**	**-**	20	10	72.7	7.27
Case 4	***H = 15 m***	0.1	0.1	***15***	10	72.7	7.27
Case 5	***H = 25 m***	0.1	0.1	***25***	10	72.7	7.27
Case 6	***K=10 m/d***	0.1	0.1	10	10	***10***	***1***
Case 7	***K=5 m/d***	0.1	0.1	10	10	***5***	***0.5***
Case 8	***Isotr. (a=1)***	0.1	0.1	10	***1***	72.7	***72.7***
Case 9	***Aniso. (a=2)***	0.1	0.1	10	***2***	72.7	***36.35***

Table 2.1 The aquifer characteristics for different types of homogeneous aquifers used for the sensitivity analysis.

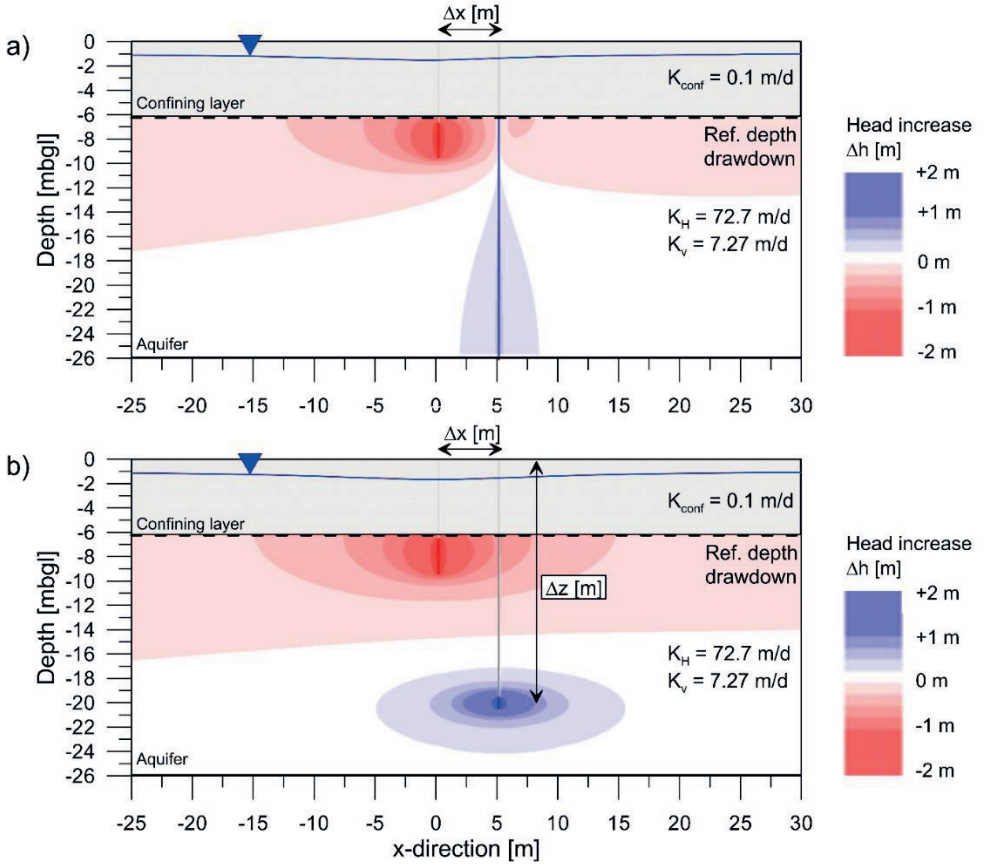

Fig. 2.4 Head increase (Δh) contours for combined abtraction at shallow aquifer depth and artificial recharge at a recharge rate of 40 m^3/h with **a)** a FPW and **b)** a PPW. This cross-section is the base case 1.1. The lateral distance between the two wells is indicated by Δh and the screen depth of the PPW is indicated by Δz for the Cases 1.1-4.

In nature, aquifers are heterogeneous and the vertical variation in hydraulic conductivity can be large. Hence, the effect of heterogeneous layering in an aquifer is investigated for dewatering and recharge with PPWs (Cases 10-14, see Table 2.2). In this part of the sensitivity analysis a hypothetical set of target aquifers is selected, all containing horizontal layers that alternate in hydraulic conductivity over depth. Various high-permeable layers in a given target aquifer are considered. Often, the variation in permeabilities of stratified aquifers with altering sand or gravel layers is simplified to an equivalent homogeneous anisotropic aquifer (e.g. Kasenow 2010). The horizontal conductivity (K_h) of a layered aquifer is the arithmetic mean of the hydraulic conductivity of each layer:

$$K_h = \frac{\sum(K_{h,i} b_i)}{H} \tag{2.5}$$

where, H [m] is the aquifer thickness, b [m] is the thickness of layer i, $K_{h,i}$ [m/d] is the horizontal of layer i. The vertical hydraulic conductivity (K_v) can be calculated using the thickness-weighted harmonic mean:

$$K_v = \frac{H}{\sum \frac{b_i}{K_{v,i}}} \tag{2.6}$$

where $K_{v,i}$ [m/d] is respectively the vertical hydraulic conductivity of layer i.

The aim of this part of the sensitivity analysis is to assess the implications of simplifying the target aquifer to one homogenous anisotropic aquifer. For each case, the heterogeneous layering of the target aquifer is considered, as well as the scenario with an equivalent homogeneous anisotropic aquifer. Isotropic layers in the target aquifer are considered for Case 10-13 (see Table 2.2). In Case 14, the same heterogeneous layering as in Case 11 is assumed considering anisotropy of 10.

	Heterogeneous layering aquifer Case (10.1-14.1)				Homogeneous anisotropic aquifer Case (10.2-14.2)	
	H_{aq} [m]		K_h [m/d]	K_v [m/d]	K_h (Eq. 2.5) [m/d]	K_v (Eq. 2.6) [m/d]
	Top	Bottom				
Case 10	6	19	47.45	47.45	72.7	51.81
	19	21	300	300		
	21	26	47.45	47.45		
Case 11	6	11	72.7	72.7	72.7	47.62
	11	19	37.73	37.73		
	19	21	300	300		
	21	26	37.73	37.73		
Case 12	6	11	72.7	72.7	72.7	8.44
	11	12	40.84	40.84		
	12	13	0.5	0.5		
	13	19	40.84	40.84		
	19	21	300	300		
	21	26	40.84	40.84		
Case 13	6	11	72.7	72.7	72.7	10.31
	11	19	6.96	6.96		
	19	21	500	500		
	21	26	6.96	6.96		
Case 14	6	11	72.7	7.27	72.7	4.762
	11	19	37.73	3.773		
	19	21	300	30		
	21	26	37.73	3.773		

Table 2.2 The hydraulic conductivities of the layered heterogeneous aquifer and the equivalent homogeneous anisotropic aquifer.

2.4.2 Numerical analysis of field data

Similar to the sensitivity analysis, a model domain of 1.5 by 1.5 km was used (see Fig. 2.2). The PPW, as well as the FPW recharge tests are simulated assuming both the derived aquifer heterogeneity as shown in Fig. 2.3c, as well as an equivalent homogeneous aquifer with the average calculated hydraulic conductivity (Eq. 2.5) of 72.7 m/d (see Table 2.3). The three-dimensional aquifer characteristics and well locations as described in section 2.3.1 '*Site and soil description*' are used. Constant head boundaries results in an equivalent background groundwater flow as observed at the field. Again, lateral and vertical grid refinement (Δx, Δy and Δz = 0.1 m) was used in the vicinity of the wells to allow for steep hydraulic gradients in this zone, which resulted in convergence of the numerical solution. Grid refinement of 1 m for Δx and Δy is applied at $660<l_x<810$ and $700<l_y<860$ m.

Both the discharge rate at the abstraction PPWs and the recharge rate at the PPWs and FPW are given in Table 2.4 for all cases. We have used a constant head for numerical simulation of steady-state recharge. This allows for non-uniformly distributed flow rate over the entire well screen, as is usually the case for PPWs and heterogeneous aquifers (e.g. Ruud and Kabala 1997; Houben and Hauschild 2011; Houben 2015a; Tügel et al. 2016).

Parameters		**Value**	**Unit**
Dimensions (l_x, l_y)		1500, 1500	m
Depth l_z		19-31 *(51-39 masl)*	m
Discretization, Δx		0.1-100	m
Discretization, Δy		0.1-100	m
Discretization, Δz		0.1-6	m
Porosity		0.32	-
K_h, K_v (Aquitard)		0.1	m/d
K_h, K_v (Aquifer north R. leap)		1	m/d
K_h, K_v (Aquifer)	Homog.	72.7	m/d
K_h, K_v (Aquifer)	Heterog.	0.8-480	m/d

Table 2.3 Parameters used for the numerical modelling of the PPW and FPW recharge tests.

FPW		Abstraction PPWs [m^3/h]	Excess recharge PPW [m^3/h]	Recharge FPW [m^3/h]	Well head at FPW Δh_{FPW} [m]
Case F.1	*Heterogen.*	-32.4	-	32.4	0.77
Case F.2	*Heterogen.*	-32.4	15.7	16.7	0.39
PPW		**Abstraction PPWs [m^3/h]**	**Excess recharge PPW [m^3/h]**	**Recharge PPW [m^3/h]**	**Well head at PPW Δh_{PPW} [m]**
Case P.1	*Heterogen.*	-23	-	23	1.51
	Homogen.	-23	-	23	4.66
Case P.2	*Heterogen.*	-23	3.5	19.5	1.28
	Homogen.	-23	3.5	19.5	3.95
Case P.3	*Heterogen.*	-23	9	14	0.91
	Homogen.	-23	9	14	2.8

Table 2.4 The discharge and recharge rates on the abstraction wells (PPWs), the excess water discharge (PPW), as well as the recharge PPW and FPW at the test site. The required well heads (Δh_{FPW} and Δh_{PPW}) to simulate the recharge rates on FPW/PPW are also given.

2.5 Results

The results in this study are presented in two parts. First, the sensitivity analysis are presented in which various simple pumping-recharge set-ups in different aquifer types and with PPW configurations are analyzed. This sensitivity analysis predicts the potential hydraulic impact reduction using recharge PPWs instead of FPWs for dewatering designs. It can be used for upscaling to dewatering procedures at the field scale with multiple abstraction and recharge wells. Finally, the efficiency of the proposed PPW configuration in the sensitivity analysis (of 1 meter filter length) is tested experimentally in a heterogeneous target aquifer. The monitored hydraulic head rise in the near-well vicinity at constant recharge rate for both experimentally tested FPW and PPW configuration are analyzed numerically, while assessing the importance of aquifer heterogeneity.

2.5.1 Sensitivity analysis on the efficiency of PPW during dewatering

The spatial three-dimensional use of recharge PPWs

In this sensitivity analysis is tested the effect of artificial recharge with a FPW and PPW on the dewatering drawdowns in the surrounding area. The results showed a significant increase in drawdown at shallow aquifer levels using the PPW at a depth of 20 mbgl (Fig. 2.4b), compared to the use of a FPW at similar distance Δx from the pumping well (Fig. 2.4a). The multiple numerical simulations (Cases 1.1-4) done for the recharge PPWs placed at different Δx and Δz show that for PPWs screened at depths of Δz>10 mbgl a significantly lower hydraulic impact in the vicinity of dewatering well is obtained compared to the equivalent scenario with a FPW at a similar recharge distance Δx (see Fig. 2.5). With increasing distance from the pumping well at Δx=50 m, the difference in hydraulic impact between the PPW and the FPW becomes negligible (Cases 1.4).

The abstraction-recharge well scheme shown in Fig. 2.4 can be used to roughly estimate the drawdown for a simplified construction dewatering design, assuming the dewatering site as bulk abstraction well and the recharge site as bulk injection well. For example, the required drawdown within a radius of 10 meters from the abstraction well(s) (Δx = 10) is ~2.4 m for construction dewatering, while considering combined abstraction and recharge at a rate of Q=250 m^3/h. The recharge PPWs are screened at 20 m depth (Δz) and at approximately 20 meter distance (Δx) from the pumping wells. Using this well configuration and ratio λ from Fig. 2.5c at Δx=10, the aimed drawdown is attained ($s_{PPW} = \lambda Q$ = 0.01·250=2.5 m), while for a FPW placed at Δx=20 the drawdown is only 1.75 m ($s_{FPW} = \lambda Q$ = 0.007·250=1.75 m). To obtain a similar drawdown at Δx=10 m with a FPW, the required distance from the pumping wells (Δx) must be 41 m (lower than the value at 50 m; $s_{FPW} = \lambda Q$ = 0.0106·250=2.66 m).

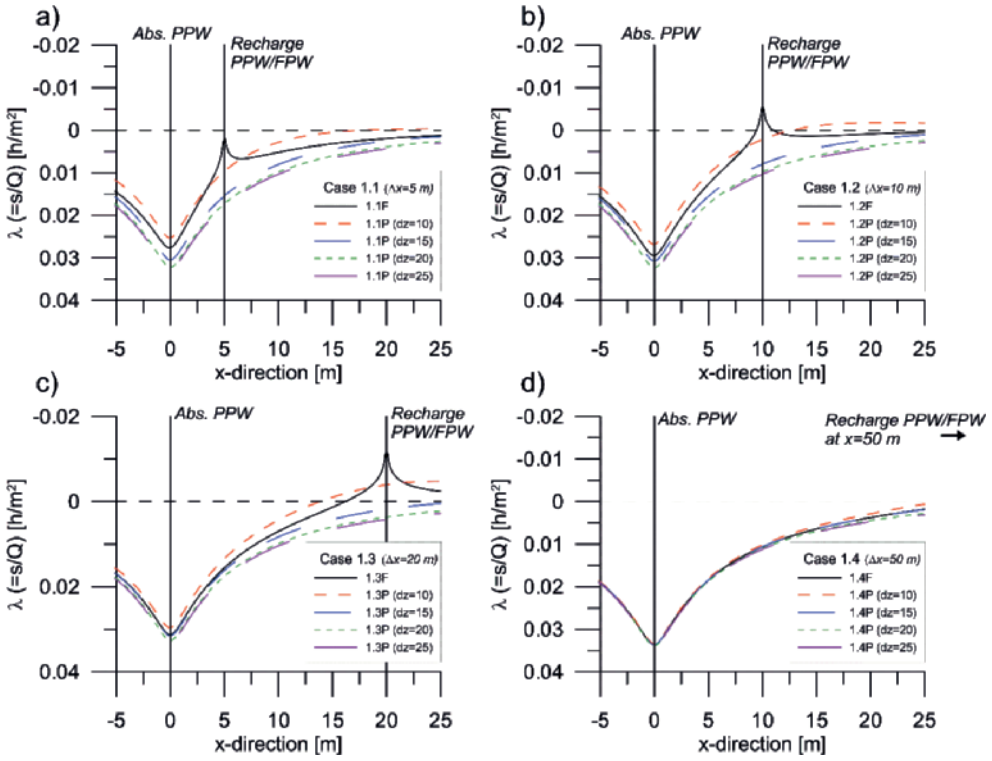

Fig. 2.5 The ratio between the drawdown over the recharge/discharge rate ($\lambda=s/Q$) at the dewatering level of 6.25 mbgl in the target aquifer over distance x with the abstraction PPW placed at x=0. This is done for both the scenarios with artificial recharge using the FPW, as well as the PPWs (at different screen depths Δz ranging between 10 and 25 mbgl) at a distance from the pumping well of **a)** Δx=5 m, **b)** Δx=10 m, **c)** Δx=20 m and **d)** Δx=50 m.

Sensitivity analysis for the homogeneous anisotropic aquifer conditions

In this section, the use of PPWs are tested in different kinds of aquifers. In this sensitivity analysis, the artificial recharge PPW is screened at Δx=20 m and Δz=20 m and compared to FPWs at a similar distance (Δx=20 m). For all scenarios (Cases 1-7) homogeneous anisotropic aquifer conditions are considered with an anisotropy of 10. Case 1-3 show that the hydraulic impact in an unconfined aquifer significantly differs from the refence scenario. The use of recharge PPWs instead of FPWs results in a relative drawdown reduction ($\Delta\lambda$) of only 0.0017 h/m^2 instead of 0.0029 h/m^2 for the fully and semi-confined scenarios at Δx=10 m. The reduction in hydraulic impact by using a recharge PPW at 20 mbgl instead of a FPW is higher in a thinner aquifer for the given configuration. The reduction in relative drawdown ($\Delta\lambda$) is 0.0036 h/m^2 for Case 4 (H=15 m), while this is 0.0023 h/m^2 for Case 5 (H=25 m) at Δx=10. Due to decreasing aquifer thickness, the required well head of the FPW for the given volumetric recharge rate increases. Hence, recharge at depth with a PPW becomes increasingly significant and the smaller penetration ratio of the PPW at given target depth results in more reduction in hydraulic impact at shallow aquifer levels.

At equal anisotropy ratios (a=10), the cases with different hydraulic conductivities (Cases 6 and 7) scale with Darcy's law (Fig. 2.6b). Naturally, the predicted drawdown by the ratio $\lambda(=s/Q)$ at a given distance is proportional to the hydraulic conductivity, so s_x (Case 1) ~ 2·s_x (Case 6) ~ 14.5·s_x (Case 7). However, for construction dewatering with recharge PPWs at depth, the anisotropy is an important parameter for predicting the hydraulic impact at shallow groundwater levels. Cases 8-9 show that the hydraulic impact reduction of using PPWs instead of FPWs on the dewatering site is significantly reduced for more isotropic target aquifers, with $\Delta\lambda$=0.0006 h/m^2 for homogeneous aquifer conditions (Case 8) and 0.0029 h/m^2 for anisotropic (a=10) aquifer conditions (Case 1) (Fig. 2.6d). For these cases, a more spherical three-dimensional head distribution and reduced lateral preferential flow paths are observed while using the PPW.

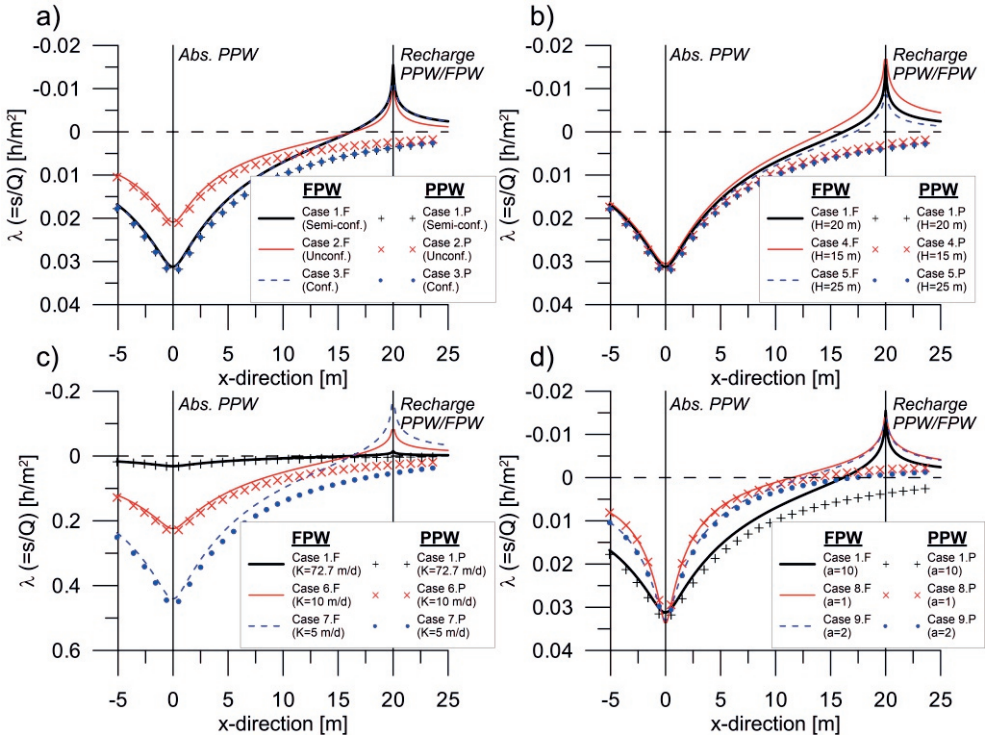

Fig. 2.6 The ratio between the drawdown *s* over the recharge/discharge rate ($\lambda=s/Q$) at the dewatering level of 6.25 mbgl in the target aquifer using FPW and PPW at a distance Δx of 20 m from the pumping well. The PPW is screened at 20 mbgl. This is done for **a)** unconfined and confined aquifer, **b)** different aquifer thickness (Cases 4-5), **c)** different hydraulic conductivity (Case 6-7), **d)** different anisotropy values (Cases 8-9).

Sensitivity analysis of PPWs for the heterogeneous aquifer conditions

Cases 10-14 assess the importance of aquifer heterogeneity. This was done by making a clear distinction between equivalent homogeneous anisotropic aquifer conditions, which are often assumed in the design stage of smaller dewatering projects, and heterogeneous conditions with alternating layers with different hydraulic conductivities. Case 10.1 considers a high-permeability layer of 300 m/d, while one single homogeneous isotropic formation is considered for the upper and lower part of the aquifer (Table 2.2). Consequently, the resulting hydraulic conductivity calculated for this formation by using a similar transmissivity as the reference case is significantly lower, and hence the drawdown due to pumping significantly higher near the pumping well (Fig. 2.7). Therefore, a hydraulic conductivity of 72.7 m/d is considered at pumping depth for the Cases 11-14 in order to compare the drawdowns between all cases.

For Cases 11, 13 and 14, a reasonable prediction can be obtained with one single homogeneous anisotropic aquifer. Again, considering an abstraction rate at the excavation site of 250 m^3/h and recharge with PPWs at approximately 20 m distance from the dewatered area the drawdown at Δx=10 m from the abstraction site is calculated. Using the simplified scheme as shown in Fig. 2.7, equivalent homogeneous anisotropic conditions instead of heterogeneous layering slightly underestimate drawdown predictions for Case 11, 13 and 14 at drawdown differences of respectively 0.09, 0.11 and 0.03 m.

However, the required well head of the recharge PPWs screened in high-permeability layers is significantly overestimated if homogeneous anisotropic conditions are assumed for heterogeneous layered aquifers. The well head Δh_{ppw} are in the range of 8.3-11.5 m for the homogeneous anisotropic aquifer conditions (Table 2.5) and hence unfavorable well hydraulics are predicted. However, taking into account the actual high-permeability layer reasonable well heads with values of 1.4-2.9 m are predicted.

In many groundwater models, the existence of small lenses of clay, peat, silt or loam are not considered. However, the three-dimensional flow paths during pumping and recharge in a given target aquifer can be strongly affected by such small lenses. The calculated relative drawdown at Δx=10 is 0.0092 h/m^2 for the anisotropic Case 12.2 and 0.0108 h/m^2 for the heterogeneous Case 12.2 with a small clay layer. Considering an abstraction rate of 250 m^3/h at the excavation site, this results in a 0.41 m more drawdown for the heterogeneous case. Therefore, the existence of small low-permeable lenses in the subsurface could have a significant reduction in hydraulic impact on the drawdown, while using PPWs instead of a FPW. This means that small heterogeneities should be considered while selecting the optimal dewatering scheme.

Overall, the results show that heterogeneous layering of the aquifer should be considered to predict the drawdown due to abstraction and artificial recharge. Especially,

the hydraulic conductivity at abstraction level, where pumping wells are screened, as well as the hydraulic conductivity at recharge PPW depth should be taken into account. In section 2.6.2 '*Hydrogeological characterization and the recharge PPW depth*', is discussed how dewatering companies identify heterogeneous layering of the aquifer with a minimum amount of hydrogeological information.

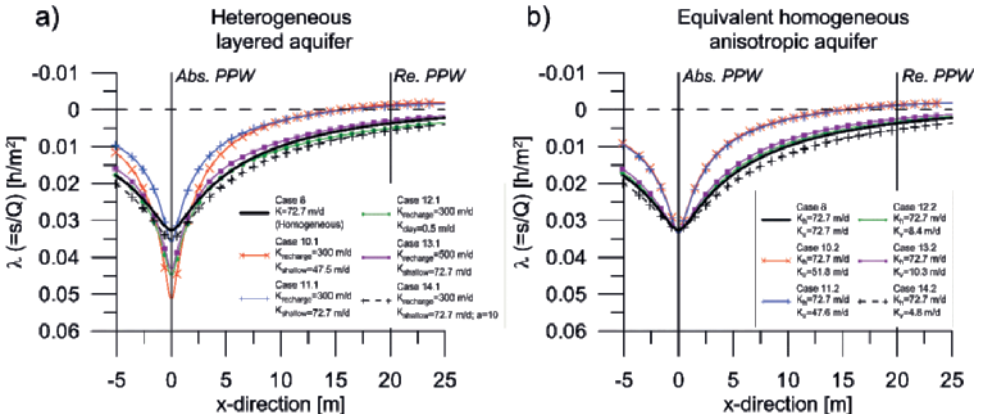

Fig. 2.7 The ratio between the drawdown over the recharge/discharge rate ($\lambda=s/Q$) at the reference level of 6.25 mbgl in the target aquifer using PPW. **a)** The effect on the ratio λ is shown for different heterogeneous layering in the target aquifer considering an overall K_h of 72.7 for all Cases 10-14.1, as well as **b)** for considering a single equivalent homogeneous anisotropic aquifer for numerical simulation (Cases 10-14.2).

	Heterogeneous aquifer characteristics	Required well head in heterogeneous layered aquifer, Δh_{PPW} [m]	Required well head in equivalent homogeneous anisotropic aquifer, Δh_{PPW}[m]
Case 10	$K_{recharge}$ = 300 m/d $K_{shallow}$ = 47.5 m/d	1.42	8.26
Case 11	$K_{recharge}$ = 300 m/d $K_{shallow}$ = 72.7 m/d	2.26	8.33
Case 12	$K_{recharge}$ = 300 m/d K_{clay} = 0.5 m/d	2.75	10.16
Case 13	$K_{recharge}$ = 500 m/d $K_{shallow}$ = 72.7 m/d	1.51	9.78
Case 14	$K_{recharge}$ = 300 m/d; a=10 $K_{shallow}$ = 72.7 m/d; a=10	2.85	11.46

Table 2.5 Required well heads for recharge PPW screened at Δx=20 m and Δz=20 m with volumetric recharge of Q=40 m^3/h in both the heterogeneous aquifer layering and the equivalent scenario considering homogeneous anisotropic conditions (see Eq. 2.5 and 2.6) Cases 10-14.

2.5.2 Experimental field test

Artificial recharge with FPW

For the constant recharge rates of 32.3 (Case F.1) and 16.7 m^3/h (F.2) that were obtained during recharge with the FPW. The hydraulic head measured at the shallow, middle and deep aquifer levels for a given radial distance are approximately equal, and therefore no vertical head gradient exist in the aquifer (Fig. 2.8). Therefore, the stationary flow around the FPW is strictly in the lateral direction, and the Dupuit-Forchheimer assumption should hold. For both cases, an excellent fit was obtained with the De Glee-Jacob-Hantush equation (Eq. 2.1), using a K of 72.7 m/d, c of 10 days, and aquifer thickness of 20 m. Despite the actual heterogeneous layering of the aquifer, the analytical approximation by considering a homogeneous semi-confined aquifer is sufficient since the hydraulic gradients over depth can be considered negligible.

Due to aquifer heterogeneity, a non-uniform screen outflow over the FPW screen length is achieved. The calculated percentage of outflow per 1 meter filter is shown in Fig. 2.9b. Approximately 38% of the outflow occurs at the high-permeability layer at 20 mbgl that is targeted for the PPW during recharge in the FPW. In the upper portion of the aquifer the percentage of outflow is negligible.

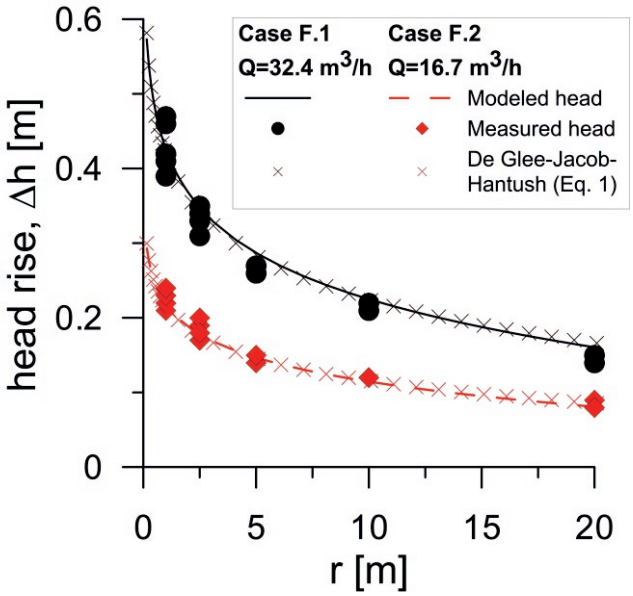

Fig. 2.8 The measured head in the monitoring wells for the stationary recharge tests on the FPW with the simulation results in a heterogeneous aquifer and the fit with the De Glee-Jacob-Hantush method (Eq. 1) with K=72.7 m/d, c=10 d, H=20 m.

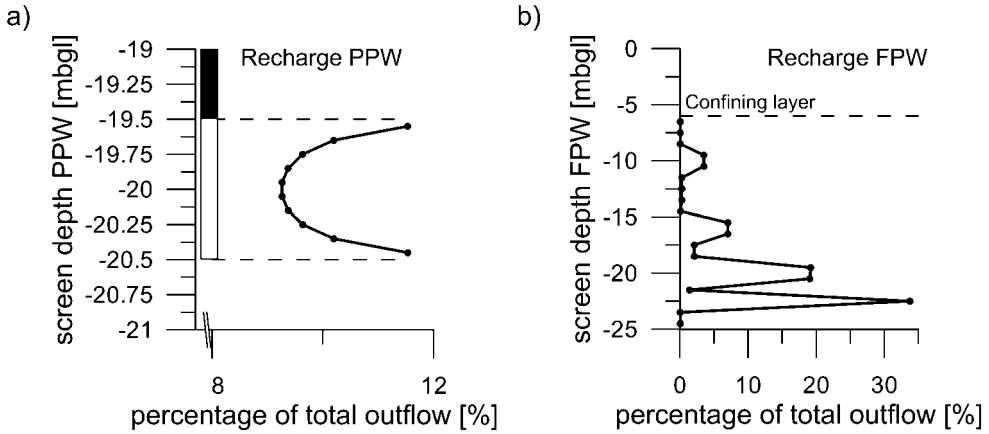

Fig. 2.9 Vertical distribution of the numerical calculated screen flow rate percentage based on aquifer tests **a)** Case P.1 with the PPW and **b)** Case F.1 with the FPW.

Artificial recharge with PPW

For the aquifer test on the PPW, constant recharge rates are used at approximately, 23 (Cases P.1), 19.5 (Cases P.2) and 14 m^3/h (Cases P.3) (Appendix A). Due to well clogging during recharge of the pumped oxic groundwater, a substantial well head increase occurred for Case P.1, starting at 0.3 bar, up to 1.5 bar. This well head increase was smaller for Case P.2 (starting at 1.2 bar, up to 1.5 bar) and Case P.3 (starting at 0.35 bar, up to 0.5 bar).

For the three selected cases, a reasonable fit of the numerical result with the actual head rise in the observation wells is obtained when assuming the homogeneous, isotropic aquifer from the FPW aquifer test (Fig. 2.11a). However, in the near-well vicinity of the well screen the head rise is drastically overestimated. Fig. 2.11a shows that the calculated head rise is 1.1 m instead of the actual value of 0.53 m for the Cases P.1 at a radial distance of 0.5 m from the well screen at 19.5 mbgl (deep aquifer depth). By accounting for the actual heterogeneity of the aquifer with the vertical variability in hydraulic conductivity as indicated in Fig. 2.3, an excellent fit with the observed field data is obtained.

In Fig. 2.11b, the strong deviation in head increase (Δh) between the tested PPW and FPW at shallow aquifer level is shown. Comparing the monitored head rise at shallow aquifer depth (9.5 mbgl) with the head rise around a FPW at an equivalent recharge rate of 23 m^3/h, the hydraulic head is considerably lower for Case P.1. The head rise is a factor 0.58 lower at 1 m radial distance from the well 9.5 mbgl, while this is still a factor 0.8 and 0.91 at 5 and 10 m radial distance.

Note that for a realistic dewatering project design, multiple artificial recharge wells are required to discharge the pumped water from the dewatered area at high the volumetric recharge rates. By the principle of superposition, the reduced head rise with the use of multiple PPWs instead of multiple FPWs will be much higher.

The outflow at PPW is simulated with the constant heads given in Table 2.4, resulting in the desired bulk recharge rates of 23, 19.5 and 14 m^3/h. The geometry of the PPW results in diverged outflow from both screen ends, resulting in higher outflow rates at the top and bottom of the well screen (Fig. 2.9a). The percentage of total out flow over 0.1 m well screen at the top and bottom is 11%, while this is 9.2% in the middle of the well screen. Simulating artificial recharge with the assumption of an uniform well-face flux boundary, as well as with the uniform head (h_{ppw}), show negligible differences in predicted head rise outside a radius of 0.5 m from the well. Differences in head rise are only simulated within a radius of 0.5 m from the well screen, resulting in relative differences up to 2% in the calculated head rise for Case P.1.

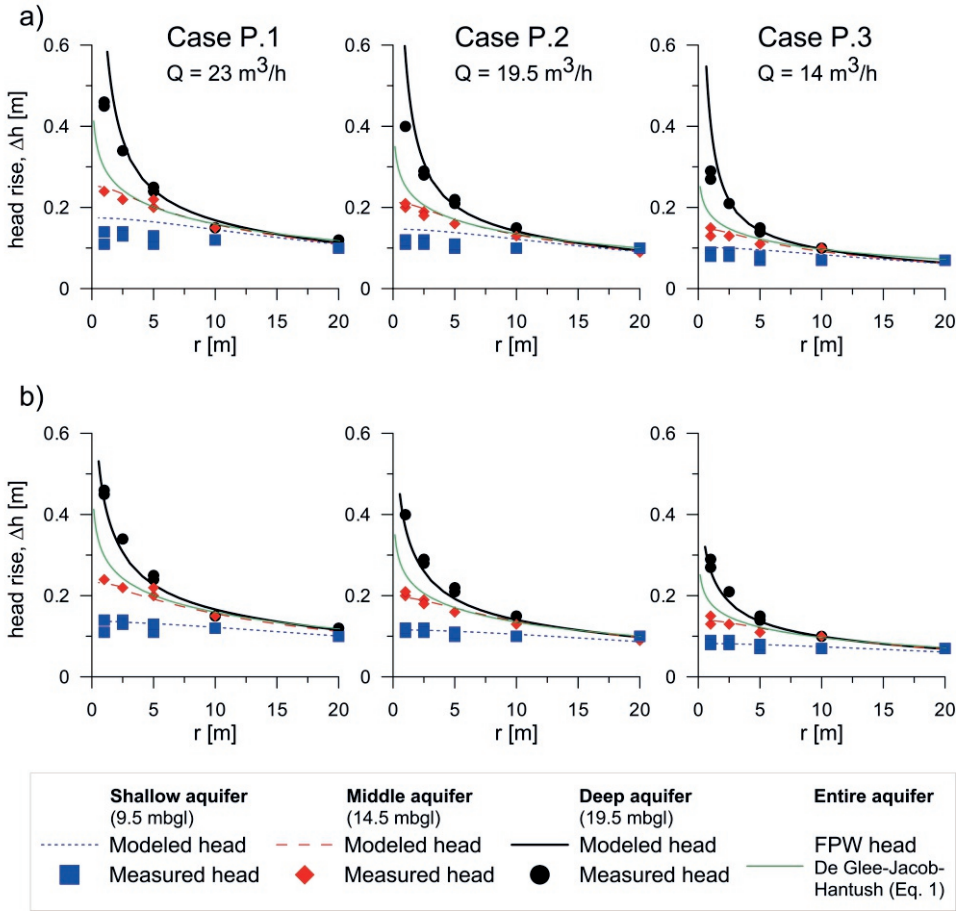

Fig. 2.10 The measured hydraulic head rise, Δh, in the observation wells, as well as the modeled hydraulic head rise, Δh, at the indicated shallow, middle and deep monitoring depths (see Fig. 2.3) in **a)** an homogeneous aquifer, as well as **b)** an heterogeneous aquifer. Also the head rise while assuming recharge by a FPRW with an equivalent Q is plotted for Case 1-3 using the De Glee-Jacob-Hantush method

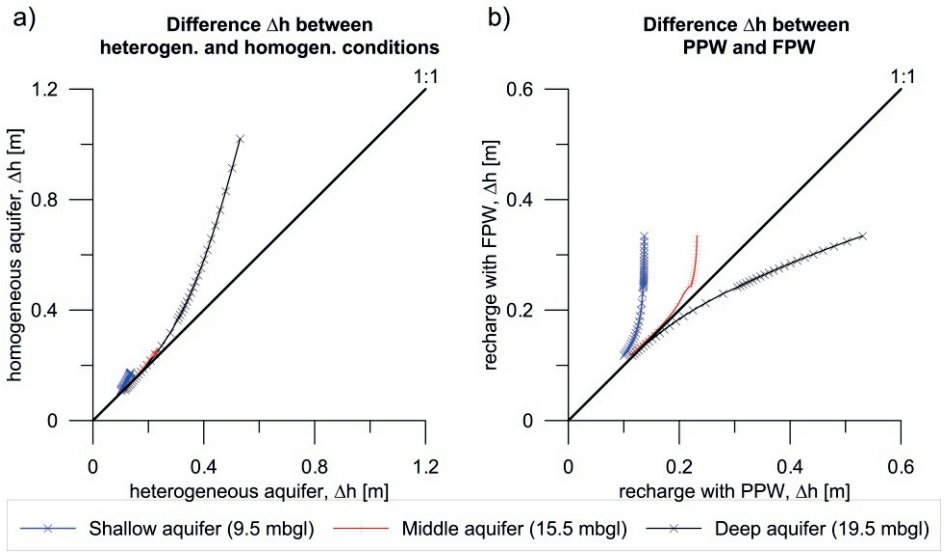

Fig. 2.11 a) The difference in head rise (Δh) between artificial recharge with a PPW in the heterogeneous layered target aquifer and an equivalent homogeneous aquifer for Case P.1. **b)** The difference in head rise (Δh) between artificial recharge with a PPW and a FPW in the target aquifer.

2.6 Discussion

2.6.1 The use of aquifer heterogeneity for efficient recharge PPWs

The present study shows that the use of recharge PPWs allow to take advantage of the vertical variability in hydraulic conductivity in the aquifer. By accounting the more and less permeable strata in the target aquifer one could select a suitable, more permeable, layer at depth for artificial recharge to improve the efficiency of the recharge PPW and the efficiency of dewatering systems that involves re-injection of dewater groundwater. At the field site, the selection of the sandy gravel layer with a hydraulic conductivity of 300 m/d at 20 mbgl provided recharge rates up to 23 m^3/h at a PPW with a wells screen of only 1 m. Considering a homogeneous aquifer instead of the actual heterogeneous layering of the aquifer resulted in a drastic overestimation of the required well head by a factor of 3.1. This means that the required well head Δh_{ppw} is 4.66 m instead of 1.51 m (see Table 2.4). Hence, the results in the sensitivity analysis (Cases 11-14) show that wrongly assuming a heterogeneous layered aquifer as an equivalent homogeneous anisotropic aquifer could result in a major efficiency loss of the recharge PPWs, as well as the abstraction PPWs.

2.6.2 Hydrogeological characterization and the recharge PPW depth

Usually, dewatering companies have to rely on a limited amount of hydrogeological information of the dewatering site. Comprehensive field investigation would drastically increase the project costs for small to medium scale dewatering projects and hence, in reality, dewatering companies often have to rely on cone penetration test data (e.g. Robertson 1990), online available soil profiles and borehole logs to obtain information about soil heterogeneity. This could already provide useful information about potential high-permeability layers in the aquifer, as well as low-permeability zones. Prior to planning the dewatering design, analysis of such information is necessary to predict the optimal artificial recharge depths for PPWs.

In the Netherlands and Germany, dewatering companies use quick and cheap straight-flush rotary drilling with clean water as drilling fluid for well completion of naturally-developed artificial recharge PPWs (so-called fast, high volume infiltration (FHVI) wells) in high permeability strata in the aquifer. Skilled drilling operators are provided with a rough hydrogeological picture of the shallow subsurface and indicate high-permeable layers in an aquifer with their straight-flush drilling rig. During straight flush rotary drilling with clean water, large quantities of the flushed water pumped down the drill-pipe are infiltrating into the surrounding soil (Powers et al. 2007). Drilling through high-permeability layers in the aquifer causes significant loss of flushed water volume into the surrounding soil and reduces the velocity of the flush in the borehole annulus. A large sudden reduction in debris flush outflow at the surface is a good indication of a high permeable layer in the aquifer and can be used by the drilling operator to place a naturally-developed PPW at the desired depth in the aquifer at a minimum of well completion and development costs. A small aquifer test could provide useful information about the maximum volumetric recharge rate of the well and the hydraulic conductivity at recharge depth. Using straight-flush rotary, multiple naturally-developed PPWs can be installed within a very short period, while the completion and development of a conventional FPW with reversed-circulation rotary drilling is time consuming.

2.6.3 Planning of dewatering design with multiple recharge PPWs

For the sensitivity analysis one abstraction PPW and one recharge PPW are considered in the simplified well scheme. However, in practice, multiple pumping wells are required to obtain the desired drawdown at the excavation site. This can be done by small filters and vacuum pumping in the top of the aquifer for smaller pumping rates, or by deep wells with larger well diameters and screen lengths for deep excavation sites and larger pumping rates (Powers et al. 2007). The amount of required recharge wells is determined by the size of the dewatering project (volumetric abstraction rate), the aquifer characteristics, as well as the recharge well type. For example, a larger amount of cheap, quickly installed naturally-developed recharge PPWs with limited screen length is required due to lower well efficiencies compared installation of proper completed recharge FPWs with filter packs to discharge the required dewatered groundwater volume.

Powers et al. (2007) show that for many dewatering problems the excavation well with a set of pumping wells can be simplified to one large single pumping well. The same can be done for the set of recharge wells. This assumption has validity for scenarios of circular dewatering systems of closely-spaced pumping wells, as well as for a similar circular set of recharge wells. For such systems, the required distance between the center of the excavation site with the set of pumping wells and the set of recharge wells can be estimated based on the sensitivity analysis (Cases 1-14) presented in this study. However, many dewatering systems are more complex and this sensitivity analysis is less useful, such as for scenarios with widely spaced pumping and/or recharge wells, larger excavation sites, as well as the use of multiple arrays of recharge wells at different locations near the excavation site. In the design stage of the construction dewatering project, dewatering companies could provide reasonable predictions of the drawdown and the minimum required distance between the dewatering wells and the artificial recharge PPWs by accounting for slightly higher discharges and drawdowns, as well as a realistic upper and lower bound for the possible aquifer anisotropy based on the available hydrogeological information. Note that optimal drawdown/head rise predictions for PPWs is more complex that for FPW and requires three dimensional modeling while considering each individual partially-penetrating recharge and pumping well in the dewatering scheme, since each well changes the performance of surrounding wells.

2.6.4 Impact of background groundwater flow

The sensitivity analysis (Cases 1-14) only account for situations without background flow. In reality, the groundwater flow could have a significant impact on the dewatering design. Especially at large hydraulic gradients, the impact on the well design can be significant. For such scenarios, lower pumping rates at the downstream side of the excavation are required than at the upstream side to obtain the desired drawdown. Ideally, artificial recharge wells are installed downstream from the extraction site to reduce pumping costs (Powers et al. 2007; Cashman and Preene 2013). The negative influence of the hydraulic head rise due to recharge at the downstream side is smaller than for a scenario with no background flow, allowing for installation of artificial recharge wells closer to the dewatering site. Hence, the difference between the allowed aboveground minimum distance from the excavation site while using a PPW or FPW is smaller than for the analyzed scenarios with no background flow in the sensitivity analysis (Case 1-14). However, a simple estimation of the actual drawdown at a given hydraulic gradient for the given scenarios in the sensitivity analysis can be obtained by using the principle of superposition.

2.6.5 Additional head loss in PPWs

The use of small well screen lengths have the advantage to target the hydraulic impact at desired depth, as well as limit the drilling cost by placement of longer filters. However, PPWs that only screen a small portion of the aquifer have the disadvantage that it results in high additional well losses with respect to an equivalent FPWs. The present study shows that the required well head for artificial recharge with a PPW in a layer of relatively high-permeability could be drastically reduced (see Table 2.5). Moreover, the use of PPWs that are screened at larger depths enable higher well heads, since the infiltration pressure is restricted to the overburden pressure of the soil at given depth. Therefore, much higher pressures on the influx pipelines towards the PPWs can be retained for dewatering systems, then when using FPWs. This might prevent depressurization of air in the pipelines and recharge PPW during aboveground groundwater transport and reduce potential risk of air clogging of the well.

The increase in pumping costs to enable optimal well heads and sufficient recharge rates for the PPWs need to be lower than the reduction of pumping costs by selection of the optimal well design that provides the smallest hydraulic impact at shallow aquifer depth at the excavation site with recharge PPWs. In practice, dewatering companies in the Netherlands and Germany are using recharge PPWs with limited screen length to optimize their dewatering design. Ideally, well heads up to 5 meter are used to recharge groundwater in the recharge PPWs (screen lengths up to 2 m). Note, that smaller well

screens of PPWs are more sensitive to clogging due to a smaller well screen surface compared to FPWs. This could cause potential increase in well head of the recharge well and reduced recharge rates over time (e.g. Olsthoorn 1982ab; Rinck-Pfeiffer 2000; Houben et al. 2018), which was observed for the recharge PPW tested in the present study (Case P.1-3).

In order to reduce the additional well head by partial penetration and well clogging PPWs with longer screens can be used. For example, if the optimal screen depth of the PPW in a high-permeability layer is determined, one could choose for a PPW with a longer screen, screened from this high-permeable layer. The results show that the controlling effect on the drawdown at excavation level of a PPW screened at 20 or 25 mbgl is more or less similar (see Fig. 2.5). Therefore, the use of a PPW with a filter length of 5 m between these two depths will result in a similar controlling effect on the drawdown at excavation level, while the risks of well-clogging are reduced.

2.6.6 Using PPWs for artificial recharge to prevent soil settlement

The present study shows, that using PPWs (Δz=10 m) in the upper part of the target aquifer obtain lower drawdowns than a FPW (Fig. 2.5). In many cases, the groundwater drawdown due to pumping in aquifers could cause soil settlements (Phien-wej et al. 1998; Pujades et al. 2014; Zhang et al. 2017). For such dewatering systems, obtaining sufficient drawdown near the excavation site is not the major concern for optimization of the dewatering scheme. In order to reduce soil settlements near the excavation site, curtain sealings and aquifer recharge are suggested to reduce the drawdown in the vicinity of the excavation site (Zhang et al. 2017). The recharge wells are screened over a large portion of the target aquifer to obtain the required drawdown and control of the settlement effects. Combining flow barrier curtain sealings with a well set-up of artificial recharge PPWs targeting the high-permeable layers at shallower aquifer depths instead of using FPWs could avoid the risks of settlement while improving the dewatering design drastically.

2.7 Conclusions

Based on the results of experimental recharge tests on a PPW and a FPW, as well as numerical results of the sensitivity analysis on a simplified pumping-recharge dewatering scheme the following is concluded:

1) The design of construction dewatering systems combined with artificial recharge for discharge of dewatered groundwater can be drastically improved by targeting recharge in relatively high-permeable layers in the aquifer with PPWs. To date, most dewatering designs consider recharge wells that screen large parts of the aquifer thickness without taking into account the vertical variability in hydraulic conductivity of the aquifer. The sensitivity analysis show that PPWs with 1 meter filter screened at depth (20 mbgl in a 25 m thick aquifer) can be installed much closer to the dewatering site than conventional recharge FPW. For example, to obtain a required drawdown of 2.4 m within a radius of 10 meters from the abstraction site a shallow groundwater level for combined abstraction and recharge at a rate of Q=250 m^3/h, PPWs can be installed at 20 m distance, while FPWs need to be installed at a distance of 41 m. Consequently, the above-ground distance between the target excavation site and the recharge site can be significantly reduced, while the re-pumping of recharged water at the excavation site, as well as the overall costs of the dewatering can be minimized.
2) Screening PPWs in relatively high-permeable layers in the subsurface allow to infiltrate large quantities of water at relative small well head. The use of equivalent homogeneous anisotropic aquifer conditions predicts erroneously high well head and near-well hydraulic gradients for the tested recharge PPWs. In the field test of present study, recharge rates up 25 m^3/h were obtained in a heterogeneous semi-confined aquifer. A gravel layer with a high hydraulic conductivity of 300 m/d was used as target layer for recharge in the aquifer.
3) The experimental data, as well as the sensitivity analysis show the importance of detailed hydrogeological characterization of the soil. Relatively high-permeable layers in the subsurface can be used to infiltrate large quantities of water with PPWs. Moreover, predicting the hydraulic head in the aquifer required three-dimensional modeling, while considering aquifer heterogeneity.

Acknowledgements

This work was supported by the foundations STW (Foundation for Technical Sciences) and O2DIT (Foundation for Research and Development of Sustainable Infiltration Techniques). The authors wish to thank Sjaak van Laanen and Thijs de Vet from dewatering company P.J. de Vet & Zonen for constructing the experimental fieldwork set-up. We are grateful to Jürgen Knops from the engineering company Gell & Partner GbR for providing geological data and the geotechnical report of the fieldwork site.

Chapter 3

The effect of grain size distribution on nonlinear flow behavior in sandy porous media

Abstract

The current study provides new experimental data on non-linear flow behavior in various uniformly graded granular material (20 samples) ranging from medium sands (d_{50}>0.39 mm) to gravel (d_{50}=6.3 mm). Generally, theoretical equations relate the Forchheimer parameters a and b to the porosity, as well as the characteristic pore length, which is assumed to be the median grain size (d_{50}) of the porous medium. However, numerical and experimental studies show that flow resistance in porous media is largely determined by the geometry of the pore structure. In this study, the effect of the grain size distribution was analyzed using subangular-subrounded sands and approximately equal compaction grades. We have used a reference dataset of 11 uniformly graded filter sands. Mixtures of filter sands were used to obtain a slightly more well graded composite sand (increased C_u values by a factor of 1.19 up to 2.32) with respect to its associated reference sand at equal median grain size (d_{50}) and porosity. For all composite sands, the observed flow resistance was higher than in the corresponding reference sand at equal d_{50}, resulting in increased a coefficients by factors up to 1.68, as well as increased b coefficients by factors up to 1.44. A modified Ergun relationship with Ergun constants of 139.1 for A and 2.2 for B, as well as the use of d_m-σ as characteristic pore length predicted the coefficients a and b accurately.

Published as: Van Lopik, J.H., Snoeijers, R., van Dooren, T.C.G.W., Raoof, A., & Schotting, R.J. (2017). The effect of grain size distribution on nonlinear flow behavior in sandy porous media. *Transport in Porous Media, 120*(1), 37–66.

3.1 Introduction

The understanding of non-linear liquid or gas flow behavior in natural and artificial porous media, such as rock, consolidated or unconsolidated material and packed-bed-reactors is a key factor in reservoir engineering applications (Wen et al. 2011; Mijic et al. 2013; Yeh and Chang 2013; Houben 2015a) and chemical and technical industries (e.g. Jafari et al. 2008). In the field of reservoir engineering, fluid flow behavior near the well screen controls the efficiency of oil/gas production wells (e.g. Holditz and Morse 1976; Aulisa et al. 2009), as well as the efficiency of injection/extraction wells in groundwater resources applications (e.g. Sen 1989; Mathias and Todman 2010; Wen et al. 2011; Wen et al. 2013; Yeh and Chang 2013; Houben 2015a; Mathias and Moutsopoulos 2016). Moreover, non-linear flow at full-aquifer scale in a broad range of geological formations, such as gravel, karstic or fractured aquifers, is widely addressed in the literature (e.g. Moutsopoulos and Tsihrintzis 2005; Moutsopoulos 2007).

Commonly, groundwater flow near wells is described using the classical Darcy's law, Darcy (1856), as:

$$i = -\frac{1}{K}q \tag{3.1}$$

where K [m/s] is the hydraulic conductivity of the porous medium and q [m/s] is the specific discharge. This empirical linear relationship for fluid flow in porous media is only applicable for a specific regime of flow where flow velocities are sufficiently low, and it becomes less accurate as flow velocities become larger. The deviation of the non-linear relationship between specific discharge and hydraulic gradient due to increased flow resistance at higher flow velocities has been widely addressed in the literature (e.g. Forchheimer 1901; Izbash 1931; Sidiropoulou et al. 2007). Forchheimer (1901) described the non-linear behavior adding a second-order quadratic term to the Darcy's law:

$$i = -aq - bq^2 \tag{3.2}$$

Comparing equations 1 and 2, a [s/m] is a parameter equal to the reciprocal of the hydraulic conductivity (i.e., $a=1/K$) and b [s^2/m^2] is the empirical Forchheimer coefficient. The Forchheimer equation is able to accurately fit the experimental data in packed-column experiments with granular material for most cases of non-Darcy flows (Sidiropoulou et al. 2007; Moutsopoulos et al. 2009; Sedghi-Asl et al. 2014; Li et al. 2017). Mathias and Moutsopoulos (2016) showed that the Forchheimer equation should be used instead of Darcy's law to account for additional head losses due to non-Darcy

flow conditions in the vicinity of injection and production wells. Other analytical studies use the Forchheimer equation to predict non-steady state, non-linear flow in gravel aquifers at early time steps when hydraulic gradients are steep (e.g. Moutsopoulos and Tsihrintzis 2005; Moutsopoulos 2007).

Besides the Forchheimer equation, other empirical equations have been proposed to describe the relation between specific discharge and hydraulic gradient for non-linear flow (Izbash 1931; Irmay 1958; Bear 1988). For example, the Izbash equation (initially proposed by Forchheimer (1901)), which is a non-linear power law function, is widely used to model the non-Darcy flow (e.g. Bordier and Zimmer 2000; Wen et al. 2013). Despite the experimental validity of the Izbash equation, it lacks any physical base (Bordier and Zimmer 2000).

Many experimental data on (post-Darcy) non-linear flow in porous media are available for coarser porous media, such as coarse sands, gravels, and glass beads (Sidiropoulou et al. 2007; Moutsopoulos et al. 2009; Sedghi-Asl and Rahimi 2011; Huang et al. 2013; Bağci et al. 2014; Salahi et al. 2014; Sedghi-Asl et al. 2014; Li et al. 2017). A relatively small amount of experimental data is available for finer unconsolidated sandy porous media. Moreover, most studies only provided porosity and the median (d_{50}) or mean grain size to describe the porous media. Relationships to predict Forchheimer coefficients a and b are based on these two parameters (e.g. Ergun 1952; Macdonald et al. 1979; Kovács 1981; Kadlec and Knight 1999; Sidiropoulou et al. 2007). However, numerical simulations, as well as experimental studies, showed that the geometry of the pore structure have a large influence on flow behavior (e.g. Hill and Koch 2002; Li and Ma 2011; Allen et al. 2013; Koekemoer and Luckos 2015). Here, we investigated the effect of non-linear flow behavior empirically for granular porous media (filter sand) with various grain size distributions for a given reference median grain size (d_{50}) and compaction grade.

3.2 Theory and background

3.2.1 Criteria for non-linear flow in porous media

Experimental and numerical studies have investigated the upper limits of the Darcy regime for fluid flow in porous media. Many attempts have been done to define a criterion to describe the upper limit of the Darcy regime. Formerly, it was believed that non-linear flow behavior in porous media was solely due to turbulent flow (inertial energy losses by highly chaotic and unsteady flow).

The Reynolds number is used to indicate whether fluid flow is laminar or turbulent. It is defined as (Bear 1988):

$$Re = \frac{\rho d_{50} q}{\mu} = \frac{\text{inertial forces}}{\text{viscous forces}} \tag{3.3}$$

where ρ [kg/m^3] is the fluid density, d_{50} [m] is the median grain size of the porous medium as a proxy for the characteristic pore length, q [m/s] is the specific discharge and μ [kg/(m s)] is the dynamic viscosity. Besides Reynolds number, which is solely based on the average particle size of the porous medium to define the properties of the medium, various other criterions have been proposed. For example, Ergun (1952) used a modified Reynolds number by including porosity, while Comiti et al. (2000) used a pore Reynolds number based on porosity, tortuosity and the dynamic specific surface area of the pore. Zeng and Grigg (2006) stated that determination of a representative pore diameter as characteristic length of the porous media is difficult, due to the complexity of pore structures. Moreover, flow through a complex pore structure significantly differs from flow in a conduit, and, hence, no sharp transition between laminar and turbulent flow can be observed in porous media. A wide range of critical particle Reynolds numbers is given in the literature for the onset of non-linear laminar flow. For example, Bear (1988); Hassanizadeh and Gray (1987); Ma and Ruth (1993) and Comiti et al. (2000) suggested critical particle Reynolds numbers ranging between 1-15. Other studies, such as Scheidegger (1974), obtained higher maximal critical particle Reynolds numbers up to a value of 75.

Ma and Ruth (1993) and Lage (1998) introduced new criteria to evaluate the onset of non-linear flow by means of a “Forchheimer number”, based on the intrinsic permeability and the non-Darcy coefficient b in the Forchheimer equation. However, such criteria require experimentally or empirically determined values for the Forchheimer coefficients a and b, while criteria such as the particle Reynolds number requires only the average grain size in order to estimate the onset of non-linear flow in a given porous media.

3.2.2 Non-linear laminar flow and fully turbulent flow in porous media

Traditionally, it was believed that the onset of non-linear flow was solely due to energy losses by the occurrence of turbulence (e.g. Ergun 1952; Ward 1964). However, flow visualization studies in porous media showed that turbulent flow occurs at much higher particle Reynold numbers than the critical particle Reynold numbers of 1-15 for the onset of non-linear flow (e.g. Chauveteau and Thirriot 1967; Dybbs and Edwards 1984; Seguin et al. 1998). Critical particle Reynolds number of 300-533 were determined for the onset of the turbulent flow regime using a uniform spheres packing with particle diameters ranging from 0.5 to 8 cm, respectively (Jolls and Hanratty 1966; Latifi et al. 1983; Rode et al. 1994; Seguin et al. 1998), as well as for cylindrical or plate arrangements (Dybbs and Edwards 1984). Hence, a non-linear laminar flow regime should be considered before fully turbulent flow develops in porous medium. A smooth transition was observed from non-linear laminar flow, to the onset of small vortices and eddies in some pore spaces, to eventually, development of fully turbulent flow in the porous medium (e.g. Dybbs and Edwards 1984; Seguin et al. 1998). In the literature, this non-linearity in the laminar flow regime is ascribed to different microscale processes (e.g. Hassanizadeh and Gray 1987; Ma and Ruth 1993; Skjetne and Auriault 1999; Hill and Koch 2002; Nield 2002). In general, it is assumed that the deviation from the linear Darcy's law at increased Reynolds numbers is due to the occurrence of microscopic inertial forces (e.g. Bear 1988; MacDonald et al. 1979; Venkataraman and Rao 1998). Other studies, such as Panfilov et al. (2003) and Panfilov and Fourar (2006), showed that the main mechanisms of energy dissipation that contribute to the non-linear flow term are due to both recirculation of eddies in closed streamline regions, as well as streamline deformation in the main area of flow. Ma and Ruth (1993) showed that the onset of non-linearity cannot be fully described by microscopic inertial terms using a simple tube model. Hassanizadeh and Gray (1987) stated that the onset of non-linear flow behavior is due to the occurrence of interfacial drag forces at increased flow velocities and inertial forces become significantly important at particle Reynold numbers of about 100. The effect of the viscous boundary layer on drag was addressed by Whitaker (1996). These studies showed that microscopic analysis should be used to fully understand macroscopic non-linear laminar flow behavior in a given complex pore structure for a given Reynolds number. Overall, the geometry of the pore structure (such as tube-like or blob-like pore surfaces), as well as the total fluid-solid interface and its interface roughness, largely determine the flow resistance due to drag force terms in the Forchheimer coefficient b (e.g. Ma and Ruth 1993; Liu et al. 1995; Thauvin and Mohanty 1998; Panfilov and Fourar 2006; Chaudhary et al. 2013).

As described above, the macroscopic transition from laminar Darcy flow, to non-linear laminar flow to eventually fully turbulent flow is a gradual process (e.g. Seguin et al. 1998). Many experimental datasets on non-linear flow behavior in granular porous media show that this gradual process can be accurately predicted by the Forchheimer equation (Eq. 3.2) for various ranges of particle Reynold numbers in the non-linear laminar flow regime, as well as in the turbulent flow regime (e.g. Venkataraman and Rao 1998; Sidiropoulou et al. 2007; Moutsopoulos et al. 2009; Bağci et al. 2014; Sedghi-Asl et al. 2014; Salahi et al. 2015; Li et al. 2017).

For example, Li et al. (2017) conducted flow experiments on sands at Reynolds numbers below 40 and, hence, investigated the onset of the non-linear laminar regime. By contrast, Sedghi-Asl et al. (2014) investigated the Forchheimer coefficients of sands and gravel experimentally at Reynold numbers ranging from 31-720 (for a sand with d_{50} of 5.5 mm) up to 2,400-30,750 (for a gravel with d_{50} of 56.8 mm). Moutsopoulos et al. (2009) evaluated coefficients *a* and *b* for different granular materials, ranging from sand, gravel, carbonate rocks up to cobbles (from a d_{50} of 2.71 to 67.2 mm). In the experimental study of Salahi et al. (2015), rounded and crushed angular grains (from a d_{50} of from 1.77 to 17.78 mm) were used. The maximum Reynolds numbers used in these studies are 437-2,709 (Moutsopoulos et al. 2009) and 714-1882 (Salahi et al. 2015).

It should be noted that the experiments for analyzing the onset of turbulence for flow in porous media (e.g. Seguin et al. 1998) are performed on spheres with one single diameter. However, natural granular material have different grain size distributions, gradations and shape irregularities. The difference in pore structure and particle roughness could result in different Reynolds numbers for the onset of turbulent flow, and the critical Reynolds numbers for turbulence might significantly differ from 300 to 533. Burcharth and Andersen (1995) stated that for such materials the transition zones between the different flow regimes are blurred and difficult to define. This might explain that a reasonable singular fit with the Forchheimer equation (Eq. 3.2) is obtained for flow experiments on sand and gravel for a wide range of Reynold numbers (e.g. Moutsopoulos et al. 2009; Sedhi-Asl et al. 2014). Similar conclusions can be obtained from numerical studies, such as Firdaous et al. (1997) and Fourar et al. (2004), which consider the Forchheimer equation (Eq. 3.2) valid over a wide range of Reynolds numbers.

Some studies have tried to characterize the non-linear flow regime in terms of a weak inertial and strong inertial regime (fully turbulent flow regime) based on macroscale flow experiments in packed spheres of uniform size and determined different Forchheimer coefficients for both regimes (e.g. Fand et al. 1987; Bağci et al. 2014). The extent of these regimes were estimated from the reduced pressure drop versus flow velocity. Bağci et al. (2014) defined a turbulent flow regime for critical particle Reynolds numbers >268, while Fand et al. (1987) obtained *Re* values >120.

3.2.3 Empirical relations for estimation of the Forchheimer coefficients

In many cases the hydraulic characteristics by means of the Forchheimer coefficients *a* and *b* for a given porous medium sample are not available. Empirical relations can be used to predict the Forchheimer coefficients by using the soil characteristics, such as the average grain size and porosity. Many studies have developed empirical relations for the coefficients *a* and *b* (see Eq. 3.2). An overview of these expressions is given in Table 3.1.

Schneebeli (1955) proposed expressions for coefficients *a* and *b* for porous media consisting of spheres. The average particle diameter (*d*) is used as characteristic pore length of the porous medium. Ward (1964) proposed similar expressions based on non-linear flow experiments with 20 different porous media consisting of material ranging from glass beads to sand and gravel, having particle diameters of 0.27 – 16.1 mm.

Based on the Kozeny-Carman relationship for Darcy flow (Carman 1937), Ergun (1952) derived an expression for the *b* coefficient. The assumption of Ergun's (1952) approach is that fluid flow in porous media is similar to flow in pipes, assuming full turbulent flow in the non-linear flow regime (Ergun 1952; Lage 1998). However, as described above, non-linear flow at intermediate Reynolds numbers is laminar. Nevertheless, Ergun's (1952) relations works quite well for non-linear flows in various kind of porous media and are, to a great extent, the most analyzed and used relationships (e.g. Sidiropoulou et al. 2007; Li and Ma 2011; Allen et al. 2013; Bağci et al. 2014). Many variations on the Ergun relations for different kind of porous media with a wide range of Ergun constants *A* and *B* are addressed in the literature (e.g. MacDonald 1979; Fand et al. 1987; Comiti and Renaud 1989). Kovács (1981), analyzed a dataset of 300 sediment samples for Re=10-100 and proposed a value of 144 for constant *A* and 2.4 for constant *B*. DuPlessis (1994) investigated the increase in flow resistance due to local flow recirculation in the pore spaces in the non-linear laminar flow regime. From these analytical results it was concluded that in the laminar flow regime the Ergun constants were higher than derived by Ergun (1952) for turbulent flow in porous media. Both constants are functions of porosity, where constant *A* increases with increasing porosity, and constant *B* decreases with increasing porosity. For porous media with a porosity ranging between 0.33-0.36, constant *A* is approximately 200, while constant *B* is 1.97. Engelund (1953) derived a similar expression as Ergun (1952) for Forchheimer coefficient *b* and stated that the constant *B* varies from a value of 1.8 for uniform spherical particles, up to a value of 3.8 for highly irregular angular grains.

MacDonalds et al. (1979) and Kadlec and Knigth (1996) suggested different forms of the Ergun relation by changing the porosity term $(1-n)^2/n^3$ and $(1-n)/n^3$ for respectively

coefficient *a* and coefficient *b* (see Table 3.1). MacDonalds et al. (1979) used analyzed experimental datasets which included a wide variety of porous media (e.g. glass beads, steel spheres (blue metal), cylindrical fibers and granular material) with porosities ranging from 0.123 to 0.919. For the equation 7b of MacDonalds et al. (1979), the constant 1.8 works well for smooth particles (see Table 3.1), while for rough particles a value of 4.0 is preferred for estimating the coefficient *b*. For intermediate surface roughness of the particles, the value should lie between these two values.

Sidiropoulou et al (2007) derived empirical relationships, which are based on linear regression analysis on both porosity and the average particle size for a large dataset from the literature. Geertsma (1974) derived an empirical relationship for estimating Forchheimer coefficient *b* based on intrinsic permeability, *k,* and porosity, examining an experimental dataset of consolidated and unconsolidated sandy porous media.

Equations		**Coefficient a [s/m]**	**Coefficient b [s^2/m^2]**
Schneebeli (1955)	(3.4)	$1100\frac{v}{gd^2}$	$12\frac{1}{gd}$
Ward (1964)	(3.5)	$360\frac{v}{gd^2}$	$10.44\frac{1}{gd}$
Ergun-type	(3.6)	$A\frac{(1-n)^2 v}{gn^3 d^2}$	$B\frac{(1-n)}{gn^3 d}$
- ***Kozeny-Carman (1937)***		$A = 180$	-
- ***Ergun (1952)***		$A = 150$	$B = 1.75$
- ***Kovács (1981)***		$A = 144$	$B = 2.4$
MacDonalds et al. (1979)	(3.7)	$180\frac{(1-n)^2 v}{gn^{3.6} d^2}$	$1.8\frac{(1-n)}{gn^{3.6} d}$
Kadlec and Knight (1996)	(3.8)	$255\frac{(1-n)v}{gn^{3.7} d^2}$	$2\frac{(1-n)}{gn^3 d}$
Sidiropoulou et al (2007)	(3.9)	$0.0033\ d^{-1.50} n^{0.0603}$	$0.194\ d^{-1.27} n^{-1.14}$
Geertsma (1974)	(3.10)	-	$(\frac{0.05}{g}(k\ 10000)^{-0.5} n^{-5.5})$

Table 3.1 Empirical relations for the Forchheimer coefficients *a* and *b.* Where *g* [m/s^2] is the acceleration due to gravity, *d* [m] is the characteristic pore length by means of an average particle diameter and *n* [-] is the porosity, *k* (=$\mu/\rho g a$) [m^2] is the intrinsic permeability.

Many studies are using the median particle diameter (d_{50}) as the characteristic length for the pore space. However, MacDonald et al. (1979) suggested that the use of the surface-volume mean diameter d_{Sm} (also referred to as Sauter mean diameter) as a more appropriate characteristic length compared to the d_{50}. It is defined as the diameter of a sphere that has the same volume/surface area ratio as the particle of interest. For a perfect spherical particle, the surface area moment mean diameter d_{Sm} equals:

$$d_{Sm} = 6\frac{V_p}{s_p} = d_{32} \tag{3.11}$$

where V_p/s_p [-] is the ratio between volume and surface area of the sphere. Note that for non-spherical particles, as well as an rougher particles this ratio decreases and, hence, the average characteristic pore length of the porous medium decreases (MacDonald et al. 1979; Li and Ma 2011; Allen et al. 2013) In general, it is challenging to determine the exact surface area of natural porous materials.

Evaluation of the empirical relations on experimental datasets of granular material

Several studies have analyzed the theoretical and empirical relationships in Table 3.1 for Forchheimer coefficients *a* and *b*. Sedhi-Asl et al. (2014) predicted the experimentally derived coefficients *a* and *b* accurately using Sidiropoulou et al. (2007) for sands with d_{50} ranging from 2.83 to 56.8 mm. A reasonable prediction for coefficient *a* was obtained using Ergun (1952) and Kovács (1981). However, coefficient *b* was systematically overestimated using Kovács (1981).

Moutsopoulos et al (2009) predicted the experimentally derived coefficients *a* and *b* accurately using Kovács (1981) for sands with a d_{50} of 2.71-67.23 mm. The equation by Ward (1964) significantly underestimated the coefficients *a* and *b*. The equation by Kadlec and Knight (1996) significantly overestimated coefficient *a*, but a good fit was obtained for the coefficient *b*. Moreover, Moutsopoulos et al. (2009) also suggested the use of d_{10} and d_{30} as particle diameter for the equation by Ward (1964), to provide good predictions for coefficients *a* and *b*.

Sidiropoulou et al. (2007) investigated a large dataset collected from the literature. For coefficient *a*, the equation by Ward (1964) significantly underestimated the experimentally derived coefficient, while the equation by Kadlec and Knight (1996) resulted in significant overestimation of the coefficient. Only the equation by Ergun (1952), resulted in a reasonable fit for coefficients *a* and *b*, where overall a underestimation was obtained for the experimentally derived coefficient. The equation by Ward (1964) resulted in significant underestimation of the values. Due to the relative

poor fits, Sidiropoulou et al. (2007) suggested to use an alternative equation for accurate estimation of the Forchheimer coefficients (see Table 3.1). Salahi et al. (2015) also suggest the use of the equation proposed by Sidiropoulou et al. (2007) to obtain the best estimates for Forchheimer coefficients a and b for their dataset. The purpose of the current study is to compare the expressions in Table 3.1 with our experimental dataset on filter sands and the experimental datasets in the literature.

3.2.4 Friction factor and Reynolds number

In the literature, many forms of the Darcy-Weisbach equation, which was initially derived for analyzing flow resistance in a conduit, are suggested for flow in porous media (e.g. Ergun 1952; Stephenson 1979; Herrera and Felton 1991). The method of Stephenson (1979) is widely used (e.g. Sedghi-Asl and Rahimi 2011; Salahi et al. 2015):

$$f = \frac{2gidn^2}{q^2} \; and \; Re_s = \frac{\rho d_{50} q}{n\mu} \tag{3.12}$$

The relation between Reynolds number Re_s and the friction factor f is usually given by:

$$f = \frac{a_s}{Re_s} + b_s \tag{3.13}$$

where a_s and b_s are dimensionless variables. Herrera and Felton (1991) used the mean grain size and standard deviation of the grains size distribution of a given sand type (d_m–σ) as characteristic pore length in Darcy-Weisbach and Reynolds number equations (Eq. 3.12 and 3.13). They stated that for well graded material with large standard deviations, finer particles fill the pores between coarser particles and the contact surface of particles with water increases. This condition increases flow resistance and decreases flow velocity and Reynolds number. We have tested both the method of Stephenson (1979) with Re_S and Herrera and Felton (1991) with Re_H.

3.3 Methods

3.3.1 Experimental set-up

In order to measure one-dimensional flow in various sandy porous media, we used the experimental set-up as shown in Fig. 3.1. It consists of the following main components; 1) the inlet, 2) the column with sandy porous medium, 3) the outlet and 4) the circulation tank of 1 m^3 with a pump. A Plexiglas sample column (2) with a length of 0.507 m, a wall thickness of 0.5 cm and an inner diameter of 9.8 cm contained the sandy porous media. The investigated sandy porous mediums have median grain sizes (d_{50}) of 0.39-

2.11 mm that are a factor 0.0040 and 0.0215 smaller than the diameter of the column, while for gravel (d_{50} of 6.34 mm) the factor was 0.065 smaller. Fand and Thinakaran (1990) stated that the ratio between d_{50} and column diameter should be lower than 0.025, to ensure that the flow parameters are substantially independent of the wall effects of the column. The highest ratio in the literature for conducted flow experiments were in the same range (0.032 for Li et al. (2017), 0.13 for Moutsopoulos et al. (2009) and 0.19 for Sedghi-Asl et al. (2014)). The water pressure in the column was measured at a distance of 0.13, 0.26, and 0.38 m from the inlet. The pressure at the inlet compartment (1) was also measured, while at the outlet compartment (3) the hydraulic head was fixed at 0.505 m. For all experiments, a linear hydraulic head gradient was obtained by interpolation of the measured water heads at the pressure monitoring points (5). The water pressure was measured with a BD Sensors pressure transmitter combined with a BD Sensors PA 430 display (5). The volumetric flow rate Q [m^3/h] was measured using a Metrima SVM F2 Energy Meter (6), which was placed between the pump (4) and the inlet compartment (1).

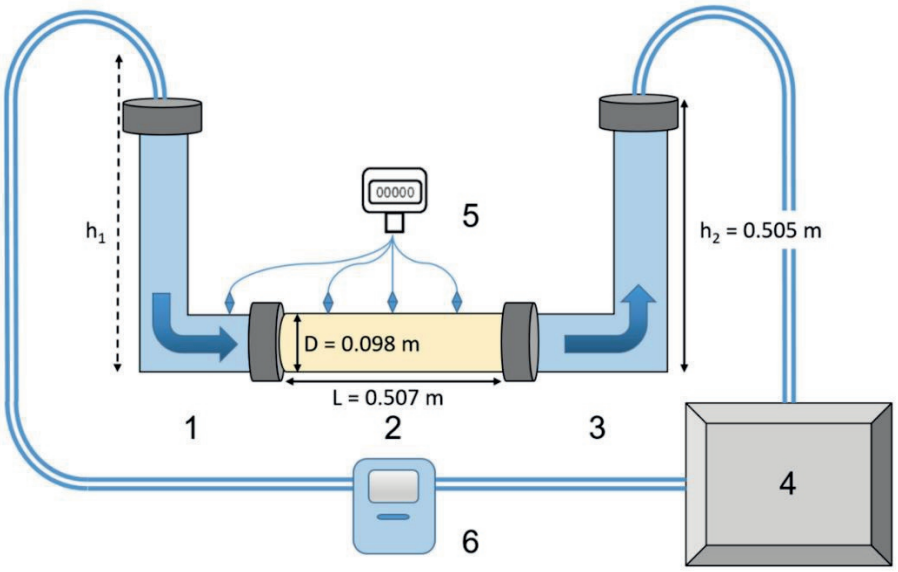

Fig. 3.1 Schematic overview of the experimental setup: 1) inlet compartment, 2) column with packed sandy porous medium, 3) outlet compartment, 4) circulating tank with pump, 5) pressure sensor and 6) volumetric flow meter.

For each experiment on a single sand sample, the flow rate was determined for various hydraulic gradients, $i\ (=(h_1-h_2)/L)$, by using different injection pressures. The pressures ranged from 0.1 to 3.2 bar (15 different injection pressures) for the finest granular material (S.1) and ranged from 0.1-1.2 bar (12 different injection pressures) for the coarsest granular material (S.11). At a given hydraulic gradient, the flow rate was determined for at least more than 29 times to ensure achievement of steady state flow conditions (defined as less than 3% variation in flow) in the porous medium. The temperature was measured in the outlet section of the experimental set-up. To ensure constant water density and viscosity, the temperature in the circulation tank was kept constant at 20 ˚C (±0.3 ˚C).

We have used the particle Reynolds number (Eq. 3.3) to determine the upper limit of the Darcy regime. For analysis, a deviation from Darcy's law is considered by observing a relative difference of 5% between the actual specific discharge described by the Forchheimer equation (Eq. 3.2) and the specific discharge described by Darcy's law (Eq. 3.1).The critical Reynolds numbers (Re_{cr}) are obtained for all investigated sandy porous media.

3.3.2 Description of the investigated sandy porous media

In this study, two sets of sandy porous media were investigated:

- At first, 11 uniformly graded filter sands (delivered by FILCOM company at Papendrecht, the Netherlands) with various median grain sizes (d_{50}) were used as reference porous media to obtain the Forchheimer coefficients a and b experimentally (Samples 1-11). These filter sands are used as gravel pack around well screens to increase well efficiency, and also for packed sand beds for drinking water or wastewater treatment.
- Subsequently, these filter sands were mixed to obtain 9 different packed sandy porous media with wider grain size distributions at a given median grain size (d_{50}) that equals one of the reference filter sands (Samples 3-8). Hence, we were able to test the effect of various grain size distributions for a given median grain size (d_{50}) on non-linear flow behavior experimentally (Samples 3.1, 4.1, 5.1 6.1-4, 7.1 and 8.1).

The porosity of each packed sample was determined by weighing the dry mass granular sand or gravel in the column. The solid phase density of the sand and gravel equal 2.66 kg/m^3 (data by FILCOM).

The granulometric sieve data for the 11 reference sands were used to analyze the grain size distributions. The median grain size (d_{50}), and the grain sizes d_{10}, d_{30} and d_{60} are listed in Table 3.2. The arithmetic method of moments was used to determine the mean particle diameter (d_m) and the standard deviation (σ) from the normal grain size distribution of the filter sands (Blott and Pye 2001), yielding:

$$d_m = \frac{\sum_{i=1}^{N} f_i d_i}{100} \tag{3.14}$$

and

$$\sigma = \sqrt{\frac{\sum_{i=1}^{N} f(d_i - d_m)^2}{100}} \tag{3.15}$$

where N is the number of used sieves for the grain size analysis, f is the passing frequency in percent on the corresponding i^{th} sieve, d_i [mm] is the average grain size diameter of the i^{th} sieve class interval. For the composite sands, specific portions of the reference sands were mixed. From the reference sand fractions, a new grain size distribution was determined and the d_m and σ were calculated based on a number of equal step intervals (N) subdividing this grain size distribution. For non-uniformly graded granular material, Herrera and Felton (1991) used the standard deviation of particle sizes and substituted the characteristic pore length d by d_m-σ. Moreover, the coefficient of uniformity C_u [-] and the coefficient of curvature C_c [-] of the grain size distribution are calculated, using:

$$C_u = \frac{d_{60}}{d_{10}} \tag{3.16}$$

and

$$C_C = \frac{(d_{30})^2}{d_{10} * d_{60}} \tag{3.17}$$

In line with the study of Moutsopoulos et al. (2009) we used the values d_{10}, d_{30} and d_{50} as characteristic pore length, d, in the empirical equation listed in Table 3.1. Also the method of Herrera and Felton (1991) was used by considering d_m-σ as the characteristic pore length.

Reference sands

The filter sands used in this study are classified as medium sand (S.1-2), coarse sand (S.3-6), very coarse sand (S.7-10) and fine gravel (S.11) (Blott and Pye 2001). The reference filter sands are uniformly graded with a C_u<1.48, C_c ranging from 0.98-1.05, and small arithmetic standard deviations (σ<0.938 mm) for all 11 samples (Table 3.2). All filter sands have a normal grain size distribution, resulting in approximately equal median grain sizes (d_{50}) and mean grain sizes (d_m). The roundness of the granular material is classified as subangular-subrounded.

	d_{50} [mm]	d_{10} [mm]	d_{30} [mm]	d_{60} [mm]	d_m [mm]	σ [mm]	$d_m - \sigma$ [mm]	C_C	C_u	n [-]
S.1	0.39	0.29	0.35	0.41	0.39	0.0845	0.31	1.05	1.39	0.344
S.2	0.39	0.28	0.34	0.41	0.39	0.0852	0.30	1.04	1.48	0.335
S.3	0.61	0.47	0.55	0.64	0.61	0.112	0.50	0.99	1.37	0.331
S.4	0.71	0.53	0.63	0.76	0.72	0.155	0.57	0.99	1.42	0.340
S.5	0.84	0.72	0.80	0.86	0.84	0.0921	0.75	1.02	1.19	0.333
S.6	0.99	0.80	0.91	1.03	0.98	0.164	0.82	1.01	1.30	0.346
S.7	1.05	0.89	0.98	1.08	1.05	0.138	0.91	1.00	1.21	0.348
S.8	1.36	1.13	1.27	1.41	1.35	0.189	1.16	1.01	1.25	0.358
S.9	1.50	1.16	1.34	1.58	1.52	0.287	1.23	0.98	1.36	0.358
S.10	2.11	1.72	1.97	2.18	2.07	0.306	1.76	1.03	1.27	0.357
S.11	6.34	5.16	5.87	6.55	6.28	0.938	5.34	1.02	1.27	0.361

Table 3.2 The grain size distribution characterization for uniformly graded filter sands used as reference.

Composite sands

Table 3.3 and Fig. B show that the d_{50} of the composite sands are equal to its corresponding reference sand. The composite sands (S.3.1-8.1) are slightly more well graded resulting in increased C_u values by a factor of 1.19 up to 1.47, while C_c values are more or less equal to the reference sands. The wider grains size distribution is also reflected by the increased standard deviation values. All composite sand samples have a normal grain size distribution, except for Sample 6.4. For that case a bimodal grain size distribution was obtained, with peaks at 0.75 and 1.38 mm. Hence, a reduced C_c value of 0.84 and an increased C_u value of 2.32 are obtained.

The use of slightly more well graded sands result in approximately equal porosities for both the reference and composite sands (with a relative errors ranging between 0.6 to 4.8%). Much wider grains size distributions are required to obtain significant reduction of porosity at a given median grain size (d_{50}). Only for the gap-graded composite sand S.6.4 with a clear bimodal grain size distribution, and for the more well graded sand S.6.1 slightly lower porosity values of respectively 0.330 and 0.332 were obtained with respect to the reference sand S.6 (n=0.345).

	d_{50} [mm]	d_{10} [mm]	d_{30} [mm]	d_{60} [mm]	d_m [mm]	σ [mm]	$d_m - \sigma$ [mm]	C_C	C_u	n [-]
S.3.1	0.62	0.40	0.53	0.66	0.62	0.168	0.45	1.06	1.63	0.334
S.4.1	0.71	0.44	0.60	0.77	0.72	0.218	0.50	1.04	1.74	0.332
S.5.1	0.84	0.57	0.73	0.89	0.84	0.203	0.64	1.06	1.56	0.337
S.6.1	0.99	0.61	0.85	1.08	1.03	0.350	0.68	1.10	1.78	0.330
S.6.2	0.99	0.68	0.89	1.03	0.96	0.208	0.75	1.12	1.52	0.344
S.6.3	0.99	0.74	0.89	1.05	1.01	0.240	0.77	1.01	1.42	0.348
S.6.4	1.01	0.53	0.74	1.23	-	-	-	0.84	2.32	0.332
S.7.1	1.06	0.71	0.91	1.12	1.07	0.311	0.76	1.06	1.58	0.337
S.8.1	1.36	0.81	1.12	1.49	1.39	0.453	0.93	1.03	1.84	0.345

Table 3.3 The grain size distribution characterization for the filter sand mixtures.

3.3.3 Preparation technique for the sandy porous media

A consistent and reproducible packing method for the column samples was used to obtain homogenously packed porous media. Different compaction preparation techniques were tested, to obtain the highest grain density and, hence, optimal compaction grades for each sample column. We followed the method by Rietdijk et al. (2010) by using a constant pluviation rate of the sand, as well a continuous manual compression of the deposited sand in a fully saturated column. This resulted in the lowest porosity values for the packed porous media samples, ranging from 0.33 for uniformly graded medium sand (Sample 1) to 0.36 for uniformly graded gravel (Sample 11) (Table 3.2). Other packing methods resulted in significantly higher porosities (up to 0.38-0.40) of the porous

medium. The lower compaction grades resulted in non-rigid pore structures at increased fluid pore pressures in the column during the flow experiment tests.
Repeatedly testing of the Rietdijk et al. (2010) method as sample preparation technique for a given filter sand showed that a reproducible compaction grade, and hence porosity (relative errors ranging between 0.02 to 1.1%) was obtained. For flow behavior, the maximal relative error for coefficient *a* was 2.0% and for coefficient *b* 3.1%. The reproducibility was tested for the reference filter sands S.2, S.3 and S.5. Therefore, we have used the Rietdijk et al. (2010) method for each sample to obtain an equal compaction grade and porosity over the entire column length and to ensure a stable pore structure of the sandy porous medium during the flow behavior experiments at increased injection pressures (up to 3 bar).

After the saturated sample preparation of the sample column inside a container filled with water, the inlet and outlet compartments were mounted under water to ensure no air inclusion occurred during the whole procedure. The water head at the inlet and outlet side provided fully saturated conditions during the installation into the experimental set-up with the measuring equipment.

3.3.4 Validity analysis of the empirical relationships for predicting Forcheimer coefficients

The experimental dataset from this study was used to analyze the validity of the empirical relationships listed in Table 3.1. In order to compare the experimentally derived coefficients *a* and *b*, with the empirically predicted coefficients by equations 4-9, the following methods are used; 1) the Normalized Objective Function (*NOF*) criterion and 2) linear regression analysis. A similar approach was used in the studies of Moutsopoulos et al. (2009), Sedghi-Asl et al. (2014) and Sidiropoulou et al. (2007). Hence, a comparison can be made between our results and the results of their studies.

The *NOF* is defined as the ratio between the Root Mean Square Error (*RMSE*) to the overall mean value *X* of the experimental data.

$$NOF = \frac{RMSE}{X}, \tag{3.18}$$

where:

$$RMSE = \sqrt{\frac{\sum_{i=1}^{N}(x_i - y_i)^2}{N}} \tag{3.19}$$

and

$$X = \frac{1}{N}\sum_{i=1}^{N} x_i \tag{3.20}$$

Here x_i are the experimental values for either the *a* coefficients or the *b* coefficients of the Forchheimer equation (Eq. 3.2) and y_i the corresponding values computed by the empirical relationship (Eq. 3.4-10) for which the *NOF* analysis is done. A *NOF* value lower than 1.0 implies a reasonable prediction of the coefficients *a* and *b* by the empirical relationships, where values close to 0.0 implies a perfect fit.

Linear regression is applied on scatter plots with the experimentally derived Forchheimer coefficient on the horizontal axis and the empirically predicted coefficient by the relationship (Eq. 3.4-10) on the vertical axis. For a good prediction, the slope of the regression line equals 1.0. Values that are lower than 1.0, imply underestimation of the Forchheimer coefficients by the empirical relationship, while values higher than 1.0 imply overestimation. Moreover, the R^2-coefficient should be close to a value of 1.0 to ensure reduced scattering of the data points along the regression line.

3.4 Results

In this section, first, the reference experimental dataset on non-linear flow behavior in the 11 samples of filter sands are presented. Subsequently, the non-linear flow behavior in the composite sands are presented and compared to the reference dataset. Moreover, a comparison between the whole dataset of this study and the experimental data of existing literature is given. Finally, the empirical relationships for estimating the Forchheimer coefficients *a* and *b* in Table 3.1 (Eq. 3.4-10) are verified using our experimental dataset.

3.4.1 Non-linear flow behavior in the reference sands

Using the Forchheimer relation for non-linear flow (Eq. 3.2) between the hydraulic gradient *i* and the specific discharge *q*, the Forchheimer coefficients *a* and *b* are determined. Fig. 3.2 shows the Forchheimer fits on the experimental data for all 11 reference sands. For all investigated samples, the non-linear flow behavior could be accurately described using the Forchheimer relation, resulting in R^2-coefficients >0.99 (see Table 3.4). The linear Darcy flow $i = aq$ is also plotted (dashed line) to show the non-linear deviation from Darcy's law at increased flow velocities. Table 3.4 shows that only samples 1-4 have a critical Reynolds number Re_{cr} for the onset of non-linear flow within the measured range Re_{min} - Re_{max}. The rest of the samples have only data in the non-linear flow regime.

The critical Reynolds numbers in this study vary between 2.21 and 4.13 (see Table 3.4), which fall in the limits of 1-15 reported in the literature (e.g. Bear 1988; Hassanizadeh and Gray 1987; Comiti et al. 2000).

For the reference sands S.1 and 2, multiple data points were in the Darcy regime and, hence, the coefficient a can be determined directly using a linear interpolation ($i = a_{Darcy}\, q$). For Sample 1, coefficient a_{Darcy} is 1962.5 with R^2>0.99 (5 data points), while for Sample 2, a_{Darcy} is 1453.5 with R^2 =0.99 (4 data points). The a_{Darcy} coefficients are in agreement with the a coefficients determined by the Forchheimer fit over the whole dataset (see Table 3.4), resulting in small relative errors of 2.1 and 1.9%, respectively. This is in agreement with the results of Venkataraman and Rao (1998), who also observed similar coefficients for Forchheimer a and a_{Darcy} . However, other studies showed that the Forchheimer coefficient a in the non-linear flow regime can significantly differ from the resistance coefficient a_{Darcy} in the Darcy regime (see Bağci et al. (2014)). Note that the coefficient a for S.2 is significantly lower than for S.1, while the grain size distribution and porosity of both filter sands are more or less identical. The decreased flow resistance for S.2 might be due to a significant difference in the geometry of the pore structure. However, such differences in geometry should be due to large contrast in particle roughness or grain shape, which is unlikely in our case with subangular-subrounded grains of the filter sands.

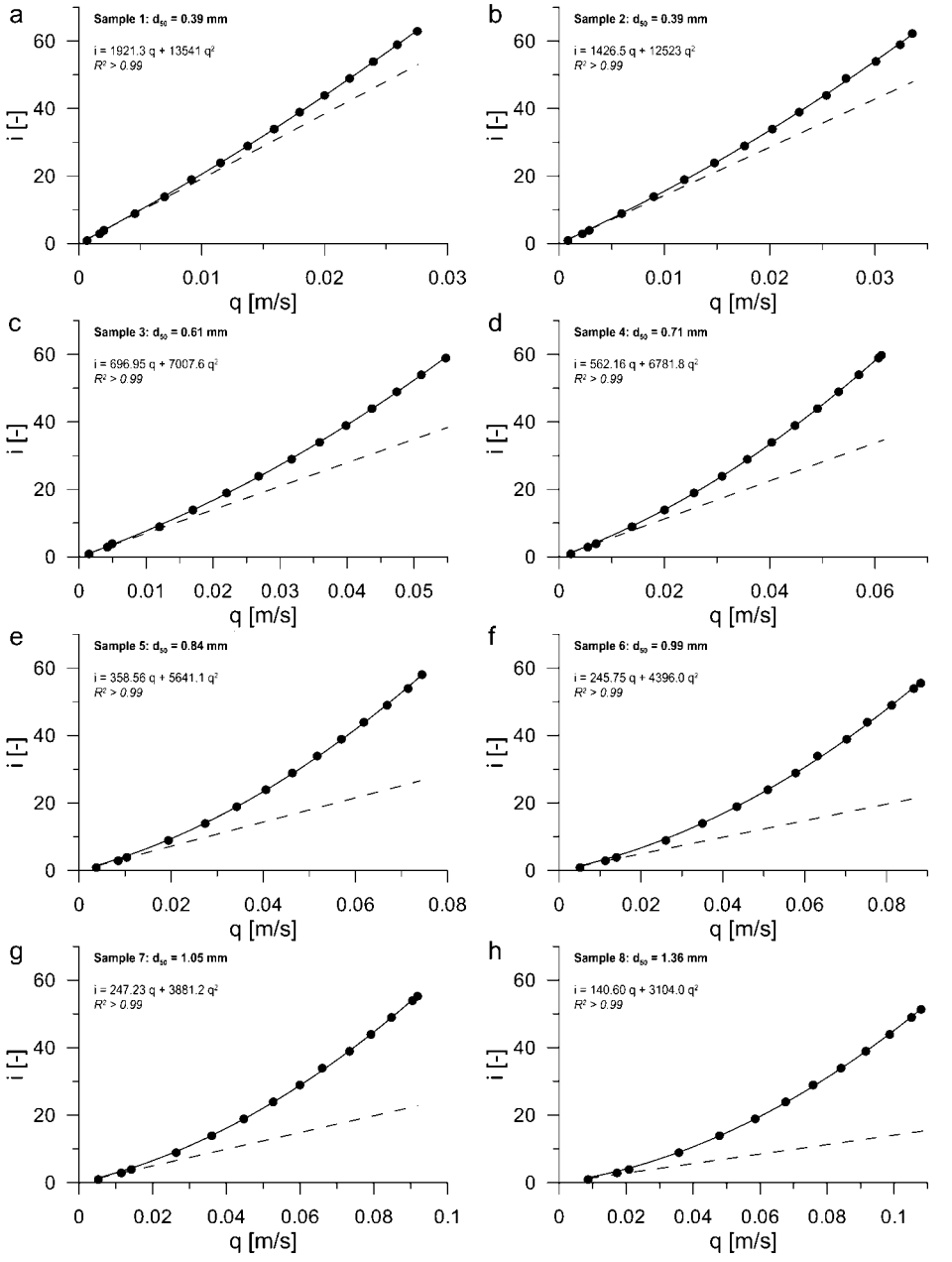
a
Sample 1: d_{50} = 0.39 mm
i = 1921.3 q + 13541 q²
R^2 > 0.99
b
Sample 2: d_{50} = 0.39 mm
i = 1426.5 q + 12523 q²
R^2 > 0.99
c
Sample 3: d_{50} = 0.61 mm
i = 696.95 q + 7007.6 q²
R^2 > 0.99
d
Sample 4: d_{50} = 0.71 mm
i = 562.16 q + 6781.8 q²
R^2 > 0.99
e
Sample 5: d_{50} = 0.84 mm
i = 358.56 q + 5641.1 q²
R^2 > 0.99
f
Sample 6: d_{50} = 0.99 mm
i = 245.75 q + 4396.0 q²
R^2 > 0.99
g
Sample 7: d_{50} = 1.05 mm
i = 247.23 q + 3881.2 q²
R^2 > 0.99
h
Sample 8: d_{50} = 1.36 mm
i = 140.60 q + 3104.0 q²
R^2 > 0.99
i [-]
q [m/s]

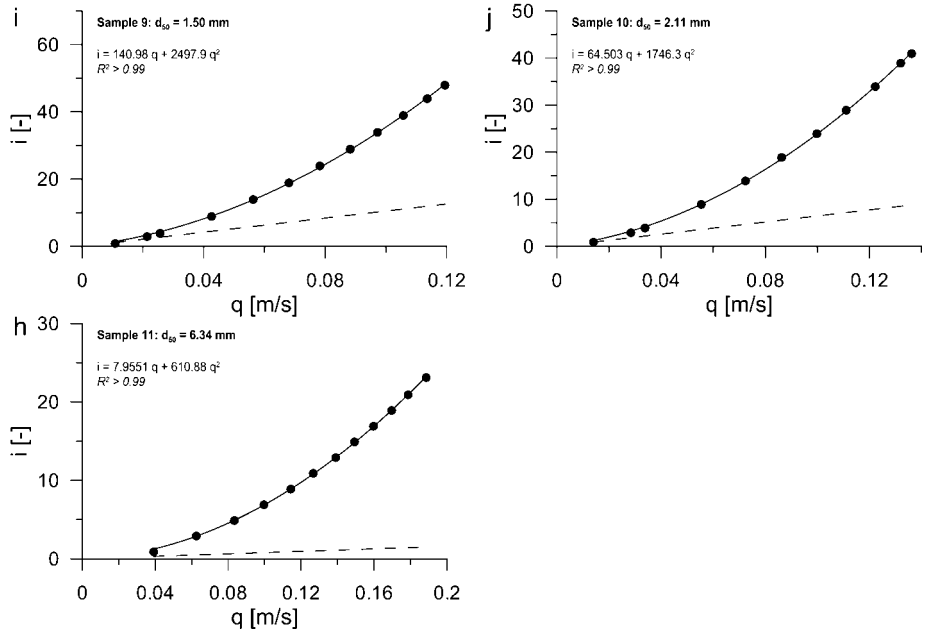

Fig. 3.2 *The i-q plots for the sandy reference porous media S1-11. The linear Darcy flow i=aq is plotted (dashed line) to visualize non-linear deviation from Darcy's law.*

Sample	d_{50} [mm]	Re_{min}	Re_{max}	Re_{cr}	a [sm^{-1}]	b [s^2m^{-2}]	R^2
1	0.39	0.26	10.72	2.76	1,921.3	13,541	>0.99
2	0.39	0.33	13.02	2.21	1,426.5	12,523	>0.99
3	0.61	1.21	34.59	2.67	696.96	7,007.6	>0.99
4	0.71	1.58	43.72	2.96	562.16	6,781.8	>0.99
5	0.84	3.28	62.07	2.69	358.56	5,641.1	>0.99
6	0.99	5.02	87.29	2.76	245.75	4,396.0	>0.99
7	1.05	5.51	96.28	3.34	247.23	3,881.2	>0.99
8	1.36	11.78	147.06	3.08	140.60	3,104.0	>0.99
9	1.50	16.33	179.44	3.16	104.98	2,497.9	>0.99
10	2.11	29.65	287.92	3.90	64.503	1,746.3	>0.99
11	6.34	248.34	1196.78	4.13	7.9551	610.88	>0.99

Table 3.4 The Forchheimer coefficients *a* and *b* for the reference sands (S.1-11)

3.4.2 Non-linear flow behavior in the composite sands

Similar to the reference sands, the non-linear flow behavior for the composite sands could be described accurately by the Forchheimer equation (Eq. 3.2). The R^2-coefficients are larger than 0.99 for all plots (see Table 3.5). Fig. 3.3 shows that for the slightly more well graded composite sands the flow resistance was increased due to an increase in the fraction of smaller particles (decreased d_{10} and d_{30} and increased C_u values) with respect to the reference sands at equal median grain size (d_{50}) (see Table 3.3 and Fig. 3.3 and Fig. C). This means that the *a* coefficients were increased by factors up to 1.68, while the *b* coefficients were increased by factors up to 1.44 with respect to the reference sands.

Four sands with different grain size distributions and similar d_{50} compared to its associated reference sand S.6 were investigated (see Fig. 3.3b). Composite sand S6.3 shows a relative increase in coarser material (i.e., tailing in the grain size distribution) with respect to the reference sand S.6, while the finer material is equal. This resulted in approximately similar *a* and *b* coefficients for both S.6 and S.6.3. For the other composite sands S.6.2, 6.1 and 6.4, the d_{10} was decreased by a factor 0.86, 0.76 and 0.66, respectively. This resulted in an increase by a factor 1.33, 1.47 and 1.68 for coefficient *a* with respect to reference sample 6. For coefficient *b*, an increase by a factor 1.18, 1.27 and 1.44 was obtained. The bimodal grain size distribution of composite sand S.6.4 has a peak in the grain size distribution at 1.38 mm. However, the relative increase in coarser material with respect to reference sand S.6 does not seem to influence the increase in flow resistance caused by the finer material.

Sample	d_{50} [mm]	Re_{min}	Re_{max}	Re_{cr}	a [sm^{-1}]	b [s^2m^{-2}]	R^2
3.1	0.617	0.97	32.38	2.67	740.18	8,219.7	>0.99
4.1	0.713	1.44	40.29	2.84	623.57	7,839.1	>0.99
5.1	0.841	2.46	58.25	2.77	418.33	6,349.4	>0.99
6.1	0.993	3.36	73.71	3.24	362.31	5,561.2	>0.99
6.2	0.988	3.86	77.58	3.11	326.26	5,181.8	>0.99
6.3	0.99	5.51	86.67	2.90	256.80	4,380.2	>0.99
6.4	1.006	3.08	70.14	3.27	412.74	6,351.4	>0.99
7.1	1.048	4.44	84.89	3.19	283.51	4,965.6	>0.99
8.1	1.363	10.16	138.27	3.26	168.36	3,518.9	>0.99

Table 3.5 The Forchheimer coefficients *a* and *b* for the composite sands.

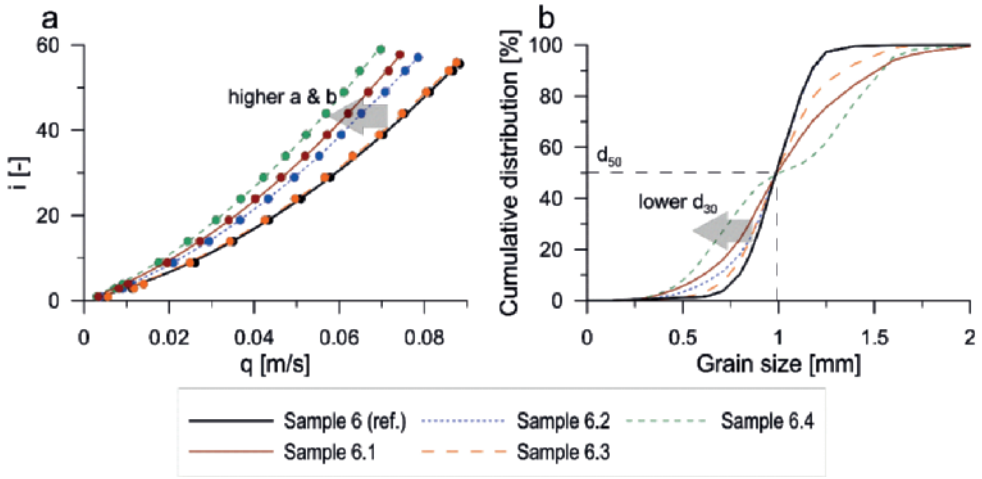

Fig. 3.3 a) The *i-q* plots and **b)** the cumulative grain size distributions for the sandy porous media S.6.1-4. Decreased d_{30} results in increased flow resistance (higher *a* and *b* coefficients) compared to the reference sand S.6.

3.4.3 Comparison with the literature

In Fig. 3.4 the experimentally determined coefficients *a* and *b* are plotted against particle size d_{50} for reference sands S.1-11, where a power function is fitted to the results. The Forchheimer coefficients increase with decreasing grain size of the porous media. The coefficients *a* and *b* for the composite sands are also plotted, but were not taken into account for fitting of the power function. A poorer fit is obtained when the composite sand samples are taken into account. In this case the R^2-coefficients are 0.98 and 0.97 for coefficient *a* ($= 0.004d^{-1.94}$) and *b* ($= 1.95d^{-1.13}$), respectively.

These results compare well to the data found by Sidiropoulou et al. (2007), who obtained the following relations; $a = 0.00859d^{-1.727}$ and $b = 0.5457d^{-1.253}$. Apart from samples 10 and 11, all other samples have a d_{50} smaller than 2 mm, while the dataset of Sidiropoulou et al. is based on a broad data set of 89 samples with an average d_{50} of 15 mm. The Forchheimer coefficients provided by Sidiropoulou et al. (2007) for sands with median grain sizes d_{50} ranging from 0.7 and 2.58 mm are selected and plotted in Fig. 3.4. For the samples with similar grain sizes in their dataset, the sample with the lowest porosity is used. Unfortunately, the porosity is not given for 8 of the samples, while for the other samples the porosity was significantly larger than in our experiments (with values of 0.381-392). This could explain the slightly lower values for the Forchheimer coefficients compared to our data, where the porosity values are significantly lower.

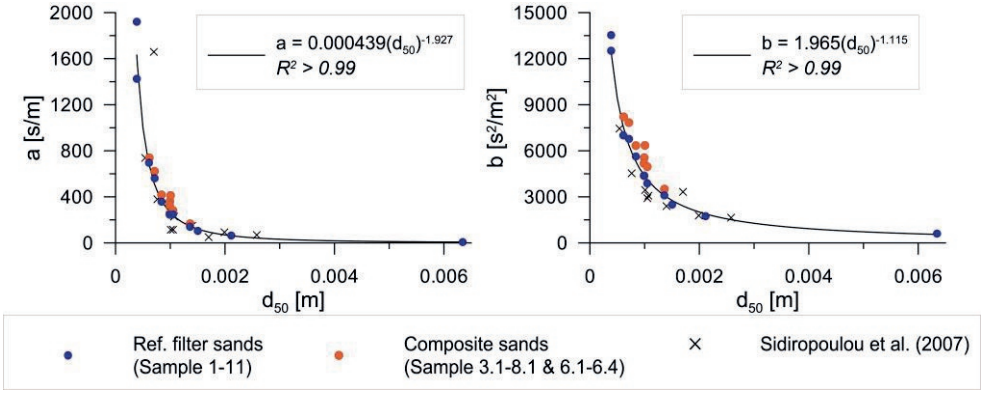

Fig. 3.4 a) Relationship between the median grain size (d_{50}) and Forchheimer coefficient a, as well as for **b)** Forchheimer coefficients b, for dataset samples 1-11. The Forchheimer coefficients of the composite sands and sands provided by Sidiropoulou et al. (2007) with median grain sizes ranging from 0.7 and 2.58 mm are also plotted.

A large dataset on the intrinsic permeability k [m^2] of sands is available in the literature, while in most cases the non-linear term b of the Forchheimer is unknown. Hence, we have plotted the Forchheimer coefficient a, which is equal to $\mu/\rho g k$ (e.g. Venkataraman and Rao (1998)), as a function of coefficient b for all samples (see Fig. 3.5) where a good correlation between both values is found. This function could be used to estimate the Forchheimer coefficient b from experimental values of the intrinsic permeability in the literature for similar subangular-subrounded uniformly graded sand types.

Our dataset is compared to the recent studies of Sidiropoulou et al. (2007), Moutsopoulos et al. (2009), Bağci et al. (2014), Sedghi-Asl et al. (2014), Salahi et al. (2015) and Li et al. (2017). The Moutsopoulos et al. (2009), Salahi et al. (2015) and Li et al. (2017) datasets on coarser granular material correspond well to the fit on our dataset of finer sands (see Fig. 3.5). The flow experiments in these studies are conducted at particle Reynold numbers in the same range as in our study (up to Re=560.97 for Moutsopoulos et al. (2009), up to Re=1882 for Salahi et al. (2015) and up to Re=40 for Li et al. 2017). The same applies to Bağci et al. (2014), where non-linear flow in packed porous media of mono-size steel balls is investigated. From the Sidiropoulou et al. (2007) dataset, the data for granular sands, gravel and round river gravel by Ahmed and Sunada (1969) (data by Ahmed), Ranganadha (1970), Tyagi and Todd (1970) and Arbhabhirama and Dinoy (1973) corresponds well. Sedghi-Asl et al. (2014) and the rest of the dataset of Sidiropoulou et al. (2007) (by Ahmed and Sunada (1969), Venkataraman and Rao (1998), Bordier and Zimmer (2002)), which mainly consists of glass spheres and crystalline rock, underestimate b for a given a, compared to our dataset.

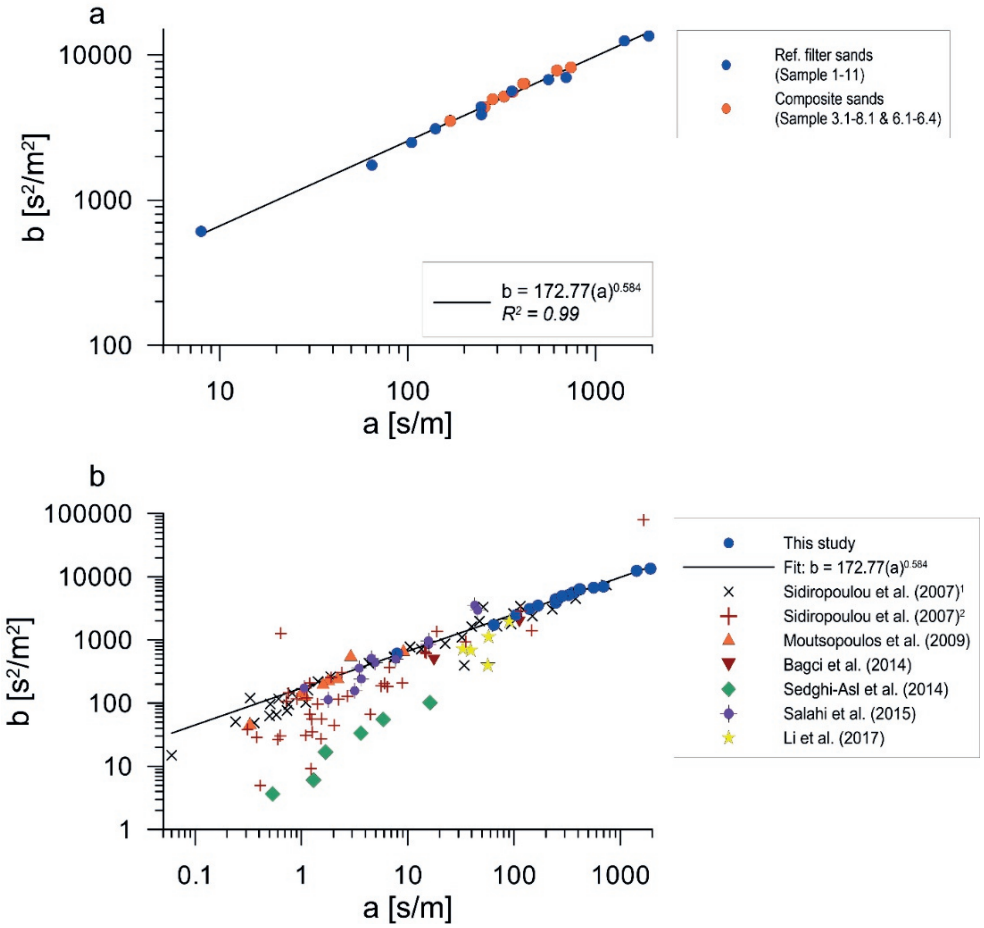

Fig. 3.5 a) Forchheimer coefficient *b* as a function of coefficient *a* for the reference and composite sands. **b)** Forchheimer coefficient *b* versus coefficient *a* for literature datasets. *[1)]Data from Sidiropoulou et al. (2017) by Ahmed and Sunada (1969) (data by Ahmed); Ranganadha (1970); Tyagi and Todd (1970) and Arbhabhirama and Dinoy (1973)). [2)] Data from Sidiropoulou et al. (2017) by Ahmed and Sunada (1969); Venkataraman and Rao (1998) and Bordier and Zimmer (2002)).*

Similar to the current study, the effect of the grain size distribution on non-linear flow behaviour was shown by Moutsopoulos et al. (2009) for different mixtures of quarry carbonate rocks. The grain size d_{10}-d_{60} values of the mixtures are shown in Fig. 3.6b. The reference material M.3 has approximately the same median grain size (d_{50}) as the composite material M.7. Similar to the present study, increased fraction of finer material (decreased value of d_{30}) for M.7 results in increased flow resistance of the porous media.

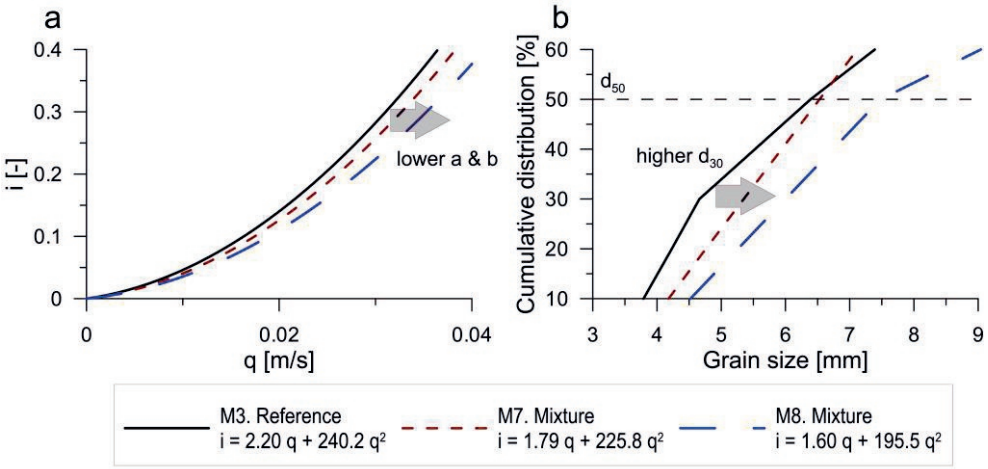

Fig. 3.6 a) Forchheimer *i-q* plot for different mixtures of quarry carbonate rocks and **b)** the associated grain size distributions (obtained from Moutsopoulos et al. (2009)). Increased d_{30} results in decreased flow resistance (lower *a* and *b* coefficients) compared to the reference material M3.

3.4.4 Analyzing of the relationships for predicting Forchheimer coefficients

The *NOF* criterion and the linear regression method (mentioned in section 3.3.4 '*Validity analysis of the empirical relationships for predicting Forcheimer coefficients*') are used to evaluate the reliability of the empirical relationships provided in Table 3.1. The entire dataset of both reference and composite sands is used for the analysis. Considering the median grain size (d_{50}), the relationships of Ergun (1952), MacDonald et al. (1979) and Kovács (1981) seem to provide the most accurate estimation for coefficient *a* with regression slopes of 1.47, 0.64 and 0.62, respectively (Table 3.6). For coefficient *b*, MacDonald et al. (1979) and Kovács (1981) obtained the best fits, resulting in a regression slope of 1.20 and 0.84, respectively (see Table 3.7). The accuracy of MacDonald et al (1979) and Kovács (1981) is also confirmed by the *NOF* analysis (see Tables 3.6 and 3.7). Overall, the relationship of MacDonald et al. (1979) overestimates the flow resistance, while Ergun (1952) and Kovács (1981) underestimate the flow

resistance, using the median grain size (d_{50}). The relationship by Sidiropoulou et al (2007) seems to be reliable for the estimation of the coefficient *b* using d_{50}, while a poor fit was obtained for coefficient *a*. In order to investigate the empirical relation of Geertsma (1974), the intrinsic permeability was calculated from the determined *a* coefficient from our experimental dataset. A poor estimation of the coefficient *b* was obtained.

Generally, the use of the characteristic pore length d_m-σ of in the empirical relationships (Eq. 3.4a-9a) results in the best estimates for coefficient *a*, except for MacDonald et al. (1979) and Kadlec and Knight (1996). MacDonald et al. (1979) also results in poor estimated for coefficient *b*. For both Ergun (1952) and Kovács (1981), the best estimations for both coefficient *a* and coefficient *b* are obtained. Also, the use of d_{10} results in reasonable regression slope values. However, for the estimation of coefficient *a* while using d_{10}, the data is more scattered around the regression line, resulting in a R^{2}-coefficient of 0.89, while 0.94 is obtained for d_m-σ.

	d_{10}			d_{30}			d_{50}			d_m- σ		
	Slope	**R^2**	**NOF**	**slope**	**R^2**	**NOF**	**slope**	**R^2**	**NOF**	**slope**	**R^2**	**NOF**
Schneebli et al. (1955) ***Eq. 3.4a***	0.808	0.93	0.341	0.530	0.95	0.664	0.418	0.96	0.815	0.701	0.96	0.438
Ward (1964) ***Eq. 3.5a***	0.265	0.93	1.026	0.174	0.95	1.151	0.137	0.96	1.202	0.229	0.96	1.074
Ergun (1952) ***Eq. 3.6a with A=150***	1.128	0.89	0.537	0.816	0.93	0.340	0.643	0.94	0.525	1.078	0.94	0.295
Kovács (1981) ***Eq. 3.6a with A=144***	1.198	0.89	0.482	0.783	0.93	0.370	0.617	0.94	0.557	1.035	0.94	0.268
MacDonald et al. (1979) ***Eq. 3.7a***	2.871	0.89	2.782	1.877	0.92	1.332	1.477	0.94	0.774	2.480	0.93	2.161
Kadlec and Kinght (1996) ***Eq. 3.8a***	4.533	0.89	5.158	2.963	0.92	2.861	2.332	0.93	1.959	3.914	0.93	4.189
Sidiropoulou et al. (2007) ***Eq. 3.9a***	0.425	0.86	0.811	0.309	0.90	0.965	0.258	0.91	1.035	0.381	0.91	0.867

Table 3.6 Linear regression slope and *NOF* value for the evaluation of the empirical relationships for the Forchheimer coefficient *a*.

	d_{10}			d_{30}			d_{50}			d_m- σ		
	Slope	**R^2**	**NOF**	**slope**	**R^2**	**NOF**	**slope**	**R^2**	**NOF**	**slope**	**R^2**	**NOF**
Schneebli et al. (1955) ***Eq. 3.4b***	0.345	0.97	0.746	0.277	0.97	0.823	0.244	0.95	0.861	0.317	0.98	0.776
Ward (1964) ***Eq. 3.5b***	0.300	0.97	0.797	0.241	0.97	0.864	0.212	0.95	0.897	0.277	0.98	0.826
Ergun (1952) ***Eq. 3.6b with B=1.75***	0.865	0.95	0.188	0.694	0.96	0.357	0.610	0.96	0.450	0.797	0.97	0.243
Kovács (1981) ***Eq. 3.6b with B=2.4***	1.186	0.95	0.258	0.951	0.96	0.115	0.836	0.96	0.209	1.093	0.97	0.148
MacDonald et al. (1979) ***Eq. 3.7b***	1.707	0.94	0.836	1.368	0.96	0.447	1.2035	0.95	0.270	1.572	0.96	0.672
Kadlec and Kinght (1996) ***Eq. 3.8b***	0.988	0.95	0.123	0.793	0.96	0.250	0.697	0.96	0.354	0.911	0.97	0.134
Sidiropoulou et al. (2007) ***Eq. 3.9b***	1.480	0.96	0.578	1.122	0.96	0.198	0.955	0.94	0.154	1.337	0.97	0.414

	k (=μ/ρga)		
	Slope	**R^2**	**NOF**
Geertsma (1974) ***Eq. 3.10***	0.2068	0.95	0.904

Table 3.7 Linear regression slope and *NOF* value for the evaluation of the empirical relationships for the Forchheimer coefficient *b*.

Derivation of Ergun constants based on the experimental dataset

The Ergun constants A and B are determined for our dataset following the linear regression procedure (mentioned in section 3.3.4 '*Validity analysis of the empirical relationships for predicting Forcheimer coefficients*'). This is done for the median grain size (d_{50}), as well as for d_{30} and d_{10}. Using the median grain size (d_{50}), or d_{30}, the Ergun constants based on our experimental dataset are higher than the values provided by Ergun (1952) and Kovács (1981) (Table 3.8).

In the literature, a wide range of different values of the Ergun constants can be found. According to DuPleisis's (1998) analytical study on flow behaviour in the non-linear laminar flow regime higher constants A and B in the range of 200 and 1.97 should be used. The Ergun constant B of 2.88 (d_{50}) and 2.53 (d_{30}) is in agreement with the value provided by Engelund (1953), who stated that a value of approximately 2.8 should be used for uniform and rounded sand grains. The range of typical suitable experimental Ergun constants for sands and gravel in the literature is large. The dataset of sand and gravel in MacDonald et al. (1979) provides an average Ergun constant A of 254.4 (range of 142-488) and an average Ergun constant of 2.024 (ranging from 2.52- 1.01). Analysis of the Li et al. (2017) dataset results in an average Ergun constant A of 349.6 and an average Ergun constant B of 1.786. From the Sidiropoulou et al. (2007) dataset, the data for granular sands, gravel and round river gravel by Arbhabhirama and Dinoy (1973), as well as Ranganadha (1970), are used, resulting in an average Ergun constant A of 257.6 and an average Ergun constant B of 2.89. For the dataset of Moutsopoulos et al. (2009) an average Ergun constant A of 220.4 (range of 144.7-429.2) is derived using d_{50}, while the derived Ergun constant A for cobbles is erroneously high (value of 1963). The average Ergun constant B is 2.26 (range of 1.95-3.39). The Ergun constants provided by these studies on non-linear flow behaviour in granular material compare well to the values we have obtained in this study.

The use of a smaller grain size d_{30}, as well as d_m-σ, for the characteristic pore length, and their associated derived Ergun constants, obtained approximately similar *NOF* values and R^2-coefficients for the regression line (see Table 3.8) as compared to fitting analysis using d_{50}. The fits using d_{10} are less accurate.

Particle size	Ergun constant (*Eq. 3.6*)		slope	R^2	NOF
d_{50}	**A**	233.5	1.00	0.94	0.260
	B	2.88	1.00	0.96	0.113
d_{10}	**A**	120.3	1.00	0.89	0.330
	B	2.03	1.00	0.94	0.124
d_{30}	**A**	183.8	1.00	0.93	0.275
	B	2.53	1.00	0.96	0.106
d_m- σ	**A**	139.1	1.00	0.94	0.254
	B	2.20	1.00	0.97	0.095

Table 3.8 Estimation of the Ergun constant *A* and *B* with linear regression analysis at γ=1.00 using all sand samples.

Ergun constants and the effect of finer material

In order to investigate the effect of the different grain size distributions of the composite sands with respect to the reference sands, linear regression analysis is applied to the reference sands S.3-8 and the corresponding sand mixtures (see Fig. 3.7 and Table 3.9). The Ergun constants derived from the entire dataset of this study were used (see Table 3.8). The use of d_{30} and d_m-σ and associated Ergun constants *A* and *B* result in only a slightly better fit with the experimental Forchheimer coefficients. It should be noted that small variations in porosity between the reference and composite sands (see Table 3.2 and 3.3) affects the prediction of coefficient *a* and coefficient *b* using Eq. 3.6. Note that the d_{30} for the composite sands is decreased by factors ranging between 0.81 up to only 0.96. Hence, the characteristic pore length of d_{30} might provide better estimations for the Forchheimer coefficients for well-graded sands with a significant increase in finer material (significantly decreased d_{30} values) with respect to uniformly graded sands at approximately equal porosity values. The same holds for the use of d_m-σ. However, compaction of typical well graded sandy soils with wide grain size distributions normally result in reduced porosity values compared to uniformly graded sands.

Particle size	Ergun constant (*Eq. 3.6*)		Slope	R^2
d_{50}	**A**	233.5	1.0502	0.89
	B	2.88	1.0464	0.93
d_{10}	**A**	120.3	0.9595	0.96
	B	2.03	1.02	0.86
d_{30}	**A**	183.8	1.0021	0.97
	B	2.53	1.032	0.93
d_m- σ	**A**	139.1	1.0001	0.95
	B	2.20	1.032	0.95

Table 3.9 Analysis of the reference sands (S.3-8) and all composite sands using the relationship of Ergun (1952) with the Ergun constants provided in Table 3.7. The used data is plotted in Fig. 3.7.

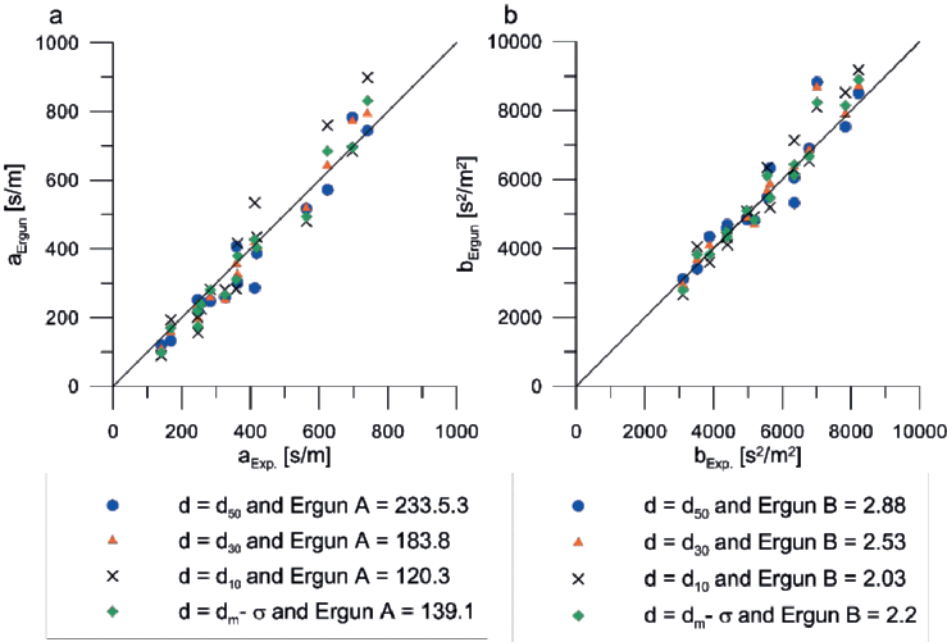

Fig. 3.7 a) Analysis of the reference sands (S.3-8) and all composite sands using the relationship of Ergun (1952) (see Eq. 3.6) for Forchheimer coefficient *a*, and **b)** Forchheimer coefficient *b*.

3.4.5 Friction factor

The friction factor calculated with Eq. 3.12 is plotted versus the Reynolds number Re_s in Fig. 3.8. We used regression analysis on out full dataset to obtain the following relationship:

$$f = \frac{1340}{Re_s} + 19.35; \quad R^2 = 0.97 \tag{3.21}$$

At Reynolds numbers Re_s higher than 9,000, f<19.5. This means that in this case Forchheimer equation reduces to bq^2 and flow can be considered fully-turbulent (Burcharth and Andersen 1995; Venkataraman and Rao 1998; Salahi et al. 2015). Our results are in agreement with Salahi et al. (2015), who obtained $f = \frac{967}{Re_s} + 9.45$ with a R^2 of 0.98 for their experimental dataset on coarse granular material.

We have also followed the method of Herrera and Felton (1991) to relate the friction factor to their proposed Reynolds number Re_H:

$$f = \frac{822.3}{Re_H} + 13.16; \quad R^2 = 0.95 \tag{3.22}$$

Herrera and Felton (1991) proposed their form of the Darcy-Weisbach equation for well-graded coarse material. However, the composite sands in our dataset are only slightly more well-graded compared to our reference dataset (C_u<1.8). Hence, no large difference between the method of Stephenson (1979) and Herrera and Felton (1991) is found for our dataset.

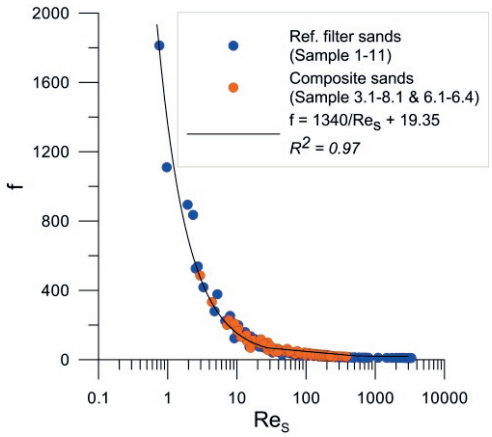

Fig. 3.8 The relationship between Reynolds number Re_S and friction factor f using the Stephenson (1979) method.

3.5 Discussion

In this study, non-linear flow behaviour experiments on the composite and the reference sands (S.1-9) were conducted at minimum particle Reynold numbers ranging between 0.26-16.33 (Tables 3.4 and 3.5). Hence, it is likely that the majority of the flow dataset at lower Reynold numbers is determined at the onset of the non-linear laminar flow regime. Experimental studies on flow behaviour in packed uniform spheres determined critical Reynolds numbers (Re>300) for fully turbulent flow (e.g. Dybbs and Edwards 1984; Seguin et al. 1998). According to Andersen and Burkharth (1995), it is challenging to define the transition from non-linear laminar flow to fully turbulent flow for granular, irregular shaped, porous media. Consequently, it is difficult to identify to what extent the fully turbulent flow is developed at increased particle Reynolds numbers in the coarser material. Overall, the grain sizes of the investigated sands in this study are significantly lower than for the sands and gravel in literature, and therefore the observed flow resistance by means of Forchheimer coefficients a and b is significantly higher (see Fig. 3.5b).

To date, complete understanding of the macroscopic non-linear flow behavior at specific Reynold numbers for different complex pore structures is hampered due to insufficient knowledge about the link between the macroscopic flow characteristics and complex microscopic pore structures. Many attempts have been made to link Forchheimer coefficients a and b, to different pore scale parameters. For example, some studies have linked the effect of the tortuosity (ratio between effective hydraulic stream line length and straight-line length between two points to characterize fluid pathways) to the Forchheimer coefficient b (e.g. Liu et al. 1995; Thauvin and Mohanty 1998). Overall, increased tortuosity of a porous medium results in increased flow resistance and, therefore, larger b coefficients. However, it is difficult to obtain the tortuosity for complex pore structures of granular porous media. Moreover, as described in section 3.2.2 '*Non-linear laminar flow and fully turbulent flow in porous media*', drag forces that determine the non-linear laminar flow in porous media are controlled by the fluid-solid interfaces of the pore structures and pore geometry (e.g. Hassanizadeh and Gray 1987; Comiti et al. 2000; Panfilov and Fourar 2006). Hence, it seems reasonable to characterize the porous media by means of the surface area and its roughness. For example, the capillary representation model of Comiti et al. (2000) used a dynamic surface area of the porous media, as well as the tortuosity, while assuming a cylindrical characterization of the pores.

The results in section 3.4.2 '*Non-linear flow behavior in the composite sands*' show that an increased fraction of finer material at fixed values of d_{50} and porosity results in an increased flow resistance. Under this condition, the use of the characteristic pore

length by means of the grain size diameter d_{30} in the modified Ergun relationships works well for accurate prediction of the Forchheimer coefficients a and b to account for finer material.

As mentioned earlier, MacDonald et al. (1979) suggest the use of the Sauter mean (Eq. 3.11) as a measure of the characteristic pore length in the relationships (Eq. 3.6 and 3.7). This definition of the characteristic pore length emphasizes the importance of specific surface area in complex pore structures. Hence, it seems sensible that the non-linearity in flow resistance due to interfacial drag forces acting on the fluid-solid interface should be upscaled to a macroscopic parameter that characterizes pore surface area. For grain size distributions considering perfect spherical grains, the d_{32} can be used. However, for more angular materials with lower sphericity values, the ratio between volume and surface area is lowered and smaller characteristic pore lengths should be considered. In our study, the d_{30} of uniformly graded sand approximately equals the Sauter mean, considering rounded sand grains. Herrera and Felton (1991) suggested to use the standard deviation of particle sizes and substituted the characteristic pore length d by d_m-σ. For more well-graded sand types, with larger standard deviations, finer particles fill the pores between coarser particles and the contact surface of particles with water increases. Tables 3.2 and 3.3 show that the characteristic pore length of d_m-σ is smaller than d_{30} and, hence, accounts more for the finer particles in the packed column sample.

Nonetheless, it should be noted that fitting of non-linear flow data with the Forchheimer relation (Eq. 3.2) over a wide range of Reynold numbers describes the gradual macroscopic transition from laminar Darcy flow to non-linear laminar flow, and, eventually, to fully turbulent flow. Hence, linking between the different macroscopic flow characteristics at a wide range of Reynold numbers and the complex microscopic pore structures by means of e.g. characteristic pore length, tortuosity, compaction grade, sphericity is complicated.

3.6 Conclusions

The current study provides new experimental data on non-linear water flow behavior in various uniformly graded granular material for 20 samples, ranging from medium sands (d_{50} >0.39 mm) to gravel (6.34 mm). The effect of the grain size distribution on the macroscopic flow resistance parameters is analyzed using the Forchheimer coefficients. As the reference dataset, we have used 11 uniformly graded filter sands. In addition, the mixtures of the filter sands are used to obtain composite sands with different grain size distributions. This provided samples with increased C_u values by a factor of 1.19 up to 2.32 at equal median grain size d_{50} and porosity relative to the associated reference sands. The main conclusions from this study are:

- Our dataset have shown that the d_{50} value is not enough to predict flow resistance accurately. Wider grain size distributions, indicated by an increase in d_{10} and d_{30} for the composite sands, result in an increased flow resistance with respect to the reference sands at equal median grain size (d_{50}). The a coefficients increased by factors up to 1.68 and the b coefficients increased by factors up to 1.44 with respect to the reference sands.
- The modified Ergun equation could provide accurate estimates of coefficients a and b. The use of Ergun constants A=183.8 and B=2.53 and the use of d_{30} as characteristic pore length is suggested to provide good fits. While using the method of Herrera and Felton (1991) with a characteristic pore length of d_m-σ, Ergun constants A=139.1 and B=2.2 are suggested.
- The derived Ergun constants of the current study are in agreement with the Ergun constants derived from other experimental datasets.
- We found a clear correlation between the experimentally derived Forchheimer coefficients a and b for our dataset of subangular-subrounded, uniformly graded filter sands at an optimal compaction grade.

Acknowledgements

This work was supported by the foundations STW (Foundation for Technical Sciences) and O2DIT (Foundation for Research and Development of Sustainable Infiltration Techniques). The authors wish to thank Tony Valkering and Theo van Velzen from dewatering company Theo van Velzen for constructing the experimental set-up and Peter de Vet from dewatering company P.J. de Vet & Zonen for optimizing set-up. We are grateful to Willem Jan Dirkx for his help and constructive input during the non-linear flow experiments. The authors wish to thank three anonymous reviewers for their constructive feedback, which allowed us to improve the manuscript significantly.

Chapter 4

Nonlinear flow behavior in packed beds of natural and variably graded granular materials

Abstract

Under certain flow conditions, fluid flow through porous media starts to deviate from the linear relationship between flow rate and hydraulic gradient. At such flow conditions, Darcy's law for laminar flow can no longer be assumed and non-linear relationships are required to predict flow in the Forchheimer regime. To date, most of the non-linear flow behavior data is obtained from flow experiments on packed beds of uniformly-graded granular materials ($C_u=d_{60}/d_{10}<2$) with various average grain sizes, ranging from sands to cobbles. However, natural deposits of sand and gravel in the subsurface could have a wide variety of grain size distributions. Therefore, in the present study we investigated the impact of variable grain size distributions on the extent of non-linear flow behavior through 18 different packed beds of natural sand and gravel deposits, as well as composite filter sand and gravel mixtures within the investigated range of uniformity ($2.0<C_u<17.35$) and porosity values ($0.23<n<0.36$). Increased flow resistance is observed for the sand and gravel with high C_u values and low porosity values. The present study shows that for granular material with wider grain size distributions ($C_u>2$), the d_{10} instead of the average grain size (d_{50}) as characteristic pore length should be used. Ergun constants A and B with values of 63.1 and 1.72 respectively resulted in a reasonable prediction of the Forchheimer coefficients for the investigated granular materials.

Published as: Van Lopik, J.H., Zazai, L, Hartog, N., & Schotting, R.J. (2019). Nonlinear flow behavior in packed beds of natural and variably graded granular materials. *Transport in Porous Media*, (27 pp.). [Published online: 10 December 2019]

4.1 Introduction

In general, flow processes in groundwater flow studies can be described by Darcy's law (1856):

$$i = -\frac{1}{K} q \tag{4.1}$$

where i [m/m] is the hydraulic gradient, K [m/s] is the hydraulic conductivity, and q [m/s] is the specific discharge. At higher flow velocities in porous media, Darcy's law does not hold and the specific discharge starts to deviate from the linear Darcy's law after a certain threshold hydraulic gradient. In 1901, Forchheimer proposed alternative equations to describe post-Darcian flow behavior, which can be categorized in the two-term, the three term and the power law (Bear 1988). Theoretical base for the different Forchheimer forms in a particular porous medium for given flow velocity ranges are provided in the literature (e.g. Hassanizadeh and Gray; 1987; Whitaker 1996; Skjetne and Auriault 1999; Chen et al. 2001; Adler et al. 2013). The second order polynomial two-term Forchheimer equation is widely used for groundwater flow problems and describes the non-linear behavior with adding a quadratic term to Darcy's law:

$$i = -aq - bq^2 \tag{4.2}$$

where a [s/m] is a parameter equal to the reciprocal of the hydraulic conductivity (i.e., $a=1/K$) and b [s^2/m^2] is the empirical Forchheimer coefficient. The onset of non-linear laminar flow behavior is ascribed to different mechanisms of energy dissipation (e.g. Hassanizadeh and Gray 1987; Ma and Ruth 1993; Lage 1998; Nield 2000; Chen et al. 2001; Panfilov and Fourar 2006).

Ergun (1952) extended the Kozeny-Carman relationship to relate the Forchheimer coefficients to the grain size and porosity of a porous medium by:

$$i = -A \frac{(1-n)^2 v}{g n^3 d^2}\, q - B \frac{(1-n)}{g n^3 d}\, q^2 \tag{4.3}$$

where g [m/s^2] is the acceleration due to gravity, d [m] is the characteristic pore length by means of the particle diameter, v [m^2/s] is the kinematic viscosity of the fluid, n [-] is the porosity, A is the Ergun constant that equals 150 and B is the Ergun constant that equals 1.75 (Ergun 1952). Many variations on the Ergun relation for different kinds of porous media and flow regimes are given in the literature (e.g. Engelund 1953; Irmay

1964; MacDonald et al. 1979; DuPlessis 1994; Sedghi-Asl and Rahimi 2011; Erdim et al. 2015; Guo et al. 2019).

The understanding of high-velocity flows over steep hydraulic gradients through hydrogeological formations is important for a broad range of large scale flow problems. Such flow problems are, for example, the flow through waste deposits (d_{10}=10 mm) up to velocities of 10 m/s (Greenly and Joy 1996), transient flow due to steep head gradients by sudden head rise or drawdown in aquifers and constructed wetlands (Moutsopoulos and Tsihtintzis 2005; Moutsopoulos 2007), as well as flow through landfill caps or leachate collection systems up to velocities of 0.6 m/s (Bordier and Zimmer 2000). Moreover, in many groundwater applications the efficiency of injection/abstraction wells is affected by non-linear head losses since flow velocities increase due to the divergence/convergence of flow lines in the vicinity of wells (e.g. Basak 1978; Mathias and Todman 2010; Yeh and Chang 2013; Wen et al. 2013; Houben 2015a; Mathias and Moutsopoulos 2016). In general, non-linear head losses will occur in the gravel pack while flow in the aquifer can be considered as linear Darcian flow for common well-designs (Houben 2015a). However, for naturally-developed wells with a well screen in direct contact with the naturally-developed aquifer material, steep hydraulic gradients and non-linear head losses occur in the aquifer material itself. Houben et al. (2018) stated that reduction of porosity in the gravel pack by clogging could have a significant influence on non-linear head losses during well operation. Besides well hydraulics, the influence of non-linear flow behavior through natural granular materials is important for analyzing slug-tests in highly permeable sandy aquifers of K>50 m/d (McElwee and Zenner 1998), as well as for analyzing packer test data (e.g. Yamada et al. 2005).

To date, a broad range of experimental studies on non-linear flow behavior in different kind of porous media is available in the literature. Experimental datasets on non-linear flow behavior through various kinds of packed beds of granular material show that the Forchheimer equation (Eq. 4.2) can be used to predict flow over a wide range flow velocities (e.g. Moutsopoulos et al. 2009; Sedghi-Asl et al. 2014; Ferdos et al. 2015; Salahi et al. 2015; Li et al. 2017; Van Lopik et al. 2017). Most literature provide data on flow through packed beds of coarser granular materials, such as gravels and cobbles with an uniform grain size distribution (e.g. Sidiropoulou et al. 2007; Moutsopoulos et al. 2009; Sedghi-Asl et al. 2014; Salahi et al. 2015). The experimental studies of Van Lopik et al. (2017) and Li et al. (2019) focus on small variations in gradation by adding only a small amount of both finer and coarser material to a given uniformly graded reference sand.

In contrast, however, for natural sand and gravel deposits the grain size distribution is usually non-uniformly graded. Only a limited amount of studies provides information about both the grain size distribution of the material and the non-linear flow behavior

through non-uniformly graded granular materials (e.g. Yamada et al. 2005; Dan et al. 2016; Wang et al. 2019). Hence, the understanding of non-linear flow behavior through packed beds of graded natural sand and gravel deposits requires a much broader experimental dataset than provided in the present literature.

The aim of this study is to provide insight in the differences in non-linear flow behavior through packed beds of a wide range of graded sand and gravel types. Therefore, in the present study the effect of non-linear flow behavior through packed beds of granular material with wider grain size distribution and lower corresponding porosities is investigated. This is done by experimental tests on packed beds of natural sands and gravels from unconsolidated aquifers in the Netherlands and Germany, as well as artificial composite mixtures of filter sands and gravels considering a broad range of grain size distributions and porosities at a given reference average grain size (d_{50}) and compaction grade. The dataset of the present study on non-linear flow behavior through packed beds of variably graded granular material is compared to the existing datasets in the literature on uniformly-graded granular material. This is done to obtain insight in the difference in non-linear flow behavior between these types of granular materials.

4.2 Experimental data from previous studies

A wide variety of experimental studies on non-linear flow behavior through packed beds of all kinds of material is provided in the literature. Investigation of fluid/gas flow through packed beds of artificial compounds is done, such as cubes, cylinders, ellipsoids, fibers, cubic arrays of spheres, as well rounded spheres of glass or metal (e.g. MacDonald et al. 1979; Sidiropoulou et al. 2007; Allen et al. 2013; Huang et al. 2013; Bağci et al. 2014; Erdim et al. 2015). Besides artificial compounds, the literature provides a broad dataset on non-linear flow behavior through all kinds of granular material, ranging from sand to cobbles. In the present study, the selection of the experimental data on non-linear flow behavior through granular material in Table 4.1 is considered in order to compare the results between uniformly-graded material and non-uniformly graded material. For detailed information about the literature dataset is referred to Appendix F.

Experimental study	Number datasets	d [mm]	C_u [-]	porosity [-]	Granular material
Sidiropoulou et al. 2007:					
Ranganadha et al. (1970)	14	1.01 – 5.5	-	0.35 – 0.44	river sand and gravel
Venkataraman et al. (1998)	23	2.88 – 28.9	-	0.36 – 0.49	sand and gravel
Moutsopoulos et al. (2009)	8	2.71 – 67.2	1.54 – 2.93	0.38 – 0.43	sand, gravel and cobbles
Li et al. (2017)	5	1.08 – 3.17	-	0.40	sand
Li et al. (2019)	21	1.08 – 2.77	1.4 – 2.3	0.36	sand
Van Lopik et al. (2017)	20	0.39 – 6.34	1.21 – 2.32	0.33 – 0.36	filter sand and gravel
Salahi et al. (2015)	12	1.77 – 17.78	-	0.38 – 0.47	angular and rounded aggregates
Sedghi-Asl et al. (2014)	6	2.83 – 56.8	-	0.32 – 0.40	alluvial rounded aggregates

Table 4.1 Selection experimental datasets from the literature on non-linear flow behavior through packed beds of (uniformly-graded) granular material.

Most studies have focused on flow through packed beds with uniform-sized grains (e.g. Sedghi-Asl et al. 2014; Salahi et al. 2015; Li et al. 2017). For the experimental studies on packed beds of granular material with wider grain size distributions, the data provides information on gradation by means of the coefficient of uniformity C_u [-] and the coefficient of curvature C_c [-] (e.g. Yamada 2005):

$$C_u = \frac{d_{60}}{d_{10}} \tag{4.4}$$

and

$$C_C = \frac{(d_{30})^2}{d_{10} * d_{60}} \tag{4.5}$$

In the studies of Van Lopik et al. 2017 and Li et al. 2019, mixtures of granular material were used to obtain slightly more well-graded composite sands. Wider grain size distributions (higher C_u values) for a material at a given average grain size and porosity resulted in increased flow resistance and, hence, increased Forchheimer coefficients *a* and *b*.

Besides gradation, the compaction grade (e.g. Dan et al. 2016; Banerjee et al. 2018) and the grain shape (e.g. Allen et al. 2013; Salahi et al. 2015) of the granular material has a significant effect on non-linear flow behavior. Packed beds of angular grains resulted in increased flow resistance compared to rounded grains (Salahi et al. 2015). The influence of particle shape is also shown for randomly packed beds of cubes and cylinders instead of rounded spheres with a diameter of 2.7 mm (Allen et al. 2013). The flow resistance for such materials is drastically increased, resulting in the highest Forchheimer coefficients for the packed beds of cubes.

4.3 Methods

The experimental set-up and procedures described in Chapter 3 (see section 3.3.1. '*Experimental set-up*') were used for the one-dimensional packed column flow experiments in the present study.

4.3.1 Characteristics of investigated granular material

Two different sets of porous media are investigated in the present study:

- Natural sand and gravel deposits obtained from drilling samples from aquifers in the Netherlands (M.1-3) and Germany (W.1-2).
- Composite mixtures of sand and gravel obtained by mixing of selected portions of different uniformly-graded filter sands and gravels (S.1-3).

Natural sand and gravel deposit samples

All natural sand and gravel samples are obtained from drilling cores in aquifers. The natural sands M.1-3 are obtained by cable tool drilling at a location near the Münsterlaan at the Utrecht University Campus (the Netherlands). The samples are from a sandy unconsolidated aquifer and are fluvial Pleistocene deposits classified as Kreftenheye formation. The samples are obtained from two different drilling locations at only 12 m distance of each other. Sand sample M.1 is obtained at a depth of 12.50-14.50 mbgl. At the other location, the sampling depth is the same for M.2 (12.50-14.50 mbgl), while the depth is 9.50-10.50 mbgl for M.3. The natural sand W.1 and gravel W.2 are reverse-circulation drilling disturbed soil samples at depths of respectively 20-21 mbgl, and 19-

20 mbgl. The samples are Pleistocene river terrace sediments obtained from a sandy unconsolidated heterogeneous-layered aquifer near Wyenhütte in Rheindahlen, about 10 km southwest of Mönchengladbach (Germany). The grain size distributions for the natural sand and gravel samples (M.1-3 and W.1-2) are obtained by sieve analysis using sieve sizes 0.063, 0.125, 0.25, 0.355, 0.5, 0.71, 1.0, 2.0, 5.3, 8, 16.0, 22.6 and 32.0 mm.

Composite mixtures of sand and gravel

Similar to the study of Van Lopik et al. (2017), uniformly-graded filter sands (with a C_u<1.5) are mixed to obtain sand and gravel material with the desired gradation (see Appendix D for the mass fraction mixing ratios of the filter sands). For the composite mixture samples with wider grain size distribution, the required gravel (grain sizes larger than 10 mm) is obtained by selection at minimum grain sizes of 10, 15, 20 and 30 mm. In the present study, the filter sands with an average grain size diameter of 1.0 (Sample 1), 1.5 (Sample 2) and 6.3 mm (Sample 3) are used as reference material. The reference samples 1, 2 and 3 are respectively samples 7, 9 and 11 in the dataset of Van Lopik et al. (2017).

Analysis of the granular material

The gradation for both kind of materials is described by means of the coefficient of uniformity C_u and the coefficient of curvature C_c (Eq. 4.4 and 4.5). The porosity of each packed sample is determined by weighing the dry mass of granular sand or gravel in the column. The solid phase density of the sand and gravel used for the composite mixtures equals 2.66 kg/m^3 (data by FILCOM, Papendrecht, the Netherlands). Moreover, the porosity of each material was determined by measuring the used granular material volume from the packed column under fully saturated conditions in a given water volume. Equal porosities are obtained for the composite mixtures of sand and gravel (Samples 1.(1-5), 2.(1-5) and 3.(1-3)) with above-mentioned methods. The characteristics of the natural, as well as the composite mixtures of sand and gravel are given in Table 4.2.

Additionally, the grain shape properties of both the natural sand and composite sands are obtained using the CAMSIZER® P4 (Retsch, Germany) image analysis technique (see Appendix E). For all samples, the grain sizes in the range of 0.063 - 2.0 mm were selected in order to determine the grain shape of the sand. The grain shape properties of the used filter sands for the artificially mixed composite sands, as well as for the natural deposit sands are similar. All investigated granular material is subangular-subrounded.

	Sample	d_{50} [mm]	d_{10} [mm]	d_{30} [mm]	d_{60} [mm]	C_c	C_u	n [-]
M.1	**Natural sand: *Münsterlaan***	0.45	0.2	0.33	0.52	1.05	2.60	0.328
M.2	**Natural sand: *Münsterlaan***	0.54	0.22	0.39	0.62	1.12	2.82	0.330
M.3	**Natural sand: *Münsterlaan***	0.77	0.29	0.49	1.12	0.74	3.86	0.293
W.1	**Natural sand: *Wyenhütte***	1.48	0.455	0.76	2.2	0.58	4.84	0.249
W.2	**Natural gravel: *Wyenhütte***	9.5	0.95	4.1	12.4	1.43	13.1	0.246
S.1	**Filter sand: *Filcom comp.***	*1.05*	*0.89*	*0.98*	*1.08*	*1.01*	*1.30*	*0.348*
1.1	**Composite sand**	1.05	0.47	0.78	1.11	1.18	2.36	0.346
1.2	**Composite sand**	1.05	0.39	0.63	1.31	0.78	3.36	0.337
1.3	**Composite sand**	1.05	0.35	0.50	1.43	0.50	4.09	0.307
1.4	**Composite sand**	1.05	0.35	0.50	1.55	0.46	4.43	0.285
1.5	**Composite sand**	1.05	0.33	0.44	4.50	0.13	13.6	0.253
S.2	**Filter sand: *Filcom comp.***	*1.50*	*1.16*	*1.34*	*1.58*	*0.98*	*1.36*	*0.358*
2.1	**Composite sand**	1.50	0.81	1.25	1.62	1.19	2.00	0.358
2.2	**Composite sand**	1.50	0.60	0.97	1.73	0.91	2.88	0.334
2.3	**Composite sand**	1.50	0.40	0.70	1.88	0.65	4.70	0.307
2.4	**Composite sand**	1.50	0.40	0.70	2.63	0.47	6.58	0.265
2.5	**Composite sand**	1.50	0.34	0.49	5.90	0.12	17.45	0.242
S.3	**Filter sand: *Filcom comp.***	*6.34*	*5.16*	*5.87*	*6.55*	*1.02*	*1.27*	*0.361*
3.1	**Composite sand**	6.34	1.84	4.85	6.86	1.86	3.73	0.324
3.2	**Composite sand**	6.34	1.36	1.91	10.00	0.27	7.35	0.252
3.3	**Composite sand**	6.34	1.18	1.47	14.55	0.13	12.33	0.227

Table 4.2 The grain size distribution characterization and porosity values for all sand and gravel samples. The samples S.1, S.2 and S.3 in italic are the reference sands obtained from dataset of Van Lopik et al. (2017) (respectively sample 7, 9 and 11 in their study).

4.3.2 Preparation procedure for the packed columns

Similar to the procedure in the study of Van Lopik et al. (2017), the consistent packing method of Rietdijk et al. (2010) is used to obtain reproducible and homogenous packed porous media. To ensure homogeneous packing over the entire length of the column, small sand/gravel portions with the required mixture of fine and coarse material are carefully poured into the fully saturated column. The column is prepared, packed and installed under fully saturated conditions in a large container filled with water. In order to obtain the highest compaction grade, the deposited sand in the column is manually compressed throughout the packing process.

The consistent use of the Rietdijk et al. (2010) method resulted in the highest grain size density for a given sample (Van Lopik et al. 2017). In Fig. 4.1, the effect of gradation on the porosity is shown for the samples listed in Table 4.2. For sand and gravels with wide grain size distributions (high C_u values), the fines tend to fill the void spaces between the larger sand particles, resulting in lower porosity values (Das 2008). For the relatively uniformly graded material (C_u<3), the porosity values are higher than 0.33. The porosity is reduced for granular material samples with wider grain size distributions (C_u>6), resulting in porosity values lower than 0.27.

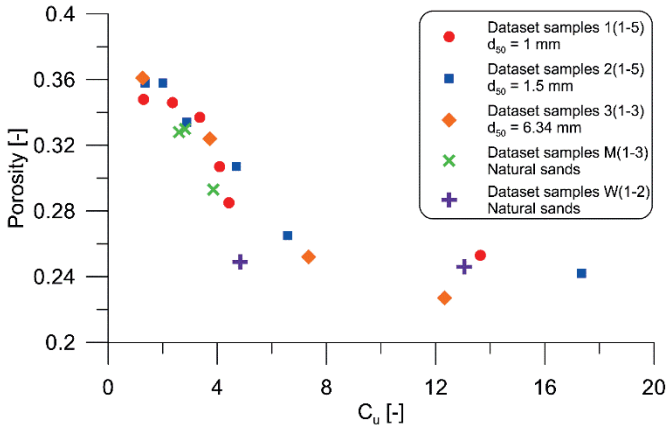

Fig. 4.1 Relationship between the coefficient of uniformity (C_u) and the porosity values for all prepared column samples with the Rietdijk et al. (2010) packing method.

4.3.3 Ergun friction factor and Reynolds number

The Reynolds number is used to indicate whether fluid flow is laminar or turbulent. The most common definition of the Reynolds number is defined as (Bear 1988):

$$Re = \frac{\rho dq}{\mu} = \frac{\text{inertial forces}}{\text{viscous forces}} \tag{4.6}$$

where ρ [kg/m^3] is the fluid density and μ [kg/(m s)] is the dynamic viscosity. In the present study, the onset of non-linear flow behavior by means of a critical Reynolds number Re_{cr} is defined as a significant non-linear deviation in specific discharge of (>5%) from Darcy's law.

For the Ergun equation (Eq. 4.3), the following form of the friction factor f and Reynolds number Re_p is obtained:

$$f = i\frac{gd}{q^2}\left(\frac{n^3}{1-n}\right) and\ Re_p = \frac{\rho dq}{(1-n)\mu} = \frac{Re}{1-n} \tag{4.7}$$

Hence, the relation between friction factor f and Reynolds number Re_p is given by:

$$f = \frac{A}{Re_p} + B \tag{4.8}$$

where A and B are the Ergun constants (which are equal to 150 and 1.75 for the Ergun equation).

4.3.4 Empirical correlation for the non-linear flow Forchheimer coefficient

The Ergun equation (Eq. 4.3) is the extended form of the Kozeny-Carman equation for non-linear flow behaviour and can be used to estimate both the Forchheimer coefficient a and b based on the average grain size diameter and porosity. In the literature, a wide variety of empirical relationships are provided which correlates the Forchheimer b coefficient to the intrinsic permeability (k), porosity and tortuosity (see Table 4.3).

In 1937, Carman already recognized that porous media exists of complex pore structures, and streamlines are far from being completely straight and parallel to each other. This effect can be described by a dimensionless parameter τ called the hydraulic tortuosity (Bear 1988):

$$\tau = \frac{L}{L_e} \tag{4.9}$$

where L [m] is the straight line length that connects the two ends of the tortuous tube of length L_e [m]. Tortuosity is difficult to measure and hence, this parameter is less practical than porous media properties such as grain size and porosity. A broad range of empirical tortuosity equations exists for simpler pore geometries, while the available information in the literature on tortuosity for granular material that consists of mixed particle beds is scarce (e.g. Mota et al. 2001; Ghanbarian et al. 2013). Mota et al. (2001) proposed an empirical tortuosity–porosity power law for binary mixtures of spherical particles:

$$\tau = n^{-0.4} \tag{4.10}$$

In the present study, Eq. 4.10 is used to investigate if the correlation forms for β of Liu et al. (1995) and Thauvin and Mohanty (1998) with the tortuosity model of Mota et al. (2001) works for the investigated non-uniformly graded granular material.

Correlation form for β [cm^{-1}]	**Units k**	**Literature**
$\beta = 0.005k^{-1/2}n^{-\frac{11}{2}}$	cm^2	Geertsma (1974)
$\beta = 1.82 * 10^{8}k^{-5/4}n^{-\frac{3}{4}}$	mD	Janicek and Katz (1955)
$\beta = 2.94 * 10^{7}\frac{\tau}{kn}$	mD	Liu et al. (1995)
$\beta = 1.55 * 10^{4}k^{-0.98}n^{-0.29}\tau^{3.35}$	D	Thauvin and Mohanty (1998)

Table 4.3 Different correlation forms for the Forchhiemer coefficient β, where $\beta=bg$.

4.4 Results

In the present study, a non-linear relationship between the hydraulic gradient i and the specific discharge q is found for the natural sand and gravel samples (M.(1-3) and W.(1-2)), as well as for the composite mixture samples (S.1-3) (Fig. 4.2-4.6). Forchheimer coefficients are determined by fitting the second order polynomial function (Eq. 4.3) over the specific discharges and corresponding hydraulic gradients. The total amount of realizations for the samples ranges between 25 and 33. Excellent Forchheimer fits were obtained for all samples (R^2>0.99). The Forchheimer coefficients a and b are listed in Table 4.4 for the natural sand and gravel samples, as well as for the composite mixture samples. In the present study, the determined critical Reynolds numbers range between 2.17-12.5. This is in line with the values of 1-15 suggested in the literature (Bear 1988; Hassanizadeh and Gray 1987; Ma and Ruth 1993; Comiti et al. 2000).

The measured ranges of $Re_{\min}$ - $Re_{\max}$ for the packed column experiments on the natural sand and gravel samples are shown in Table 4.4. For the sand samples from the

Münsterlaan (M.1-3), multiple data points are in the Darcy regime before flow is increased above the critical Reynolds number Re_{cr} and hence, the onset of non-linear flow is observed (respectively 7, 5 and 3 datapoints for samples M.1, M.2 and M.3). For the composite mixtures, multiple datapoints are measured in the Darcy regime for sample S.1(1-5) and S.2(3-5). The measured datapoints are solely in the non-linear flow regime for the remaining composite mixtures and the samples from Wyenhütte W.(1-2).

4.4.1 Non-linear flow in natural sands and gravels

The same non-linear flow behavior characteristics are observed for the samples M.1 and M.2 with approximately similar gradations, average grain sizes and porosity values. Compared to M.(1-2), the samples M.3 and W.1 have a wider grain size distribution (with C_u values of 3.86, and 4.84) and lower porosity values. The flow resistance was reduced for these samples with a higher average grain size, which resulted in lower Forchheimer coefficients *a* of 1334.9 (M.3) and 1326.1 s/m (W.1) compared to the values obtained for samples M.1-2 (Table 4.4). However, the Forchheimer coefficients *b* for these samples are respectively a factor 1.5 (sample M.3) and 2.5 (sample W.1) higher than for sample M.2. For these samples, reduced porosity values (up to 0.25) due to wider grain size distributions resulted in significantly higher coefficients *b*, while only a small difference is observed between the coefficients *a*.

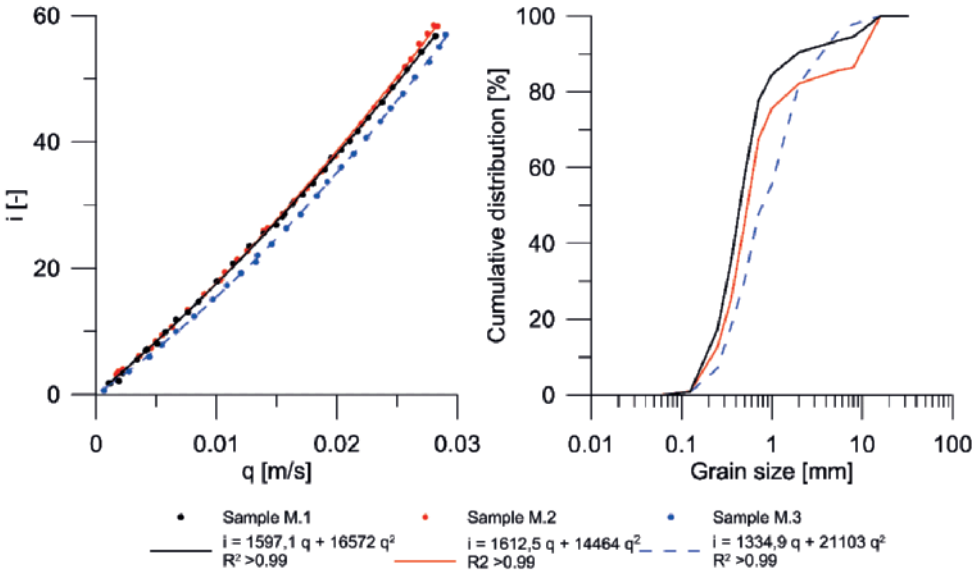

Fig. 4.2 Non-linear relationships between the hydraulic gradient and the specific discharge and the grain size distributions for M.1-3.

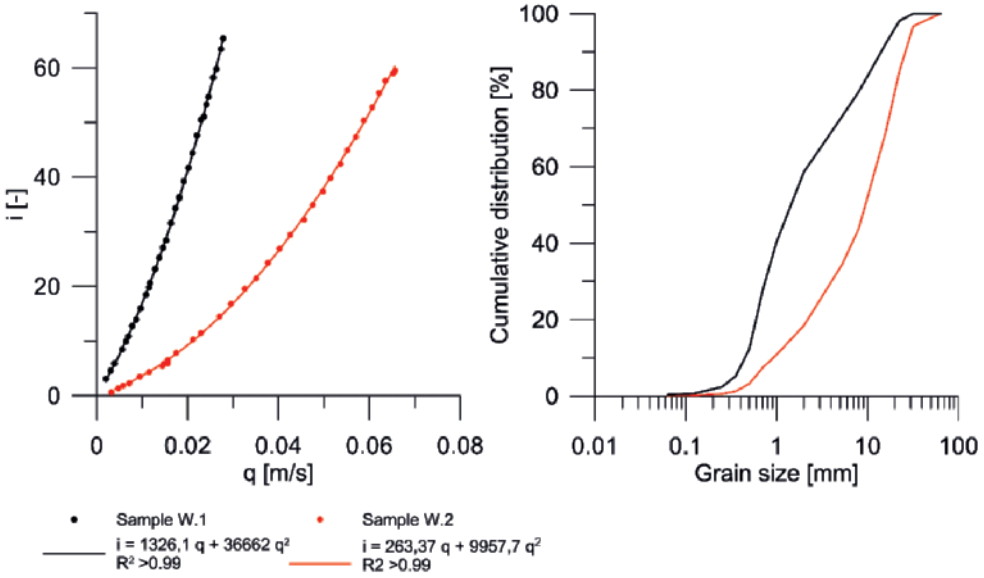

Fig. 4.3 Non-linear relationships between the hydraulic gradient and the specific discharge and the grain size distributions for W.1-2.

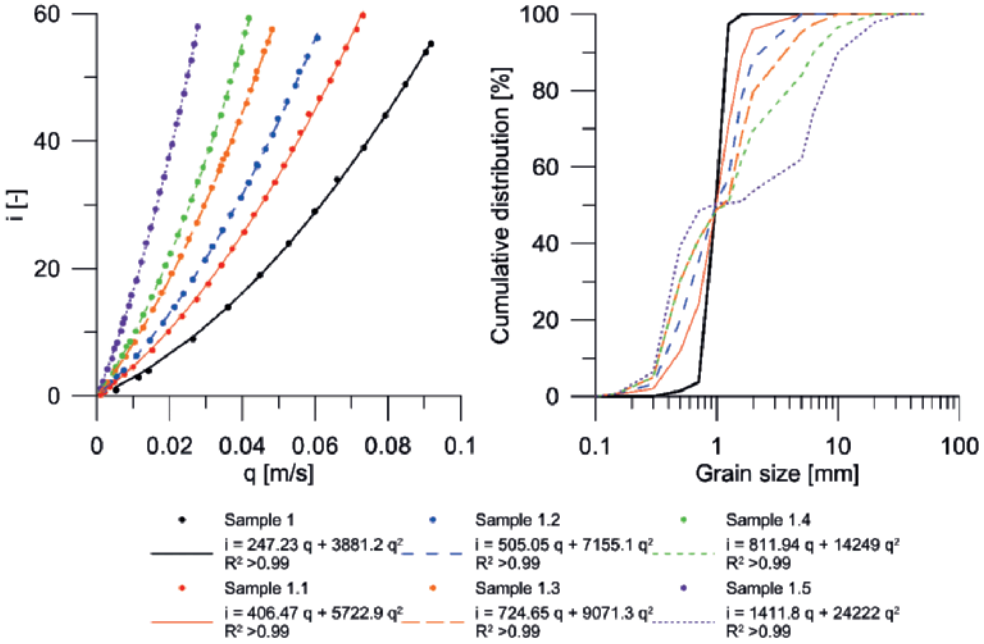

Fig. 4.4 Non-linear relationships between the hydraulic gradient and the specific discharge and the grain size distributions for S.1.1-5.

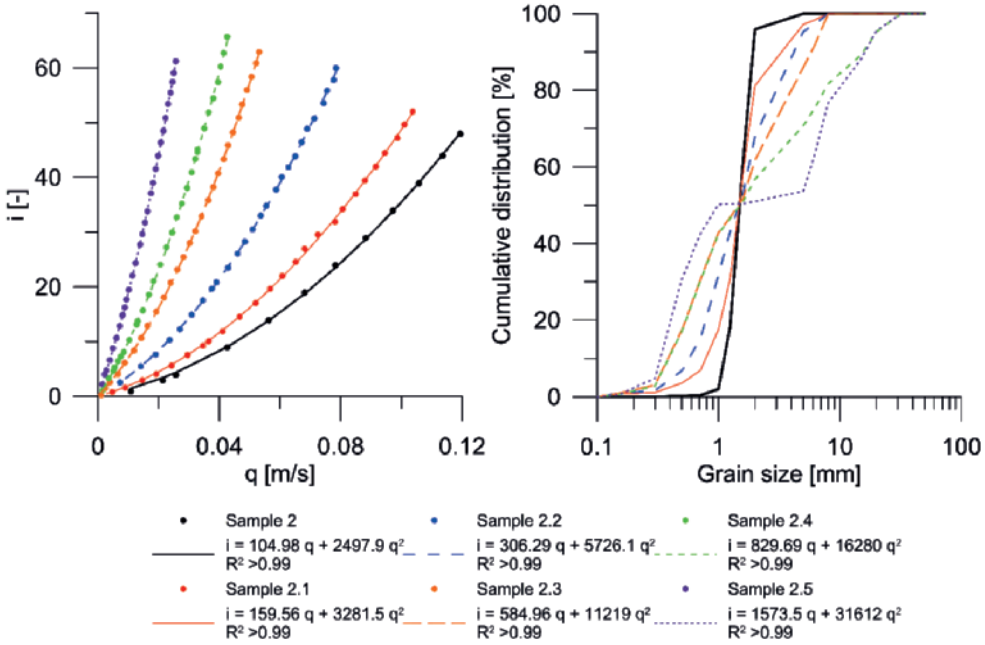

Fig. 4.5 Non-linear relationships between the hydraulic gradient and the specific discharge and the grain size distributions for S2.1-5.

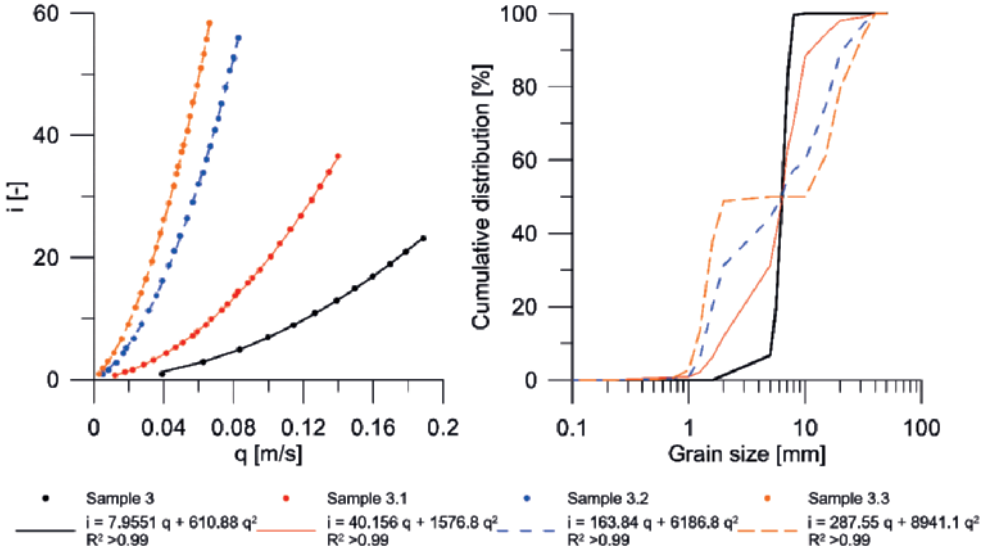

Fig. 4.6 Non-linear relationships between the hydraulic gradient and the specific discharge and the grain size distributions for S.3.1-3.

Sample		Data points	Re_{min}	Re_{max}	Re_{cr}	a [sm^{-1}]	b [s^2m^{-2}]	n [-]	R^2
M.1 (d_{50}=0.45 mm)	**Natural sand: *Münsterlaan***	27	0.46	12.68	2.17	1597.1	16,572	0.33	>0.99
M.2 (d_{50}=0.54 mm)	**Natural sand: *Münsterlaan***	34	0.64	15.31	3.01	1612.5	14,464	0.33	>0.99
M.3 (d_{50}=0.77 mm)	**Natural sand: *Münsterlaan***	33	0.51	22.34	2.43	1334.9	21,103	0.29	>0.99
W.1 (d_{50}=1.48 mm)	**Natural sand: *Wyenhütte***	33	3.00	41.20	2.68	1326.1	36,662	0.25	>0.99
W.2 (d_{50}=9.5 mm)	**Natural gravel: *Wyenhütte***	32	30.79	624.13	12.5	263.37	9957.7	0.25	>0.99
1 (Ref) (d_{50}=1.05 mm)	**Filter sand: *Filcom comp.***	14	5.51	96.28	3.34	247.23	3881.2	0.35	>0.99
1.1	**Artificially mixed filter sand**	27	1.03	73.17	3.55	406.47	5722.9	0.34	>0.99
1.2	**Artificially mixed filter sand**	26	2.03	60.62	3.53	505.05	7155.1	0.34	>0.99
1.3	**Artificially mixed filter sand**	27	1.69	48.21	3.74	724.65	9701.3	0.31	>0.99
1.4	**Artificially mixed filter sand**	27	1.18	41.76	2.85	811.94	14,249	0.29	>0.99
1.5	**Artificially mixed filter sand**	27	1.03	27.66	2.92	1411.8	24,222	0.25	>0.99
2 (Ref) (d_{50}=1.50 mm)	**Filter sand: *Filcom comp.***	12	16.33	179.44	3.16	104.98	2497.9	0.36	>0.99
2.1	**Artificially mixed filter sand**	25	7.13	155.61	3.65	159.56	3281.5	0.36	>0.99
2.2	**Artificially mixed filter sand**	26	10.94	117.66	4.01	305.29	5726.1	0.33	>0.99
2.3	**Artificially mixed filter sand**	28	1.55	79.71	3.92	584.96	11,219	0.31	>0.99
2.4	**Artificially mixed filter sand**	32	2.26	63.91	3.81	826.69	16,280	0.27	>0.99
2.5	**Artificially mixed filter sand**	29	2.04	38.45	3.74	1573.5	31,612	0.24	>0.99
3 (Ref) (d_{50}=6.34 mm)	**Filter sand: *Filcom comp.***	12	248.34	1196.78	4.13	7.955	610.88	0.36	>0.99
3.1	**Artificially mixed filter sand**	30	76.35	885.81	8.08	40.156	1576.8	0.32	>0.99
3.2	**Artificially mixed filter sand**	27	32.22	525.32	8.50	163.84	6186.8	0.25	>0.99
3.3	**Artificially mixed filter sand**	27	19.38	419.79	10.2	287.55	8941.1	0.23	>0.99

Table 4.4 The Forchheimer coefficients *a* and *b* for the natural (M.1-3 and W.1-2), as well as for the composite mixtures of sand and gravel (S.1-3).

4.4.2 Non-linear flow in the composite mixtures of sand and gravel

The results show that gradation of a granular material has a large impact on non-linear flow behavior (Fig. 4.4-4.6). For all tested composite mixture samples, a wider grain size distribution (i.e. increased C_u value) resulted in increased flow resistance with respect to the uniformly-graded reference sand. This results in a poor correlation between the average grain size d_{50} and the Forchheimer coeffients *a* and *b* (Fig. 4.7a-b). Using the d_{10} as characteristic poor length, the correlation is significantly improved (Fig. 4.7c-d).

The d_{30} is decreased by a factor of 0.80 and 0.64 with respect to the reference sample S.1 for respectively S.1.1 and S.1.2 (Table 4.2). Consequently, this results respectively in increased coefficients *a* by a factor of 1.64 and 2,04, as well as increased coefficients *b* by a factor of 1.47 and 1.84 (Table 4.4). The porosity was only slightly reduced to a value of 0.34, compared to the value of 0.35 for the reference sample S.1. For S.1.5, the d_{30} is decreased by a factor of 0.44 with respect to reference sample S.1. This resulted in an increase by a factor up to 5.71 for coefficient *a* and up to 6.24 for coefficient *b*. In this case, the porosity was significantly lower than the reference sample with a value of 0.25. Similar trends are also observed for the composite mixtures dataset S.2.(1-5). For the composite gravel S.3.3, the relative increase in flow resistance and, hence Forchheimer coefficients *a* and *b,* compared to its reference sample S.3 was the highest of all samples with increases by a factor of 36.1 and 14.6 respectively.

Equal amounts of finer material were used for the samples S.1.3 and S.1.4 (Table 4.2 and Fig. 4.4). Composite mixture S.1.4 shows a relative increase in coarser material (i.e., tailing in the grain size distribution) with respect to S.1.3, which resulted in a porosity of 0.29 for S.1.4 instead of the 0.31 for S.1.3. Consequently, for S.1.4 the coefficient *a* is increased by a factor of 1.43 and the coefficient b is increased by a factor of 1.36 compared to the coefficients of S.1.3. A similar trend is observed for the composite mixtures S.2.3 and S.2.4, where also an equal amount of fine material was used (at d_{30} of 0.7 mm). In this case the porosity was reduced to 0.27 for S.2.4, compared to a value of 0.31 for S.2.3 and coefficient *a* and *b* were increased by a factor of 1.41 and 1.45 respectively.

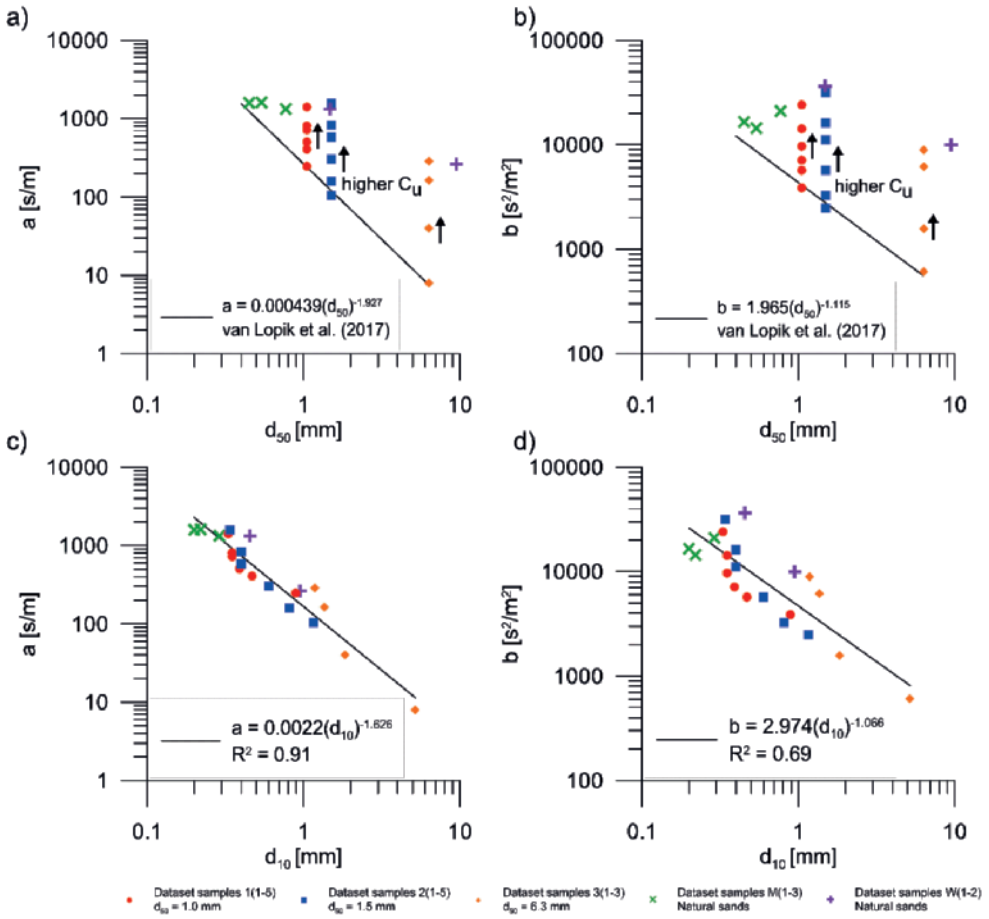

Fig. 4.7 a) Relationship between the median grain size (d_{50}) and Forchheimer coefficient a, as well as for **b)** Forchheimer coefficient b, for the investigated sands. The increase in flow resistance for the sands with a higher C_u value is also indicated. **c)** Relationship between the grain size (d_{10}) and Forchheimer coefficient a, as well as for **d)** Forchheimer coefficient b, for the investigated sands. Note that the shown relationships between the grain size and Forchheimer coefficients are calculated based on d [units in m].

4.4.3 Ergun constants for granular material

In the present study, we have used the Ergun form of the friction factor (Eq. 4.7 and 4.8) to analyze the dataset from the literature (see Table 4.1), as well as the dataset from the present study on non-uniformly graded material (Fig. 4.8). For the characteristic pore length the grain size d_{50} were used to calculate the friction factor f and Re_p. Van Lopik et al. (2017) obtained the following relationship for the friction factor on their dataset of 20 different uniformly-graded filter sands and gravels (C_u<2):

$$f = \frac{233.5}{Re_p} + 2.88; \quad for\ d_{50}\ and\ C_u < 2 \tag{4.11}$$

Similarly, a relationship can be obtained from the results from present study:

$$f = \frac{498.7}{Re_p} + 5.03; \quad for\ d_{50}\ and\ C_u > 2 \tag{4.12}$$

For the present study, a poor relationship between friction factor and Reynolds number is obtained for the entire dataset of the present study while using d_{50} as characteristic pore length (see Fig. 4.8a). A wide range of Ergun constants of A are obtained, ranging from 254 for sample M.1 up to 6477 for sample W.2 (Table 4.5). Ergun constants of B are in the range of 3.5 (S1.1 and S2.1) and 19.3 (W.1). Especially for the coarser granular material samples (d_{50}>1.5 mm) with wider grain size distributions (C_u>5), the obtained Ergun constants are significantly higher (A>750 and B>6) compared to uniformly-graded materials.

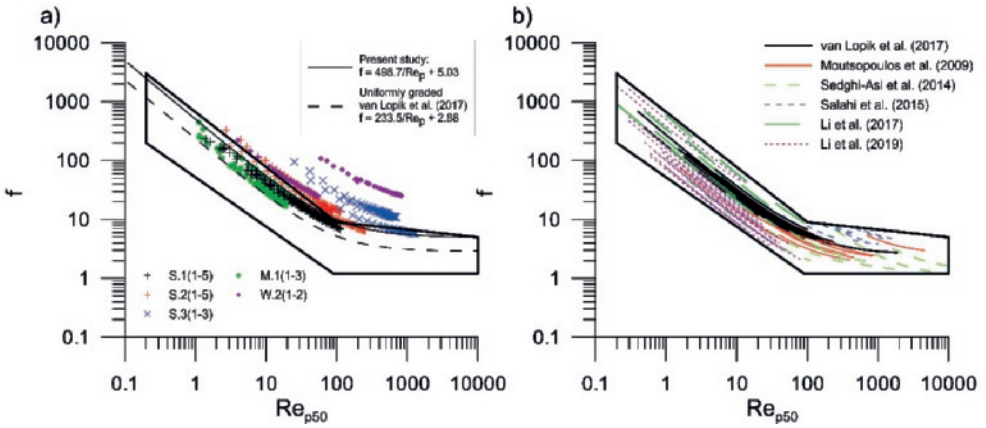

Fig. 4.8 a) Correlation of the friction factor f and the calculated Re_p using grain size d_{50}. The dashed correlation line is based on the dataset of 20 uniformly-graded filter sands (Van Lopik et al. 2017), which includes the reference samples 1-3 of the present study. The solid correlation line is based on the dataset of the present study. **b)** The friction factor based on non-linear flow through packed beds of different kinds of granular material using the literature dataset listed in Table 4.1. The studies that provides the ranges of Reynolds numbers over which the experiments were conducted are plotted. The envelope in both figures shows the upper and lower limits of the literature dataset on uniformly-graded material.

Sample	d_{50} [mm]	C_u [-]	n [-]	d_{50}		d_{30}		d_{10}	
				A	B	A	B	A	B
M.1	0.45	2.60	0.328	254	3.92	137	2.89	50.2	1.74
M.2	0.54	2.82	0.330	369	4.11	193	2.97	61.3	1.67
M.3	0.77	3.86	0.293	376	5.80	152	3.48	53.3	2.06
W.1	1.48	4.84	0.249	792	11.1	209	5.69	74.8	3.41
W.2	9.5	13.05	0.246	6477	19.3	1206	8.34	64.8	1.93
S.1	*1.0*	*1.30*	*0.348*	*264*	*2.58*	*231*	*2.41*	*190*	*2.19*
1.1	1.0	2.36	0.346	386	3.56	235	2.77	85.3	1.67
1.2	1.0	3.36	0.337	431	4.05	171	2.55	65.6	1.58
1.3	1.0	4.09	0.307	428	3.97	107	1.99	52.5	1.39
1.4	1.0	4.43	0.285	361	4.52	90,2	2.26	44.2	1.58
1.5	1.0	13.64	0.253	402	5.15	77,8	2.27	43.8	1.70
S.2	*1.5*	*1.36*	*0.358*	*259*	*2.63*	*206*	*2.35*	*154*	*2.03*
2.1	1,5	2.00	0.358	392	3.45	272	2.88	114	1.86
2.2	1,5	2.88	0.334	566	4.71	237	3.05	90.6	1.89
2.3	1,5	4.70	0.307	778	6.89	169	3.22	55.3	1.84
2.4	1,5	6.58	0.265	629	6.07	137	2.83	44.7	1.62
2.5	1,5	17.35	0.242	857	8.70	91,4	2.84	44.0	1.97
S.3	*6.3*	*1.27*	*0.361*	*362*	*2.80*	*310*	*2.59*	*239*	*2.28*
3.1	6.3	3.73	0.324	1164	4.90	690	3.77	99.3	1.43
3.2	6.3	7.35	0.252	1825	8.18	167	2.48	85.0	1.77
3.3	6.3	12.33	0.227	2192	8.36	119	1.95	76.9	1.57
Median value (present study)				**498.7**	**5.03**	**168.0**	**2.86**	**63.1**	**1.72**
Uniformly graded (C_u<2.32) Van Lopik et al. (2017)				**233.5**	**2.88**	**183.8**	**2.53**	**120.3**	**2.03**

Table 4.5 The resulting Ergun constants *A* and *B* from the present study based on the grain sizes d_{10}, d_{30} and d_{50}.

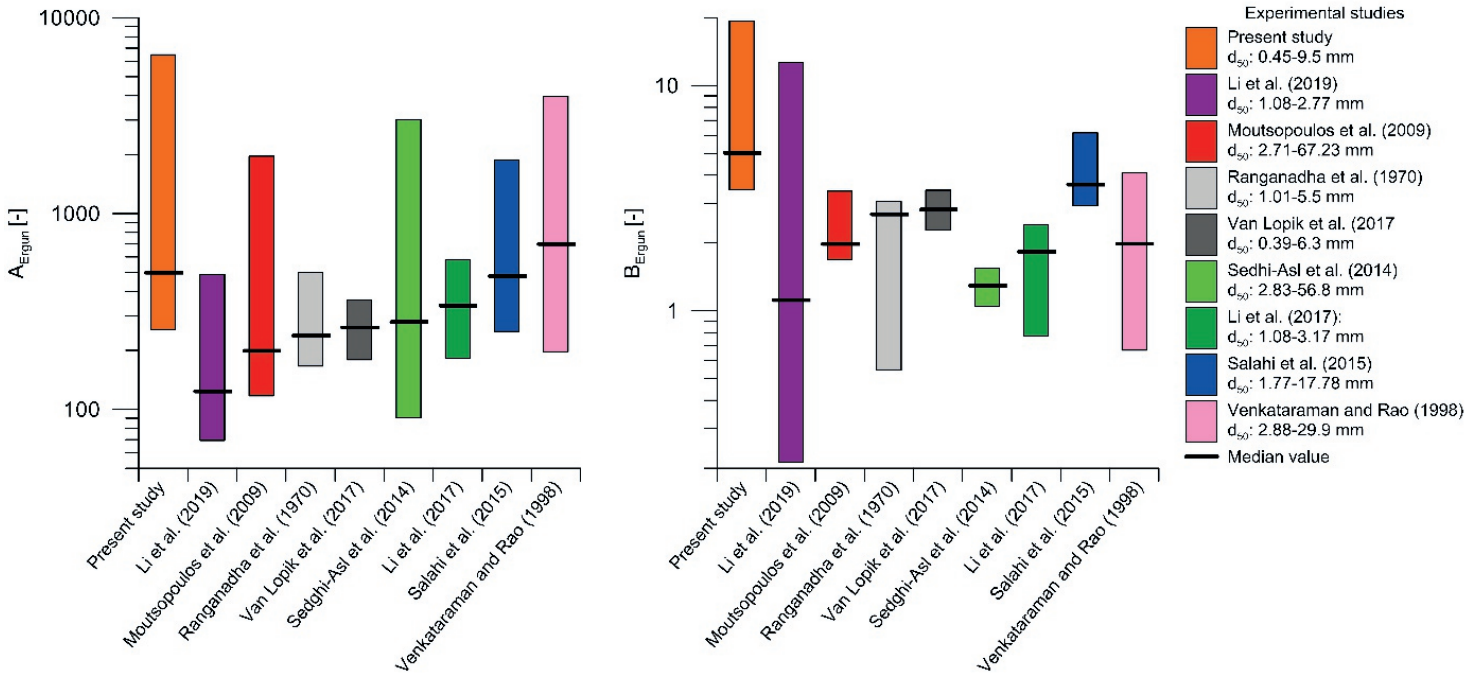

Fig. 4.9 Overview of dataset from the literature (see Table 4.1) of the resulting Ergun constants obtained from the provided grain sizes, porosity values and Forchheimer coefficients *a* and *b* in the literature for **a)** Ergun constant *A* and **b)** Ergun constant *B*.

Using the dataset from the literature (Table 4.1) and the average grain size d_{50} of the tested porous medium, the resulting Ergun constants A and B are obtained from the relationship between Reynolds number and friction factor (Fig. 4.9b). The literature provides Reynolds number ranges over which the packed beds were tested on non-linear flow behavior. However, the definition of the Reynolds number differs for the given studies in Table 4.1, and therefore we recalculated these values to equivalent Re_p values (based on the d_{50} and n, see Eq. 4.3). The individual analysis of the different packed beds with granular material provides a nice overview of the range of possible Ergun constants for different kind of uniformly-graded granular material (see Fig. 4.9).

A wide variety of A and B values is obtained for granular material at given average grain size d_{50}. Comparing the dataset of uniformly-graded granular material, the Ergun constant A seems to increase with increasing grain size (see Venkataraman and Rao 1998; Moutsopoulos et al. 2009; Salahi et al. 2015; Sedghi-Asl et al. 2014; Li et al. 2017; Van Lopik et al. 2017). For example, estimating non-linear flow behavior through packed beds of coarse gravel (d_{50}>20 mm) requires Ergun constants A that are much higher than for other granular material (values up to 4000, see Fig. 4.9a). The Ergun constant B is in general higher than the value of 1.75 (average value B of 2.8 for Ranganadha et al. 1970; Moutsopoulos et al. 2009; Salahi et al. 2015; Li et al. 2017; Van Lopik et al. 2017) (Fig. 4.9b). This is line with the values suggested by Kovács (1981) (B=2.4) for sediments, as well as the values from Engelund (1953), who stated that for smooth particles B is 1.8, while for angular particles B is 3.8.

The Ergun constants for granular materials with wider grain size distributions are notably higher compared to the dataset on uniformly-graded granular material (Table 4.5 and Fig. 4.9). Hence, the present dataset of graded granular material is also analyzed using the Ergun form of the friction factor (Eq. 4.7 and 4.8) while using the d_{30} and d_{10} as characteristic pore length (Fig. 4.10). For uniformly-graded filter sands and gravels (C_u<2) using d_{30} and d_{10}, the friction factors are (Van Lopik et al. 2017):

$$f = \frac{183.8}{Re_{p30}} + 2.53; \quad for\ d_{30}\ and\ C_u < 2 \tag{4.13}$$

$$f = \frac{120.3}{Re_{p10}} + 2.03; \quad for\ d_{10}\ and\ C_u < 2 \tag{4.14}$$

While for the dataset of the present study with granular material of wider grain size distributions (C_u>2), the friction factor is:

$$f = \frac{168.0}{Re_{p30}} + 2.86; \quad for\ d_{30}\ and\ C_u > 2 \tag{4.15}$$

$$f = \frac{63.1}{Re_{p10}} + 1.72; \quad for\ d_{10}\ and\ C_u > 2 \tag{4.16}$$

Considering the entire dataset of the present study, the overall correlation between friction factor and Re_p with d_{10} is good (Fig. 10b). Hence, we suggest the use of 63.1 and 1.72 for respectively Ergun constants A and B, while using the d_{10} as characteristic pore length for sand and gravel with wider grain size distributions.

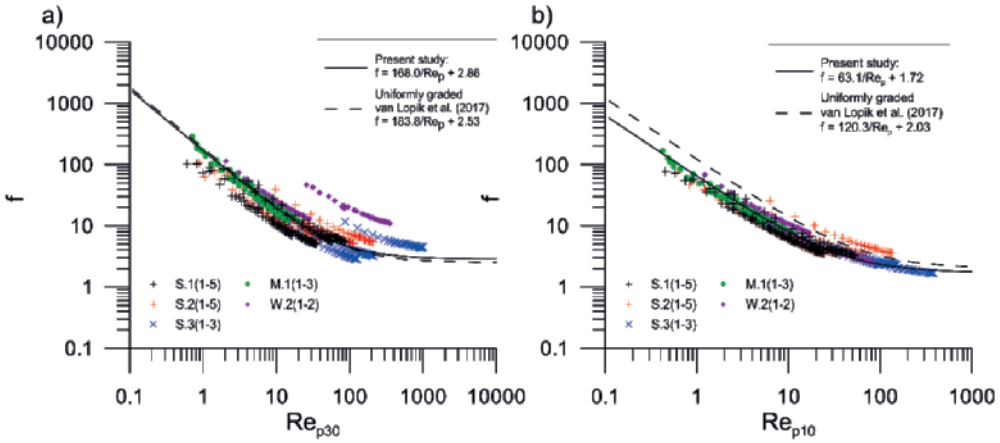

Fig. 4.10 a) Correlation of the friction factor f and the calculated Re_p with a characteristic pore length of d_{50}, **b)** as well as for a characteristic pore length of d_{50}. The dashed correlation line is based on the dataset of 20 uniformly-graded filter sands (Van Lopik et al. 2017), which include the reference samples 1-3 of the present study. The solid correlation line is based on the dataset of the present study.

4.4.4 Correlation forms for Forchheimer coefficient b

The differences between the experimentally obtained Forchheimer coefficients b and the derived coefficients from empirical relationships listed in Table 4.3 are shown in Fig. 4.11. Using the correlation form of Geertsma (1974) for Forchheimer β, the estimation of the experimentally obtained values is poor (Fig. 4.11a). The derived Forchheimer coefficients b are highly overestimated and the scattering around the linear regression slope is high with a R^2-coefficient of 0.70. Due to the relative importance of the porosity term ($n^{-5.5}$) in the Geertsma (1974) equation in comparison with the other equations in Table 4.3, the low porosity values (0.25<n<0.33) of the samples in this study results in

this significant overestimation. For Janicek and Katz (1955), the fit is reasonable with a R^2-coefficient of respectively 0.76 (Fig. 4.11b).

The scattering around the linear regression slope is significantly reduced for the empirical relationships that included the tortuosity model of Mota et al. (2001) for mixed particle beds (Fig. 4.11c). Combining this tortuosity model with the correlation forms of Liu et al. (1995) and Thauvin and Mohanty (1998), the R^2-coefficients are respectively 0.86 and 0.88. In order to obtain a better correlation with the experimental data, the coefficients in these correlation forms are modified (Fig. 4.11d). The modified correlation form of Liu et al. (1995) is:

$$\beta = 3.1 * 10^6 \frac{\tau}{kn} = 3.1 * 10^6 k^{-1} n^{-1.4} \qquad with\ R^2 = 0.86 \tag{4.17}$$

where k [in mD] is the intrinsic permeability.

The modified correlation form of Thauvin and Mohanty (1998) is:

$$\beta = 2.0 * 10^3 k^{-0.98} n^{-0.29} \tau^{3.35} = 2 * 10^3 k^{-0.98} n^{-1.63} \qquad with\ R^2 = 0.88 \tag{4.18}$$

where k [in D] is the intrinsic permeability.

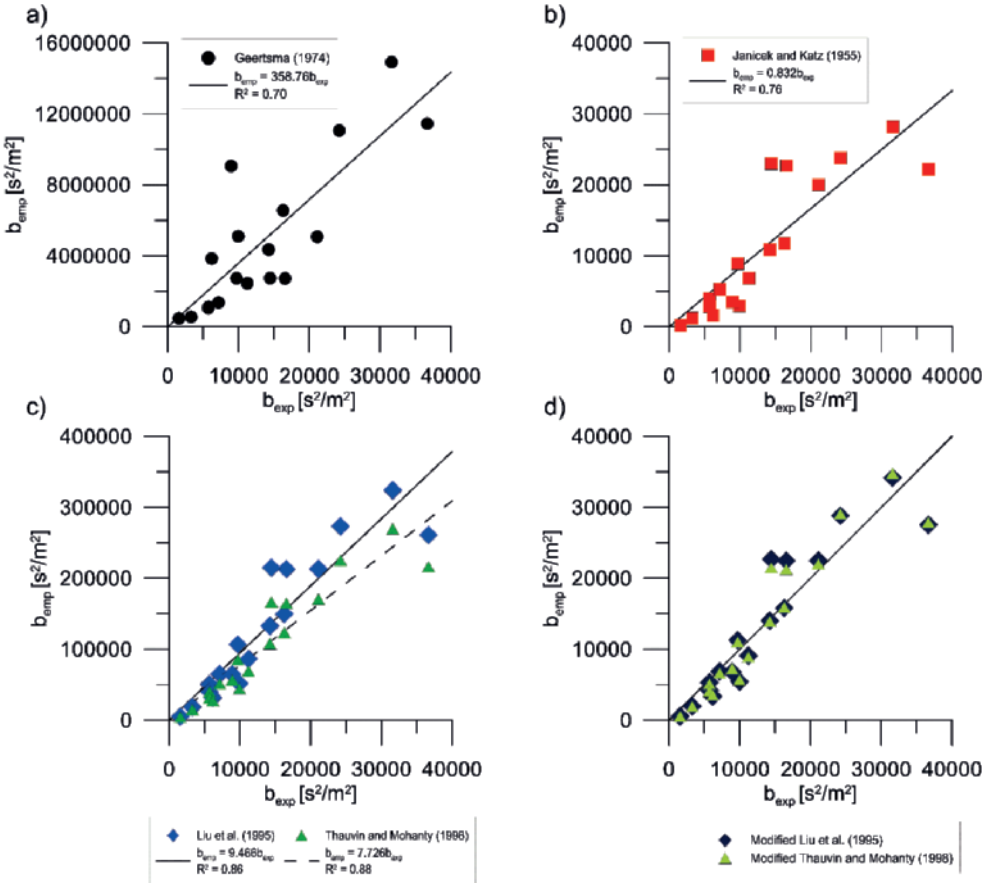

Fig. 4.11 Linear regression analysis of the Forchheimer coefficient *b* using the correlation form of **a)** Geertsma (1974), **b)** Janicek and Katz (1955), **c)** Liu et al. (1995) and Thauvin and Mohanty (1998) and **d**) the modified correlation forms Eq. 4.17-18.

4.5 Discussion

Non-linear flow behavior in porous media is controlled by the microscale processes at the fluid-solid interfaces of the pore structures and pore geometry (e.g. Dybbs and Edward 1984; Hassanizadeh and Gray 1987; Ma and Ruth 1993; Panfilov and Fourar 2006). Moreover, these microscale processes differ over the different Reynold number ranges. Commonly, post-Darcian non-linear flow is separated in two flow regimes. These are the non-linear laminar flow regime (also known as Forchheimer regime or transition flow regime) and the fully-turbulent flow regime (Burcharth and Andersen 1995; Lage 1998; Houben 2015a). This is done by flow visualization studies in porous media that determined the onset of turbulent flow (e.g. Dybbs and Edwards 1984; Seguin et al. 1998), as well as analysis of macroscale flow experiments on packed beds (e.g. Venkataraman and Rao 1998; Sedghi-Asl and Rahimi 2011; Bağci et al. 2014). This transition between the different flow regimes in the post-Darcian flow regime is hard to define for natural irregular and graded granular materials such as used in this study (Burcharth and Andersen 1995).

In practice, the traditional Ergun-type formulations are still widely used to provide estimates for the Forchheimer coefficients a and b (Eq. 4.3), since these are based on the easy measurable parameters such as a particle diameter for the characteristic pore length and the porosity. Previous studies have shown that besides the particle diameter and porosity, also the particle shape and packing arrangement has a significant impact on non-linear flow behavior (e.g. Engelund 1953; Allen et al. 2013; Salahi et al. 2015). Experimental studies on non-linear flow behavior on cubic arrays of smooth glass spheres show that the flow resistance is drastically lower compared to granular material (Huang et al. 2013). This study showed that the Ergun constants provided by Irmay (1964) with values A and B of respectively 180 and 0.6 suffice to predict the experimental data. The cubic arrangement of the smooth spheres allowed for the use of low B values of 0.6. However, for randomly packed beds of smooth particles, resulting in non-cubic arrangements, the resulting Ergun constants are much higher. Even for randomly packed beds of smooth spheres a wide variety of Ergun constants is obtained in the literature due to the varying pore structures (e.g. MacDonald et al. 1979; Fand et al. 1987; Bagci et al. 2014; Erdim et al. 2015). For angular shaped particles, which usually vary in shape for each granular particle, it is even harder to obtain one single specific characteristic pore length to account for the entire pore geometry of the packed bed of granular material. Moreover, during packing of asymmetric elongated particles, no isotropic packing arrangement will be obtained, since the particles tend to align during packing in such way that the larger areas are parallel to the bottom of the outlet (Allen et al. 2003). Packing the grains in such way that they align with the flow direction, significant

reduction in flow resistance is observed. In the present study slightly elongated subangular-subrounded sands were used (Appendix E), and anisotropy in packed beds of the mixed granular material will have an impact on the flow resistance. However, the differences in grain shape between the used sands in this study are very small (Appendix E) and hence, the variations in the flow resistance are mainly due to differences in the pore geometry by different grain sizes and packing arrangement of the non-uniformly graded granular material.

The present study shows that non-linear flow behavior through packed beds of granular material with wide grain size distributions (C_u>2) deviates drastically from flow through uniformly-graded material (Fig. 4.7). The packing arrangements of such granular material differ from uniformly-graded material, which is reflected by the decreased porosities of the tested granular material (Fig. 4.1). The heterogeneity of the packed bed with a wide grain size distribution results in increased complexity of the pore structure, smaller pore spaces and hence, higher tortuosity values. The use of the correlation forms for the non-linear Forchheimer coefficient β of Liu et al. (1995) and Thauvin and Mohanty (1998) in combination with the tortuosity model of Mota et al. (2001) for mixed spherical particles beds resulted in a reasonable prediction of the experimental dataset. However, the actual values for tortuosity in both Darcian and non-Darcian flow regimes are difficult to measure for a given pore structure of the packed bed. Therefore, one heavily relies on the different empirical relationships for tortuosity provided in the literature (e.g. Ghanbarian et al. 2013).

4.6 Conclusions

Non-linear flow behavior through packed beds of 5 different types of natural sand and gravel from unconsolidated aquifers, as well as 13 different composite mixtures of uniformly-graded filter sands at different grain size distributions and porosity values are investigated. This broad set provides data on the hydraulic characteristics for sand and gravel types with C_u values of 2.00-17.5 and porosity values of 0.23-0.36. The comparison of the dataset of the present study on sand and gravel with wide grain size distributions (C_u>2) with datasets in the literature on uniformly-graded sand and gravel (C_u<2), shows that the gradation has a significant effect on non-linear flow behavior. For graded gravels (d_{50}=6.3 mm, C_u=12.3), Forchheimer coefficients a and b are increased by a factor of 36 and 15 respectively with respect to uniformly-graded gravel (d_{50}=6.3 mm, C_u=1.27).

Considering the Ergun relationship for empirical correlation of the experimental dataset while using the average grain size d_{50}, a wide range of Ergun constants A and B is obtained with values of respectively 233.5 and 2.88 for uniformly-graded filter sands

up to values of 2192 and 8.36 for poorly gap-graded gravel (C_u=12.33). In order to estimate the Forchheimer coefficients of granular material with wide grain size distributions (C_u>2), the d_{10} should be used as characteristic pore length with the Ergun constants of A and B of 63.1 and 1.72 respectively.

Moreover, for granular material with wider grain size distributions (C_u values of 3.86-17.35) and low porosities (n<0.30), the Forchheimer coefficient b for a given coefficient a is significantly higher than for more uniformly-graded granular material. Hence, the quadratic term in the Forchheimer that accounts for increase in non-linear flow resistance by additional energy dissipation is higher for such granular material.

Acknowledgements

This work was supported by the foundations STW (Foundation for Technical Sciences) and O2DIT (Foundation for Research and Development of Sustainable Infiltration Techniques). The authors wish to thank Georg J. Houben from the Bundesanstalt für Geowissenschaften und Rohstoffe for commenting on this manuscript and providing the grain shape analysis, Tony Valkering and Theo van Velzen from dewatering company Theo van Velzen for constructing the experimental set-up and Peter de Vet from dewatering company P.J. de Vet & Zonen for optimizing this set-up. Moreover, we wish to thank Sjaak van Lanen (from P.J. De Vet & Zonen) for providing the natural sand samples from the Wyenhütte fieldsite and Fugro GeoServices for providing the samples from the Münsterlaan fieldsite.

Chapter 5

Contribution to head loss by partial-penetration and well completion: implications for dewatering and artificial recharge water wells

Abstract

A wide variety of well drilling techniques and well completion methods is available in construction dewatering for the installation of dewatering and artificial recharge water wells. The selection of the optimal well-type is always a trade-off between the overall costs of well completion and development, the optimal well hydraulics of the well itself, the hydraulic impact of the well on its surroundings, as well as the required operational life-span of the well. The present study provides an analytical framework that can be used by dewatering and drilling companies to quantify the contribution to head loss of typical dewatering and artificial recharge well configurations. The analytical analysis shows that the placement of PPWs in high-permeability layers could promote the use of quick and cheap installation of naturally-developed wells using jetting or straight-flush rotary drilling instead of using fully-penetrating wells completed with filter pack and with extensive well development to remove the fines from the filter cake layer. The amount of total head loss during discharge/recharge at a volumetric rate Q of 20 m^3/h per meter filter length into or from a gravely aquifer layer is reduced by factors of 3 to 4 while using naturally-developed well-types instead of well-types that are drilled by reversed-circulation rotary drilling and contain a filter cake layer due to borehole smearing.

Submitted as: Van Lopik, J.H., Sweijen, T., Hartog, N., & Schotting, R.J. Contribution to head loss by partial-penetration and well completion: implications for dewatering and artificial recharge water wells. *Hydrogeology Journal*.

5.1 Introduction

In order to obtain an optimal, energy-efficient well design, thorough understanding of the well hydraulics is required to minimize head losses during pumping or recharge of water into the subsurface (Driscoll 1986; Barker and Herbert 1992; Houben 2015ab). For a properly designed and developed water well, the largest head loss occurs in the aquifer material (Powers et al. 2007; Houben 2015b).

To date, most studies have investigated the efficiency of abstraction wells for fresh water supply (e.g. Driscoll 1986; De Zwart 2007; Van Beek et al. 2009ab; Houben 2015ab; Houben et al. 2018). These studies focus on typical well-designs for drinking water wells (Barker and Herbert 1992; Houben 2015b), as well as the well efficiency reduction over time by mechanical or chemical clogging (e.g. Houben et al. 2018). Drinking water wells are designed to operate for decades, and hence high costs of proper extensive well development and completion usually overcome the additional pumping costs of cheaper but poorly developed and completed abstraction wells. Typically, such wells are screened over a large portion over the aquifer in order to reduce additional head loss by partial-penetration.

However, for many water well applications partially-penetrating wells (PPWs) are unavoidable to optimize the entire well-system. Water well systems, such as combined dewatering and recharge systems at construction sites (Powers et al. 2007), aquifer storage and recovery (ASR) systems (Zuurbier et al. 2014), high temperature aquifer thermal energy storage (HT-ATES) systems (Buscheck et al. 1983) can be improved with PPWs that target specific portions of the aquifer. During construction dewatering, PPWs (deep-wells or vacuum point-wells) are screened at required drawdown depth for the construction site. The installation of such dewatering PPWs require less drilling and completion costs compared to wells that screen a large portion of the aquifer. For combined well systems of dewatering and artificial recharge wells to re-infiltrate the abstracted groundwater in the target aquifer, dewatering companies in the Netherlands and Germany have started using partially-penetrating recharge wells to minimize the hydraulic impact at shallow subsurface levels during construction dewatering (see Chapter 2). Often, such PPWs are naturally-developed (installed without filter pack) with quick, relatively cheap drilling methods such as jetting or straight-flush rotary (Powers et al. 2007; Cashman and Preene 2013) to save the costs of the entire dewatering scheme for an excavation. Consequently, the well hydraulics of such artificial recharge wells differ significantly from conventional artificial recharge wells.

Particularly for dewatering at construction sites, a wide range of well completion methods are used to install dewatering wells (e.g. deep-wells or vacuum points-wells) to lower the groundwater table and, optionally, artificial recharge wells to re-inject water

into the aquifer. The selected type of well completion of such water wells largely determines the entire efficiency of the dewatering system (Powers et al. 2007). Therefore, the efficiencies of the various abstraction and artificial recharge well-types in construction dewatering are critical to reduce the pumping costs and overall carbon footprint during dewatering operation. Dewatering companies have the opportunity to select from a wide range of drilling techniques to install the most suitable, least-expensive well-type based on the extent and operational time of the dewatering system. In general, the operational life-span of a dewatering abstraction or artificial recharge well is significantly lower than in other well applications. Hence, the costs and time of proper well completion and development need to be balanced with the overall pumping costs for a specific dewatering application.

During artificial recharge and pumping, the effect of additional head losses by non-linear flow behaviour in the filter pack, as well as in the aquifer material, can be significant due to increased flow velocities by diverging/converging flow lines in the vicinity of wells (e.g. Basak 1978, Barker and Herbert 1992; Houben et al. 2015ab). In the initial stage of well operation of proper designed and developed drinking water wells in sandy aquifers, hardly any effect of non-linear flow behaviour is observed (<4% of additional head loss) (Barker and Herbert 1992; Houben et al. 2015b). However, during well operation, clogging of abstraction and injection wells can cause additional head losses (Olsthoorn 1982ab; De Zwart 2007; Powers et al. 2007; Van Beek 2009ab; Martin 2017; Houben et al. 2018). Severe clogging of wells could result in reduced porosity values in the filter pack and drastic increase of non-linear flow behaviour (Houben et al. 2018).

In the present study, the important aspects of well hydraulics of typical well-types used for construction dewatering are investigated using analytical equations. To date, the well specification of such wells are generally based on the equipment and expertise of the drilling or dewatering company (Powers et al. 2007; Cashman and Preene 2013). Existing literature focusses on the well hydraulics of typical drinking water well-types that are completed with a proper filter pack (e.g. Barker and Herbert 1992; Houben 2015ab). However, naturally-developed wells with a collapsed aquifer zone using cheap, quick well completion methods, such as jetting and straight-flush rotary drilling, instead of proper well completion with a filter pack are often used in practice for dewatering projects (e.g. Powers et al. 2007). In order to compare the well efficiency of naturally-developed wells and proper completed wells with filter pack screened in different kind of aquifer types (ranging from sand to gravel), the contributors of the individual head components to the total head loss outside the well screen are evaluated. This is done by using actual hydraulic properties for a broad range of filter sands and natural sand and gravel deposits from aquifers that include the non-linear flow behaviour characteristics

obtained from experimental datasets (Van Lopik et al. 2017; Van Lopik et al. 2019). Besides the wide variety in well completion methods used in construction dewatering, the effect of partial penetration on well efficiency is investigated. Generally, additional head loss of PPWs that only screen a small portion of the aquifer results in large additional head losses (e.g. Barker and Herbert 1992; Houben et al. 2015a; Tügel et al. 2016). However, accounting for the aquifer heterogeneity during PPW placement in high-permeability strata of the aquifer instead of considering homogeneous anisotropic conditions for the aquifer might significantly reduce additional head losses due to partial penetration. The current analytical analysis will provide insight to what extend cheap installation of naturally-developed wells, as well as PPWs that only screen a small portion of the aquifer, can be used at reasonable well efficiency during operation compared to more costly well completion with a filter pack and wells that screen a large portion of the aquifer for dewatering purposes.

5.2 Theory

5.2.1 Well completion with various drilling techniques

In practice, a broad variety of well-types are available for dewatering with deep-wells or injection with artificial recharge wells (Powers et al. 2007). The selection of the well-type (e.a. borehole diameter, well diameters, filter screen, filter pack, screen slot dimensions) depends on the pumped or injected volumes, aquifer characteristics and operational life span of the well. For example, relative cheap PVC wells that need to be operative for a couple of weeks usually suffice for most dewatering projects. Moreover, the expertise of each specific dewatering company, as well as the availability of specific drilling equipment, also largely determines well design in practice (especially for smaller dewatering projects).

In the present study, typical drilling and well completion methods for dewatering and recharge water wells in unconsolidated soils used by the dewatering companies are considered. Two different well completion methods are investigated:

- Naturally-developed wells assuming completion without a filter pack with a larger borehole diameter than the well diameter and a zone of aquifer collapse (Well-types WAC1-2, see Fig. 5.1a and Table 5.1).
- Well completion with a filter pack and filter cake (Well-types WFP1-2, see Fig. 5.1b and Table 5.1).

	Aquifer collapse with no filter pack		Stable borehole with filter pack	
Well-type	WAC1	WAC2	WFP1	WFP2
Drilling procedure	Jetting	Straight-flush rotary	Reversed-circulation rotary	Reversed-circulation rotary
r_0 [m]	500	500	500	500
r_b [m]	0.04	0.1	0.2	0.25
r_s [m]	0.03	0.055	0.1	0.15
n_c [-]	32	60	100	150
w_s [m]	0.0003	0.0003	0.0007	0.0007

Table 5.1 Typical well configuration of artificial recharge wells used for discharge into aquifers during dewatering (see Fig. 5.1). The configuration of well-types WFP-1 and WFP-2 can also be used for pumping deep-wells in dewatering systems. These configurations are used as reference to determine head losses during recharge or pumping.

Aquifer collapse with no filter pack (naturally-developed wells)

In practice, manual jetting and straight-flush rotary drilling are suitable methods for relatively cheap and quick installation of dewatering and artificial recharge naturally-developed wells without artificial filter pack (Powers et al. 2007). Similar to manual jetting, during mechanical drilling by straight-flush rotary, a drilling-fluid is pumped down the drill-rod of the drilling rig to flush out the debris mixture of water and soil. A rotating drill-bit cuts and penetrates the soil. The velocity of the drilling fluid in the borehole annulus must be sufficient to lift the debris up to the surface level. Large quantities of the flushed water volume pumped down the drill-pipe are infiltrated into the surrounding soil during this drilling method (Powers et al. 2007). Drilling through high-permeable layers in the aquifer causes a significant loss of flushed water volume into the surrounding soil and a sudden reduction in debris flush velocity in the borehole annulus. This allows for quick and cheap placement of partially-penetrating recharge wells in high-permeability strata in the aquifer without a filter pack using straight-flush rotary or jetting.

Typical drilling fluids for jetting or straight flush rotary are water, bentonite-mud and polymeric drilling fluids (Powers et al. 2007). If water is used as drilling fluid, well completion with a filter pack in sandy aquifers is practically unfeasible due to a unstable borehole after drilling by the lack of filter cake formation on the borehole wall. In

practice, this is often done by dewatering companies in the Netherlands and Germany to allow for quick placement of artificial recharge water wells with a relative small operational lifespan. After proper well development, such naturally-developed wells could have a negative well skin, due to improved hydraulic conductivities in the vicinity of the well by easy mobilization of finer particles during well development after jetting or straight-flush rotary drilling with a clean drilling fluid, limited formation of filter-cake, as well as aquifer collapse within area between well and the outer borehole diameter after placement ($r_s<r<r_b$) (Discroll 1986; Roscoe Moss Company 1990). Moreover, the filter-cake formed due to precipitation of fines by the up-flowing debris along the borehole collapses and mixes with the aquifer material (Fig. 5.1a). Generally, the borehole radius of jetting and straight-flush rotary drilled wells in stratified soils is highly irregular. In the present study, we have used the radius r_b as outer radius of the skin zone (collapsed aquifer).

Stable borehole with filter pack

For prolonged recharge or dewatering purposes, reversed-circulation rotary drilling is a widely-used method for well placement (Powers et al. 2007). This method enables drilling of large diameter boreholes, and hence large diameter wells can be placed while allowing for proper completion with a filter pack. The drilling method also uses a rotating drilling bit to penetrate and cut the soil. However, the drilling fluid flows down the borehole outside the drill-rod and lift the water and soil to surface level through the drill-rod by suction.

Usually, filter cake at the borehole surface is formed due to precipitation of fines and drilling mud during well placement, causing a small positive skin zone of low permeability. If the well is properly designed and developed, the second-most significant portion of the total additional well loss occurs in this well skin (e.g. Houben 2015b; Houben et al. 2016). Prolonged, costly well development procedures are required to minimize the additional head loss due to well skin. Hence, in practice, significant head loss often occurs due to positive well skin in dewatering deep-wells and artificial recharge wells.

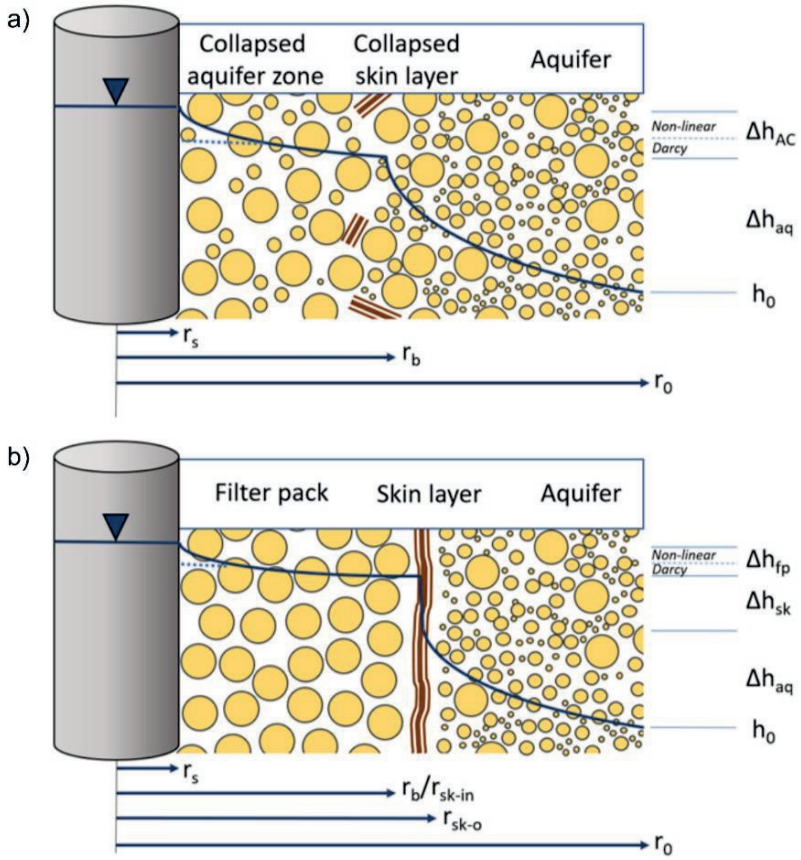

Fig. 5.1 Head losses (blue line) during artificial recharge in an aquifer for **a)** a naturally-developed well drilled with jetting or straight-flush rotary considering aquifer collapse (well type with aquifer collapse WAC) and **b)** a well drilled with reversed-circulation rotary drilling considering filter pack and filter cake with positive skin layer (well-type with filter pack WFP).

5.2.2 Non-linear flow behaviour in porous media

Commonly, the Reynolds number (*Re*) is used to indicate whether flow is in the laminar Darcian flow regime or in the non-linear flow regime (Bear 1988):

$$Re = \frac{d_{50} q}{v} \tag{5.1}$$

where v [m^2/s] is the is the kinematic viscosity of the fluid and d_{50} [m] is the characteristic pore length by means of the median particle diameter. Most studies consider Reynolds numbers ranging from 1-10 for transition between laminar Darcian flow and non-linear flow (e.g. Bear 1988; Houben 2015a; Van Lopik et al. 2017; Van Lopik et al. 2019). Non-linear post-Darcian flow behavior can be described by the alternative flow law of Forchheimer (1901):

$$i = -aq - bq^2 \tag{5.2}$$

where a [s/m] is a parameter equal to the reciprocal of the hydraulic conductivity (i.e., $a=1/K$) and b [s^2/m^2] is the empirical Forchheimer coefficient. Similar to the Kozeny-Carman relationship, Ergun (1952) related the Forchheimer coefficients to the grain size and porosity by:

$$i = -A\frac{(1-n)^2 v}{g n^3 d^2}\, q - B\frac{(1-n)}{g n^3 d}\, q^2 \tag{5.3}$$

where g [m/s^2] is the acceleration due to gravity, d [m] is the characteristic pore length by means of the particle diameter, n [-] is the porosity, A and B [-] are the Ergun constants.

Natural sand and gravel deposits

In the literature, a broad dataset of Forchheimer coeffients a and b for granular material are present (e.g. Moutsopoulos et al. 2009; Van Lopik et al. 2017; Van Lopik et al. 2019). Most studies provide data related to uniformly-graded material with coefficients of uniformity ($C_u=d_{60}/d_{10}$) smaller than 3. The study of Van Lopik et al. (2019) shows that for a wide range of grain size distributions with $C_u>3$ and low porosity values, the amount of fines (characteristic pore length of d_{10}) can be used to predict the Forchheimer coefficients a and b. For the present study, experimentally derived Forchhheimer coefficients from packed bed experiments on natural sands and gravel are used (Table 5.2).

Filter pack	d_{10} [mm]	d_{50} [mm]	C_u	K_{fp} [m/d]	a_{fp} [s/m]	b_{fp} [s^2/m^2]	n [-]
FP-MS1 Medium sand	0.28	0.39	1.48	60.57	1426.5	12523	0.34
FP-CS1 Coarse sand	0.53	0.71	1.42	153.7	562.16	6781.8	0.34
FP-CS2 Coarse sand	0.80	1.0	1.30	351.6	245.75	4396.0	0.35
FP-VCS1 Very coarse sand	1.16	1.5	1.36	823.0	104.98	2497.9	0.36
FP-VCS2 Very coarse sand	1.72	2.1	1.27	1339	64.503	1746.3	0.36
Aquifer material	d_{10} [mm]	d_{50} [mm]	C_u	K_{aq} [m/d]	a_{aq} [s/m]	b_{aq} [s^2/m^2]	n [-]
A-CS1 Coarse sand	0.29	0.77	3.86	53.58	1612.5	14,464	0.33
A-VCS1 Very coarse sand	0.46	1.5	4.84	65.15	1326.1	36,662	0.25
A-CG1 Coarse gravel	0.95	9.5	13.1	328.0	263.37	9957.7	0.25
A-CG2 Coarse gravel	1.36	6.3	7.35	527.3	163.84	6186.8	0.25

Table 5.2 Typical hydraulic characteristics of different types of filter packs and aquifer material. Forchheimer coefficient *a* and *b* for non-linear flow behaviour are obtained from packed bed flow experiments (Van Lopik et al. 2017; Van Lopik et al. 2019).

Filter packs

Usually, basic criteria for the selection of suitable filter packs are provided in the literature for artificial recharge and dewatering deep-wells (Pyne 2005; Powers et al. 2007). Ideally, the used filter pack is based on the aquifer material and grain size analysis of the aquifer is required (Driscoll 1986; Roscoe Moss Company 1990; Powers et al. 2007):

- The filter pack is as coarse as possible. However, selection of filter packs with to coarse grain sizes allows passing and migration of fines, from the aquifer towards the well screen during abstraction. In highly-stratified soils, filter packs should be based on the finest strata. During well development of artificial recharge wells, the risk of mobilization of fines into the filter pack should be taken into account and hence, selection of filter pack is approximately similar to that of dewatering deep-wells.
- The filter material is uniformly-graded (C_u<3). More specifically, the filter pack should have a lower C_u than the aquifer material.

- The median grain size (d_{50}) of the filter pack should be 4-6 times higher than the aquifer material.

Due to high flow velocities (Re>10) by converging or diverging flow lines in the filter pack of respectively abstraction and recharge wells, head loss due to non-linear flow behaviour occurs (e.g. Houben 2015ab). Van Lopik et al. (2017) investigated the non-linear flow behaviour through packed-bed experiments of typical filter pack sands and gravels (with C_u<3). We have selected 5 types of different filter material ranging from medium to very coarse sand in order to investigate the non-linear flow head losses in wells (Table 5.2).

5.2.3 Well hydraulics of artificial recharge and deep-wells

The present study focusses on the different individual components of head loss in the filter pack and aquifer for typical artificial recharge wells and deep-wells used by dewatering companies in various parts of the world. In order to investigate the head losses during artificial recharge or groundwater abstraction in a confined aquifer by a vertical, fully-penetrating well, analytical equations are used to obtain a general overview for different well-types (see Houben 2015b). Typical geometry and parameters for deep-wells and artificial recharge wells are used, see Table 5.1 for specifications. In general, additional head loss due to free flow in the well interior (well casing and screen) and through the screen slots is very small (Barker and Herbert 1992; Houben 2015b). Hence, we solely focus on the head losses outside the well screen.

Darcian and non-Darcian flow towards a well

For classical abstraction or recharge wells that screen large parts of the aquifer, flow is solely in the lateral direction and radial-symmetric flow conditions can be assumed. Hence, steady-state groundwater flow to and from such abstraction or recharge wells in a fully confined homogeneous aquifer can be described by Thiem's equation (1870):

$$\Delta h = \frac{Q}{2\pi KH} \ln\left(\frac{r_2}{r_1}\right) \qquad (5.4)$$

where Δh [m] is the head loss, Q [m^3/s] is the volumetric well discharge/recharge, H [m] is the aquifer thickness and r_1 and r_2 [m] are the radial distances.

At high abstraction or injection flow-velocities in the vicinity of the well, Reynolds numbers are high (Re>10) and non-linear flow behaviour could occur (e.g. Engelund 1953; Basak 197); Houben 2015ab). The extended form of Thiem's equation can be used to account for non-linear Forchheimer flow head losses in the gravel pack or aquifer:

$$\Delta h = \frac{Q}{2\pi KH}\ln\left(\frac{r_2}{r_1}\right) + b\left(\frac{Q}{2\pi H}\right)^2\left(\frac{1}{r_1} - \frac{1}{r_2}\right) \quad (5.5)$$

Eq. 5.5 is used to account for the individual components of head loss in both the collapsed aquifer zone (Eq. 5.8) as well as the aquifer itself (Eq. 5.9) for the well-types WAC1-2 (Table 5.3). Similarly, Eq. 5.5 is used to account for the individual components of head loss in both the filter pack (Eq. 5.11) as well as the aquifer itself (Eq. 5.13) for the well-types WFP1-2. To obtain a rough estimate of the additional head loss due to the formation of a filter cake (positive skin), the Thiem equation is considered (Eq. 5.10). In general, the hydraulic conductivity and thickness of the well skin is difficult to predict, since in-situ samples are required to make proper estimates (Powers et al. 2007; Houben et al. 2015b; Houben et al. 2016). In the present study, we have assumed a filter cake layer of 1 mm at r_b ($r_{sk\_in}<r<r_{sk\_out}$) with a hydraulic conductivity (K_{sk}) of 1e-6 m/d, which are reasonable values for water wells (Houben et al. 2016).

Well-types WAC1-2	
Div. Flow (Eq. 5.7)	$\Delta h_{div} = \frac{Q}{2\pi n_c K_{AC} H}\ln\left[\frac{2}{1-\cos(\delta\pi)}\right] + \frac{b_{AC}}{r_s}\left(\frac{Q}{2\pi n_c H}\right)^2$
Collapsed aq. zone (Eq. 5.8)	$\Delta h_{AC} = \frac{Q}{2\pi K_{AC} H}\ln\left(\frac{r_b}{r_s}\right) + b_{AC}\left(\frac{Q}{2\pi H}\right)^2\left(\frac{1}{r_s} - \frac{1}{r_b}\right)$
Aquifer (Eq. 5.9)	$\Delta h_{aq} = \frac{Q}{2\pi K_{aq} H}\ln\left(\frac{r_0}{r_b}\right) + b_{aq}\left(\frac{Q}{2\pi H}\right)^2\left(\frac{1}{r_b} - \frac{1}{r_0}\right)$
Well-types WFP	
Div. Flow (Eq. 5.10)	$\Delta h_{div} = \frac{Q}{2\pi n_c K_{fp} H}\ln\left[\frac{2}{1-\cos(\delta\pi)}\right] + \frac{b_{fp}}{r_s}\left(\frac{Q}{2\pi n_c H}\right)^2$
Filter pack (Eq. 5.11)	$\Delta h_{fp} = \frac{Q}{2\pi K_{fp} H}\ln\left(\frac{r_b}{r_s}\right) + b\left(\frac{Q}{2\pi H}\right)^2\left(\frac{1}{r_s} - \frac{1}{r_b}\right)$
Positive Skin layer (Eq. 5.12)	$\Delta h_{sk} = \frac{Q}{2\pi K_{sk} H}\ln\left(\frac{r_{sk-o}}{r_{sk-in}}\right)$
Aquifer (Eq. 5.13)	$\Delta h_{aq} = \frac{Q}{2\pi K_{aq} H}\ln\left(\frac{r_0}{r_b}\right) + b_{aq}\left(\frac{Q}{2\pi H}\right)^2\left(\frac{1}{r_b} - \frac{1}{r_0}\right)$

Table 5.3 The different components of additional head losses for well types WAC1-2 (see Fig. 5.1a) and for well types WFP1-2 (see Fig. 5.1b).

Flow convergence/divergence near screen slots

Close to the screen slots, the convergence or divergence of flow lines to or from the screen slots causes an additional head loss. The equation for flow line convergence/divergence by Boulton 1947 (as cited by Houben 2015b) during abstraction or injection is verified and extended for both Darcian and Forchheimer flow (see Appendix H):

$$\Delta h_{div} = h_1 - h_2 = \frac{Q}{2\pi n_c K_h H} \ln\left[\frac{2}{1-\cos(\delta\pi)}\right] + \frac{b}{r_s}\left(\frac{Q}{2\pi n_c H}\right)^2 \quad (5.6)$$

This extended equation is applied for the component of head loss due to flow convergence/divergence in the collapsed aquifer zone for well-types WAC1-2 (Eq. 5.7), as well as the filter pack for well-types WFP1-2 (Eq. 5.9) (Table 5.3).

5.3 Methods

The different components of head losses for typical artificial recharge and dewatering deep-wells are estimated analytically for four different kind of well-types (Table 5.1). In the present study, the effects of non-linear flow behaviour in well hydraulics were investigated using the provided experimental datasets on packed bed flow experiments of filter sands (Van Lopik et al. 2017) and natural sands (Van Lopik et al. 2019) (Table 5.2). The impact on well hydraulics is investigated for:

- The individual components of total head loss of the different well types in the different aquifer materials ranging from coarse sand to coarse gravel (Table 5.2). The contributions to the total head loss in the collapsed aquifer zone (Δh_{AC}) and aquifer (Δh_{aq}) are investigated for well types WAC1-2, as well as in the filter pack (Δh_{fp}), skin (Δh_{sk}) and aquifer (Δh_{aq}) for WFP1-2.
- The efficiency of the filter packs ranging from medium to very coarse sand are investigated and compared to a hypothetical case with no filter pack (assuming the characteristics of aquifer material within the borehole radius).
- The effect of well-clogging in the filter pack.
- The effect of additional head loss by partially penetration of the well.

5.3.1 Individual components of total head losses in different aquifer types

To calculate the individual components of head loss, the analytical equations listed in Table 5.3 are used. For the well types with filter pack (WFP1-2), completion with very coarse sand (FP-VCS1 with K_{fp}=823 m/d) is considered. The associated hydraulic properties of the filter pack FP-VCS1 and the aquifer materials are listed in Table 5.2.

For the collapsed aquifer zone around the well drilled by jetting/straight flush rotary (well types WAC1-2), an improved hydraulic conductivity which is two times lower than the actual aquifer material is assumed. For estimation of the reduced non-linear flow resistance, coefficient b is estimated by: $b = 172.77a^{0.548}$ (see Van Lopik et al. 2017).

5.3.2 Additional head loss in the filter pack

Selection of a suitable filter pack is key for a proper well completion. Ideally, the filter pack is selected such that the flow resistance is lower than the aquifer material (see section 5.2.2 '*Filter packs*'). Hence, in order to compare the efficiency of different filter pack types with equivalent scenarios considering only aquifer material within the well bore zone, the additional head losses by laminar Darcy flow, non-linear flow and flow convergence/divergence to screen slots within the zone of $r_s<r<r_b$ are calculated for the sand types listed in Table 5.2.

5.3.3 Clogging of the filter pack

Clogging of water wells could occur inside the well interior, screen slots and the filter pack (Olsthoorn, 1982ab; De Zwart et al. 2007; Van Beek et al. 2009ab; Houben et al. 2018). Usually, severe clogging of well screens and well interior by biofouling of incrustation of dewatering deep-wells or artificial recharge well (Powers et al. 2007) can be reversed after proper well development. However, well development does not remove all clogging particles in the filter pack, at the borehole wall, and in the aquifer itself (Houben et al. 2016; Houben et al. 2018). The most important factor in well clogging is the clogging of the filter pack (Houben et al. 2018).

Therefore, similar to this latter study on filter pack ageing of drinking water wells, the increase in head losses due to porosity reduction in the filter pack is investigated for well-type WFP1 and the hydraulic properties of filter and natural sand based on Van Lopik 2017 and 2019. The Ergun relation (Eq. 5.3) is used with the Ergun constants A and B of respectively 233.5 and 2.88 and d_{50} for filter pack clogging. These values have shown representative prediction of non-linear flow behaviour through packed beds of various filter sands and gravels (Van Lopik et al. 2017). The effect of reduced porosity values by clogging on the hydraulic conductivity and Forchheimer coeffient b is shown

in Fig. 5.2 for the filter packs of medium sand (FP-MS1), coarse sand (FP-CS2) and very coarse sand (FP-VCS2). Moreover, the effect of porosity reduction by clogging of well-type WAC2 considering the aquifer materials of A-VCS1 and A-CG1 in the collapsed aquifer zone for an naturally-developed well is shown. For these cases, the modified form of the Ergun relationship (Eq. 5.3) for natural sands is considered (Van Lopik et al. 2019). Hence, Ergun constants A and B of respectively 69.0 and 1.85 and the grain size of d_{10} as characteristic length scale are assumed to estimate the effects of porosity reduction by the formation of positive skin layer due to aquifer clogging (see Fig. 5.2b). The filter sands with hydraulic conductivities of 60.6 m/d (FP-MS1), 351 m/d (FP-CS1) and 1339 m/d (FP-VCS2) are used as reference and tested for additional head loss by well clogging.

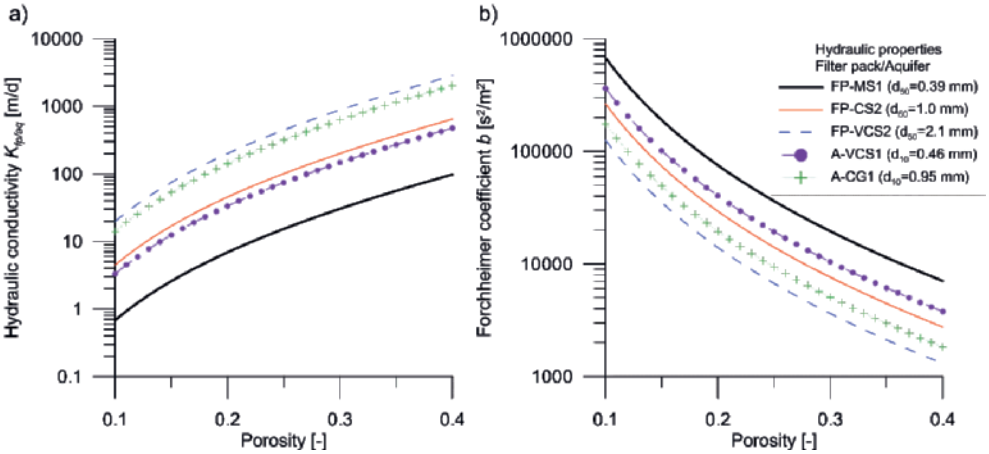

Fig. 5.2 Approximation of the hydraulic properties of the filter pack using the modified Ergun relation (Van Lopik et al. 2017; Van Lopik et al. 2019) obtained from packed bed flow experiments on filter sands and gravel (C_u<3) and aquifer material (C_u>3) for the **a)** hydraulic conductivity and **b)** Forchheimer coefficient b.

5.3.4 Effect of partially-penetration on additional head loss

In the above-mentioned scenarios, axi-symmetric flow in solely the lateral direction is considered using the Thiem equation, which is valid when the Dupuit-Forchheimer approximation holds, see Eq. 5.3 and 5.4. However, well-types for dewatering and artificial recharge at construction sites such as given in Table 5.1 are generally not fully-screened over the entire depth of the aquifer. Dewatering deep-wells are placed at depth of required drawdown for construction. Artificial recharge wells could be screened in deeper parts of the aquifer to minimize hydraulic impact on the excavation site and allowing for closer placement to the dewatered area (see Chapter 2).

In order to estimate additional head loss by partial penetration compared to an equivalent scenario of full penetration over the entire aquifer thickness, multiple equations have been postulated (e.g. Barker and Herbert 1992; Kasenow 2010; Houben et al. 2015a). In the present study, the equation of Barker and Herbert (1992) is used to account for anisotropic aquifer conditions and determine analytically the impact of different aquifer characteristics on head loss for PPWs. Additional head losses by partial penetration of the well in a homogeneous, anisotropic aquifer can be calculated by:

$$\Delta h_{pp} = h_1 - h_2 = \frac{Q}{2\pi K_h H} \frac{1-p_p}{p_p} \ln \left[\frac{p_p(1-p_p)}{2-\varepsilon^2} \frac{H}{r_b} \sqrt{\frac{K_h}{K_v}} \right] \quad (5.14)$$

where p_p [-] is the partial penetration ratio between screen length (L_w) and the aquifer thickness (H) and ε [-] is the eccentricity of the well, described by:

$$\varepsilon = \frac{2z_c}{H(1-p_p)} \quad (5.15)$$

where z_c [m] is the vertical distance between the middle of the aquifer and the centre of the well screen. Note that Eq. 5.14 is only applicable for Darcian-flow conditions and p_p ratios between 0.1 and 0.9. Considering non-linear flow behaviour only occurs in the near vicinity of the well (e.a. filter pack or collapse aquifer zone), this equation is valid to estimate additional head loss by partial penetration.

Generally, high-permeability layers in a given target aquifer are selected in order to optimize the well design (Fig. 5.3a). Often, poor aquifer characterization by a rough estimate of the horizontal hydraulic conductivity and vertical hydraulic conductivity based on an assumed anisotropy factor with typical educated guesses for $a=K_h/K_v$ values that range from 2-10 for natural aquifers (e.g. Kasenow 2010) results in poor well design. The predicted additional head loss by partial penetration is highly overestimated due to underestimating the in-situ aquifer permeability at injection depth (Fig. 5.3b). In order to estimate the overestimation in head loss, we considered a high-permeability layer (hydraulic conductivity of K_1 and thickness of B_1) under- and overlain by low-permeability layers (K_2) of equal thickness (B_2) (Fig. 5.3a). The average horizontal hydraulic conductivity $K_{h,av}$ over the entire aquifer thickness (Fig. 5.3b) is calculated by (Kasenow 2010):

$$K_{h,av} = \frac{\sum K_{h,i} H_i}{H_{tot}} \quad (5.17)$$

The average horizontal hydraulic conductivity $K_{z,av}$ for both the heterogeneous aquifer, as well as the equivalent anisotropic homogeneous aquifer (see Fig. 5.3) is calculated by (Kasenow 2010):

$$K_{z,av} = \frac{H_{tot}}{\sum \frac{H_i}{K_{z,i}}} \tag{5.18}$$

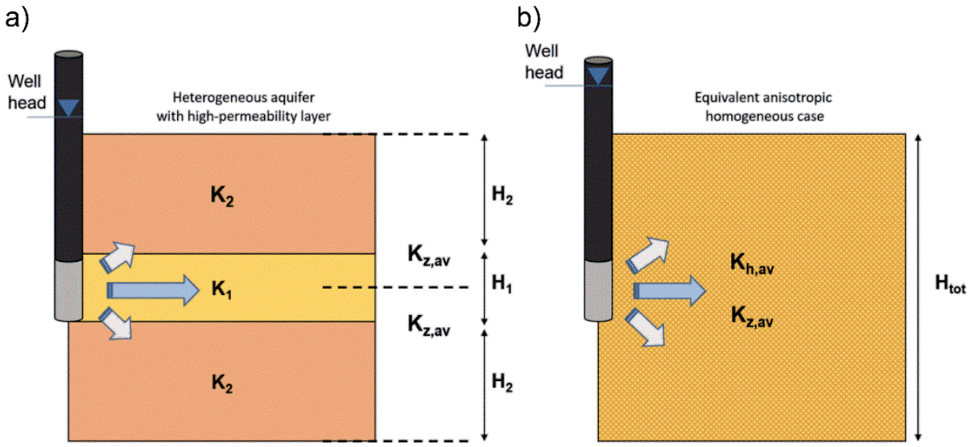

Fig. 5.3 Estimation of the additional well loss due to partial penetration, **a)** assuming the well screened in a high-permeability layer in the aquifer (K_1) and **b)** assuming an equivalent anisotropic homogeneous aquifer.

5.4 Results

5.4.1 Components of head loss in artificial recharge or dewatering deep-wells

The maximum recharge/discharge rate that is investigated for the sandy aquifers (ACS-1 and AVCS-1) is 20 m^3/h. This results in very high total head losses in the range of 10.7 to 15.7 m (Fig 5.4a-b). At a rate of 10 m^3/h, the total head losses are in the range of 5.3 to 7.8 m, which are still high for well operation in such sandy aquifers. Comparing the analysis on the components of head loss between the well-types WAC1-2 and WFP1-2, the difference in total head loss between the two well completion methods is large for the wells screened in coarse gravely aquifers (A-CG1-2; Fig. 5.4c-d). At recharge/discharge rates of 20 m^3/h in aquifer A-CG1-2, the total head losses are only 2.45 and 2.16 m for WAC1 and WAC2 respectively. The total head losses for WFP1-2 are much higher, with values of 6.35 and 5.39 m respectively (Fig. 5.4c).

For well completion with filter pack of well-types WFP1-2 with very coarse filter sand (FP-VCS1) in gravely aquifers A-CG1-2, the head loss in the skin layer is the most important contributor to the total head loss due to the assumption of a low-permeability skin layer (K_{sk} = 1E-6 m/s). At volumetric recharge/discharge rates of 20 m^3/h, the percentage of relative head loss due to skin ranges between 65-80% of the total head loss for well-types WFP1-2 that are screened in A-CG1-2. Hence, extensive well development after reversed-circulation rotary drilling is required to remove filter cake and lower the K_{sk} to values of approximately 1E-3 m/s in order to achieve similar head loss of 1.3 m as for the equivalent case with WAC2.

For the estimated additional head loss components in the aquifer and collapsed aquifer zone for the naturally-developed well-types WAC1-2, a higher hydraulic conductivity (negative skin) for the collapsed aquifer is assumed (Fig. 5.1a). This results in slightly reduced head losses in the collapsed aquifer zone. For example, a volumetric recharge/discharge rate of 20 m^3/h for WAC2 screened in the gravely aquifer ACG-1 results in an estimated head loss of only 0.06 m in the collapsed aquifer zone, which is only 4.3% of the total head loss (see Fig. 5.4c). Compared to a scenario with no formation of negative skin layer and permeability enhancement after completion and development of well-type WAC2 in the borehole area ($r_s<r<r_b$), the estimated head loss is 0.21 m (Fig. 5.5c), which is only 9.3% of the total head loss. Only for severe reduction of permeability (positive skin) in the borehole area ($r_s>r>r_b$), the contribution to the total head loss can be significant. For example, in order to obtain a similar total head loss as for WFP1 at a discharge recharge rate of 20 m^3/h in A-CG1 (total head loss of 6.35 m; Fig. 5.4c), the hydraulic conductivity in the borehole area ($r_s>r>r_b$) need to be reduced from 328 to a value of 19 m/d (with *b*-coefficients 23700 s^2/m^2) for WAC2. This can be

the case for scenarios with poor or no well development in the borehole area in WAC1-2.

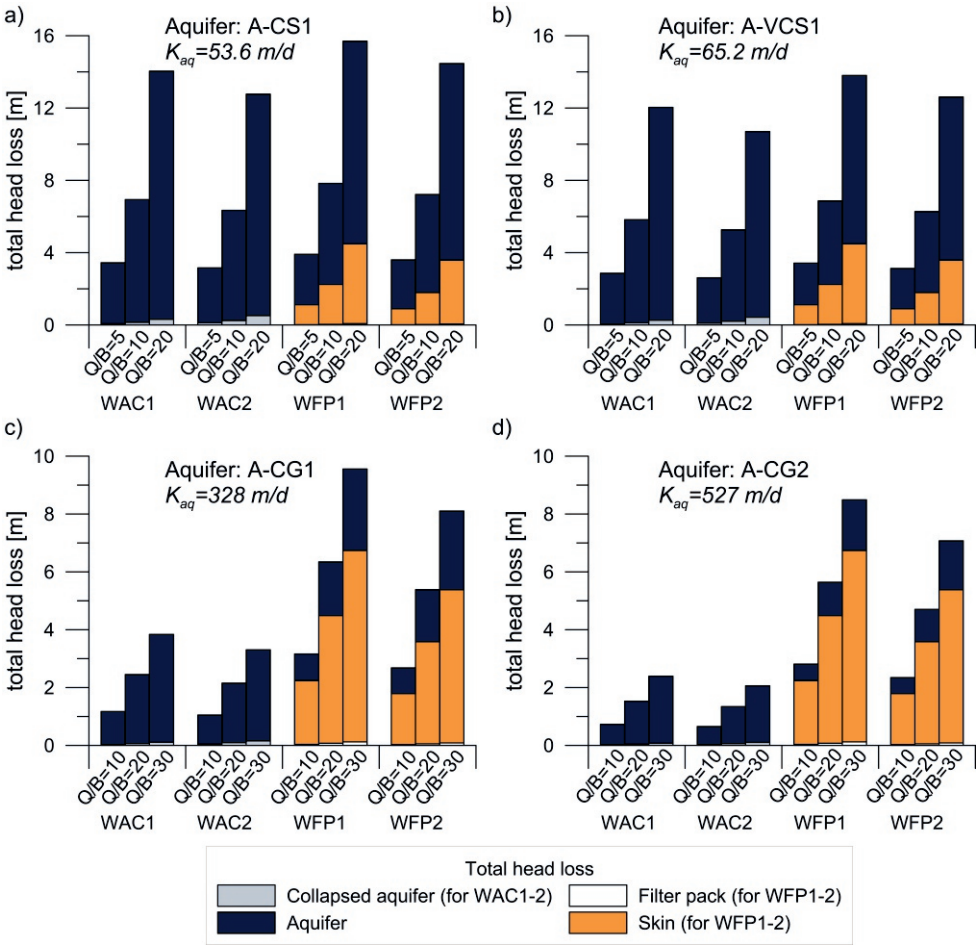

Fig. 5.4 Head losses in the aquifer during artificial recharge/dewatering with the four different well-types (Table 5.1) at volumetric discharge/recharge rates over 1 meter filter length (Q/B) of 10, 20 and 30 m^3/h. The aquifer types in Table 5.2 are used with **a)** A-CS1 (d_{50}=0.77 mm), **b)** A-VCS (d_{50}=1.5 mm), **c)** A-CG1 (d_{50}=9.5 mm), **d)** A-CG2 (d_{50}=6.3 mm). Note that for well types WAC the collapsed aquifer hydraulic conductivity is two times higher than the aquifer material and for well types WFP the filter pack F-VCS1 is considered.

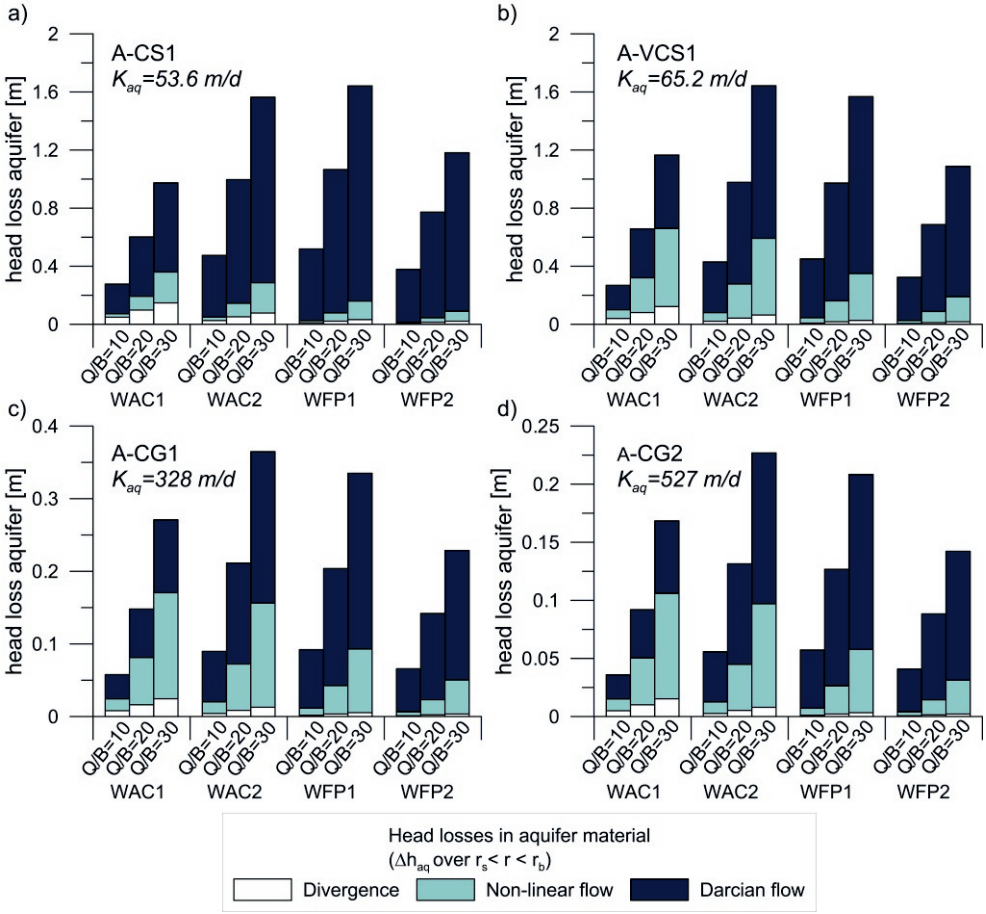

Fig. 5.5 Head losses in the borehole area of the aquifer during artificial recharge/dewatering with the four different well-types (Table 5.1) at volumetric discharge/recharge rates over 1 meter filter length (*Q/B*) of 10, 20 and 30 m^3/h. The head loss is calculated within the radius of the borehole ($r_s<r<r_b$), to compare and investigate the efficiency increase with well completion using a filter pack. The aquifer types in Table 5.2 are used with **a)** A-CS1 (d_{50}=0.77 mm), **b)** A-VCS (d_{50}=1.5 mm), **c)** A-CG1 (d_{50}=9.5 mm), **d)** A-CG2 (d_{50}=6.3 mm).

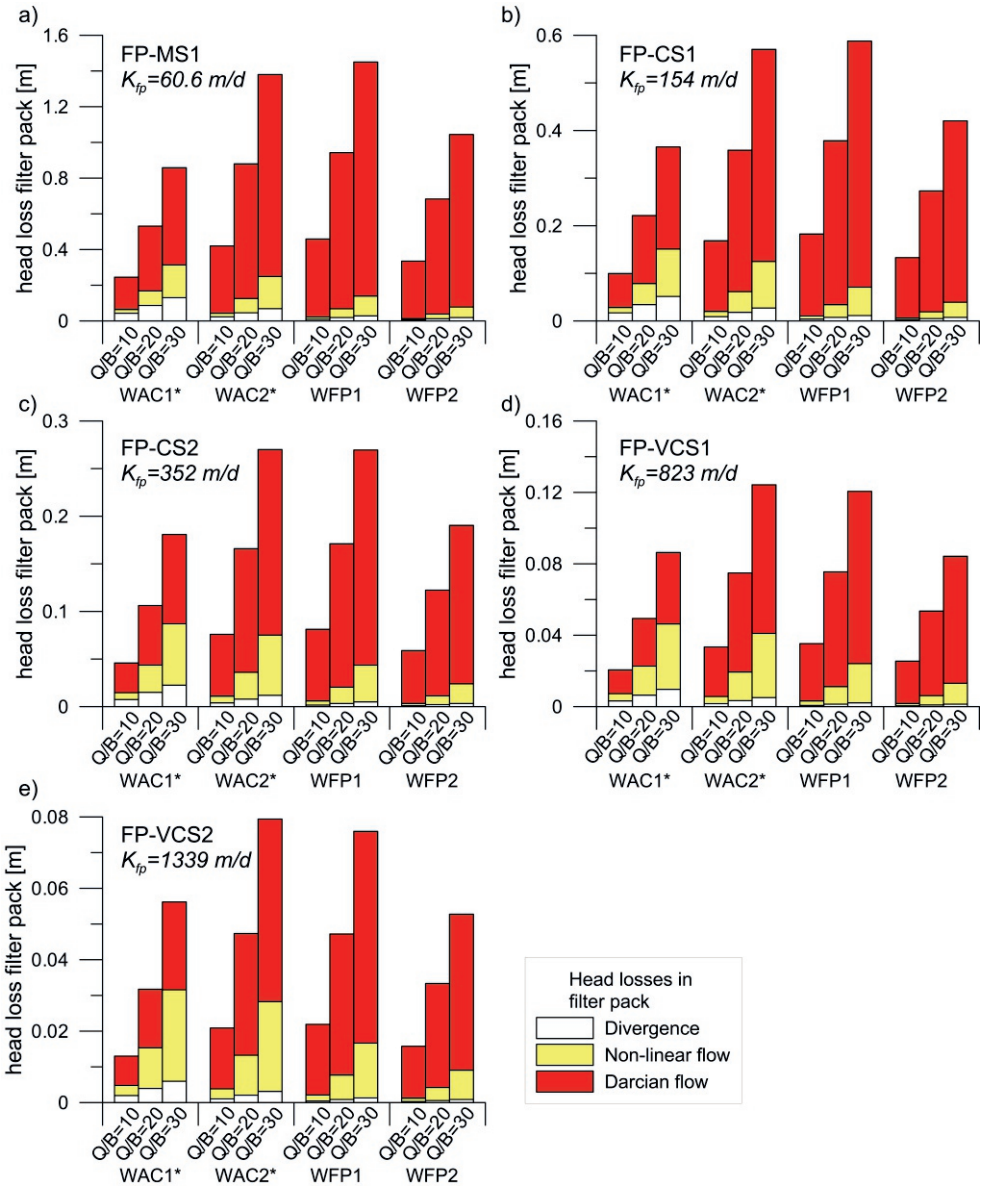

Fig. 5.6 Head losses in the filter pack during artificial recharge/dewatering with the four different well-types (Table 5.1) at volumetric discharge/recharge rates over 1 meter filter length (Q/B) of 10, 20 and 30 m^3/h. The considered types of filter packs (Table 5.2) are used with **a)** FP-MS1 of medium sand (d_{50}=0.39 mm), **b)** FP-CS1 of coarse sand (d_{50}=0.71 mm), **c)** FP-CS2 of coarse sand (d_{50}=1.0 mm), **d)** FP-VCS1 of very coarse sand (d_{50}=1.5 mm) and **e)** FP-VCS2 of very coarse sand (d_{50}=2.1 mm). *Note that well-types WAC1-2 are usually completed without filterpack.

5.4.2 Head losses in the filter pack and collapsed aquifer zone

The selection of a proper very coarse filter sand (FP-VCS1 with K_{fp}=823 m/d) for well-types WFP1-2 results in limited additional head loss in the filter pack compared to head losses in the skin layer and aquifer. The hydraulic conductivity of the filter pack is a factor of 15.4 and 12.6 higher than the aquifer hydraulic conductivities of A-CS1 and A-VCS1 respectively. In contrary, the advantage of well completion with filter pack FP-VCS1 (d_{50}=1.5 mm) in coarse gravel deposits (A-CSG1-2) is limited, resulting in higher aquifer hydraulic conductivities by a factor of only 2.5 and 1.6 respectively. Therefore, the advantage of using filter pack FP-VCS1 instead of the actual aquifer material in the borehole area ($r_s<r<r_b$) is small in the gravely aquifers (A-CG1-2). For example, the difference in head loss at 20 m^3/h with WFP1 between the filter pack (Δh_{fp}=0.075 m; Fig. 5.6d) and a hypothetical scenario of aquifer material A-CG2 in the borehole area (Δh_{aq}=0.126 m; Fig. 5.5d) is negligible. For the sandy aquifers the difference in head loss is much higher, where Δh_{aq} equals 0.97 m (A-CS1) and 1.06 m (A-VCS1) (Fig 5.5a-b). The selection of coarser, more permeable filter packs in homogeneous gravel aquifers could potentially increase the well efficiency. The use of filter pack FP-VCS2 in a high-permeability layer of A-CG2 could reduce the head loss significantly by a factor of 2.7. However, the selection of coarser gravel packs (d_{50}>2 mm) could result in mobilization of fine material from the well-graded gravel with fine sand/silt and the risk of sand pumping (Powers et al. 2007). In practice, the selected grain size of the uniformly-graded filter packs by dewatering companies for well completion in sandy natural aquifers are commonly 1.0-2.0 mm (e.a. FP-CS2 and FP-VCS1-2).

For wells screened in stratified aquifers, filter packs should be based on the finest strata. As a consequence, the selection of filter packs for well-types WFP1-2 based on the finer low-permeability layers in highly heterogeneous sandy or gravely aquifers does not necessarily mean significant reduction in well losses compared to naturally-developed well-types without filter pack (WAC1-2). Most flow will occur in the high-permeability layers in the aquifer such as A-CG1 (K=328 m/d) and A-CG2 (K=527 m/d). In such case, the use of WFP1-2 with filter pack for dewatering and artificial recharge does not necessarily result in a better well performance than well-types WAC1-2.

The non-linear flow head losses in the filter packs are small compared to the total head loss (Fig. 5.4 and 5.6). Due to relative high Forchheimer coefficients b with respect to the hydraulic conductivity of natural sands and gravels with high C_u values and low porosity values compared to filter sands (Table 5.2), the component of head loss due to non-linear flow behaviour is slightly higher for ACG1-2 (Fig. 5.5c-d). Considering the use of well-type WAC1-2 with no collapsed aquifer zone (negative skin) in these aquifer types, the percentage of non-linear flow head loss is approximately still only 4% of the total head loss. Note that in typical collapsed aquifer zones (after well completion by

jetting of straight-flush rotary), the porosity is increased and the relative fraction of non-linear flow behaviour head loss is lower. Therefore, we can state that the effect of non-linear flow behaviour on head loss is limited for both naturally-developed (WAC1-2) and filter pack well-types (WFP1-2) in sandy, to fine gravelly aquifers after proper well completion and development. This is in line with the non-Darcian head losses in common water wells (Barker and Herbert 1992; Houben et al. 2015ab).

However, in uniformly-graded gravely to boulder-type aquifers, the effect of non-linear flow behaviour will become more significant. For example, considering a high-permeability aquifer with the aquifer characteristics of FP-VCS2 (K=1339 m/d) and no well skin or filter pack on WAC2, the total head loss will be 0.84 m with a non-Darcian head loss component of 7% at Q=30 m^3/d. Therefore, screening well-types WAC1-2 in high-permeable gravel layers (K>1000 m/d) the additional head loss by non-linear flow behaviour should be taken into account.

Similar to Houben (2015b), the additional head loss due to flow convergence/divergence in the filter pack is negligible (e.g. only <0.03% of the total head loss for WAC1-2 and WFP1-2 with FP-VCS1; Fig. 5.4 and 5.6d). The additional head losses due to convergence/divergence are calculated based on the assumption that the flow lines solely convergence/diverge at the interface between the filter pack and well screen, see Appendix H. To determine if this is a proper assumption, numerical modelling and experimental work is required. Presumably, convergence or divergence of flow lines during respectively abstraction or injection will not solely occur at this interface, but over a wider region in the filter pack and is much more complex than the assumption made in Appendix H for Boulton's equation (1947) (Eq. 5.6). Therefore, the components of head loss due to divergence or convergence in the present study should be taken as a proxy. Nonetheless, it makes sense that the major contribution of head loss occur by the axi-symmetric Darcian and non-linear flow as shown in Fig. 5.5-5.6, and the zone of diverging/converging flow lines occurs in the nearest vicinity of the screen, and is very small.

5.4.3 Clogging of the filter pack

Severe clogging of the filter pack of artificial recharge and dewatering deep-wells (well-type WFP1), could result in high additional head losses (Fig. 5.7). For example, considering filter pack FP-CS2, a porosity reduction to a value of 0.18 by clogging could result in increased total head loss by a factor 2 during abstraction or recharge in aquifer A-VCS1 (see Fig. 5.4b and 5.7). The reduction in well-efficiency due to clogging by lower porosity values is the highest for the filter pack with the lowest average grain size (FP-MS1; d_{50}=0.39). Assuming a reduction of the porosity from a value of 0.34 to a value of 0.25, the additional head loss is increased by a factor of 7.5. This is only a factor of 2.4 for the filter pack FP-VCS2 (d_{50}=2.0 mm). Note that for naturally-developed well types (with natural sands and gravels with C_u>3 within the area r_s<r<r_b) the initial porosities can be significantly lower than for uniformly-graded filter sands. Hence, well-types WAC1-2 with lower initial porosities of the aquifer material in the vicinity of the well screen compared to equivalent cases with filter pack might be more susceptible for additional head loss due to well clogging.

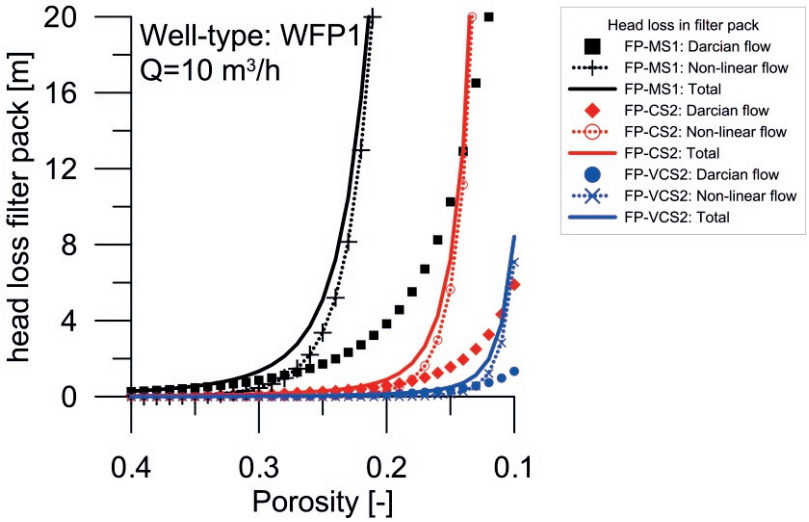

Fig. 5.7 Additional head loss in the filter pack for well-type WFP1 (with FP-MS1, FP-CS2 and FP-VCS2) due to porosity reduction by clogging. The components of head loss due to hydraulic conductivity reduction (Fig. 5.2a) and non-linear flow increase (Fig. 5.2b) are shown.

5.4.4 Effect of partial-penetration of wells

In general, optimal efficiency for water wells is obtained when the filter is screened over a large portion of the aquifer in order reduce head losses due to converging or diverging flow lines in the vertical direction due to partial penetration (e.g. Houben 2015a). However, in construction dewatering PPWs are used to target the desired hydraulic impact at a given depth in the aquifer. Hence, the reduction in well efficiency on the one hand, and the desired hydraulic impact at given aquifer depth at the other hand need to be taken into account in order to define the optimal well design. The optimal ratio of partial penetration is a trade-off between these two issues.

The latter scenarios in the present study, assuming the Dupuit-Forchheimer approximation with lateral flow behaviour in the entire aquifer system, can be considered as a upper estimate of the maximum head loss of a PPW screened in a given portion of the aquifer. In such scenario, all flow in the screened portion of the aquifer (Q/B) is assumed to be in the lateral direction, and no flow in the vertical to over and underlying aquifer layers occurs.

In Fig. 5.8, the additional head loss due to partial penetration in aquifer type A-VCS1 is shown using Eq. 5.14. Especially partial penetration ratios smaller than 0.2 the additional head loss is significant, while considering an anisotropic, homogeneous aquifer. Screening PPWs in the top or bottom of the aquifer (ε=1 in Eq. 5.15), the additional head loss due to partial penetration is the highest. PPWs screened in the middle of the aquifer (ε=0 in Eq. 5.15) result the smallest additional head loss for a given partial penetration ratio (Fig. 5.8). These results are in line with the numerical modelling results of Tügel et al. (2018). while considering uniform screen inflow at the PPW. However, note that in practice, inflow and outflow over a PPW screen is not constant over the entire filter length (e.g. Ruud and Kabala 1997; Houben et al. 2015a; Tügel et al. 2016; Zhu and Wen 2019). The volumetric flow rate at the top and bottom end of a PPW is generally higher than in the middle portion of the well screen. Moreover, factors such as aquifer heterogeneity (Ruud and Kabala 1997), the pump position (Tügel et al. 2016) or non-linear flow behaviour in the well vicinity (Zhu and Wen 2019) could have an impact on additional head loss calculations and require a numerical approach and flow meter logs for more detailed investigation (e.g. Houben 2015b).

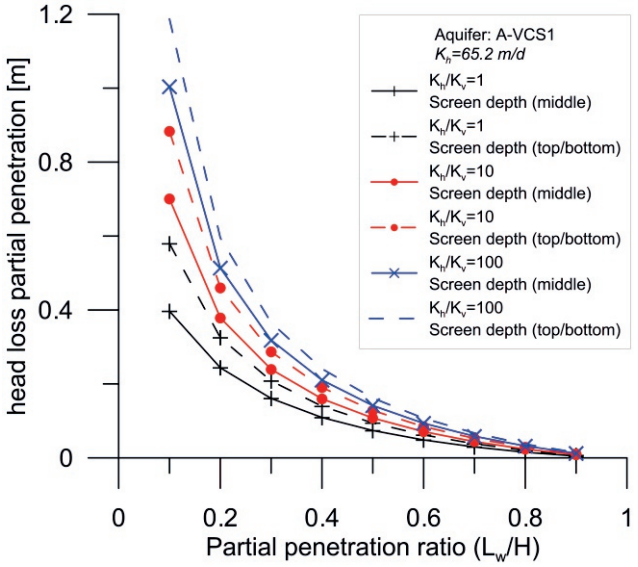

Fig. 5.8 Additional head due to partial-penetration compared to an equivalent scenario of a fully-penetrating well for well-type WFP1 and a volumetric discharge/recharge rate (Q) of 10 m^3/h in an aquifer of very coarse sand (A-VCS1: d_{50} = 1.5 mm). The solid lines represent PPWs screened in the centre of the aquifer. The dashed lines represent PPWs screened at the top/bottom of the aquifer (well screen top or end at confining unit).

For heterogeneous aquifers the use of an equivalent anisotropic homogenous aquifer does not yield for wells with a low partial penetration ratio ($0.1<p_p<0.5$) screened in a high-permeability layer. The actual horizontal hydraulic conductivity can be drastically underestimated by using a simplified characterization of the aquifer by assuming anisotropic homogeneous conditions. Table 5.4 shows that poor aquifer characterization by using one bulk $K_{h,av}$ and $K_{v,av}$ for the anisotropic homogeneous aquifer results in drastic overestimation of the additional head loss by partial penetration. Using a PPW of well-type WFP-1 that screens a 2 meter thick high permeability layer of 328 m/d, under and overlain by lower permeability layers of 32.8 m/d of each 9 meter thick, the additional head loss by partial penetration is only 0.52 m (Table 5.4). If the high-permeability layer is not taken into account and the simplified equivalent anisotropic homogenous aquifer is considered, the additional head loss is overestimated by a factor of 4 (2.0 m). Hence, the selection of the screen interval depth of a dewatering deep-well or artificial recharge PPW should be based on good soil characterization in order to minimize additional head loss by partial penetration. Especially the placement of artificial recharge PPW to discharge dewatered groundwater in a high-permeability layer overlain by low-permeability strata could reduce the hydraulic impact on the overlaying dewatered strata at a minimized additional head loss due to partial penetration.

	p_p [-]	K_1 [m/d]	K_2 [m/d]	B_1 [m]	B_1 [m]	Heterogen. Δh_{pp} [m] (see Fig. 5.3a)	An. Homogen. Δh_{pp} [m] (see Fig. 5.3b)
Aquifer A-VCS1	0.1	65.2	65.2	2	9	1.74	1.74
	0.1	65.2	6.52	2	9	2.61	10.3
	0.1	65.2	0.652	2	9	3.52	24.4
Aquifer A-VCS1	0.2	65.2	65.2	4	8	0.98	0.98
	0.2	65.2	6.52	4	8	1.35	4.01
	0.2	65.2	0.652	4	8	1.75	7.07
Aquifer A-CG1	0.1	328	328	2	9	0.35	0.35
	0.1	328	32.8	2	9	0.52	2.04
	0.1	328	3.28	2	9	0.70	4.82
Aquifer A-CG1	0.2	328	328	4	8	0.19	0.19
	0.2	328	32.8	4	8	0.27	0.80
	0.2	328	3.28	4	8	0.35	1.40

Table 5.4 Estimated additional head loss considering well-type WFP1 in a heterogeneous high-permeability layer and an equivalent case with anisotropic homogeneous aquifer conditions using Eq. 5.14.

5.5 Discussion

5.5.1 Differences in head loss due to well completion method

The results in the present study suggest that use of relative cheap and quick drilling methods (jetting and straight flush rotary) for well completion of well-types WAC1-2 without placement of a filter pack does not necessarily mean increased head losses and higher pumping costs. Especially, well screen placement in high-permeability aquifers (A-CG1-2) with WAC1-2 results in higher well performance compared to placement of WFP1-2 with reversed-circulation rotary drilling (Fig. 5.4c-d). Comparing the well-types WAC1-2 with no clear formation of a thin skin layer by filter cake and a zone of collapsed aquifer (Fig. 5.1a) with wells drilled by reversed-circulation rotary drilling with a positive skin layer (well-types WFP1-2) (Fig. 5.1b), the amount of total head loss by discharging/recharging water at Q of 20 m^3/h into or from the gravely aquifers (A-CG1-2) is reduced by factors of 3 to 4.

5.5.2 Uncertainties in the hydraulic characteristics of the well skin and collapsed aquifer zone

We have assumed a filter cake layer of 1 mm at r_b ($r_{sk\_in} < r < r_{sk\_out}$) with a hydraulic conductivity (K_{sk}) of 1e-6 m/d. Ideally, well development in formations of high hydraulic conductivity should be a applied for hours and development in formations of low hydraulic conductivity may take days to remove the filter cake (Powers et al. 2007). However, in practice, dewatering companies often choose to apply well development over a limited time span for the smaller dewatering projects that are operational over only a small period time. Especially compared to drinking water, ASR- or ATES wells that are operational over a much longer time span, the impact of skin layers on total head loss in dewatering deep-wells and artificial recharge wells can be large. As a consequence, well completion with reversed-circulation rotary drilling of such wells (e.g. WFP1-2) could have a distinct skin layer. Drilling with drilling mud, which is usually done with reversed-circulation rotary drilling, will always result in a filter cake and poorer well performance over time compared to drilling techniques without drilling additives (Timmer et al. 2003). Hence, the assumption of a skin layer with K_{sk} of 1e-6 m/d for well-types WFP1-2 is good indication for the potential contribution of head losses due to skin in dewatering and artificial recharge wells. In practice, the actual thickness and hydraulic conductivity of the skin layer of such wells are unknown since no samples of the skin layer are available, and these properties should be determined indirectly from pumping tests (Houben 2015a, Barrash et al. 2006). So far, only a few in-situ skin layer samples have been analyzed by permeameter tests (e.g. Houben et al. 2016). Similar to the latter study, in-situ sampling of the borehole area at well-types such as WFP1-2 and WAC1-2 could provide useful insight in the hydraulic characteristics of the skin layer and filter pack at the one hand and the collapsed aquifer zone at the other hand.

For well types WAC1-2, the assumption of an improved collapsed aquifer zone (negative skin) with a hydraulic conductivity reduction by a factor 2 is an optimistic estimate. In reality, similar to the hydraulic conductivity of the skin permeability in the filter cake for WFP1-2, the permeability in this collapsed aquifer zone could vary for each well depending on aquifer type, well completion, as well as well development method. Using clean water as drilling fluid, the amounts of fines in this zone will be low and the assumption of enhanced permeability is reasonable. However, poor well development or the use of a bentonite-mud, or muddy-water as drilling fluid could cause permeability reduction in the collapsed aquifer zone. Generally, dewatering companies in the Netherlands are using relative clean surface- or groundwater to drill up to depths of 20 meter below ground level. Therefore, considering no permeability

reduction/enhancement in the collapsed zone should provide a good estimate for the upper limit of head losses in well-types WAC1-2 after drilling and a reasonable well development.

Only severe reduction of permeability in the collapsed aquifer zone due to poor well development after well completion with jetting and straight-flush rotary drilling for WAC1-2 will result in high contributions to the total head loss in the borehole area ($r_s<r<r_b$) . Note that the absence of a filter cake after aquifer collapse for WAC1-2 (Fig. 5.1a) allows for easier, less extensive well development, which makes the assumption of enhanced permeability or in-situ aquifer permeability within the borehole area ($r_s<r<r_b$) reasonable. Hence, the reduced total head loss in gravely aquifers by using WAC1-2 is a good indication of the potential advantage of using WAC1-2 instead of WFP1-2.

5.5.3 Predicting additional head loss by well clogging

Well ageing of abstraction and recharge wells can occur due to mechanical and geochemical clogging (De Zwart 2007; Van Beek et al. 2009ab; Houben et al. 2018). Well ageing could occur due to clogging of the filter pack, screen slots and well casing interior (Houben et al. 2018). The most important contributor to head loss by well ageing is clogging of the filter pack, while increased head loss only occurs at severe clogging of the screen slots and well casing interior. In practice, clogging of the filter pack and screen slots can be observed by the increasing difference in head over time between the abstraction water well itself and the observation well in its gravel pack (Van Beek et al. 2009b). Moreover, clogging could occur at the borehole interface between filter pack and aquifer material by the formation of a thin skin layer (Timmer 2003; De Zwart 2007; Van Beek et al. 2009b). Ongoing accumulation of fine materials at the borehole wall causes this zone to slowly expands outwards and increase in thickness and hence flow resistance over time during abstraction (higher Δh_{sk} for Eq. 5.12).

During artificial recharge in a water well, the recharged water always contain impurities that cause well clogging (plugging) over time (Olsthoorn 1982ab; Bouwer 2002; Bear 2007; Powers et al. 2007; Martin 2017). These impurities can range from organic matter, air entrainment, to fine aquifer material (such as clay, loam or silt) or precipitates of minerals (such as manganese- or iron-oxides and calcite). For recharge wells, suspended solids or chemicals are transported into the filter pack and aquifer. Moreover, rapid clogging of artificial recharge wells immediately after the start of the recharge procedure could occur due to degassing of depressurized water and formation of air bubbles in the filter pack or aquifer (Olsthoorn 1982ab; Martin 2017). Generally, clogging during recharge occurs in the gravel pack (if present), the borehole interface and in the target formation immediately surrounding the bore (Martin 2017).

The clogging of the filter pack or aquifer material by particle migration, biofouling and mineral precipitation, or free gas could result in significant porosity reduction. In the present study, the clogging mechanism is determined by only reducing porosity in the Ergun relationships (Eq. 5.3) based on packed bed experiments of filter sands at porosity values of 0.25-0.35. Exact determination of non-linear flow behaviour through severely clogged packed beds are required to investigate to what extent non-linear flow behaviour causes additional head losses. This should be done for the various mechanisms of clogging to obtain a more detailed overview to what extent well clogging could cause additional head losses during well operation. During well operation, there are methods to analyze the clogging potential of an artificial well, such as membrane filtration index (MFI; for the suspended-solid content of the recharged water) and assimilable organic carbon content (AOC; for the growth potential of microorganisms in water) (Bouwer 2002).

Increasing injection pressure to maintain the desired recharge rate of the well is not a successful solution to overcome the problems of clogging. Such solution could even led to enhanced clogging potential, due to enhanced inflow of clogging mass and compression of the clogging layer (Bouwer 2002). However, discontinues recharge schemes with periods of rest could significantly enhance the well efficiency and reduce the effects of clogging (Olsthoorn 1982ab; Bouwer 2002; De la Loma 2017) by remobilization of finer particles by switching from a rest period to recharge. A similar procedure is suggested for groundwater abstraction (Van Beek et al. 2009ab). Such well schemes might be preferable for artificial recharge wells near dewatering sites using a buffer container or two sets of artificial recharge wells. Well development of artificial recharge and deep-wells can be realized by a wide range of methods, such as brushing or scratching the inner-screen surface, surge (flushing) pumping, air lifting, or the use of chemicals (Olsthoorn 1982ab; Powers et al. 2007). In most cases, well development could remove clogging particles from the well screen. However, the development of the filter pack, skin and aquifer is more difficult, due to fractions of clogging particles that remain in the filter pack or aquifer.

5.6 Conclusions

The present study provides a detailed overview of the contributions to the head loss for typical well configurations of dewatering deep-wells and artificial recharge wells. Typical well completion methods in unconsolidated aquifers used by dewatering companies are considered. To investigate the hydraulics of such water wells, the method described by Houben (2015b) while using the hydraulic characteristics of the filter pack and aquifer material obtained from packed bed flow experiments conducted by Van Lopik et al. (2017 and 2019) are used.

The well efficiency of wells drilled by relative cheap and quick drilling methods, such as jetting and straight flush rotary, without a proper well completion with a filter pack does not necessarily mean increased head losses and higher pumping costs compared to wells completed with a filter pack (with reversed-circulation rotary-drilling). The main component of head loss occurs in the aquifer for well completion without filter pack by jetting or straight-flush rotary drilling. In such case, the formation of negative skin in the borehole area and no filter cake layer continuously spread over the borehole wall can be considered due to aquifer collapse after removing the drilling- or jetting-rod from the unconsolidated soil. Only severe permeability reduction by residual mud additives or fine sand in the collapsed aquifer zone after poor well development could result in positive skin for such wells. In well-types with a filter pack (WFP), besides the component of head los in the aquifer itself, the contribution to the total head loss by a positive skin layer of filter cake after well completion can be significant. Especially for high-permeability aquifers, the absence of a positive skin layer in wells completed without a filter pack results in equal or better well performance compared to the more expensive drilling method of reversed circulation rotary drilling. Intensive, costly well development would be required to lower the amount of positive well skin on such wells to operate at similar efficiency.

Selection of a proper filter pack (with average grain size of 1.0-2.0 mm) for wells screened in sandy to gravely aquifers ($50<K<500$ m/d) results in only a minor contribution to the total head loss. The component of head loss due to non-linear flow behavior in filter pack or aquifer is small, if sandy to gravely aquifers ($K<500$ m/d) and maximum discharge or recharge rates of 30 m^3/h are assumed.

Clogging of the filter pack is considered by assuming uniform reduction of the porosity values. Due to the reduction of the pore space, the main contributor to additional head loss by filter pack clogging is the effect of non-linear flow behavior. Filter packs or aquifer material with a smaller grain size are more suspectable for the increase in head losses due to porosity reduction by clogging.

It is recommended that dewatering companies investigate the characteristics of the aquifer prior to well installation of dewatering wells and artificial recharge wells. Especially for PPWs, good aquifer characterization is required to screen dewatering and artificial recharge wells in high-permeability strata. Not accounting for heterogeneity in aquifers with gravely strata could easily overestimate the required well head by factors higher than 2 for PPWs with small partial penetration ratios. Good exploration of the dewatering site could promote the use of dewatering deep-wells and artificial recharge PPWs to minimize the hydraulic impact of short-term dewatering operations. Moreover, the selection of high-permeability layers could promote the use of quick and cheap well completion without a filter pack using jetting or straight-flush rotary drilling instead of using fully-penetration wells completed with filter pack and extensive well development to remove the fines from the filter cake layer.

Acknowledgements

This work was supported by the foundations STW (Foundation for Technical Sciences) and O2DIT (Foundation for Research and Development of Sustainable Infiltration Techniques). The authors wish to thank Georg J. Houben from the Bundesanstalt für Geowissenschaften und Rohstoffe for his critical comments on prior drafts of this paper. Moreover, the authors wish to thank dewatering companies Theo van Velzen, Henk van Tongeren and P.J. de Vet & Zonen for providing well specification of typical dewatering deep-wells and artificial recharge wells

Chapter 6

Heterogeneous aquifer characterization by divergent flow heat and bromide tracer testing with a partially penetrating recharge well

Abstract

Experimental characterization of solute and heat transport in heterogeneous aquifers is important broad range of recharge and abstraction well applications. In this study, heat and bromide tracer experiments with a partially penetrating recharge well were conducted under divergent flow conditions. A detailed hydrogeological site investigation provided a accurate overview of the aquifer heterogeneity. The conservative bromide ion tracer test is conducted at a solute density contrast of only 0.04%. Similarly, the heat tracer test is conducted at a negligible density and viscosity contrasts (maximum relative viscosity difference of only 3.9% with ΔT<1.4 ºC). The hydraulic and transport characteristics from this hydrogeological characterization are used for numerical prediction of the observed multi-level bromide ion BTCs at different depths in the aquifer. In the well vicinity, conservative solute breakthrough was accurately predicted with a solute macrodispersivity α_l of 0.03. No asymptotic formation-specific scaling of the solute macrodispersivity values is observed for this small scale divergent flow test. However, at larger transport distance less accurate and less disperse fits were obtained with a solute macrodispersivity α_l of 0.03. Presumably, besides aquifer heterogeneity, under diverging flow conditions the mixing behavior at high flow velocities in the near-well vicinity (well distance <1 m) of the PPW is also determined by the hydraulic characteristics of the naturally-developed pack, well skin, as well as the occurrence of non-linear flow behaviour.

Multi-level temperature monitoring over aquifer depth is done with a fully-looped optic fiber cable with a DTS system to obtain a detailed spatial and temporal distribution of the temperatures in the aquifer during the heat tracer test. In the well vicinity, model calibration showed that the disperse breakthrough of heat cannot be fully ascribed to thermal conduction. Heat mixing in in the well vicinity (r<2 m at recharge level) under divergent flow conditions during injection in a PPW occurs due to both thermal conduction and additional heat mixing translated into the thermal macrodispersivity by model calibration.

6.1 Introduction

Reliable quantification of solute and heat transport in heterogeneous aquifers is important for a broad range of water well applications, such as management and remediation of contaminated groundwater (Ptak et al. 2004; Khan et al. 2004), aquifer thermal energy storage (ATES) (Bloemendal et al. 2014; Fleuchhaus et al. 2018) or fresh water storage in brackish aquifers with aquifer storage and recovery (ASR) (Pyne 2005; Maliva and Missimer 2010). To obtain the optimal well design and highest performance efficiency during well operation, detailed knowledge of the spatial three dimensional variability of hydraulic and transport properties of the aquifer is required to provide accurate numerical simulations and predictions of groundwater flow and transport behavior. For example, partially-penetrating wells (PPWs) in construction dewatering and groundwater remediation (Powers et al. 2007), as well as HT-ATES (e.g. Molz et al. 1983ab; Buscheck et al. 1983) and ASR systems (Maliva and Missimer 2010; Zuurbier et al. 2014), have to rely insight in on vertical variability in aquifer properties to obtain the optimal well performance during injection and abstraction.

Tracer tests are an efficient tool to provide useful information about the hydraulic properties (hydraulic conductivity, porosity and specific yield), as well as the solute properties (macrodispersivity and sorption) at a site relevant scale (Ptak et al. 2004). In practice, various types of tracers are used (Leibundgut et al. 2009). Conservative salt tracers such as chloride and bromide are widely applied and have proved their merit and reliability (e.g. Freyberg 1986; Jim Yeh et al. 1995; Ptak et al. 2004; Leibundgut et al. 2009; Zheng et al. 2011). However, execution of a proper conservative solute tracer test is generally expensive and time consuming (e.g. Ma et al. 2012). For example, multi-level groundwater sampling over depth in heterogeneous aquifers is required to track preferential flow paths in both the vertical and lateral extent. New methods have been introduced to overcome these limitations of conservative solute tracer testing by the use of electrical conductivity (EC) monitoring or electrical resistivity tomography (ERT) (e.g. Cassiani et al. 2006; Vienken et al. 2017). However, to obtain a detectable electrical conductivity signal the required concentration contrast between injection fluid and ambient groundwater needs to be sufficiently high. This might induce density-driven flow due to buoyancy differences between the injected tracer fluid and ambient groundwater (Barth et al. 2001), as well as it might have a significant impact on groundwater quality.

The use of heat as a tracer is a low-cost alternative to identify the hydraulic and transport characteristics of the aquifer and to track preferential flow paths (Anderson 2005). Combined hydraulic head and temperature data loggers are widely available and can be easily installed at monitoring screen depth, while recently the use of ERT or fiber

optic distributed temperature sensors (DTS) have proven to provide reliable spatial and temporal temperature monitoring in aquifers (e.g. Macfarlane et al. 2002; Tyler et al. 2009; Hermans et al. 2015; Robert et al. 2019). To date, various natural gradient (e.g. Engeler et al. 2011; Wagner et al. 2014) and forced gradient heat tracer tests in aquifers have been performed. Various in-situ forced gradient heat tracer tests are conducted at different transport scale lengths. This can be done by push-pull tests (e.g. Vandenbohede 2009; Klepikova et al. 2016a), dipole tests with groundwater abstraction from one well, and re-injection of heated water into another well (e.g. Macfarlane et al. 2002; Wildemeersch et al. 2014; Klepikova 2016b), and heat injection tests in aquifer (Ma et al. 2012; Seibert et al. 2014; Sarris et al. 2018). Moreover, heat injection tests combined with subsequent storage and/or recovery were done by Molz et al. 1983; Buscheck et al. 1983; Palmer et al. 1992; Molson et al. 1992; Vandenbohede 2011. Similar to solute tracer experiments, the temperature contrast between the heated tracer fluid and cooler ambient groundwater should be carefully assessed during heat tracer experiments to minimize viscosity and density effects (Ma et al. 2012).

For heat tracer tests, additional parameters (thermal dispersity, thermal diffusivity and heat capacity) are required for accurate groundwater flow and heat transport modeling. Similar to solute macrodispersion, thermal macrodispersiton is used for model calibration and describes the additional heat mixing processes during heat transport in the aquifer. However, during heat transport in aquifers, the mixing due to thermal diffusivity (thermal conduction through both soil and groundwater) is significantly higher than solute mixing by molecular diffusion. At low flow velocities mixing of heat becomes conduction dominated (e.g. Bloemendal and Hartog 2018). As a consequence, heat transport becomes insensitive to mechanical mixing and thermal dispersivities cannot be reliably estimated from heat tracer test data (Giambastiani et al. 2013). To date, controls on solute macrodispersion at field scale has been widely assessed in the literature (e.g. Dagan 1989; Gelhar et al. 1992; Ptak et al. 2004; Zech et al. 2015), while the magnitude of thermal macrodispersion is strongly debated in the literature (Bear 1988; Sauty et al. 1982; Hopmans et al. 2002; Anderson 2005; Vandenbohede et al. 2009; Ma et al. 2012).

Commonly, solute mixing described by solute macrodispersion at field scale is attributed to small scale heterogeneities in the aquifer (e.g. low-permeability clay/peat lenses or gravely zones of high permeability), which usually manifests in increasing macrodispersity values with increasing transport distances (Gelhar et al. 1992). Zech et al. (2015) showed that scaling of the solute macrodispersivity values is formation-specific, presumably asymptotic. Thus, modeling of transport cannot be related to one unique scaling law.

Besides local variability in aquifer heterogeneity, the numerically fitted macrodispersivity values might also be affected by other mixing processes. This can be mixing due to the the type of tracer method (e.a. natural gradient, divergent, di-pole or convergent flow test, see Gelhar et al. 1992) or the occurrence of density and viscosity contrasts during solute or heat transport (e.g. Welthy and Gelhar 1991). Selection of a proper tracer concentration is important to obtain the characteristics of the aquifer. Often, the selected tracer concentration for a solute tracer test or the temperature contrast for a heat tracer test is too high and density-driven or viscosity-dependent flow during the tracer experiment occurs. Hence, the reliability of the tracer experiment can be significantly reduced (Welthy and Gelhar 1991; Barth et al. 2001; Woumeni and Vauclin 2006). In such cases, besides aquifer heterogeneities, the determined macrodispersivities after model calibration also account for mixing processes due to density and viscosity contrasts between injection water and ambient ground water during the tracer test. Therefore, density-dependent and viscosity-dependent transport models have to be used for accurate numerical prediction of such tracer tests (e.g. Ma and Zheng 2010).

To our knowledge, no field experiment data exists on the mixing behavior in the near-well vicinity of PPWs under diverging flow conditions for both heat and solute transport. In practice, different hydraulic characteristics of gravel, or naturally-developed pack, well skin, as well as the occurrence of non-linear flow behavior during divergent and di-pole tracer experiments at relative high injection rates in aquifers with coarser granular material might impact the mixing behavior.

Therefore, in the present study, divergent flow heat tracer, as well as a solute tracer experiments on a PPW are conducted in a heterogeneous aquifer for multi-level aquifer characterization. The heat tracer test is conducted at a small temperature difference with ambient groundwater (ΔT<1.4 ºC) and therefore, a negligible density and viscosity contrast (maximum relative viscosity difference of only 3.9%) is ensured throughout the tracer test. Moreover, a conservative bromide ion tracer test is conducted with the recharge PPW at a solute density contrast of only 0.04%. Both tracer experiments are conducted to assess the differences between solute and heat transport in the aquifer at the field site. Prior to performing the solute and heat tracer tests, a detailed hydrogeological site investigation is conducted to identify aquifer heterogeneity. Multi-level breakthrough curves (BTCs) over aquifer depth are obtained by multi-level groundwater sampling to determine the bromide ion concentrations, while Distributed Temperature Sensing (DTS) with an optic-fiber cable is used for multi-level temperature monitoring. Solute and thermal macrodispersion is assessed numerically as a fitting parameter during model calibration for both tracer tests to account for near-well mixing due to small scale variability in heterogeneity.

6.2 Field site description

The experimental field site is shown in Fig. 6.1, which is located at the Utrecht Science Park in Utrecht (the Netherlands). The unconfined sandy aquifer of 50 meter thickness consists of unconsolidated Holocene and Pleistocene fluvial deposits (TNO-GDN 2019). Prior to planning and performing the tracer test, a thorough geological and hydrogeological site investigation was conducted in the upper 30 meters of the aquifer. A detailed three-dimensional characterization was executed using multiple measurement techniques: cone penetration tests (CPTs), hydraulic profiling tool (HPT) tests, borehole logging during drilling, undisturbed soil sampling with liners (see Appendix I2), as well as aquifer tests on multiple PPWs with a detailed multi-level head monitoring configuration system (see Appendix I1). In Fig. 6.2, the locations used for the three-dimensional hydrogeological characterization in the near-well vicinity of PPW-1 are shown.

The experimental field set-up consists of four different infiltration PPWs with ⌀0.110 m and a filter length of 2 meter. The location of the PPWs is shown in Fig. 6.2a and Appendix I. Aquifer tests using constant-injection rates, as well as step-injection rates were performed on four different PPWs to estimate the hydraulic properties at different depths and locations in the aquifer (see Appendix I1). The groundwater response during the aquifer tests was observed with the multi-level head monitoring wells screened in the vicinity of the PPWs (see Appendix I1). The injection water required for the aquifer tests on the PPWs, as well as for the heat and bromide ion tracer tests is pumped from abstraction deep-well DW with ⌀0.160 m screened from 7.3 to 17.3 mbsl (see Fig. 6.1).

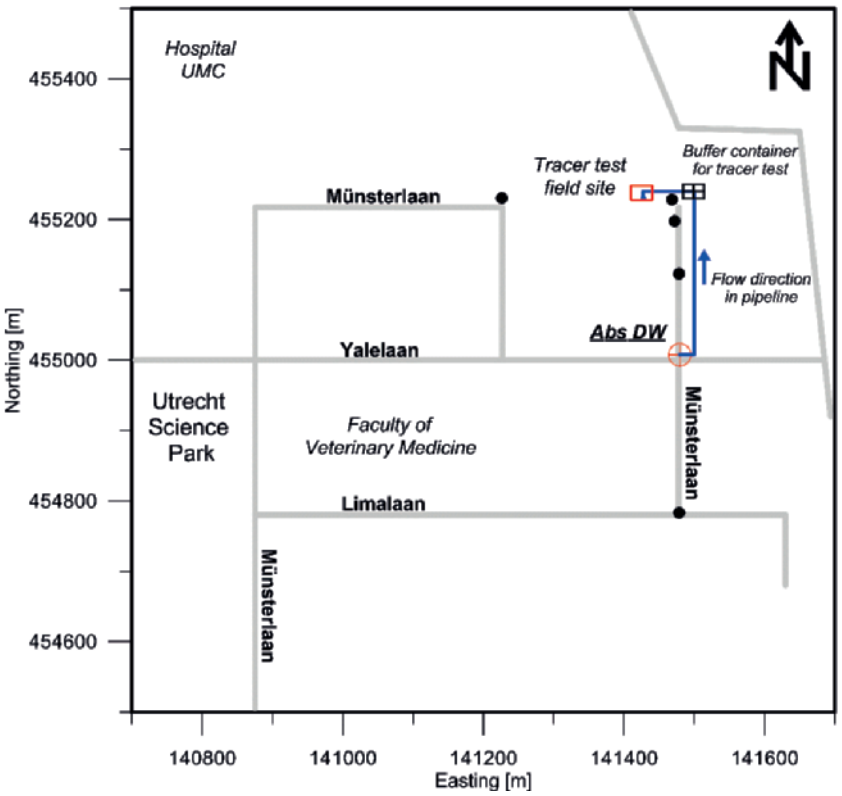

Fig. 6.1 Plan view of the tracer test field location at the Utrecht Science Park.

6.2.1 Hydrogeological site characterization

In total, 13 cone penetration tests (CPTs) were performed up to depths of 24-34 mbsl. Soil classification was done with the method of Robertson (1990). To obtain a detailed overview of the spatial variability in relative permeability over depth, five CPTs were performed in combination with the direct-push hydraulic profiling tool (HPT) technology (McCall et al. 2007; Dietrich et al. 2008; Köber et al. 2009). During CPT with the HPT technology, a small water volume is injected at a constant rate (Q) while the required injection pressure (P) is monitored. This is done while the cone with the HPT tool is penetrated at a constant rate into the soil. The ratio between the volumetric injection rate (Q) and injection pressure (P) provides the relative permeability (Q/P) over aquifer depth.

Undisturbed sediment cores were obtained by sampling with liners during cable tool drilling. This was done at 6 different locations. In the vicinity of PPW-1, a total of 16 undisturbed 0.4 m long core samples were taken with PVC liners (∅0.06 m) with core catchers to obtain a detailed vertical hydrogeological characterization. The samples were

prepared for grain size analysis, permeameter tests and thermal property analysis. The thermal conductivity of the oven-dried sand samples is in the range of 3.43-3.60 W/mK at sampling depths of 8.5, 12 and 14.5 mbsl.

A porosity value of 0.35 and the median grain size d_{50} as characteristic pore length are assumed in the Kozeny-Carman equation (see Eq. 2.3, Chapter 2) to obtain the hydraulic conductivity based on the grain size analysis K_{gr}. Moreover, permeameter test were performed on the soil samples. The hydraulic conductivities of the permeameter tests of BS1 ($5<K_{perm}<86$ m/d) are significantly lower than the hydraulic conductivities obtained from the aquifer tests on the PPWs and the estimated hydraulic conductivity based on the grain size analysis ($19<K_{gr}<227$ m/d, see Fig. 6.3b). Since, the undisturbed samples obtained with the liners cut the soil in the vertical direction the small scale vertical hydraulic conductivity instead of the horizontal hydraulic conductivity is actually obtained with the permeameter test. Sample heterogeneity due to the presence of small clay or silt lenses in an overall high-permeability sand liner sample could result in significant lower hydraulic conductivities (Vienken and Dietrich 2011). These effects are already smaller if an undisturbed sample is oven dried and sieved for grain size analysis, since such small heterogeneities are mixed with the bulk mass of the sand.

During cable tool drilling of the obs-5 borehole, disturbed soil samples were taken for grain size analysis by sieving (Fig. 6.3b). The estimated hydraulic conductivity of BS2 based on the grain size analysis compare with those of BS1 ($40<K_{gr}<149$ m/d).

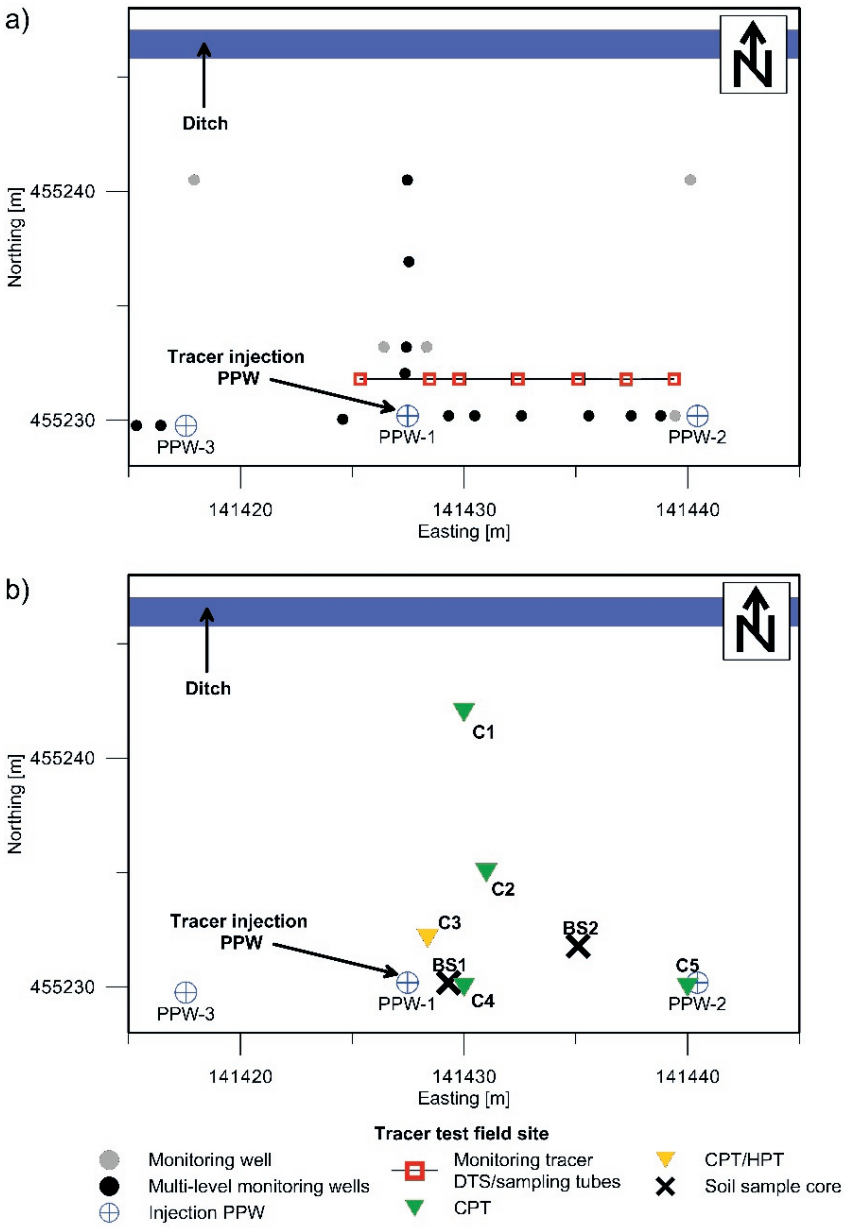

Fig. 6.2 Plan view of the tracer test site location for the **a)** artificial recharge PPWs, multi-level monitoring wells and tracer observation points, **b)** as well as the hydrogeological site investigate in the vicinity of PPW-1. Multi-level head monitoring was done during the tracer tests at the shown monitoring wells with both divers and manual measurements. The hydrogeological site investigation in the near-well vicinity of the injection PPW-1 is shown (C1-5 ad BS1-2).

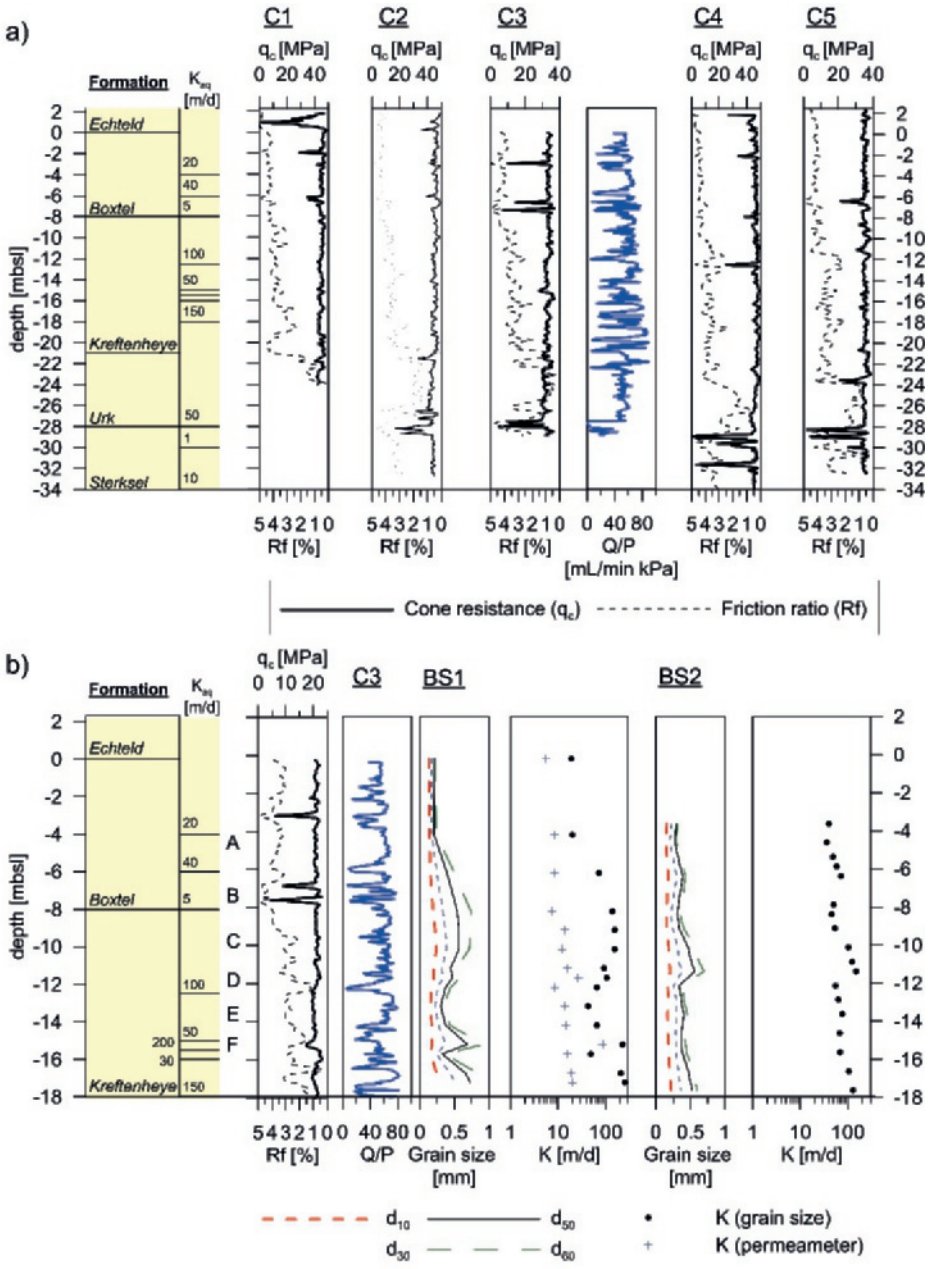

Fig. 6.3 a) Soil and hydrogeological site investigation of the cone penetration tests (C1-5), hydraulic profiling tool (C3) and **b)** the soil sampling (BS1-2) at the location indicated in Fig. 6.2b. The hydraulic conductivity K_{aq} is based on the aquifer tests on PPW1-4 and used for numerical simulation of the tracer tests. The tracer observation depths are indicated by A-F.

6.2.2 General geological and hydrogeology description

The Holocene top soil consists of silty fine sands with small clay and loam layers (Echteld Formation). The upper portion of the aquifer (0-8 mbsl) consists of Pleistocene deposits from the Boxtel formation (fine to medium sands), which lies on top of the Kreftenheye formation that consists of gravely very coarse sands (8-21 mbsl). Analysis of the liner soil samples provided porosity values ranging from 0.37 to 0.41 for the Kreftenheye formation. Based on the CPT data and the borehole logs, a sharp interface between the Boxtel and Kreftenheye formation exists (Fig. 6.3). The bottom of the Boxtel formation (8-10 mbsl) consists of a 1-2 meters thick low-permeability layer of silty fine sand with small clay and peat lenses (K_{aq}=5 m/d).

The Kreftenheye formation is stratigraphically underlain by the Urk formation that consists of varying units of medium to very coarse sand layers (21-28 mbsl). At the bottom, a low-permeability clay/peat layer is present at 28-30 mbgl (see C2-5 in Fig. 6.3a). The lower portion of the aquifer consists of fine to medium sand belonging to the Sterksel formation with a K_{aq} of approximately 10 m/d (TNO-GDN 2019). At 50 mbgl, the confining Waalre clay layer of 5 meter thick is the base of the unconfined sandy aquifer.

Based on the regional mapping of average groundwater levels at the Utrecht Science Park in 2013 an average hydraulic gradient of 2.25E-4 m/m is observed (Utrecht, Gemeente 2013; TNO-GDN, 2019). This results in a moderate southwest regional groundwater flow direction. However, head monitoring in the observation wells at the field site in the vicinity of the ditch shows that no hydraulic gradient is observed in the upper portion of the aquifer (<18 mbsl). Constant water level in the ditch, as well as hydraulic heads in the monitoring wells before and after the solute and heat tracer experiments are observed. Hence, no background flow was considered during the modelling of the tracer tests. The background hydraulic head at the field site was +0.95 m above sea level during the heat tracer test (5 April 2018). The background hydraulic head was lower during the bromide ion tracer test at 16 July 2018 with a value of +0.73 m above sea level.

6.3 Methods

6.3.1 Monitoring set-up for the tracer experiments

The tracer tests were performed with PPW-1 (⌀0.110 m) that is screened at 11.0 to 13.0 mbsl. In the vicinity of PPW-1, the hydraulic head is monitored at approximately 2, 7, 12 and 17 mbsl. Continuous head monitoring in the observation wells was done with pressure transducers (with the Schlumberger mini-diver DI501, Solinst Leveloger 3001, ElliTrack-D). Manual hydraulic head measurements were done to check the diver data. During injection on PPW-1, the volumetric flow rate was measured and logged continuously.

For solute and heat tracer monitoring, seven boreholes were drilled with a cable tool rig in the vicinity of PPW-1 (Fig. 6.3 and 6.4). PVC-filters of ⌀0.160 m were installed (obs-(1-7)) in the boreholes. The upper 5 meter of the PVC-filter was non-screened, while the perforated well screen of the lower 15 meters allowed for groundwater flow into and out the PVC-filter. Outside the PVC-filters obs-(1-7) of ⌀0.160, multilevel sampling at various depths was enabled by installation of six sampling mini-filters (⌀0.007 m of 1 meter length). To allow accurate monitoring of the BTC at the screened interval of the mini-filters, bentonite clay plugs were installed during borehole completion while the screened interval was completed with filter sand. The mini-filter depths indicated by capital letters *A-F* for obs-(1-7) are shown in Fig. 6.4. The use of these mini-filters allowed for pumping of only small amounts of groundwater volume by sampling of <4 L. This results in a minimum hydraulic impact during the tracer test to obtain reliable bromide BTCs. Hence, the pumping for groundwater sampling on the mini-filters is not simulated in the numerical model.

Distributed temperature sensing (DTS) with the optic-fiber cable was used to monitor the temperature BTCs over depth. DTS allowed for detailed and rapid profiling of temperature in the aquifer over space and time using fiber-optic cables and is a successful monitoring technique for heat tracer experiments (e.g. Tyler et al. 2009; Leaf et al. 2012; Hermans et al. 2015). To obtain the temporal temperature profile over depth, a fully-looped optic-fiber cable of 400 m length inside the PVC filters obs-(1-7) was installed with a small PVC tube (⌀0.063 m) (see Fig. 6.4). After installation of the PVC tubes with the fully-looped optic-fiber, the PVC filters of ⌀0.160 m were completed with filter sand and small bentonite clay plugs (0.2 m) for each meter depth in order to prevent the occurrence of preferential flow and advective heat transport inside the ⌀0.160 m PVC-filters of obs-(1-7). This enabled logging of an accurate temperature profile over depth over time with the DTS set-up. The shallow depth interval of the DTS signal for obs-(1-7) does not represent the aquifer temperature, since the upper portion of the well filters of ⌀0.160 m are non-screened. Below aquifer depths of 8 mbsl,

accurate groundwater temperature monitoring was provided with the DTS set-up. Hence, temperature BTCs are obtained over the depth interval 8 to 18 mbsl, where constant background groundwater temperatures were observed over time. The monitoring length interval in the optic-fiber cable was set to 1 meter, while the time interval was set to one hour. The observed temperature with the DTS set-up was calibrated with temperature logging with divers in the monitoring well. The DTS set-up allowed for a measurement accuracy of ΔT=0.1 ºC.

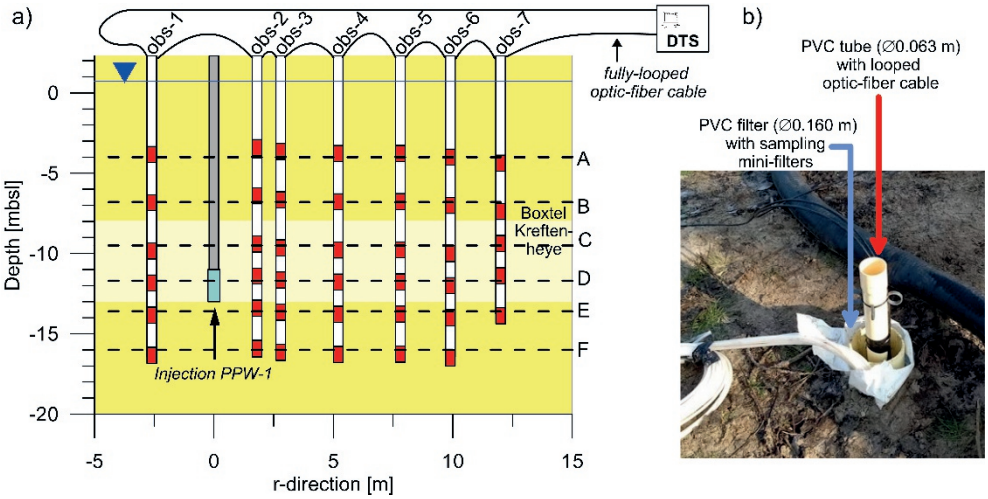

Fig. 6.4 a) Cross-section of the tracer test monitoring set-up with the screen depths of the mini-filters for multilevel groundwater sampling. See Fig. 6.3 for the exact location of the monitoring well location (obs-(1-7)) with respect to PPW-1. **b)** Picture of the PVC-tube (⌀0.063 m) with looped optic-fiber cable installed in the PVC filter (⌀0.160 m) with the attached 6 mini-filters as indicated in the cross-section view.

6.3.2 Bromide ion tracer test configuration

The bromide ion concentration tracer test started on 16 July 2018 at 11:00 in the morning, and was ended after 14 days of recharge on 30 July 2018 at 17:00. For the tracer test, groundwater from the abstraction deep well (see Abs. DW in Fig. 6.1) was discharged to a small 1 m^3 tank for artificial mixing with NaBr to obtain the desired bromide ion tracer concentration. Per 1 m^3 abstracted groundwater, 0.510 kg of NaBr was mixed in the container, before it was discharged to a second buffer tank. This enabled infiltration of approximately 400 mg/L bromide ion concentration at a constant injection rate of 3 m^3/h from the second buffer tank into PPW-1 for 8 hours (Fig. 6.5). The average background concentration of total dissolved solids (TDS) in groundwater over the elevation range of 9-18 mbsl is approximately 530 mg/L. The selected bromide concentration (addition of only 510 mg/L NaBr to the groundwater) results in a density

contrast between tracer solution and ambient contrast of only 0.04%. This prevents density-induced convection during the bromide ion tracer test and density effects can be neglected (e.g. Woumeni and Vauclin 2006).

After applying the bromide ion injection pulse in the injection well, abstracted groundwater with associated background solute concentration from the deep well (Abs. DW) was directly injected on PPW-1 at a constant injection rate of 3 m^3/h for 4 days. After 4 days, the volumetric recharge rate was increased up to 6 m^3/h (Fig. 6.5).

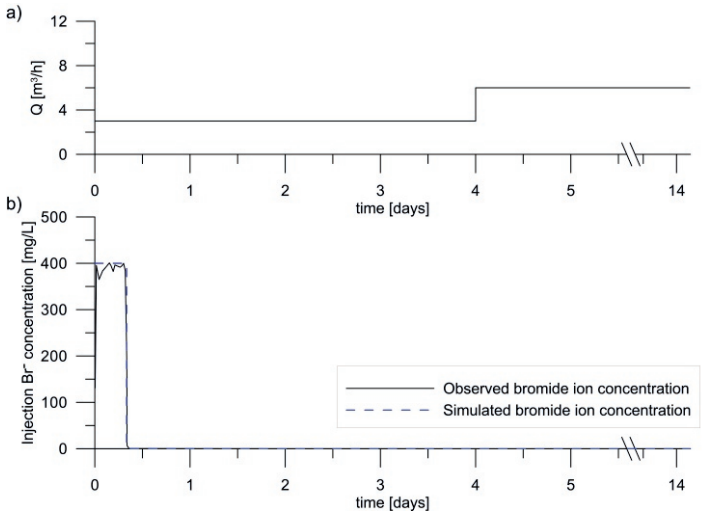

Fig. 6.5 a) Volumetric recharge rate at PPW-1 during the bromide ion tracer test. **b)** Observed and simulated bromide ion tracer pulse.

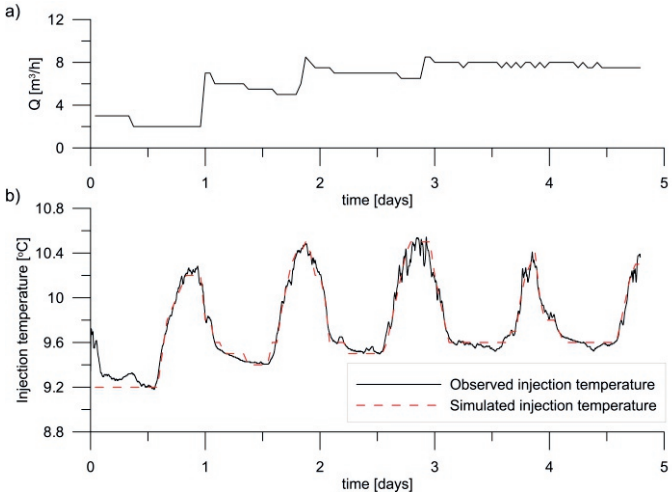

Fig. 6.6 a) Volumetric recharge rate *Q* at PPW-1 during the heat tracer test. **b)** Observed and simulated heat tracer pulses.

6.3.3 Heat tracer test configuration

The heat tracer test started on 5 April 2018 at 18:00 and was ended after 5 days of recharge at 10 April 2018 at 13:00. For the heat tracer test, groundwater was pumped from the abstraction deep well into a buffer storage container. Throughout the heat tracer test a volume of approximately 1.8 m^3 was stored in the buffer container. At daytime, the groundwater flowing through the pipelines and stored in the buffer container was heated solar radiation to maximum temperature increases of ΔT of 1.4 ^oC. This resulted in the five elevated temperature pulses as shown in Fig. 6.6. The recharged groundwater volumes in PPW-1 and the injection temperature over time are shown in Fig 6.6. Continuous temperature logging during injection in PPW-1 was done with a combined pressure transducer and thermometer using a Schlumberger mini-diver DI501.

The use of a small temperature gradient between the injection water and ambient groundwater (ΔT<1.4 ^oC) reduces the density and viscosity effects during the heat tracer test. Especially the groundwater viscosity is very sensitive to small temperature variations in the temperature range of 0-25 ^oC. The maximum relative viscosity difference is only 3.9% at the limited temperature contrast of ΔT<1.4 ^0C. Similarly to the bromide ion tracer test, the small temperature contrast between the heated water pulses and cooler ambient groundwater enabled efficient decoupled modelling of groundwater flow (with MODFLOW2000) and heat transport (with MT3DMS) (e.g. Ma and Zheng 2010; Sarris et al. 2018) in the present study. This increases the computational efficiency strongly.

During the heat tracer test, anoxic groundwater from the abstraction deep well was stored in the buffer container. As a consequence, the oxic conditions in the buffer container resulted in precipitation of iron-oxide and severe well-aging during the heat tracer test. This resulted in the observed decrease in volumetric recharge rate over time in PPW-1. The volumetric recharge rate was adjusted three time. First, to increase the volumetric recharge rate of 3 m^3/h to 6 m^3/h and in a later stage to overcome the decreasing volumetric flow rate in PPW due to well clogging.

6.3.4 Numerical modeling of solute and heat transport

Groundwater flow was modeled using the MODFLOW2000 code (Harabaugh et al. 2000). Solute transport of the bromide tracer, as well as the heat tracer, was done with the multi-species transport model MT3DMS (Zheng and Wang 1999). The differential equation for solute transport takes into account advection, dispersion, molecular diffusion and retardation:

$$\nabla[\theta(\alpha v + D_m)\nabla C] - \nabla[\theta v C] - q_s C_s = R\frac{\partial(\theta C)}{\partial t} \qquad (6.1)$$

where θ [-] is the porosity, v [m/s] is the pore water velocity, α [m] is the dispersivity tensor, D_m [m^2/s] is the molecular diffusion coefficient, q_s [s^{-1}] is the sink or source volumetric flow rate per volume unit aquifer, R [-] is the retardation factor that account for the local equilibrium sorption reaction.

The differential equation for heat transport is translated in terms of the solute transport equation (Eq. 6.1), to allow for describing heat transport in the MT3DMS code. The molecular diffusion coefficient can be used to describe conductive heat transport of the temperature species by a bulk thermal diffusivity D_T term:

$$\mathrm{D_T} = \frac{\lambda_f \theta + (1-\theta)\lambda_s}{\theta \rho c_{pf}} \tag{6.2}$$

where λ_f and λ_s [J/(d m ºC)] are respectively the thermal conductivity of water and solid phase, c_{pf} [J/(ºC kg)] is the specific heat of water and ρ [kg/m^3] is the water density. Moreover, thermal equilibrium between the water and solid phase during heat transport is represented by a thermal distribution factor:

$$\mathrm{K_{dT}} = \frac{c_{ps}}{\rho c_{pf}} \tag{6.3}$$

where c_{ps} [J/(ºC kg)] is the specific heat of solid phase. Therefore, the thermal retardation R_T can be described in the same manner as solute retardation:

$$R_T = 1 + \frac{\rho_b}{\theta} K_{dT} \quad where\ \rho_b = \rho_s(1-\theta) \tag{6.4}$$

6.3.5 Model description of the field site

A model domain of 300 m by 300 m was used for the 50 meter thick aquifer at the field site to simulate groundwater flow during infiltration at PPW-1. The model domain was discretized into 158 columns, 158 rows, and 72 layers. Lateral grid refinement (Δx, Δy = 0.1 m) was used in the vicinity of PPW (up to a lateral distance of 8 m) to allow for steep hydraulic, solute concentration and temperature gradients in this zone. Similarly, vertical grid refinement of Δz = 0.2 m is used for the strata between depths of 8 and 18 mbsl. With increasing distance from PPW-1, coarser grid sizes are used ranging from Δx and Δy values of 1 to 50 m.

The hydraulic, solute and heat properties listed in Table 6.1 are used, where only the macrodispersivity for both solute and heat transport is used for model calibration with parameter fitting for both tracer experiments. The hydrogeologic site investigation and

aquifer tests on the four PPWs are used to obtain the hydraulic conductivity K_{aq} of the different isotropic strata in the heterogeneous layered aquifer (Fig. 6.3). Numerical prediction of the three-dimensional head response during the aquifer tests combined with the data of the hydrogeological site investigation provided the hydraulic conductivities for the different geological strata in the aquifer (Fig. 6.3b). The hydraulic conductivity K_{aq} of the different strata in the heterogeneous layered aquifer is shown in Fig. 6.3. In the lateral extent, no variability in hydraulic conductivity is considered. PPW-1 is screened in the high-permeable upper portion of the Kreftenheye formation (K_{aq}=100 m/d).

Constant head is used for the outer model boundaries and the ditch located 17 meters northwards from PPW-1. This results in the background hydraulic head as observed in the field prior to the bromide ion tracer test, as well as the heat tracer test. The indicated volumetric recharge rates for the bromide ion concentration (Fig. 6.5), as well as the heat tracer experiment (Fig. 6.6) are used.

Aquifer properties	**Parameter values**
Porosity	$\theta = 0.38$
Dry bulk density	$\rho_b = 1720$ kg/m^3
Specific heat of the solid	$c_{ps} = 710$ J/kg °C
Thermal conductivity of solid	$\lambda_s = 3.5$ W/m °C
Thermal distribution coefficient*	$K_{dT} = 1.98 \cdot 10^{-4}$ m^3/kg
Thermal retardation factor*	$R_T = 1.90$
Bulk thermal diffusivity*	$D_T = 0.130$ m^2/day
Aquifer thickness	$H_a = 50$ m
Groundwater properties	
Specific heat of the fluid	$c_{pf} = 4186$ J/kg °C
Thermal conductivity of the fluid	$\lambda_l = 0.58$ W/m °C
Molecular diffusion	$D_m = 8.64 \cdot 10^{-5}$ m^2/day
Calibrated solute transport property	
Longitudinal dispersion	$\alpha_l = 0.03$ m
Transversal dispersion	$\alpha_t = 0.003$ m

Table 6.1 Hydraulic, solute and heat transport properties of the aquifer. The thermal distribution coefficient (K_{dT}), thermal retardation factor (R_T), bulk thermal diffusivity (D_T) are calculated for heat transport simulation in the MT3DMS code using Eq. 6.2-4.

6.4 Results

The results of the tracer tests are presented in two parts. First, the experimental data of the bromide ion tracer test and the numerical analysis for estimation of the transport characteristics of the aquifer are presented. Also the hydraulic characterization of the aquifer obtained from the aquifer tests and hydrogeological site investigation is validated with the BTCs of the bromide ion tracer test. Similarly, the experimental data of the heat tracer test and numerical analysis for the estimation of the transport characteristics are presented.

6.4.1 Bromide ion tracer test

The evolution of the observed bromide ion concentration BTCs at different depths in the aquifer is shown in Fig. 6.7. Peak breakthrough of bromide ion concentration in the lateral extent occurred after 0,34, 0.75, 2.1 and 5.3 days at radial distances of respectively 1.8 (obs-2), 2.8 (obs-3), 5.2 (obs-4) and 7.8 m (obs-5). After 4 days of injection at a recharge rate of 3 m^3/h, prolonged injection at an increased recharge rate of 6 m^3/h resulted in slight bromide ion concentration increase (11 mg/L) after 14 days at a radial distance of 9.9 m (obs-6).

Calibration with the solute macrodispersivity value α_l of 0.03 m results in accurate numerical prediction of the BTCs in the well vicinity at radial distances of respectively 1.8 m (obs-2(C-E)) and 2.8 m (obs-3(C-E)). Moreover, the porosity value of 0.38, as well as the hydraulic properties based on the hydrogeological site investigation resulted in accurate breakthrough prediction in the well screen vicinity. The numerical prediction of the bromide ion BTCs in the lower portion of the aquifer obs-2F and obs-3F is reasonable. Prediction of solute transport in the lower portion of the Kreftenheije formation at 15-20 mbsl is difficult due to the relative large vertical variability in soil characteristics (see Fig. 6.3). The heterogeneous layering derived from the aquifer test on PPW-4 (see Appendix I), as well as the grain size analysis and CPT/HPT data results in a reasonable prediction of BTCs at obs-2F and obs-3F.

At larger transport distances and associated lower pore flow velocities in the aquifer, the fit of the numerical BTCs with the field data is significantly poorer. For example, the numerically predicted breakthrough at injection level is delayed with 0.3 days compared to the measured breakthrough in the field at a radial distance of 5.2 m (obs-4(C-D)), while assuming the site hydrogeology (as described in Fig. 6.3b) and the average porosity value of 0.38. Moreover, less disperse breakthrough of bromide ion concentration is observed for the BTCs of obs-4(C-D) and obs-5(C-D) at a radial distances of respectively 5.2 and 7.8 m. This suggests that the required solute macrodispersivity value to fit the

observed BTCs is smaller with increasing transport distance and decreased flow velocities.

No bromide ion concentration breakthrough was observed in the upper mini-filter obs-2A at a depth of 4 mbsl (not shown in Fig. 6.7). At a depth of 7 mbsl (obs-2B), the bromide ion concentration starts to slightly increases after 1.5 days due to reduced transport velocity in the low-permeability layer with clay and peat lenses at a depth of 6-8 mbsl. The numerical breakthrough occurs at a later stage, suggesting a higher hydraulic conductivity for the stratum with clay and peat lenses.

At infiltration depth of 12 mbsl (level D), the BTCs obs-(3-5) show clear tailing. This was not observed in the sampling mini-filters screened above and below infiltration depth. The tailing might be explained by small scale heterogeneous layering at injection level and associated preferential solute transport in a small high-permeability layer, as well as delayed transport in the lower permeability layer in the lateral direction. This does not hold for the BTCs obtained above and below injection depth, since small scale heterogeneous layering does not result in tailing during vertical conservative solute transport.

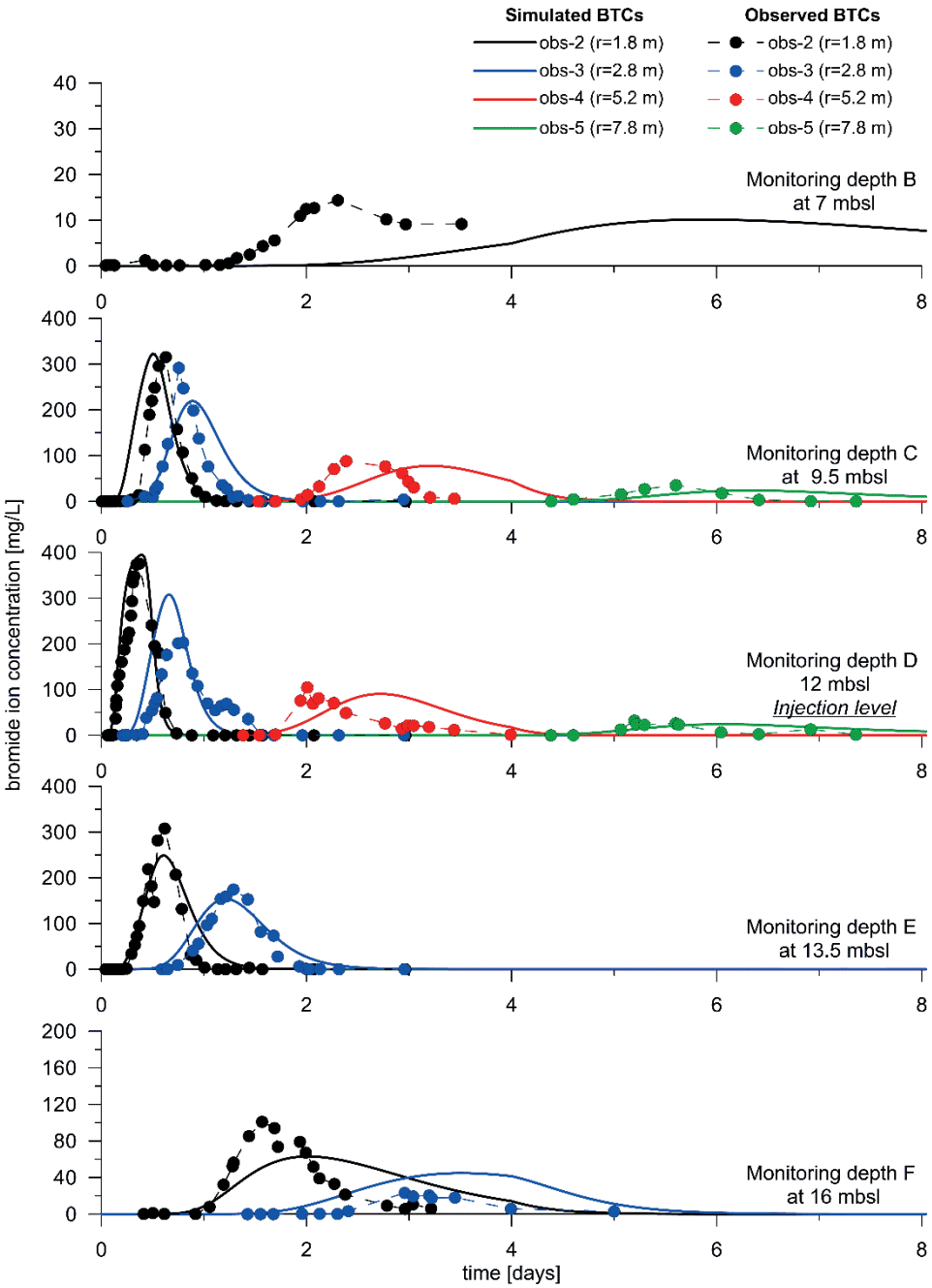

Fig. 6.7 Multi-level observed and simulated bromide ion concentration BTCs at obs-(2-5).

6.4.2 Heat tracer test

The observed multi-level thermal breakthroughs at obs-(1-4) at injection depth (12 mbsl) and at a depth of 10 and 15 mbsl are shown in Fig 6.8. The five different peaks of the injected heat pulses applied by the groundwater heating at daytime in the buffer container is clearly reflected in the BTCs in the near-well vicinity (see Fig. 6.8b, e-g, j).

The DTS-derived vertical temperature distribution over depth is shown in Fig. 6.9. A good fit between the observed and simulated data is obtained. In Fig. 6.9d, simulated breakthrough of the third high temperature pulse (T=10.4 ^{o}C) is determined at injection level (see Fig. 6.8e), while this is not the case for the observed temperature distribution in the field. Slight delay in thermal breakthrough resulted in a huge difference between simulated and observed temperatures (ΔT=0.4 ^{o}C) in the initial stage of heat pulse breakthrough.

Cross-section of the numerically calculated temperature distribution after 1, 2, 3 and 4 days are shown in Fig. 6.10. Fig 6.10d shows that after 4 days the first and second heat pulses are blended, while the third and fourth heat pulse are clearly visible.

At larger well distance from the well screen (distances higher than 3 m), the distinct daily heat pulses in the BTCs are hardly detected due to heat mixing by thermal conduction. The thermal energy of the injected heat tracer is stored in both the groundwater and aquifer material, depicted by the thermal diffusivity term used in the heat transport model (Eq. 6.2). At larger distance from the PPW, the pore flow velocity significantly decreases. As a consequence, heat transport by convective transport with transport distance is reduced while the relative importance of thermal conduction increases for this divergent flow heat tracer test at the PPW.

To compare the feasibility of heat tracers for aquifer characterization, similar hydraulic properties as for the solute transport model is used. The calculated thermal retardation of 1.9 was based on the aquifer porosity of 0.38 and resulted in good prediction of thermal breakthrough of the heat pulse in the well vicinity.

Fig. 6.8 shows that the use of a small thermal dispersivity value (α_l) similar to the solute macrodispersivity of 0.03 m results in less dispersed temperature breakthrough of the heat pulses compared the use of a the thermal macrodispersivity of 0.13 m. However, the sensitivity of thermal dispersivity value (α_l) is significantly lower than for the solute macrodispersivity. Good agreement between the numerical and experimental thermal BTCs in the vicinity of PPW-1 is obtained (see Fig. 6.8b, e-g, j).

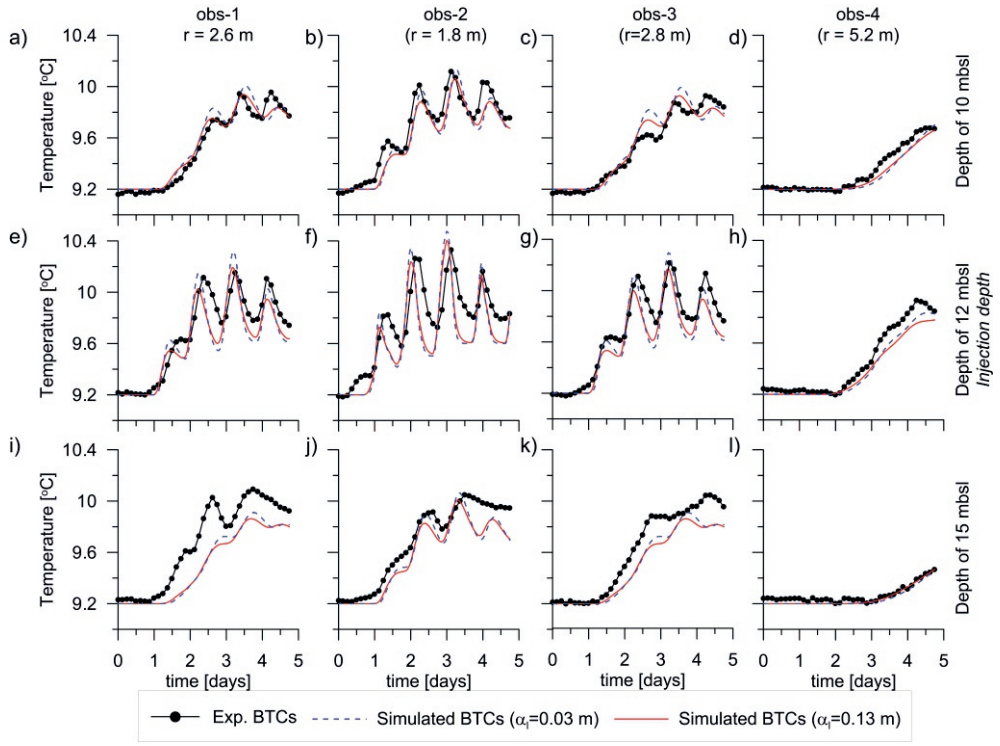

Fig. 6.8 The simulated and observed temperature BTCs at the locations obs-(1-4).

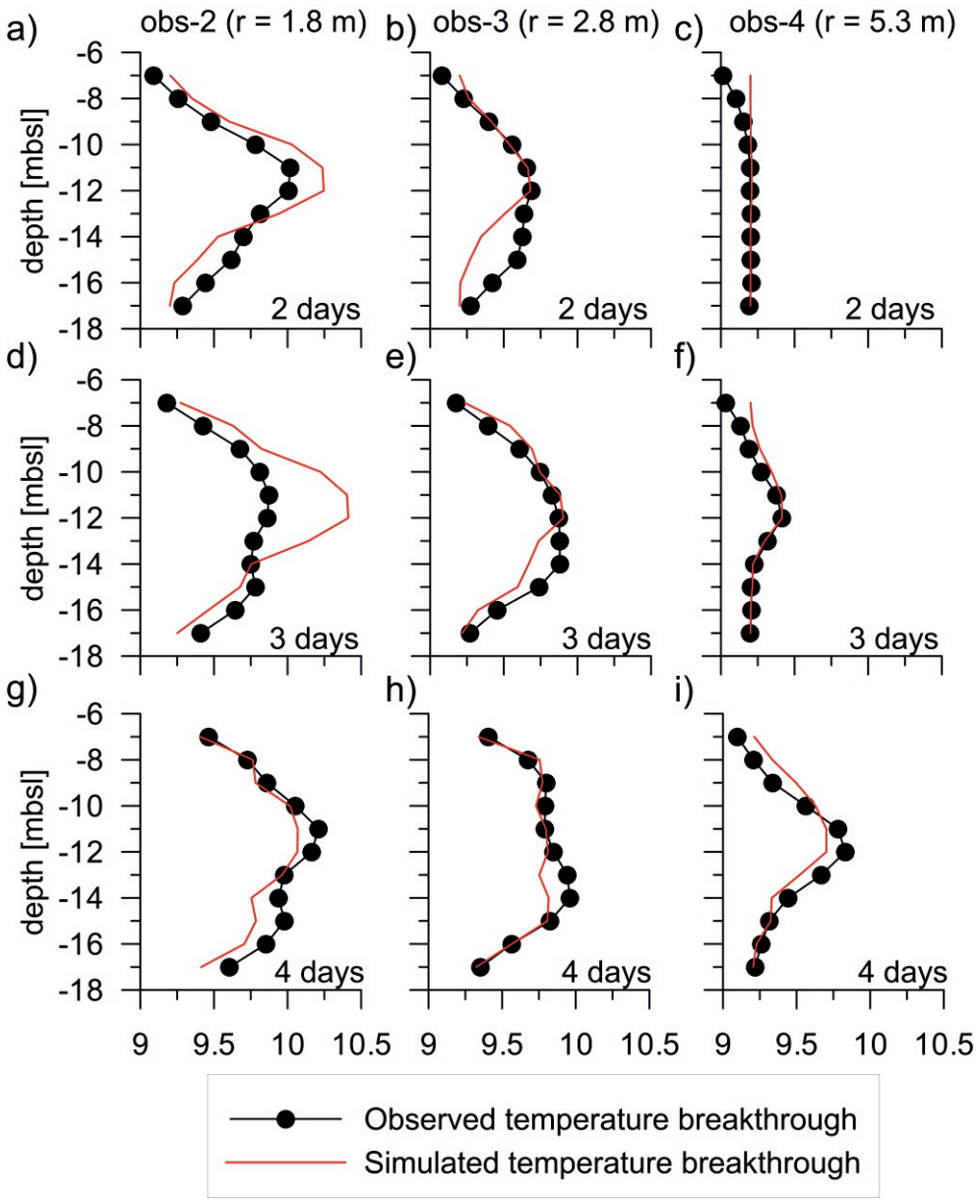

Fig. 6.9 Observed and simulated temperature profiles with the DTS set-up at obs-(2-4).

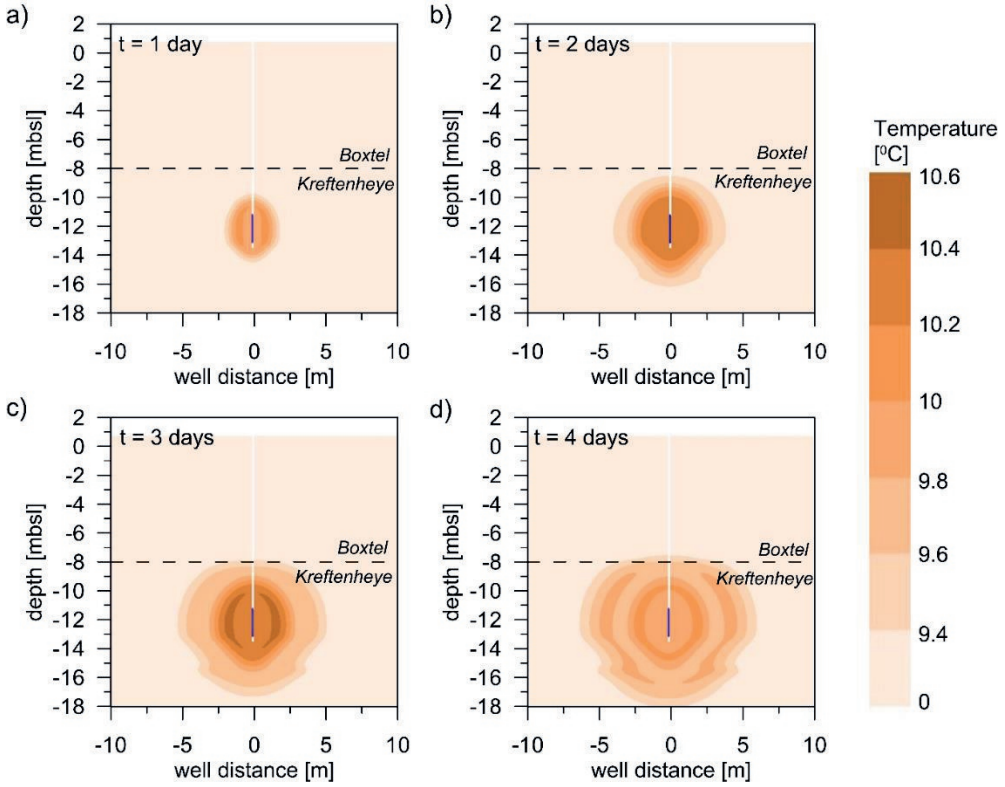

Fig. 6.10 Cross-section of the simulated temperature distribution for the conducted heat tracer test at PPW-1 after **a)** 1 day, **b)** 2 days, **c)** 3 days, **d)** 4 days. The boundary between the bottom of the Boxtel formation and Kreftenheye formation is indicated by the dashed line.

6.5 Discussion

6.5.1 Model calibration with macrodispersivity

The present study only includes the macrodispersivity as fitting parameter to account for small scale variabilities in aquifer heterogeneity. This resulted in a small longitudinal dispersivity value (α_l=0.03 m) that worked reasonably well over a minimum transport length of 1.8 m and a maximum transport length of 5.2 m. The transversal dispersivity was assumed to be a factor 0.1 lower than the longitudinal dispersivity and is assumed to be of negligible importance since the bromide ion contrasts mainly occur in the flow direction for the divergent flow conditions of the present tracer test.

The estimated longitudinal dispersivity for the given transport scale is in agreement with the literature (e.g. Gelhar et al. 1992; Zech et al. 2015). This dispersivity value enabled reasonable predictive modeling of lateral and vertical solute transport during injection in the aquifer with the PPW. No scaling of the solute macrodispersivity value with increasing solute transport distance is observed for this partially penetrating divergent flow solute tracer test. However, the observed BTCs at larger transport distances are slightly less disperse than the simulated BTCs.

One should take into account that the macrodispersivity at field scale is a fitting parameter to account for the additional mixing of unknown aquifer heterogeneity, as well as other near-well mixing processes. For a natural gradient tracer test the macrodispersivity is mainly an artificial fitting parameter to account for small scale heterogeneity, since not every aquifer heterogeneity can be included in the model. However, for convergent, divergent, di-pole push-pull tracer tests conducted in the near-well vicinity, unknown additional mixing could also be translated in the macrodispersivity term during model calibration. Under divergent flow conditions, the highest pore flow velocities occur in the vicinity of the well screen. For example, the tracer injection was performed on a PPW that obtains a naturally-developed pack with different hydraulic characteristics compared to the aquifer material. Prior to both the heat tracer test, as well as the bromide ion concentration test, air surging was used for well development of PPW-1. However, remaining clogging material in the well screen vicinity could have a major impact on the local hydraulic properties. Lack of knowledge about skin conductivity, the extent of the skin layer and the occurrence of non-linear flow behavior might result in additional mixing factors that can be translate in the macrodispersion term during model calibration.

6.5.2 Hydrodynamic thermal dispersion during the heat tracer test

Accurate modelling of the thermal BTC at injection depth in the near-well vicinity is done with a thermal macrodispersivity value of 0.13 m. However, still a slightly less disperse numerical thermal BTC than the observed thermal BTCs at obs-2 was obtained (Fig. 6.8e). This results in significant numerical underestimation of the lower injection temperatures in between the elevated temperatures of the heated water pulses compared to the observed temperatures with the DTS set-up (ΔT=0.2 °C). For the current heat tracer dataset, only the thermal macrodispersion was used for model calibration. Calibration at lower thermal macrodispersivity resulted in a larger discrepancy between observed and simulated breakthrough of the heat pulse peaks (T>10 °C) in the near-well vicinity. However, the sensitivity of the thermal macrodispersivity is significantly smaller than for the solute macrodispersivity. Fig. 6.8e-f showed that slightly less dispersed temperature breakthrough is predicted in the well vicinity using a thermal macrodispersivity value of 0.03 (equal to the solute macrodispersivity).

Mixing during heat transport is determined by the thermal hydrodynamic dispersivity ($\alpha_l v+D_T$). This value accounts for the overall heat mixing during transport by both the thermal diffusivity of the aquifer (D_T=1.3 m^2/d) and the thermal macrodispersivity (α_l=0.13 m) used for model calibration. In Fig. 6.11, the thermal hydrodynamic dispersion over radial distance at injection depth of PPW-1 is shown for a constant volumetric recharge rate of 7 m^3/h. The pore flow velocities rapidly decreases with radial distance, resulting in a significant reduction of the thermal macrodispersion term with increasing distance from the well screen.

With increasing heat transport distance, the thermal hydrodynamic dispersivity becomes mainly determined by the thermal diffusivity term D_T. Hence, at larger heat transport distance mixing is solely determined by thermal conduction (e.g. Bloemendal and Hartog 2018). However, within a radial distance of 1 m from the injection PPW, high pore flow velocities resulted in significant mixing due to macrodispersion. This explains the sensitivity of model calibration on the BTCs in the near well-vicinity with the thermal macrodispersivity value, while it has relative negligible effect on temperature breakthrough at larger transport distance.

In the literature, the magnitude of thermal dispersion is widely debated in the literature (e.g. Bear 1988; Sauty et al. 1982; Hopmans et al. 2002; Anderson 2005; Ingebritsen et al. 2006; Vandenbohede et al. 2011; Giambastiani et al. 2013). For example, Vandenbohede et al. (2011) concluded that thermal dispersion cannot be ignored in heat transport models, while other authors (e.g. Bear 1988; Hopmans et al. 2002; Ingebritsen et al. 2006) suggest that thermal dispersion can be considered negligible compared to thermal conduction. The present study show that the heat transport during the divergent flow tracer test on the PPW cannot be described by heat

mixing solely due to thermal convection. Additional mixing processes during the divergent flow conditions in the near-well vicinity of the PPW have to be considered by means of the fitting thermal macrodispersivity parameter to the BTCs.

The Peclet number (*Pe*) can be used to indicate the ratio between convective and hydrodynamic dispersive heat transport in the system. The Peclet number for heat transport can be defined as:

$$Pe = \frac{vl}{a_l v + D_t} \tag{6.5}$$

where l [m] is the characteristic length of the heat breakthrough in the system. Peclet numbers higher than 1 indicate a conduction dominated heat transport system. Rau et al. (2012) concluded that in homogeneous coarse sands, thermal dispersion terms can be neglected when the thermal Peclet number is less than 0.5. Their experimental laboratory results demonstrate that heat transport at a given range of pore flow velocities can reach a transition zone between conduction and convection at Peclet numbers ranging from 0.5 to 2.5. In the near-well vicinity, the calculated thermal Peclet numbers over radial distance at a volumetric recharge rate are in the range of this transition zone (Fig. 6.11b).

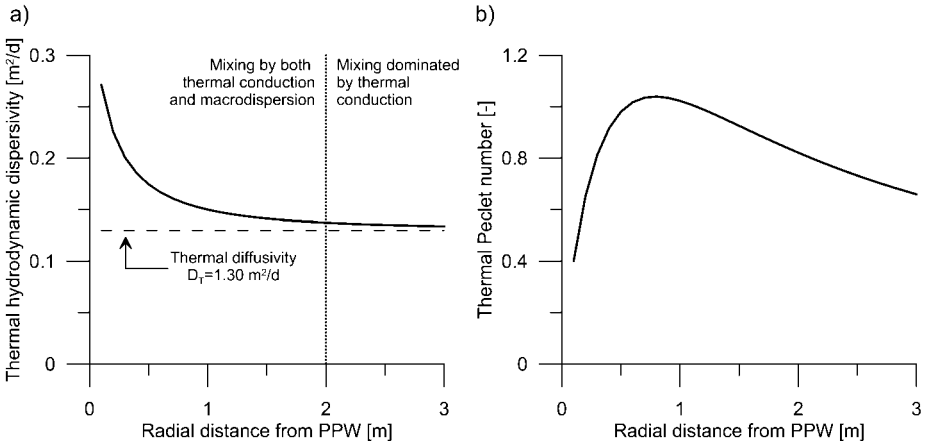

Fig. 6.11 a) Thermal hydrodynamic dispersivity ($\alpha_l v + D_T$) over radial distance from the PPW-1. The pore flow velocities are obtained at injection depth with a volumetric recharge rate Q of 7 m^3/d. **b)** The associated thermal Peclet number over transport distance.

6.6 Conclusions

Two different tracer tests are conducted at a partially penetrating recharge well under divergent flow conditions. A bromide ion concentration test was performed, using a injection pulse of tracer concentration of 8 hours. Multi-level ground water sampling at filter screened at different depths in the aquifer obtained a detailed vertical distribution of the bromide ion concentration test over time. Similarly, a heat tracer test at a small temperature contrast with ambient ground water (ΔT<1.4 ^{o}C) was performed on the PPW, while a fully-looped optic fiber cable with DTS system obtained a detailed spatial and temporal distribution of the temperatures in the aquifer. Prior to the tracer testing at the field, a thorough aquifer characterization was performed in order to obtain the properties of the different hydrogeological strata in the aquifer. The obtained hydraulic and transport characteristics from this hydrogeological characterization are used for numerical prediction of the observed multi-level BTCs at different depths in the aquifer.

The present study shows that the use of small temperature contrasts during heat tracer testing provide reliable hydraulic and transport properties of the aquifer. The small temperature contrast between heated water pulses and cooler ambient groundwater (ΔT=1.4 ºC) resulted in a negligible density and viscosity contrasts during a heat tracer test. This enabled efficient decoupled modelling of groundwater flow and accurate predictive modelling of the multi-level thermal BTCs.

In the well vicinity, model calibration showed that the disperse breakthrough of heat cannot be fully ascribed to thermal conduction. Heat mixing in the aquifer under divergent flow conditions during injection in a PPW occurs due to both thermal conduction and additional heat mixing translated into the thermal macrodispersivity by model calibration.

Acknowledgements

This work was supported by the foundations STW (Foundation for Technical Sciences) and O2DIT (Foundation for Research and Development of Sustainable Infiltration Techniques). The authors wish to thank dewatering companies Bouten Nederland, Theo van Velzen, and Henk van Tongeren for construction of the experimental fieldwork set-up and the soil investigation with CPTs. We wish to thank Fugro GeoServices for conducting the HPT tests and lab experiments on the soil samples. Moreover, we would like to thank Inventec for installation of the optic-fiber cables at the field site, and KWR Watercycle Research for providing their DTS-unit.

Chapter 7

The use of salinity contrast for density difference compensation to improve the thermal recovery efficiency in high-temperature aquifer thermal energy storage systems

Abstract

The efficiency of heat recovery in high-temperature (>60 °C) aquifer thermal energy storage (HT-ATES) systems is limited due to the buoyancy of the injected hot water. This study investigates the potential to improve the efficiency through compensation of the density difference by increased salinity of the injected hot water for a single injection-recovery well scheme. The proposed method was tested through numerical modeling with SEAWATv4, considering seasonal HT-ATES with four consecutive injection-storage-recovery cycles. Recovery efficiencies for the consecutive cycles were investigated for six cases with three simulated scenarios: a) regular HT-ATES, b) HT-ATES with density difference compensation using saline water, and c) theoretical regular HT-ATES without free thermal convection. For the reference case, in which 80 °C water was injected into a high-permeability aquifer, regular HT-ATES had an efficiency of 0.40 after four consecutive recovery cycles. The density difference compensation method resulted in an efficiency of 0.69, approximating the theoretical case (0.76). Sensitivity analysis showed that the net efficiency increase by using the density difference compensation method instead of regular HT-ATES is greater for higher aquifer hydraulic conductivity, larger temperature difference between injection water and ambient groundwater, smaller injection volume, and larger aquifer thickness. This means that density difference compensation allows the application of HT-ATES in thicker, more permeable aquifers and with larger temperatures than would be considered for regular HT-ATES systems.

Published as: Van Lopik, J.H., Hartog, N., & Zaadnoordijk, W.J. (2016). The use of salinity contrast for density difference compensation to improve the thermal recovery efficiency in high-temperature aquifer thermal energy storage systems. *Hydrogeology Journal, 24* (5), 1255-1271.

7.1 Introduction

The rising demand for sustainable energy sources and CO_2 emission reduction has led to intensified use of seasonal aquifer thermal energy storage (ATES) systems (Sanner et al. 2003). Thus far, ATES is mainly used for seasonal heating and cooling of buildings, where hot water is injected in the subsurface during summers and extracted during winters, and vice versa. Currently, the majority of ATES systems have limited temperature differences (ΔT<15 °C) between the ambient groundwater on the one hand, and the injected warm and cold water on the other hand. The number of high temperature aquifer thermal energy storage (HT-ATES) systems is still limited, although the storage of water with higher temperatures (e.g. >70°C) increases both the energy storage capacity and overall energy efficiency (e.g. Kabus and Seibt 2000; Sanner et al. 2005; Réveillère et al. 2013). A huge amount of waste heat is produced world-wide in a wide range of industrial processes, such as from incinerator and electricity plants (Meyer and Todd 1973). Therefore, HT-ATES systems can play a critical role in buffering the temporal mismatch between (continuous) heat supply and (seasonal) demand.

To date, most of the technical challenges induced by the high temperatures that hampered the early growth in the number of HT-ATES systems have now been resolved, such as appropriate water treatment and material selection to prevent the occurrence of mineral scaling and corrosion (Sanner et al. 2003). However, the economic feasibility of HT-ATES systems is largely determined by the thermal recovery efficiency, and relative low thermal recoveries up to values of only 0.42 were obtained during HT-ATES field experiments conducted in both confined and unconfined sandy aquifers (e.g. Mathey 1977; Palmer et al. 1992; Molz et al. 1979; 1983ab).

Besides heat loss due to thermal conduction to colder surrounding formations (e.g. Doughty et al. 1982), free thermal convection during HT-ATES negatively impacts thermal energy recovery (e.g. Buscheck et al. 1983; Molz et al. 1983a). The temperature difference between hot injection water and cold ambient groundwater results in a net buoyancy difference. Therefore, buoyancy forces cause upward flow of hot injection water which results in tilting of the initially vertical hot water front (Fig. 7.1a-b). Also, the viscosity of water at elevated temperatures is lowered, resulting in enhanced free thermal convection (Hellström et al. 1979). Field experiments (e.g. Molz et al. 1983a) show that HT-ATES in high-permeability aquifers at high temperature contrasts between injected water (81 °C) and ambient groundwater (20 °C) result in significant free thermal convection and hence a low thermal recovery (0.45).

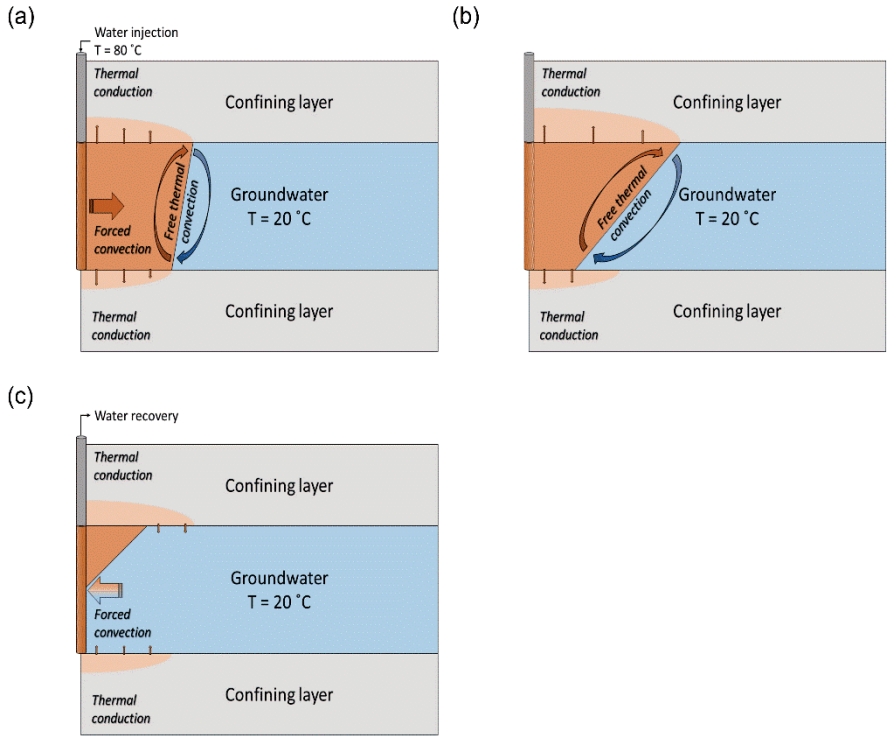

Fig. 7.1 Schematic overview of a full HT-ATES recovery cycle in a confined aquifer for **a)** injection, **b)** storage and **c)** extraction periods. Heat loss occurs by thermal conduction and free thermal convection.

The use of lower storage temperatures and the selection of low-permeability target aquifers are currently seen as the main design options for HT-ATES systems to reduce heat losses due to density-driven flow (e.g. Doughty et al.1982; Schout et al. 2014). However, besides limiting the range of suitable aquifers and the use of lower, energetically less attractive, storage temperatures, the selection of low-permeability aquifers negatively impacts the hydraulic capacity of a HT-ATES system, and therefore the heat storage capacity. Moreover, the selection of low-permeability aquifers increases the risk of well clogging by particles (e.g. Olsthoorn 1982ab). Therefore, the work reported here studies the possibility of minimizing free thermal convection in HT-ATES systems by using saline water for heat storage to compensate for the density difference with the ambient, cooler and less saline groundwater. Potentially, this would significantly increase recovery efficiencies and enable the use of higher permeability aquifers and higher injection temperatures for HT-ATES systems. This study explored the potential of this approach with numerical density-dependent flow simulations of a) regular HT-ATES systems, b) HT-ATES systems with density difference compensation

using saline water, and c) theoretical regular HT-ATES cases that consider no free thermal convection by neglecting density differences due to the temperature contrast between hot injection water and cold ambient groundwater. The latter scenario provided an upper bound for the improvement obtainable with density difference compensation. Firstly, a sensitivity analysis was performed by simulating multiple seasonal HT-ATES recovery cycles at various aquifer and environmental conditions. Secondly, the density difference compensation method was simulated for an actual HT-ATES system, a pilot in a highly permeable aquifer (Molz et al. 1983a; Buscheck et al. 1983).

7.2 Methods

7.2.1 SEAWAT

To simulate water, heat and solute transport during the HT-ATES recovery cycles, SEAWATv4 was used (Langevin et al. 2008; Guo and Langevin 2002). This code is a coupled version of the groundwater flow simulation program MODFLOW2000 (Harbaugh et al. 2000) and the multi-species mass transport simulation program MT3DMS (Zheng and Wang 1999), which enables simulation of variable-density groundwater flow. To allow for heat transport, the differential equations for solute transport in SEAWATv4 were translated in terms of heat transport following the approach described by Langevin et al. (2008).

Equations of state for density and viscosity were used to describe both fluid density and viscosity as a function of temperature and salt concentration. Fluid viscosity as a function of temperature and salt concentration is described by the following equation (Voss 1984):

$$\mu(C_s, T) = 2.394 \cdot 10^{-5} \cdot (10^{\frac{248.37}{T+133.15}}) + 1.923 \cdot 10^{-6}(C_s) \qquad (7.1)$$

where μ [kg/(m day)] is the dynamic fluid viscosity, T [°C] is the temperature of the water and C_s [kg/m^3] is the solute concentration of the water.

A non-linear density equation of state derived by Sharqawy et al. (2010) was used in the SEAWAT code as described by Van Lopik et al. (2015) to accurately simulate the temperature-density relation over large temperature ranges. This density relationship based on experimentally derived datasets for both salt concentration and temperature at 1 atm pressure from Isdale and Morris (1972) and Millero and Poisson (1981) is shown in Fig. 7.2.

$$\rho(T,S) = (999.9 + 2.034 \cdot 10^{-2}T - 6.162 \cdot 10^{-3}T^2 + 2.261 \cdot 10^{-5}T^3 - 4.657 \cdot 10^{-8}T^4) + (802.0S - 2.001\frac{S}{1000}\,T + 1.677 \cdot 10^{-2}\frac{S}{1000}\,T^2 - 3.060 \cdot 10^{-5}\frac{S}{1000}\,T^3 - 1.613 \cdot 10^{-5}(\frac{S}{1000})^2\,T^2 \quad (7.2)$$

where ρ [kg/m^3] is the fluid density and S [g/kg] is the salinity of the water.

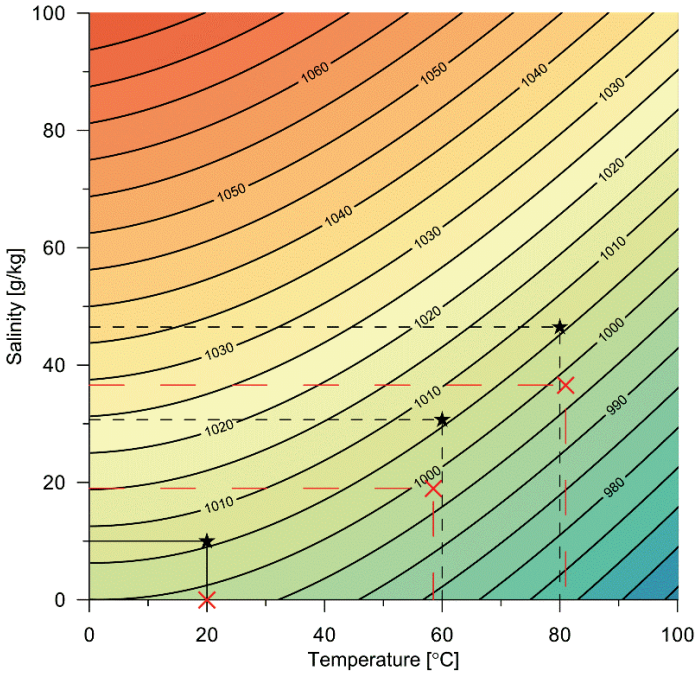

Fig. 7.2 Water density as a function of temperature and salinity (Sharqawy et al. 2010, Eq. 7.2). *Solid lines* represent equal water densities (isopycnals). The *black stars* show the required salinity for HT-ATES water injection at temperatures of 60 and 80 °C into brackish groundwater with a temperature of 20 °C [brackish = 10 g/kg]. The *red crosses* are for water injection at temperatures of 58.5 and 81 °C into fresh groundwater with a temperature of 20 °C.

7.2.2 Model set-up

The modeling in the present study is done in two parts. Firstly, a sensitivity analysis is performed by simulation of seasonal HT-ATES with four consecutive recovery cycles (see section '*Generalized HT-ATES cases used for the sensitivity analysis*', below). Secondly, the density difference compensation method was tested for an actual HT-ATES field pilot of two recovery cycles in a high-permeability aquifer conducted by Molz et al. 1983a (see section '*Pilot study at the Auburn University*', below). For both

the sensitivity analysis on seasonal HT-ATES and the numerical simulation of the field pilot, a confined sandy aquifer was considered to simulate HT-ATES recovery cycles at the various temperature and salt-concentration contrasts between injected water and ambient groundwater. Groundwater flow and associated heat and salt transport were simulated axi-symmetrically, following the approach introduced by Langevin (2008). This approach has been validated for transport of solute (Wallis et al. 2013) and heat (Vandenbohede et al. 2014). Although the displacement of heat and solutes by regional groundwater flow cannot be considered with the axi-symmetric approach, the regional groundwater flow is generally low in deep brackish aquifers targeted for HT-ATES systems (e.g. Sauty et al. 1982). Hence, neglecting heat and solute loss by regional groundwater flow during HT-ATES is considered a reasonable assumption.

The axi-symmetric model domain has a radius of 500 m with an aquifer thickness of 21 m. The overlying and underlying aquitards are 10 and 9 m thick. The grid resolution is Δr = 0.5 m by Δz = 0.5 m. Constant head, temperature and concentration boundaries were used for the outer, upper and lower boundaries of the model domain, following Buscheck et al. (1983). The inner boundary is impermeable inside the aquitards and simulates the well inside the aquifer. The well used for both injection and extraction has a radius of 0.1 m. The groundwater flow is solved using the Preconditioned Conjugate Gradient 2 (PCG2) package. The modified method of characteristics (MMOC) is applied as an advection package with a Courant number 0.2. In order to simulate heat conduction accurately, the convergence criterion of relative temperature is set to 10^{-10} °C (Vandenbohede et al. 2014).

Generalized HT-ATES cases used for the sensitivity analysis

The aquifer characteristics used for the simulation of seasonal HT-ATES are based on the aquifer used for the Auburn University (USA) field experiment conducted by Molz et al. (1983a). A homogeneous anisotropic aquifer has been used for the sensitivity analysis instead of the heterogeneous layering described by Buscheck et al. (1983). The aquifer characteristics for this base of the sensitivity analysis (Case 1) are listed in Table 7.1. The ambient groundwater in the sensitivity analysis has a brackish salinity of 10,000 ppm (C_s = 10 kg/m^3).

Aquifer properties	Parameter values
Specific storage	$S_s = 6 \cdot 10^{-4}$ m^{-1}
Porosity	$\theta = 0.25$
Dry bulk density	$\rho_b = 1950$ kg/m^3
Specific heat of the solid	$c_{ps} = 696.15$ J/kg °C
Thermal conductivity of aquifer	$\lambda_s = 2.29$ W/m °C
Thermal distribution coefficient*	$K_{dT} = 1.66 \cdot 10^{-4}$ m^3/kg
Thermal retardation factor*	$R_T = 2.29$
Bulk thermal diffusivity*	$D_T = 0.189$ m^2/day
Overall horizontal hydraulic conductivity	$k_h = 53.4$ m/day
Overall vertical hydraulic conductivity	$k_v = 7.7$ m/day
Aquifer thickness	$H_a = 21$ m
Aquitard properties	
Specific storage	$S_s = 9 \cdot 10^{-2}$ m^{-1}
Porosity	$\theta = 0.35$
Dry bulk density	$\rho_b = 1690$ kg/m^3
Specific heat of the solid	$c_{ps} = 696.15$ J/kg °C
Thermal conductivity	$\lambda_s = 2.56$ W/m °C
Thermal distribution coefficient*	$K_{dT} = 1.66 \cdot 10^{-4}$ m^3/kg
Bulk thermal diffusivity*	$D_T = 0.151$ m^2/day
Horizontal hydraulic conductivity	$k_h = 53.4 \cdot 10^{-5}$ m/day
Vertical hydraulic conductivity	$k_v = 7.7 \cdot 10^{-5}$ m/day
Groundwater properties	
Specific heat of the fluid	$c_{pf} = 4186$ J/kg °C
Thermal conductivity of the fluid	$\lambda_l = 0.58$ W/m °C
Solute transport properties	
Longitudinal dispersion	$\alpha_l = 0.5$ m
Transversal dispersion	$\alpha_t = 0.05$ m
Molecular diffusion	$D_m = 8.64 \cdot 10^{-5}$ m^2/day

Table 7.1 Aquifer and aquitard properties of the Auburn University field experiment (Molz et al. 1983a). *The thermal distribution coefficient (K_{dT}), thermal retardation factor (R_T), bulk thermal diffusivity (D_T) are calculated for SEAWATv4 heat transport simulation (see Langevin et al. 2008).

A seasonal HT-ATES system was assumed, with injection, storage, extraction and rest periods each of 90 days. Four consecutive cycles were simulated to investigate how the thermal recovery efficiency develops with time. An equal injection and extraction volume of 56,700 m^3 and an injection temperature of 80 °C were assumed for each cycle in the *reference scenario* (*Case 1*, Table 7.2). Three types of *simulations (named a, b and c*) were conducted for all cases in the sensitivity analysis: regular HT-ATES (e.g. Case 1.a for the reference scenario), HT-ATES with density difference compensation

using saline water (e.g. Case 1.b for the reference scenario), and a theoretical regular HT-ATES case that considers no free thermal convection and hence only heat loss by thermal conduction (e.g. Case 1.c for the reference scenario). In the latter simulation (c), density-driven flow was not considered (no free thermal convection) as an upper bound for the improvement that can be obtained with density difference compensation. In the additional five cases with each three types of simulations, the sensitivity of the modeling results was investigated by varying HT-ATES conditions and aquifer characteristics (Table 7.2).

	k_h [m/day]	k_v [m/day]	T_{in} [°C]	H_a [m]	V_{in} [m^3]
Case 1	53.4	7.7	80	21	56,700
Case 2	15*	1.5*	80	21	56,700
Case 3	53.4	7.7	60*	21	56,700
Case 4	53.4	7.7	80	10*	56,700
Case 5	53.4	7.7	80	21	28,350*
Case 6	53.4	7.7	80	21	113,400*

Table 7.2 Summary of the input parameters used for the sensitivity analysis. Values with an asterisk (*) indicate a variation on the reference scenario (Case 1).

Pilot study at the Auburn University

The simulation (Buscheck et al. 1983) and experimental results (Molz et al. 1983a) of the HT-ATES field experiment conducted at the Auburn University were used to test the potential of density difference compensation with respect to the regular HT-ATES operated in this specific field experiment. The main aspects from Buscheck et al. (1983) and Molz et al. (1983a) are summarized here.

Two injection-storage-recovery cycles (injection temperatures of 58.5 and 81°C) were conducted in a highly permeable sandy confined aquifer. The first cycle was of 3 months duration, while the second cycle had a duration of 7.3 months. The determined average production and injection volume rates and injection temperatures over time as presented by Buscheck et al. (1983) were used in the simulations of this study (Table 7.3). The characteristics of the aquifer and the confining layers used for the numerical modeling of this field experiment are listed in Table 7.1. A three-layered heterogeneous aquifer was considered with a 2.5-fold higher hydraulic conductivity for the middle layer than for the upper and lower layers (Table 7.4) in order to predict the two recovery cycles numerically (Buscheck et al. 1983). The ambient groundwater temperature is 20 °C and contains only 280 ppm or 0.28 kg/m^3 of total dissolved solids (Molz et al. 1983b). Due to low recovery temperatures of extracted water during the second recovery cycle, the well configuration was changed. The original fully penetrating well screen was replaced

by a partially penetrating well screen after two weeks of extraction to increase thermal energy recovery, resulting in a recovery efficiency of 0.45 (Molz et al. 1983a). Molz et al. (1983a) estimated a thermal energy recovery efficiency of 0.40 without the partially penetrating well screen modification. Buscheck et al. (1983) simulated the second recovery cycle for a fully penetrating well screen. The same procedure is followed in the numerical simulation with SEAWATv4.

Phase	Length [days]	Volumetric flow rate [m^3/day]	Injection temperature [°C]
Cycle-1			
Injection	20	760	60
	7	1100	58
	4	600	52
Storage	32	-	-
Extraction	2	-1684.8	-
	21	-1054.1	-
Rest	26	-	-
Cycle-2			
Injection	8	954	85
	24	-	-
	7	600	82
	4	-	-
Storage	85	545	80
	34	-	-
Extraction	14	-1088.6	-
	2	-	-
	39	-1088.6	-

Table 7.3 Injection and extraction flow rates, as well as injection temperatures during the first and second cycle of the Auburn University field pilot (Buscheck et al. 1983). These values are used for the numerical simulation in this study.

Hydraulic conductivity	Value
Horizontal hydraulic conductivity	
Upper layer (10 m thick)	k_h = 38.2 m/day
Middle layer (5 m thick)	k_h = 96.4 m/day
Lower layer (6 m thick)	k_h = 38.2 m/day
Vertical to horizontal hydraulic conductivity ratio	1:7

Table 7.4 Hydraulic conductivity of the heterogeneous aquifer at Auburn University, according to Buscheck et al. (1983).

7.2.3 Density difference compensation using saline water for heat storage

The required salinity for the density difference compensation was calculated for the heat injection temperature based on the non-linear density equation (Eq. 7.2) as illustrated in Fig. 7.2. Salt mass transport was modeled conservatively and adsorption or precipitation reactions were not incorporated in the numerical simulations.

In the sensitivity analysis for various HT-ATES conditions (see section 7.2.2 '*Generalized HT-ATES cases used for the sensitivity analysis*'), a brackish salinity of 10,000 ppm (10 kg/m^3) was selected for the ambient groundwater, as environmental considerations typically preclude the use of HT-ATES in fresh groundwater aquifers. The salt concentration required to establish the same water density as ambient groundwater (T=20 °C and C_s=10 kg/m^3) for hot injection water at temperatures of 60 and 80 °C is shown in Fig. 7.2. The required salt concentrations are 30.7 and 46.5 kg/m^3, respectively.

For the HT-ATES pilot study at Auburn University (see section 7.2.2 '*Pilot study at the Auburn University*'), the density difference between hot injection water and ambient groundwater was calculated for both cycles with injection temperatures of 58.5 and 81°C, respectively. Consequently, the required salt concentration to overcome buoyancy difference between injected water and ambient groundwater was 19 kg/m^3 for cycle-1. For cycle-2, a salt concentration of 36.6 kg/m^3 was required (Fig. 7.2).

7.2.4 Metrics to quantify salt and heat recovery

Critical in the operation of HT-ATES systems is how much of the injected heat can be recovered following storage, expressed as thermal recovery efficiency. The thermal recovery efficiency (ε_H) is defined as the ratio between the total injected heat (Q_{in}) and the total recovered heat after extraction (Q_{ex}). The total injected and recovered heat is calculated from the temperatures of injected and extracted water:

$$\varepsilon_H = \frac{Q_{ex}}{Q_{in}} = \frac{\sum(V_{ex}\ \rho_{ex}(T,S)\ c_{pf}\ (T_{ex}-T_a))}{\sum(V_{in}\ \rho_{in}(T,S) c_{pf}\ (T_{in}-T_a))} \tag{7.3}$$

where $V_{ex/in}$ [m^3] are the volumes per time step of the extracted water and the injected water, $T_{ex/in}$ [°C] are the temperatures of the extracted water and the injected water, T_a [°C] the ambient groundwater temperature, c_{pf} [J/(kg °C)] the specific heat of water and $\rho_{in/ex}$ (T,S) [kg/m^3] the densities of the extracted water and the injected water as a function of salt concentration and temperature (Eq. 7.2). In the sensitivity analysis (Cases 1-6), summation is done over the output time steps for salinity and temperature (Δt=5 days) to calculate Q_{in} and Q_{ex}. For the Auburn University HT-ATES field experiment, smaller output time steps of 1 day are used.

For density difference compensation, the recovery of salt mass (ε_S) is an important variable in this study. The salt mass recovery efficiency is defined as the ratio between the total injected salt mass (M_{Sin}) and the total recovered salt mass after extraction (M_{Sex}):

$$\varepsilon_S = \frac{M_{sex}}{M_{sin}} = \frac{\sum(V_{ex}\ (C_{sex}-C_{sa}))}{\sum(V_{in}\ (C_{sin}-C_{sa}))} \tag{7.4}$$

where $C_{S,ex/in}$ [kg/m^3] are the salt concentrations in each time step of the extracted water and the injected water and $C_{S,a}$ [kg/m^3] is the ambient groundwater concentration.

Spreading of hot and saline water

In the sensitivity analysis, theoretical optimal HT-ATES cases that considered only heat loss by thermal conduction (e.g. Case 1.c) are run and compared to density difference compensation (e.g. Case 1.b). Considering an optimal case with no heat loss, the shape of the stored hot water in the aquifer will be cylindrical. Therefore, the dimensions of the hot water volume can be described in terms of the maximum radial extent of the injected hot water (r_{th}) and a given aquifer thickness (H_a).

Equilibration of heat between the solid and water phase occurs during heat transport in the aquifer. Therefore, the temperature front progresses at a lower rate into the aquifer than the effective flow velocity during hot water injection. The thermal radius of the hot injection water (r_{th}) is defined by the cylinder formed by retarded advective transport only:

$$r_{th} = \sqrt{\frac{V_{in}}{\pi\, H_a\, \theta\, R_T}} \tag{7.5}$$

where θ [-] is the porosity, H_a [m] is confined aquifer thickness and R_T [-] is the thermal retardation factor:

$$R_T = 1 + \frac{\rho_b}{\theta}\frac{c_{ps}}{\rho_f c_{pf}} \tag{7.6}$$

where ρ_b [kg/m^3] is the dry bulk density and c_{ps} [J/(kg °C)] is the specific heat of the solid.

Similar to the thermal radius, a solute radius (r_s) can be defined considering conservative advective solute transport and neglecting molecular diffusion and dispersion:

$$r_s = \sqrt{\frac{V_{in}}{\pi\, H_a \theta}} \tag{7.7}$$

7.3 Results

The results of this study are presented in two parts. First, the sensitivity analysis are presented in which various seasonal HT-ATES cases have been simulated for three scenarios: a) a regular setup, b) a setup with density difference compensation using saline water, and c) a setup under the theoretical condition of no free thermal convection. Secondly, the results of the SEAWATv4 modelling of the two recovery cycles of the Auburn University field experiment performed with and without density difference compensation are presented.

7.3.1 Sensitivity analysis

Several cases were simulated to test the potential of density difference compensation for HT-ATES and its sensitivity for various conditions (see section 7.2.2 '*Generalized HT-ATES cases used for the sensitivity analysis*'). Four parameters were varied with respect to the reference scenario (Case 1, Table 7.2): a lower aquifer hydraulic conductivity (Case 2), a lower injection temperature (Case 3), a smaller aquifer thickness (Case 4), and a smaller and larger injection volume (Cases 5 and 6).

Reference scenario (Case 1)

In Case 1, a seasonal HT-ATES system with injection temperatures of 80 °C is simulated both with and without density difference compensation. Without density difference compensation, the results showed strong free thermal convection during injection and storage for regular HT-ATES (Case 1.a, Fig. 7.3). Consequently, unheated ambient groundwater is recovered at the lower part of the well screen and overall recovered water temperatures over time ranged between 49.6 and 33.5 °C for cycle-1 (Fig. 7.4). The thermal recovery is low, ranging from 0.31 to 0.40 for the four recovery cycles (Fig. 7.5). Initially, the increase in thermal recovery efficiency is large ($\Delta\varepsilon_H$=0.051), but for the subsequent cycles the increase in recovery efficiency gradually decreases to an $\Delta\varepsilon_H$ increase of only 0.015 from cycle-3 to cycle-4. The buoyancy of the injected hot water decreases for each consecutive recovery cycle, which results in less pronounced thermal convection. Also the heat loss by thermal conduction decreases due to a lower temperature difference between injection water and ambient groundwater.

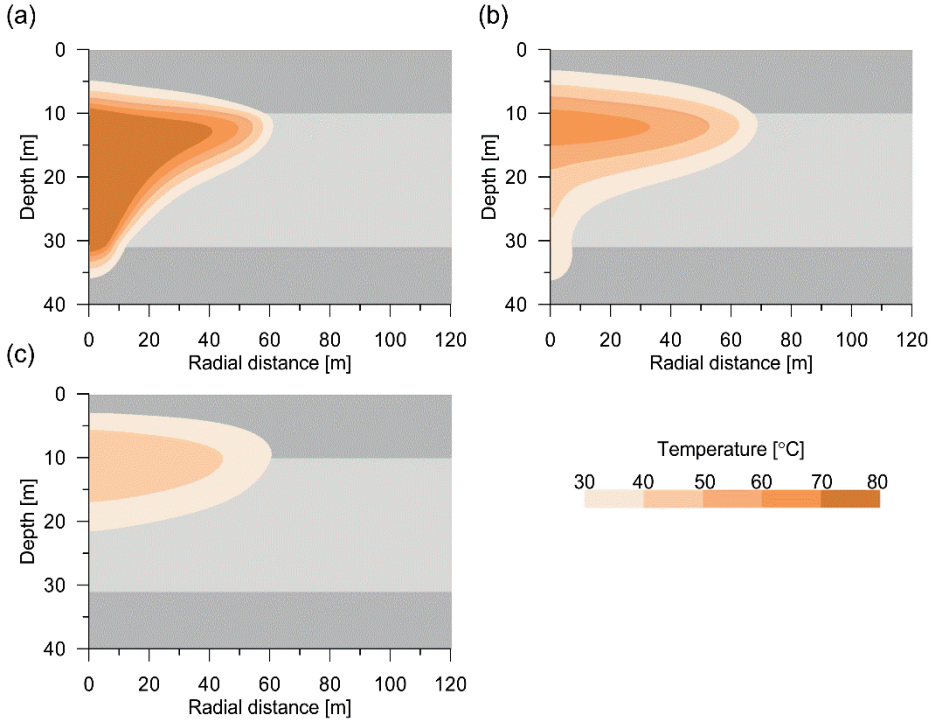

Fig. 7.3 Temperature distribution for the reference scenario of regular HT-ATES without density difference compensation (Case 1.a): **a)** at the end of the injection period, **b)** at the end of the storage period and **c)** at the end of the extraction period.

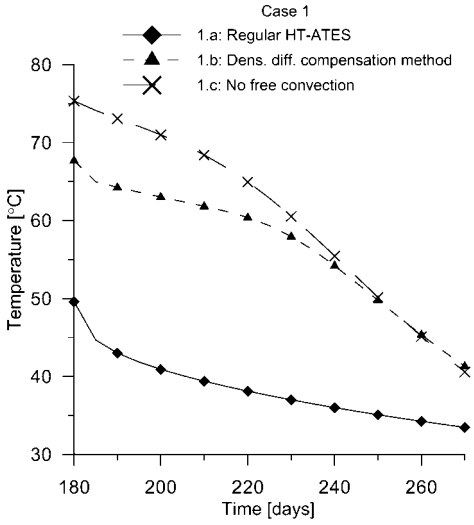

Fig. 7.4 Production temperatures over time for the first recovery period of Case 1.

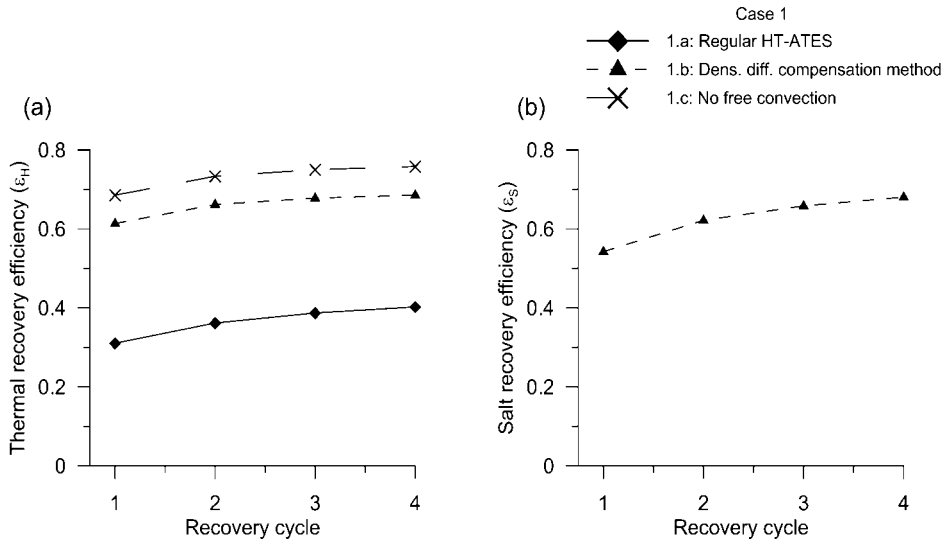

Fig. 7.5 Calculated **a)** thermal and **b)** salt mass recovery efficiency per cycle for the reference Case 1.

For the scenario with density difference compensation (Case 1.b), the required salt concentration to reduce the density contrast between the hot injection water and the ambient groundwater is 46.5 kg/m^3 (Fig. 7.2). This means that a total salt mass of $2.07 \cdot 10^6$ kg was injected for each recovery cycle. The results show that free thermal convection during injection and storage was successfully countered (Fig. 7.6). A large increase in thermal recovery ($\Delta\varepsilon_H$=0.29) was obtained with respect to the regular HT-ATES (Case 1.a) for each recovery cycle (Fig. 7.5). Moreover, the recovery temperatures over time were significantly better preserved with respect to the injection temperature (Fig. 7.4). The production temperature slightly decreases during the first 50 days of extraction when the stabilized hot water volume is recovered. This resulted in increased recovery temperatures up to 20 °C with respect to the regular HT-ATES (Case 1.a). After 50 days a rapid decline in production temperature is observed during recovery. In this period, hot water was recovered which was largely affected by the radial heat loss due to thermal conduction into the aquifer in the preliminary injection and storage stages, as was by the similar temperature decline when modeling the scenario without accounting for free thermal convection (Case 1.c). Thus besides reducing the heat loss due to free thermal convection, applying density difference compensation also reduced the heat loss by thermal conduction in comparison to the regular HT-ATES. This is due to the more compact, cylindrical hot water volume in the aquifer that is maintained when applying density difference compensation, which resulted in a smaller total contact area of both the colder surrounding aquifer and colder confining layers where heat is lost by thermal

conduction (Fig. 7.6). The difference in thermal recovery between density difference compensation (Case 1.b) and the theoretical case with no free thermal convection (Case 1.c) is small ($\Delta\varepsilon_H$=0.07). This means that for Case 1.b the main heat loss occurs by thermal conduction. However, as reflected by the initially lower recovery temperatures compared to the scenario that ignores free thermal convection (Case 1.c) for the first 50 days of extraction (Fig. 7.4), a small fraction of heat loss still occurs by a different mechanism. This is due to the fact that in the density difference compensated HT-ATES system free convection is determined by the density contrasts resulting from both the salt concentration and temperature differences in the aquifer. The thermal retardation (Eq. 7.6) affects heat transport, resulting in faster advective solute transport than heat transport during injection operations (e.g. Miotliński and Dillon 2015; Seibert et al. 2014). Therefore, plume separation of hot water (see Eq. 7.5) and saline water (see Eq. 7.7) occurs during HT-ATES with density difference compensation (Case 1.b). This results in a cold saline water plume in front of the hot water volume. Oldenburg and Pruess (1999) showed that plume separation of saline and hot water highly affects convective flow patterns if the salt concentration and the temperature contrasts are large. For HT-ATES with density difference compensation (Case 1.b), the injected salt concentration of 46.5 kg/m^3 creates a strong density contrast at ambient temperature with the ambient groundwater concentration (C_s=10 kg/m^3) of approximately 28 kg/m^3 (1034 kg/m^3 vs. 1006 kg/m^3, Fig. 7.2). Hence, a downward buoyancy force is exerted on the cooled salt water front resulting in downward transport (Fig. 7.6d-e). Due to downward density-driven flow of cold salt water, the hot water volume at the bottom of the aquifer is displaced towards the well screen. Therefore, cold saline water was recovered at the lower part of the well screen (Fig 7.6b), resulting in lower recovery efficiencies than the theoretical optimal case when not considering free thermal convection (Case 1.c). In the last stage of the extraction period (after 260 days) the recovered temperature is slightly higher for Case 1.b than for Case 1.c (Fig. 7.4). The displacement of the cold saline water towards the well screen resulted in lateral transport of heated water away from the well screen in the upper part of the aquifer. Consequently, the heated water volume in the upper part of the well screen has moved further from the well than in the no free thermal convection scenario (Case 1.c). In the final stage of extraction this displaced heated water volume at the top of the aquifer is recovered, resulting in slightly higher recovery temperatures for the density difference compensation method.

In addition to the thermal recovery, the salt recovery was determined for the density difference compensation method, at 0.54 for the first cycle after which it increases to a value of 0.68 in the fourth cycle (Fig. 7.5b). This resulted in an unrecovered salt mass of $1.21 \cdot 10^6$ and $8.42 \cdot 10^5$ kg, respectively. Salt mass accumulates at the bottom of the aquifer after each extraction period. Only a small amount of salt water is accumulated in

the upper clay layer due to molecular diffusion during the injection and storage phase (Fig. 7.6f). For the first cycle, salt water (C_s>12 kg/m^3) is transported up to a radial distance of 124 m along the bottom of the aquifer, while this is 201 m for cycle-4.

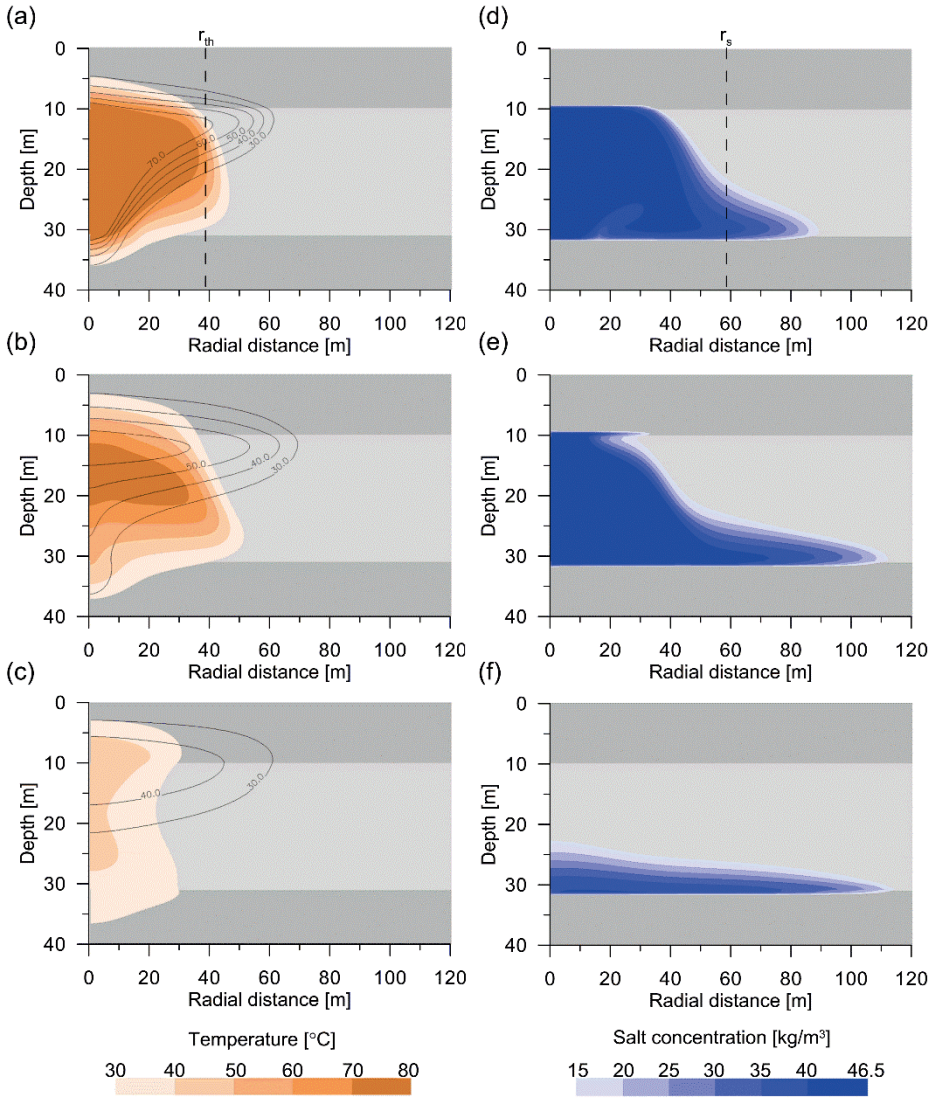

Fig. 7.6 Temperature distribution for the reference case with density difference compensation (Case 1.b) at the end of **a)** the injection period, **b)** of the storage period, and **c)** of the extraction period. *Black contour lines* indicate the temperature distribution for the regular reference Case 1.a. The same is done for the salt concentration distribution at the end of **d)** the injection period, **e)** of the storage period, and **f)** of the extraction period.

Hydraulic conductivity of the aquifer (Case 2)

Currently, low-permeability aquifers are selected for HT-ATES systems to reduce free thermal convection and to obtain sufficiently high thermal recovery efficiencies (e.g. Doughty et al. 1982; Schout et al. 2014). For Case 2, an aquifer with a horizontal and vertical hydraulic conductivity of 15 and 1.5 m/day, respectively, was considered to account for such aquifers characteristics (instead of 53.4 and 7.7 m/day for Case 1). The thermal recovery efficiencies for the regular HT-ATES (Case 2.a) are elevated compared to the reference scenario (Case 1.a) with values of 0.58 and 0.64, for the first cycle and fourth cycle (Fig. 7.7a), respectively. Although the effect was less, density difference compensation (Case 2.b) still improved thermal recovery efficiency ($\Delta\varepsilon_H$) with 0.10 compared to regular HT-ATES (Case 2.a). The recovered temperature declines substantially during extraction (Fig. 7.8). The downward salt-water transport between the solute and thermal front causes less displacement of the hot water towards the well screen due to decreased flow velocities. Therefore, the difference in thermal recovery ($\Delta\varepsilon_H$) between density difference compensation (Case 2.b) and the optimal case with no free thermal convection (Case 2.c) is only 0.02 for cycle-4 (Fig. 7.7a). Despite the significantly lower permeability, the efficiency of regular HT-ATES (Case 2.a) was lower than for the density difference compensation in the high-permeability reference scenario (Case 1.b).

Salt mass recovery efficiency is much higher for Case 2.b, compared to the reference scenario, Case 1.b (Fig. 7.7b). Downward density-driven flow of cold salt water is restricted due to decreased hydraulic conductivity of the aquifer. Consequently, the accumulation rate of salt mass at the bottom of the aquifer is low compared to Case 1.b.

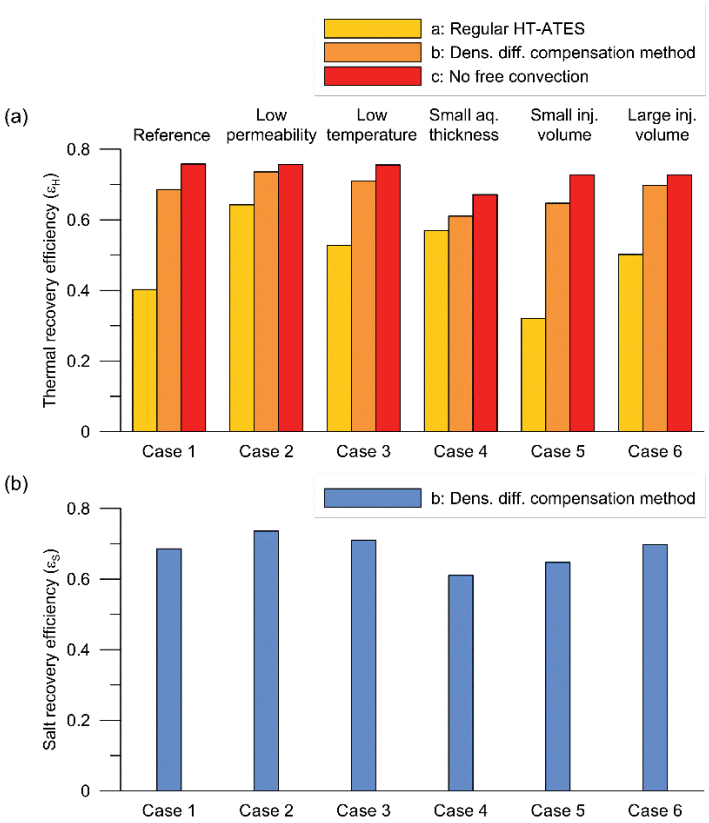

Fig. 7.7 a) Calculated thermal and **b)** salt recovery efficiency of cycle-4 for all cases.

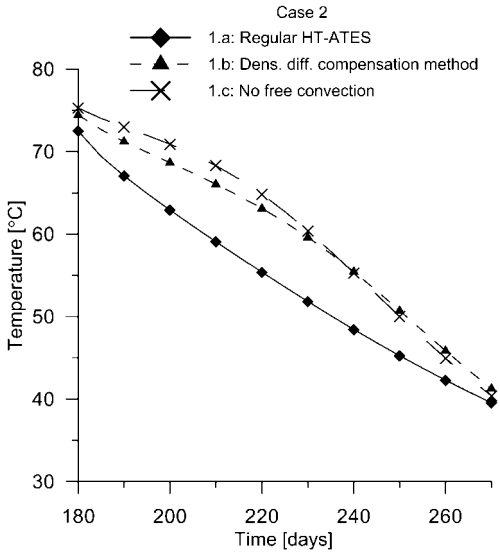

Fig. 7.8 Production temperatures over time of cycle-1 for Case 2.

Injection temperature (Case 3)

An injection temperature of 60 °C was considered for Case 3, to test the effect of a lower temperature difference between hot injection water and ambient groundwater (Table 7.2). For regular HT-ATES, a higher thermal recovery efficiency was achieved with a lower injection temperature (Case 3.a; T_i=60 °C) than for the reference scenario (Case 1.a; T_i=80 °C), due to less pronounced free thermal convection. For the theoretical cases where no free thermal convection was considered (Case 1.c and Case 3.c), the calculated thermal recovery efficiency was 0.76 for both. This independence of recovery efficiency on the injection temperature is due to the linear increase of both heat loss by thermal conduction and the total injected heat (Q_{in}), with the resulting temperature contrast between hot injection water and the cold surrounding aquifer and aquitards.

For the density difference compensation scenario, a salt concentration of 30.7 kg/m^3 (Fig. 7.2) was required to overcome the buoyancy difference between hot injection water and ambient groundwater. The HT-ATES scenario with density difference compensation (Case 3.b), resulted in a net recovery efficiency increase ($\Delta\varepsilon_H$) of 0.18, with respect to regular HT-ATES (Case 3.a). The recovery efficiency was close to the theoretical case with no free thermal convection (Case 3.c) with a $\Delta\varepsilon_H$ value of only 0.05 (Fig. 7.7a). This is caused by the less-pronounced downward salt water transport for this scenario than in the reference scenario (Case 1.b), due to the lower salt concentration contrast with the ambient groundwater. Consequently, the induced hot water displacement towards the well screen is less pronounced. In addition, the calculated salt recovery efficiency is higher for Case 3.b than for the reference scenario (Case 1.b), since the accumulation rate of salt at the bottom of the aquifer is lowered (Fig. 7.7b).

Aquifer thickness and injection volume (Cases 4-6)

The sensitivity of the recovery efficiency for regular HT-ATES and with density difference compensation was tested for different injection volumes and aquifer thickness (Table 7.2). This was done simulating a two times smaller aquifer thickness (Case 4), as well as a two times smaller (Case 5) and a two times larger injection volume (Case 6) with respect to the reference (Case 1).

For the regular HT-ATES Cases 4.a and 6.a, the recovery efficiencies are higher and the maximum radii of heated volume are larger (r_{th}, Table 7.5). The contrary is observed for the case with the smaller volume (Case 5.a) which has the smallest r_{th} value. For regular HT-ATES in a high-permeability aquifer, heat loss is mainly determined by free thermal convection. Consequently, thermal front tilting close to the well screen (e.g. Case 5.a) resulted in recovery of large amounts of cool ambient groundwater at the lower part of the well screen during the extraction stage. Therefore, the largest increase in

thermal recovery efficiency with density difference compensation is obtained for the scenarios with a small r_{th} value, resulting in a $\Delta\varepsilon_H$ value of 0.28 for Case 1.b (compared to 1.a) and 0.33 for Case 5.b (compared to 5.a), respectively. A smaller aquifer thickness (Case 4.b) results in an increase of only 0.04, while for a higher injection volume (Case 6.b) this is 0.20 (Fig. 7.7a).

The differences in thermal recovery between density difference compensation and the theoretical scenario without free thermal convection are small, with $\Delta\varepsilon_H$ ranging from 0.06 to 0.08 for Cases 1 and 4-6 (Fig. 7.7a). The hot water volume is not completely stabilized with density difference compensation, since hot water is displaced towards the well screen due to downward transport of the cold salt water behind the solute front. However, this effect on thermal recovery is small and heat loss is mainly due to thermal conduction. Table 7.5 shows that the highest energy recovery is obtained for Case 6.c, where the ratio between the outside area and thermal volume in the aquifer is lowest (0.13 m^{-1}). A smaller injection volume (Case 5.c) results in a larger ratio of 0.17 m^{-1} and a lower recovery efficiency. For small injection volumes, the overall surface area will be relatively large compared to the thermal volume. Therefore, the heat losses due to thermal conduction will be high.

The relative conductive heat loss to the surroundings with respect to the total amount of stored heat is highest for Cases 4.b-c, with an area volume ratio of 0.24 m^{-1}. Hence, the lowest thermal recovery (0.61) was obtained with the density difference compensation method (Case 4.b) compared to all other scenarios.

Salt mass recovery efficiency is smallest for the scenarios with the cold salt water front close to the well screen (e.g. Case 5.b; Table 7.5 and Fig. 7.7b). Although the injection volume in Case 5.b is only half of the reference scenario (Case 1.b), salt water (C_s>12 kg/m^3) is already transported up to a radial distance of 105 m along the bottom of the aquifer for Case 5.b for the first cycle, while this is 124 m for Case 1.b. This means that the relative salt displacement away from the well screen is larger for cases with a cold salt water front closer to the well screen. For scenarios with a larger radius of injected salt water (r_s), the cold salt water can be transported over a larger distance towards the well screen and hence the relative salt mass loss due to lateral transport away from the well screen is lowered (e.g Cases 4.b and 6.b; Table 7.5).

Scenario	r_{th} [m]	A_{tot}/V_H [m^{-1}]	ε_H [-]		r_s [m]	ε_S [-]
			Dens. diff. compensation	*No free convection*		
Case 1 *Reference*	38.75	0.15	0.69	0.76	58.63	0.68
Case 4 H_a = *10 m*	56.15	0.24	0.61	0.67	84.97	0.78
Case 5 V_i = 28,350 m^3	27.40	0.17	0.65	0.73	41.46	0.59
Case 6 V_i = 113,400 m^3	54.79	0.13	0.70	0.78	82.99	0.74

Table 7.5 Overview of the sensitivity analysis on thermal and salt recovery efficiency for cycle-4. The associated thermal radii (r_{th}, Eq. 7.5), the solute radii (r_s, Eq. 7.7), and the ratio between the outside area and the thermal volume of the theoretical cylinder in the aquifer (A_{tot}/V_H).

7.3.2 Modeling of the pilot study at Auburn University

The numerical SEAWATv4 modeling results of the two injection, storage and extraction cycles as conducted in the Auburn University field pilot (Molz et al. 1983a) corresponded well with the modeling results by Buscheck et al. (1983). They simulated the two cycles of the field experiment with the computer program PT using a non-linear temperature-density relationship (Bodvarsson 1982).

Fig. 7.9 shows the calculated temperature distributions at the end of the first injection period with an injection temperature of 58.5 ºC. The observed preferential flow in the middle high-permeability layer is reproduced. Similar to the modeling results of Buscheck et al. (1983), the higher injection temperature (81 ºC) in the second cycle led to stronger free thermal convection resulting in no discernible preferential flow due to the heterogeneous layering (Fig. 7.10). The thermal recovery efficiency calculated for the simulations of the two cycles was 0.58 and 0.41, respectively, similar to both the experimental results of Molz et al. (1983a) and the numerical calculations by Buscheck et al. (1983), as shown in Table 7.6. For the second cycle, a smaller transition zone between the hot water volume and ambient groundwater was obtained in this study compared to the results of Buscheck et al. (1983) (see Fig. 7.10). Moreover, enhanced free thermal convection is observed in the SEAWAT modeling results of this study. These differences are likely explained by the smaller grid sizes used in the thermal zone in the SEAWAT model (Δr=0.5 m) than in the model (Δr=4.0 m) of Buscheck et al. (1983), causing less numerical dispersion for heat transport.

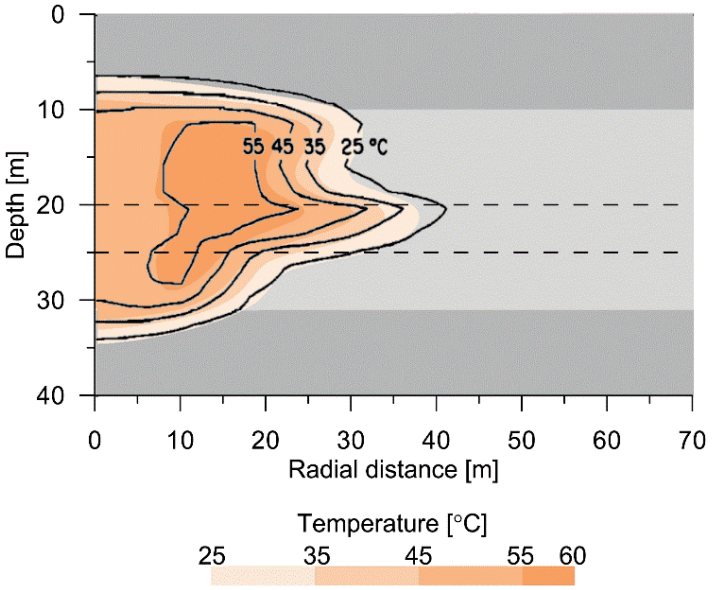

Fig. 7.9 The color intensity indicates the temperature distribution calculated by SEAWAT at the end of the injection period for cycle-1. *Black contour lines* indicate the temperature distribution modeled by Buscheck et al. (1983).

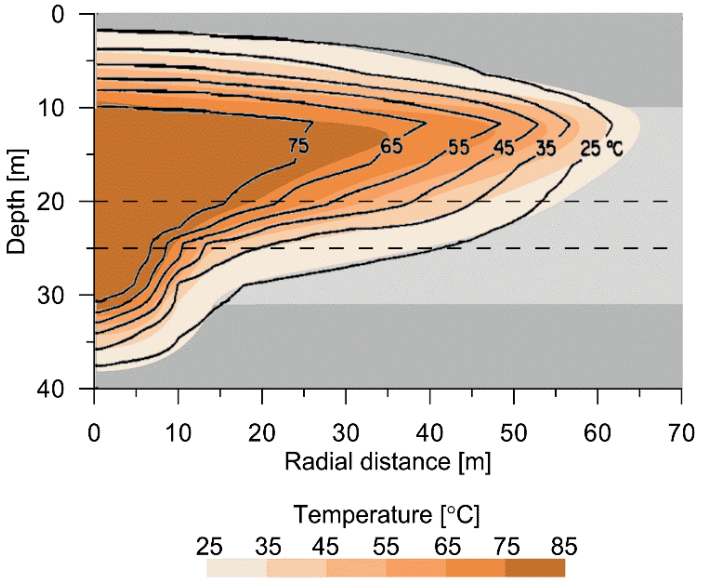

Fig. 7.10 The color intensity indicates the temperature distribution calculated by SEAWAT at the end of the injection period for cycle-2. *Black contour lines* indicate the temperature distribution calculated by Buscheck et al. (1983).

	Experimental (Molz et al. 1983a)	Numerical estimate (Buscheck et al. 1983)	Numerical estimate (SEAWATv4, this study)
Cycle-1	0.56	0.58	0.58
Cycle-2	0.40*	0.40	0.41

Table 7.6 Comparison between experimental and calculated recovery efficiencies. *Estimated value by Molz et al. 1983a assuming no well screen modification during production.

Simulating density difference compensation for the Auburn University pilot study

The potential of the density difference compensation method was tested using the model that adequately modeled the Auburn University field pilot. The required salt concentrations to overcome the buoyancy difference between hot injection water (58.5 °C for cycle-1 and 81 °C for cycle-2) and the ambient groundwater (20 °C) are 19 and 36.6 kg/m^3, respectively (Fig. 7.2). Free thermal convection was successfully countered for the second cycle (Fig. 7.11), so that the preferential flow of the hot, saline water in the most permeable layer is more pronounced (compare Fig. 7.11 with Fig. 7.10). The preferential flow of saline water into the middle layer of the heterogeneous aquifer results in injected cold salt water overlying cold fresh ambient groundwater in the bottom layer. The salinity contrast of 36.6 kg/m^3 results in a density difference between ambient fresh water (998.0 kg/m^3) and the cold salt water front (1026.1 kg/m^3). Therefore, downward transport of cold salt water mass is observed which results in more accumulation of salt mass at the bottom of the aquifer over time in this heterogeneous aquifer than in the homogeneous aquifer used in the sensitivity analysis. Consequently, increased displacement of the hot water volume at the bottom of the aquifer towards the well screen is observed. For both cycles, density difference compensation increased the thermal recovery efficiency to 0.68 and 0.66 for cycle 1 and 2 respectively (Table 7.7). The relative increase in thermal recovery efficiency was large (60.8 %) for cycle-2, which had an efficiency of 0.41 in the regular HT-ATES. The salt recovery efficiency was 0.69 for cycle-1 and 0.63 for cycle-2.

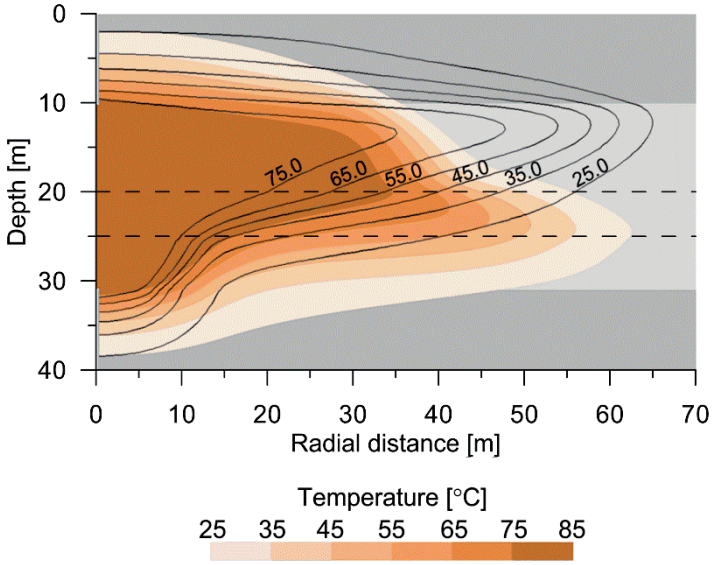

Fig. 7.11 The color intensity indicates the temperature distribution calculated by SEAWAT at the end of the injection period for cycle-2 with density difference modification. *Black contour lines* indicate the temperature distribution calculated by SEAWAT for regular HT-ATES.

	Thermal recovery efficiency		**Relative recovery increase**	**Salt recovery efficiency**
	Regular HT-ATES	*Dens. diff. compensation*		
Cycle-1	0.58	0.68	17.2 %	0.69
Cycle-2	0.41	0.66	60.8 %	0.63

Table 7.7 Calculated recovery efficiencies and relative increase with density modification.

7.4 Discussion

In this study is shown that free thermal convection during HT-ATES can be countered by using saline water for heat storage. This density modification allows a significant increase of recovery efficiency, bringing it close to the theoretical situation without free thermal convection. This has the advantage that HT-ATES systems are no longer restricted to low-permeability aquifers to achieve sufficient heat recoveries. Also, larger temperature differences between the hot water volume and cold ambient groundwater can be used, which increases the capacity and efficiency of the building systems.

7.4.1 Optimization of thermal recovery efficiency

The recovery efficiency of regular HT-ATES systems is significantly influenced by both thermal conduction and free thermal convection. The thermal front tilting due to free thermal convection causes unheated ambient groundwater to be recovered at the lower part of the well screen, especially for cases with a small thermal radius (r_{th}, Case 5.a). Therefore, feasibility of regular HT-ATES is limited (Doughty et al. 1982; Schout et al. 2014). In the past, several suggestions have been put forward to optimize energy recovery during HT-ATES. In order to reduce the heat loss by free thermal convection during injection and storage, partially penetrating wells can be used to increase energy recovery (Buscheck et al. 1983). However, only a small increase in recovery efficiency was obtained ($\Delta\varepsilon_H$<0.09). Most research on optimizing well designs of partially-penetrating well systems is done in the field of aquifer storage and recovery (ASR), where density-driven flow occurs due to the salinity contrast between injected freshwater and brackish groundwater (Ward et al. 2007). For these cases, well systems with multiple injection and recovery wells (Miotliński et al. 2013) or multiple partially penetrating wells can be used to successfully increase the recovery of freshwater (e.g. Zuurbier et al. 2014). Also prolonged injection of hot water during the first cycle can be applied to reduce the temperature differences and associated heat loss in subsequent recovery cycles (Sauty et al. 1982).

This study showed that the thermal recovery efficiency of HT-ATES systems can be efficiently increased by applying density difference compensation using saline water. Consequently, heat loss due to thermal conduction remains as the main factor affecting thermal recovery efficiency. This enables the optimization of HT-ATES heat recovery by minimizing conductive heat loss, rather than mitigating heat losses by free thermal convection. The conductive heat loss is related to the compactness of the heated volume. Relatively large outside areas of the injected hot water volume result in a strong increase of heat loss by thermal conduction (e.g. Case 4.b).

Besides the heat loss due to thermal conduction, the application of the density difference compensation method also induces displacement of hot water volume towards the well along the bottom of the aquifer due to downward density-driven flow of the cold salt water between the solute front and the thermal front (Fig. 7.6). Although this only has a slight negative impact on the thermal recovery efficiency, these double-advective effects on heat and salt transport during HT-ATES need to be taken into account to fully optimize the thermal and salt recovery efficiency, especially for heterogeneous aquifers where the effect of plume separation of the heated and saline water volume could have a large impact on convective flow patterns due to the density contrasts (see section 7.3.2 '*Simulating density difference compensation for the Auburn University pilot study*').

The calculated recovery efficiency for the simulation of seasonal HT-ATES in this study is determined by assuming equal injection and production volumes. In practice, the extraction period may be reduced by maintaining a minimum temperature for extraction. The calculated production temperature over time is significantly higher for HT-ATES with density difference compensation, compared to regular HT-ATES (Fig. 7.4 and 7.8). Therefore, the increase in recovery efficiency while using density difference compensation is larger when applying a minimum extraction temperature. For example, the thermal recovery efficiency increase with density difference compensation is relatively small for a low-permeability aquifer (Fig. 7.7a, Case 2.b) while using equal injection and production volumes. However, if a minimum temperature of 60 °C is used, the extractable volume at a constant extraction rate of 630 m^3/day for regular HT-ATES (Case 2.a) was only 17,010 m^3 while this is 30,870 m^3 using density difference compensation (Case 2.b).

7.4.2 Model validation on the Auburn University field experiments

Recently, Vandenbohede et al. (2014) validated the approach of Langevin (2008) for heat transport on an ATES test case, where water with a temperature of 17.5 °C was injected into an aquifer with an ambient groundwater temperature of 10 °C. Due to this small temperature contrast, no density-driven flow was considered for this study. However, the temperature contrasts during HT-ATES are so high that free thermal convection occurs and a density equation of state is required for the simulation. To the best of the authors' knowledge, this is the first study that validates the approach of Langevin (2008) for axi-symmetric density-driven groundwater flow and thermal heat transport at high temperature contrasts (ΔT = 40-60 °C).

For accurate simulation of the thermal convection, a non-linear density equation of state was implemented in the SEAWATv4 code (Van Lopik et al. 2015). The modeling results accurately reproduce the experimental and numerical data sets of the field experiment at Auburn University (Molz et al. 1983a; Buscheck et al. 1983), while using

both an axi-symmetric SEAWATv4 model domain and the incorporated non-linear density equation of state (Section 7.3.2 '*Simulating density difference compensation for the Auburn University pilot study*').

7.4.3 Salinity management of density difference compensated HT-ATES systems

For this study, a single injection-recovery HT-ATES well through which heat was injected and extracted was considered. Using saline water for heat storage to compensate the density difference with the surrounding cold groundwater results in a significant increase of thermal recovery. From a water resources and economic perspective, rather than adding salt to the water used for HT-ATES, saline water sources could be used e.g. deeper, more saline groundwater, seawater, or reverse osmosis concentrate (Pérez-Gonzaléz et al. 2012).

In practice, most HT-ATES systems use a doublet well configuration where the hot injection-recovery well, as well as the cold supply well are screened in the same aquifer (e.g. Molz et al. 1983a). For such systems, the use of the density difference method with saline water will result in salt loss due to the salinity contrast between ambient groundwater and injection water for both wells. Alternatively, the use of a mono-well configuration (e.g. Zeghici et al. 2015) allows the cold supply well to be screened in a deeper, more saline aquifer which acts as the source for the required salinity.

Depending on the saline water source used for density difference compensation, the chemical composition of the water varies. For regular HT-ATES systems, the risk of mineral-precipitation-induced clogging of wells by e.g. carbonate and silica minerals is already well-known (e.g. Griffioen and Appelo 1993). For most natural saline water sources, however, salinity is mainly defined by sodium and chloride concentrations for which the solubility is controlled by the halite (NaCl) mineral. Since this mineral has temperature dependent solubilities that are well above the salt concentrations required for the HT-ATES relevant temperature range (10-120 °C, Fig. 7.2), using saline water for density difference compensation is not expected to further increase the risk of mineral precipitation and clogging around the wells.

Besides the risk of temperature dependent mineral precipitation, a high salinity contrast between injection water and ambient groundwater may cause clay particles in the aquifer to swell, or shrink and migrate. Osmotic swelling of clay particles is known to occur when fresh water with a low ion concentration is injected into a brackish or saline aquifer (Brown and Silvey 1977; Molz et al. 1979). The use of saline water for density difference compensation for HT-ATES in brackish or saline aquifers as described in this study, will minimize these effects.

7.4.4 Salinization of the aquifer

In this study an ambient salinity of 10,000 ppm was assumed for the simulated cases, since HT-ATES is currently only allowed in brackish or saline aquifers in the Netherlands. This is due to induced (bio)geochemical reactions during hot water storage (Brons et al. 1991; Hartog et al. 2013; Bonte et al. 2013) that could make fresh water unusable for other purposes. The numerical simulations in this study show that the calculated salt mass recovery efficiencies for fully operative seasonal HT-ATES systems range from 0.59 to 0.82 (Fig. 7.7b) resulting in a net salinization of the aquifer. However, the risk of salinization of overlying aquifers appears to be negligible as molecular salt diffusion and salt water seepage into the upper aquitard was limited in the simulations (Fig. 7.6d-f). The accumulated salt mass at the bottom of the aquifer after thermal recovery could be recovered by a partially penetrating well screened at the bottom of the aquifer either to minimize the salinization of the aquifer or for re-use in the salinity management of the density difference compensation HT-ATES system.

7.5 Conclusions

Density difference compensation using saline water can be used in HT-ATES systems to overcome the density difference between hot injection water and colder ambient groundwater and prevent free thermal convection of the injected hot water.

Thermal recovery efficiency is significantly increased. For example, calculations for a regular seasonal HT-ATES at a temperature of 80 °C in a high-permeability aquifer resulted in a recovery efficiency of 0.40 for the fourth cycle, while density difference compensation gave an efficiency of 0.69.

HT-ATES with density difference compensation can be applied in aquifers with higher hydraulic conductivities and at larger temperatures. This means that a much broader range of aquifers are suitable for HT-ATES and higher capacities can be achieved.

The thermal front moves at a lower velocity than the solute front during hot saline water injection due to thermal retardation. Consequently, downward density-driven flow of the cold salt water in between the two fronts is triggered by the salt concentration contrast between injected cold salt water and less saline ambient groundwater. Some local displacement of the hot water front towards the well screen is observed, due to the lateral transport of cold salt water along the bottom of the aquifer.

Salt water accumulates at the bottom of the aquifer during the extraction period due to continued downward density-driven salt water flow. Consequently, the total injected salt mass is not fully recovered after extraction. The salt recovery efficiency ranges from 0.59 to 0.82 for the simulated scenarios.

Axi-symmetric density-driven flow simulation in the SEAWATv4 code with an implemented non-linear density equation of state was validated on experimental (Molz et al. 1983a) and numerical results (Buscheck et al. 1983) of a HT-ATES experiment conducted at Auburn University.

Acknowledgements

The authors wish to thank two anonymous reviewers for their constructive feedback, which allowed us to improve the manuscript significantly.

Chapter 8

The use of multiple partially-penetrating wells to improve thermal recovery efficiencies of high-temperature aquifer thermal energy storage systems

Abstract

Free convection during seasonal high-thermal aquifer thermal energy storage (HT-ATES) in high-permeability aquifers could result in significant heat loss and low thermal recovery efficiencies. This study investigates the potential to improve the efficiency by using multiple partially penetrating wells (MPPW) for a single injection-recovery well scheme. A MPPW configuration of three PPWs with a filter length of 5 meter was tested numerically at various injection and recovery schemes. This MPPW approach with different injection and recovery well schemes is tested for target aquifers with different aquifer characteristics (hydraulic conductivity and anisotropy ratio) and injection temperatures.

Injection and recovery with a MPPW scheme can be used to increase the thermal recovery efficiency of seasonal HT-ATES systems. For a high-permeability aquifer (K_h=53.4 m/d) with an anisotropy ratio (K_h/K_v) of 7, the injection of hot water at temperatures of 80 ºC for 90 days in the lower part of the aquifer and abstraction for 90 days in the upper part resulted in a thermal recovery efficiency increase of $\Delta\varepsilon_H$ of 0.14 for cycle-1 compared to a well scheme of full injection and abstraction over the entire aquifer thickness. The use of an injection PPW in the lower part of the aquifer results in heat transport by free thermal convection in solely the vertical direction during injection. As a consequence, no thermal front tilting occurs in the early injection stage. The start of thermal front tilting for such PPW configuration highly depends on the temperature contrast between hot injection water and cold ambient groundwater, as well as on the aquifer characteristics. The optimal well scheme for injection, as well as abstraction depends on both the horizontal and vertical hydraulic conductivity of the aquifer and therefore, good hydraulic characterization of the aquifer is required to obtain the highest thermal recovery efficiency with a MPPW configuration.

8.1 Introduction

As described in the previous chapter, high-temperature aquifer thermal energy storage (HT-ATES) systems can play a critical role in buffering the temporal mismatch between (seasonal) heat demand and heat supply (e.g. geothermal energy, industrial waste heat, solar thermal energy, but also converted energy from wind turbines and solar panels). The storage of water with higher temperatures (e.g. >70°C) increases both the energy storage capacity and overall energy efficiency of ATES systems. Despite recent research on the potential of HT-ATES for specific regions and purposes (e.g. Xiao et al. 2016; Opel et al. 2017; Winterleitner et al. 2018; Ueckert and Baumann 2019), to date only a limited amount of HT-ATES systems is in operation worldwide (Kabus and Seibt 2000; Holstenkamp et al. 2017; Fleuchaus et al. 2018).

Experimental HT-ATES field pilots (e.g. Molz et al. 1983ab), as well as numerical simulation studies (e.g. Buscheck et al. 1983; Schout et al. 2014; Van Lopik et al. 2016) have shown that free thermal convection during HT-ATES can negatively impact the thermal energy recovery. At large temperature contrasts between hot injection water and cold ambient groundwater, buoyancy forces cause upward flow of hot injection water. This results in tilting of the initially vertical hot water front during infiltration of hot water while using fully-penetrating wells in confined aquifers (Hellström et al. 1978; Doughty et al. 1983; see Fig. 7.1a-b in Chapter 7). For smaller HT-ATES systems in permeable aquifers this can have significant impact on the thermal recovery efficiency, since cooler groundwater will be recovered in the lower portion of the well during the recovery stage (see Fig. 7.1c). This results in low production temperature over time and lower thermal recovery efficiencies (Molz et al. 1983a; Buscheck et al. 1983; Schout et al. 2014; Van Lopik et al. 2016)

So far, studies, such as Doughty et al. (1982) and Schout et al. (2014) suggest the use of lower storage temperatures, as well as the selection of target aquifers with a low vertical permeability to minimize heat losses by thermal front tilting due to free thermal convection. However, in reality, typical aquifer anisotropy ratios (K_h/K_v) are in the range of 2-10 (Bear 1988), which would mean that HT-ATES systems would have to target low permeability aquifers. Although low-permeability aquifers have the benefit of reducing the impact of free thermal convection and increase the thermal recovery efficiency, they negatively impact the hydraulic capacity of a HT-ATES system and therefore, its heat storage capacity and also increase the clogging risks. Methods to counter or reduce the effects of free convection and to maintain a stable hot water plume during storage would drastically broaden the range of potential target aquifer for HT-ATES. Van Lopik et al. (2016) investigated the potential to improve the recovery efficiency through compensation of the density difference by using higher salinity for

the stored hot water compared to that of ambient groundwater for a single injection-recovery HT-ATES well scheme.

The experimental field study of Molz et al. (1983a) and the numerical study of Buscheck et al. (1983) showed that thermal recovery at the top of the aquifer with a partially-penetrating well (PPW) can result in increased thermal recovery efficiencies. Buscheck et al. (1983) performed optimization simulations of the field pilot of Molz et al. (1983a) by employing different PPW set-ups in the heterogeneous target aquifer for the injection and recovery stage. However, they did only account for the given target aquifer at the Auburn University site and for the conducted recovery cycles in the field. Similarly, the use of a multiple PPW configuration is successfully applied for aquifer storage and recovery (ASR) to counter the negative impact on fresh water recovery efficiency by free convection due to the density contrast between injected fresh water and ambient brackish groundwater in practice (Zuurbier et al. 2014).

Therefore, in this study, the possibility of minimizing the effects of free thermal convection during seasonal HT-ATES by using a multiple partially penetrating wells (MPPW) configuration with various injection and recovery schemes is investigated (see Fig. 8.1) for multiple recovery cycles. The potential of this approach is explored numerically by assuming:

a) Density-driven flow during HT-ATES with a MPPW configuration that allows for injection and/or abstraction in the upper, middle and/or lower portion of a 21 m thick aquifer using PPWs with a filter length of 5 m.

b) A theoretical HT-ATES case with no free thermal convection neglecting density differences due to the temperature contrast between hot injection water and cold ambient groundwater and full injection and abstraction in the upper, middle and lower portion of the aquifer for the given MPPW configuration. The latter scenario provided an upper bound for the improvement obtainable with the MPPW configuration.

Presumably, the extent of forced and free convection in the vertical direction during injection and abstraction with a MPPW scheme is an important factor that determines overall thermal recovery efficiency of the HT-ATES system. Therefore, this approach with different well schemes is tested for target aquifers with different aquifer characteristics (hydraulic conductivity and anisotropy ratio).

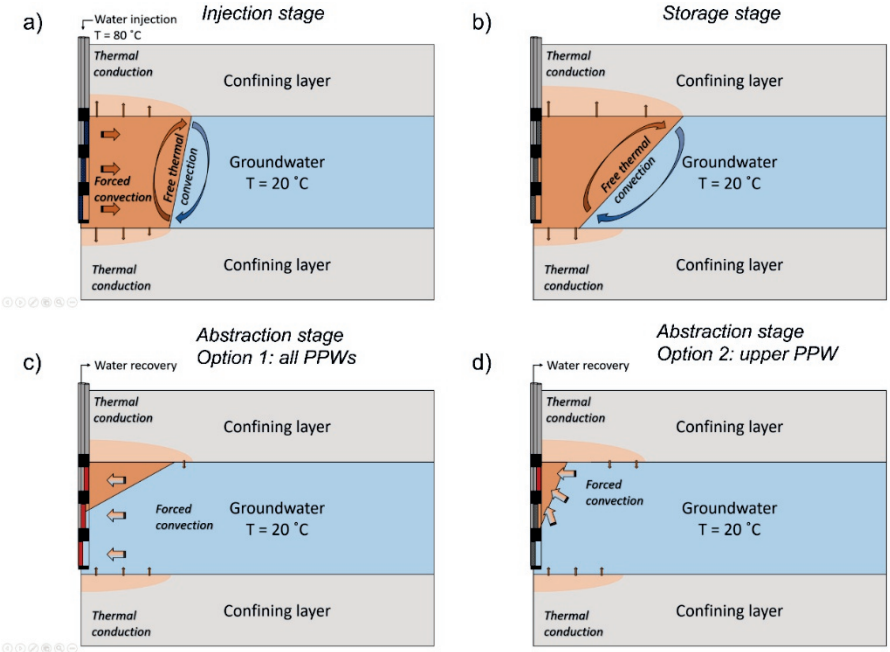

Fig. 8.1 Schematic overview of a full HT-ATES recovery cycle in a confined aquifer for **a)** injection, **b)** storage. For abstraction period, two different option of well operation are shown, with **c)** abstraction at the upper, middle and lower PPWs, **d)** and abstraction at the upper PPW. Heat loss occurs by thermal conduction and free thermal convection.

8.2 Methods

8.2.1 SEAWAT: buoyancy-driven flow and heat transport model

In the present study, the same modelling approach as described in Chapter 7 was used to test the efficiency of the HT-ATES systems. Hence, the SEAWATv4 code was used to enable simulation buoyancy-driven flow (Langevin et al. 2008; Guo and Langevin 2002). In the present study, no salinity contrasts are taken into account and buoyancy-driven flow solely occurs due to temperature contrasts. Equations of state for density and viscosity were used to describe both fluid density and viscosity as a function of groundwater temperature. Fluid viscosity as a function of temperature and salt concentration is described by the following equation (Voss 1984):

$$\mu(T) = 2.394 \cdot 10^{-5} \cdot (10^{\frac{248.37}{T+133.15}}) \qquad (8.1)$$

where μ [kg/(m day)] is the dynamic fluid viscosity and T [°C] is the temperature of the water. To account for the non-linear dependence of water density on temperature, the

adjusted SEAWAT code as described by Van Lopik et al. (2015) is used to accurately simulate the temperature-density relation over large temperature ranges. Disregarding the influence of groundwater salinity, the density equation of state derived by Sharqawy et al. (2010) equals:

$$\rho(T,S) = (999.9 + 2.034 \cdot 10^{-2}T - 6.162 \cdot 10^{-3}T^2 + 2.261 \cdot 10^{-5}T^3 - 4.657 \cdot 10^{-8}T^4) \quad (8.2)$$

where ρ [kg/m^3] is the fluid density.

8.2.2 Model set-up

Simulation of seasonal HT-ATES with four consecutive recovery cycles is performed in the axi-symmetric model with the same numerical settings as described in section 7.7.2 '*Model set-up*'. The aquifer characteristics used for the simulation of seasonal HT-ATES are also based on the aquifer used for the Auburn University (USA) field experiment conducted by Molz et al. (1983a). A homogeneous anisotropic high-permeability target aquifer is used as base case for the sensitivity analysis of this study (see Table 7.1 for hydraulic and heat transport characteristics). This enables comparison of the numerical dataset of the present study with the latter study (see *Chapter 7*) on improving thermal recovery efficiencies by the use of salinity contrasts to compensate for density differences.

The present study focuses on improving the recovery efficiency with a MPPW configuration for seasonal temperature storage. At the centre of the axisymmetric model domain, the MPPW HT-ATES system was placed, using no flow cells for the non-screened parts of the well. Three MPPWs with a screen length of 5 meter and a radius of 0.1 m were placed at different aquifer depths (see Fig. 8.1 for schematic overview). The *upper* PPW was screened at depth of $11<z<16$ m, the *middle* PPW at $18<z<23$ m and the *lower* PPW at $25<z<30$ m. This MPPW configuration is used for all simulated scenarios in the sensitivity analysis.

A seasonal HT-ATES system using the MPPW configuration was assumed, with injection, storage, extraction and rest periods each of 90 days. An equal injection and extraction volume of 56,700 m^3 was assumed for four consecutive recovery cycles in the *base case* (Case 1), (see Table 8.1). If one PPW in the well configuration is in operation during the injection or recovery stage, the volumetric flow rate of the PPW is 26.25 m^3/h, while for two and three wells in operation the volumetric flow rate is respectively 13.13 and 8.75 m^3/h. At the given MPPW configuration, different types of simulations were conducted to test various injection and recovery schemes (*named a-f*) for all simulated

scenarios in the sensitivity analysis (see Table 8.2). Injection and consecutive abstraction at all three PPWs is considered as the base reference scheme (*named ref.*). Six additional well injection and recovery schemes are tested that consider infiltration in the lower portion of the aquifer, as well as abstraction in the upper portion of the aquifer. A theoretical HT-ATES case that considers no free thermal convection and hence only heat loss by thermal conduction is considered for the base reference scheme with injection and recovery in all three PPWs. In the latter simulation, density-driven flow was not considered (no free thermal convection) as an upper bound for the improvement that can be obtained for the given MPPW configuration.

Various HT-ATES conditions and aquifer characteristics are tested in the sensitivity analysis (see Table 8.1):

- Case 1: Injection of hot water with a temperature of 80 ^{0}C in a high-permeability, anisotropic homogeneous aquifer.
- Case 2: Injection of hot water with a temperature of 60 ^{o}C in a high-permeability, anisotropic homogeneous aquifer.
- Case 3: Injection of hot water with a temperature of 80 ^{o}C in a low-permeability, anisotropic homogeneous aquifer. These aquifer characteristics were based on the aquifers considered by Schout et al. (2014) in their modeling study to obtain moderate effects of buoyancy-driven flow and associated reasonable thermal recovery efficiencies using a fully-penetrating well for injection and recovery (ε_H>60%).
- Case 4: Injection of hot water with a temperature of 80 ^{o}C in a high-permeability, highly anisotropic homogeneous aquifer with the K_v of Case 2 (high anisotropy ratio of K_h/K_v=35.6).
- Case 5: Injection of hot water with a temperature of 80 ^{o}C in a low-permeability, anisotropic homogeneous aquifer with the K_v of Case 1 (low anisotropy ratio K_h/K_v=1.9).

	K_h [m/day]	K_v [m/day]	$a=K_h/k_v$	T_{in} [°C]	H_a [m]	V_{in} [m^3]
Case 1	53.4	7.7	6.9	80	21	56,700
Case 2	53.4	7.7	6.9	60*	21	56,700
Case 3	15*	1.5*	10*	80	21	56,700
Case 4	53.4	1.5*	35.6*	80	21	56,700
Case 5	15	7.7	1,9	80	21	56,700

Table 8.1 Summary of the input parameters used for the sensitivity analysis. Values with an asterisk (*) indicate a variation on the base scenario (Case 1).

Well scheme	Injection stage			Recovery stage		
	Upper	*Middle*	*Lower*	*Upper*	*Middle*	*Lower*
Reference scheme	X	X	X	X	X	X
Scheme a	X	X	X	X		
Scheme b	X	X	X	X	X	
Scheme c		X	X	X		
Scheme d		X	X	X	X	
Scheme e			X	X		
Scheme f			X	X	X	

Table 8.2 Summary of the well injection and recovery schemes for the MPPW configuration.

8.2.3 Quantification of thermal energy recovery and thermal front tilting

The thermal recovery efficiency (ε_H) is defined as the ratio between the total injected heat (Q_{in}) in the PPWs and the total recovered heat (Q_{ex}) from the PPWs (see section 7.2.4 '*Metrics to quantify salt and heat recovery*'; Eq. 7.3). The average temperature over time of the abstracted hot water in the PPWs is calculated and used to obtain the total recovered heat.

Considering an optimal case of HT-ATES in a confined aquifer with no heat loss, cylindrical dimensions of the hot water volume can be described in terms of the maximum radial extent of the injected hot water (r_{th}) and a given aquifer thickness (H_a), see section 7.2.4 '*Metrics to quantify salt and heat recovery*'; Eq. 7.5. The thermal radius (r_{th}) of the hot water in the present study is 38.75 m for all cases in the sensitivity analysis in this study. This only holds for HT-ATES with fully-penetrating injection and abstraction wells (FPWs) in confined aquifers.

During HT-ATES, the temperature difference between hot injection water and cold ambient groundwater results in a net buoyancy difference and causes upward flow of the heated water volume (free thermal convection). For FPW conditions in confined aquifers, this free thermal convection results in tilting of the initially vertical hot water front (Fig. 8.1). However, for PPWs that are infiltrating hot water in the lower portion of the aquifer, tilting does not occur in the initial stage and buoyancy difference only causes upward flow of the heated water until it reaches the top of the aquifer. Free convection due to buoyancy differences depends on three major system properties (e.g. Holzbecher 2004). Thermal diffusivity reduces the density gradient and its effect on fluid motion, while high viscosity of the fluid and low permeability of the porous medium prevent

flow by the existing density differences. Hence, free thermal convection and associated thermal front tilting at elevated water temperatures are enhanced due to lower viscosity of the hot water (Hellström et al. 1979). Moreover, a relatively sharp thermal interface between hot injection water and cold ambient groundwater results in higher tilting rates compared to cases with a more diffusive thermal front.

To characterize the spreading of hot water during injection and storage, the starting time of thermal front tilting for the different infiltration PPW schemes is identified. Moreover, the thermal radius of the temperature contour of 60 ºC in the upper portion (*upper* PPW depth at 13.5 m) and lower portion (*lower* PPW depth at 27.5 m) of the aquifer is determined over time. Based on these thermal radii, the angle of tilt of the thermal front is calculated with respect to the *vertical*. Thermal front tilting is considered after breakthrough of elevated temperatures at *upper* PPW depth, when the thermal radius is larger than that of *lower* PPW depth. Besides free thermal convection due to the buoyancy differences, the infiltration in lower PPWs results in a forced upward vertical flow component and potentially impacts thermal front tilting.

8.3 Results

The potential thermal recovery efficiency improvement of a seasonal HT-ATES system using the proposed MPPW configuration with the different well schemes is tested for different aquifer characteristics and injection temperatures. First, the reference scenario of the high-permeability homogeneous anisotropic aquifer (similar to the pilot study at the Auburn University (Molz et al. 1983ab)) is presented. Subsequently, the use of a lower temperature contrast between hot injection water and ambient groundwater (ΔT= 40 ºC) is presented. Finally, the efficiency of the various MPPW injection and abstraction schemes are investigated for different aquifer types with various hydraulic conductivities and anisotropy ratios.

8.3.1 Reference scenario (Case 1)

In Case 1.ref, a seasonal HT-ATES system with an injection temperature of 80 °C is simulated assuming full injection and abstraction in the upper, middle and lower PPWs. Due to the high vertical hydraulic conductivity of the aquifer (7.7 m/d), as well as the high temperature contrast between hot injection water and cold ambient groundwater (ΔT=60 ºC), strong free thermal convection is observed during injection (Fig. 8.2a-c) and storage (Fig. 8.3a-b).

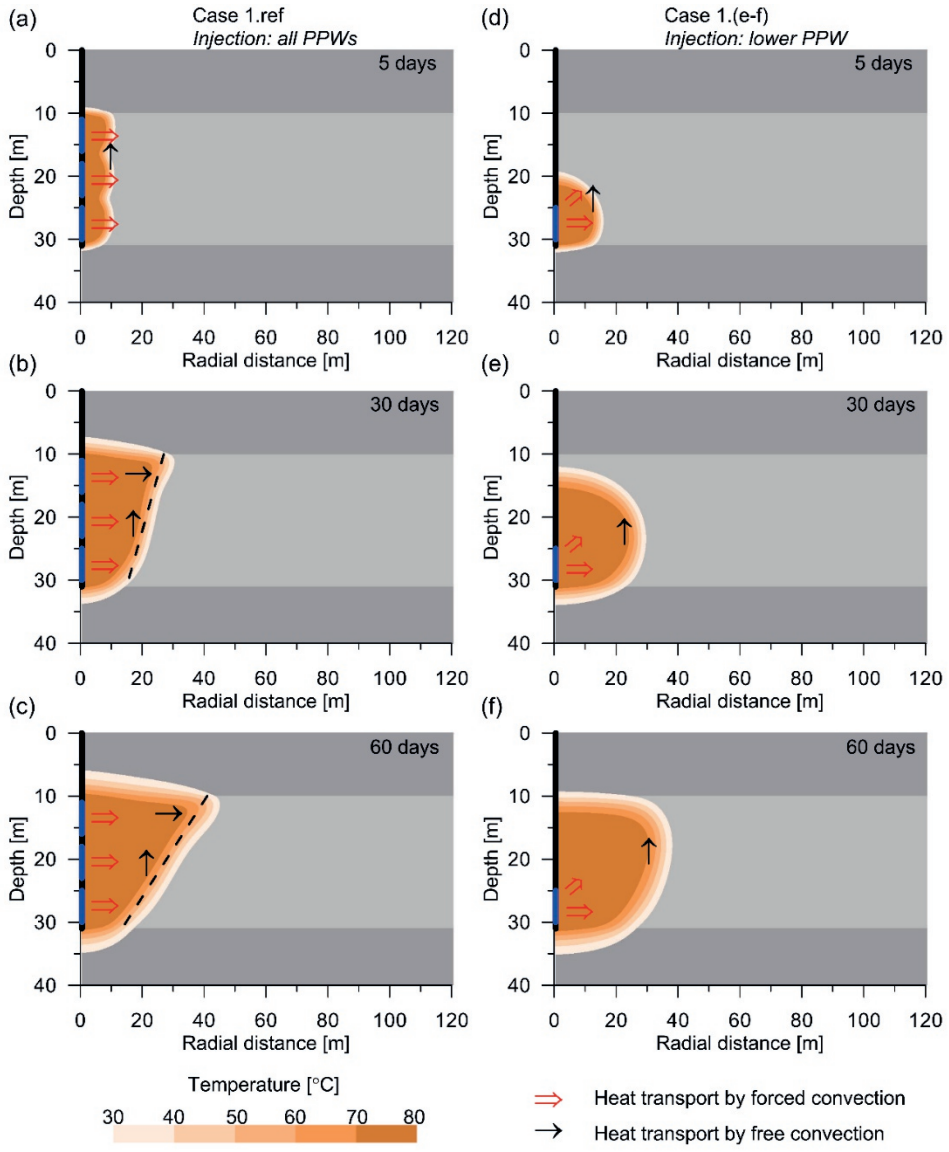

Fig. 8.2 The temperature distribution contour lines in the aquifer for Case 1.ref during injection in the upper, middle and lower PPWs are shown after **a)** 5 days, **b)** 30 days and **c)** 60 days. Similarly, the temperature distribution contour lines in the aquifer are shown for an equivalent scenario with injection in only the lower PPW (Cases 1.e-f) after **d)** 5 days, **e)** 30 days and **f)** 60 days. Thermal front tilting is indicated by the dashed line.

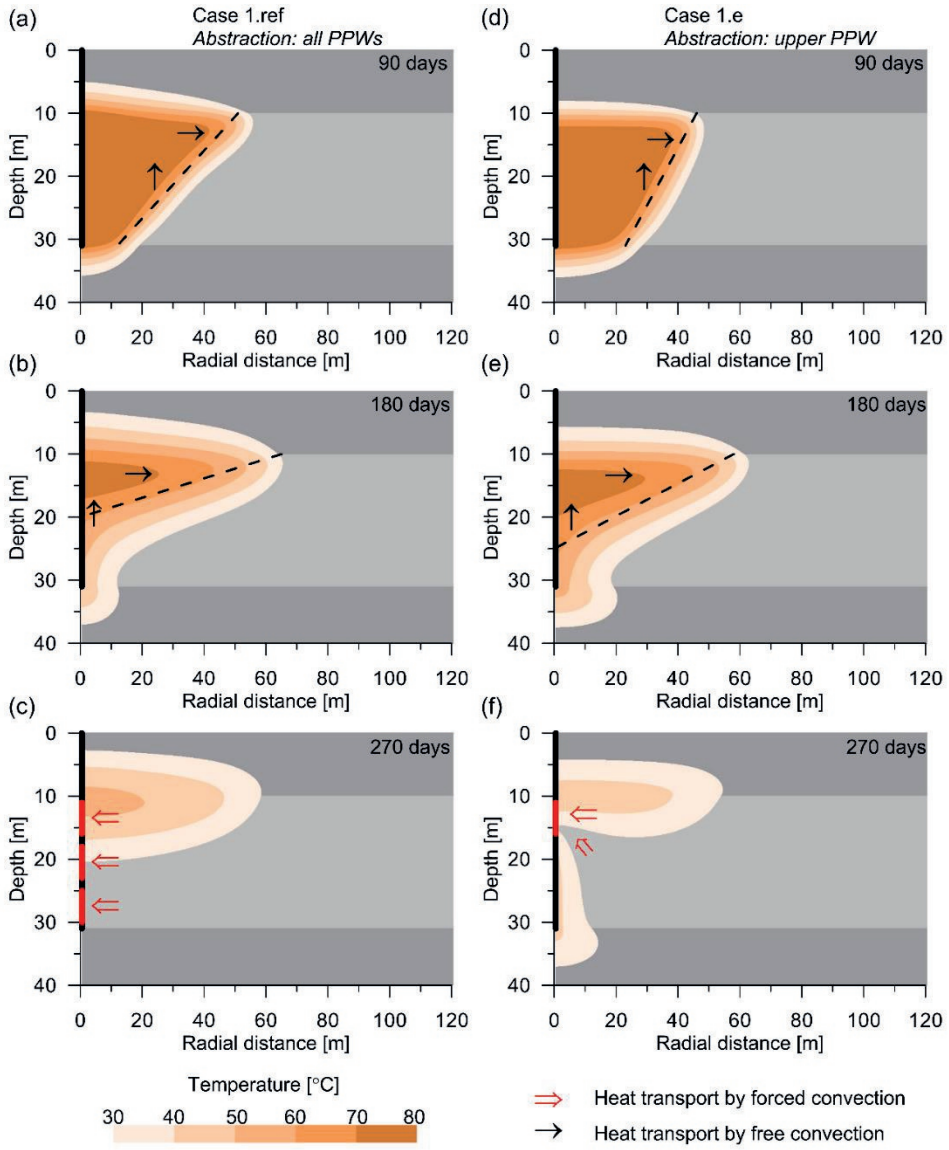

Fig. 8.3 The temperature distribution contour lines in the aquifer for Case 1.ref (injection and abstraction in the upper, middle and lower PPWs) during storing and abstraction are shown after **a)** 90 days (end of injection stage), **b)** 180 days (end of storage stage) and **c)** 270 days (end of recovery stage). Similarly, the temperature distribution contour lines in the aquifer are shown for an equivalent scenario (Case 1.e; injection in the upper, and abstraction in the lower PPW) during storing and abstraction stage after **d)** 90 days (end of injection stage), **e)** 180 days (end of storage stage) and **f)** 270 days (end of recovery stage). Thermal front tilting is indicated by the dashed line.

Fig. 8.4 shows that the recovery efficiency of a FPW regular HT-ATES system (see Chapter 7; Case 1a) is lower than Case 1.ref with the MPPW configuration, with values ranging from 0.31 to 0.40 for the four recovery cycles. The thermal recovery for the abstraction scheme Case 1.ref of injection and recovery in all PPWs ranges from 0.36 to 0.46 for the four recovery cycles (Fig. 8.4).Forced convection due to injection at the upper, middle and lower PPWs results in a slightly different tilting interface of the hot water after the injection stage and a lower amount of heat stored in the upper portion of the aquifer. The tilting angle is 68º (Fig. 7.3a) for the FPW scenario instead of 63º (Fig. 8.5a) for the PPW scenario (Case 1.ref) after 90 days of injection. The thermal radius at *lower* PPW depth (z=27.5 m) is only 13 m for the FPW scenario, while this is 19.5 m in Case 1.ref. Heat loss by thermal conduction into the overlying confining unit is reduced due to injection in a PPW that is not screened directly below the confining unit. Comparing the temperature distribution in the aquifer after injection stage of both scenarios, a more diffusive thermal front is observed in the upper portion of the aquifer for the FPW HT-ATES system (see Fig. 7.3a and Fig. 8.3a).

In the injection stage of Case 1.ref, besides thermal conduction, heat transport occurs by mixed convection (e.a. forced convection during injection, as well as free convection due to the buoyancy effects at the instable interface between hot injection water and cold ambient groundwater). Significant thermal front tilting occurs in the initial stage of injection, resulting in a tilting angle of 40º after 40 days of injection (see Fig. 8.5c). Over time, the more diffusive interface between hot injection water and ambient cooler groundwater at the thermal front interface results in lower rates of thermal front tilting. After injection of 90 days, the tilting angle is 63 º for Case 1.ref (see Fig. 8.3a and Fig. 8.5c). The maximum average thermal radius of the hot water volume after 90 days of injection is 38.75 m, while the thermal radius at *upper* PPW depth is 46.75 m and at *lower* PPW depth is 9.25 m (Fig. 8.5a-b), resulting in a cone-shaped hot water volume in the confined aquifer (Fig. 8.3b).

In the storage stage of Case 1.ref, flow occurs solely by free convection (Fig. 8.3a). The rate of thermal front tilting at a more diffusive interface is significantly lower in the storage stage (Fig. 8.3c). The maximum thermal radius at *lower* PPW depth is achieved after injection stage (27.75 m) and tilting of the thermal front results in smaller thermal radii over time during storage stage (Fig. 8.5b). After 140 days, thermal front tilting results in temperatures lower than 60 ºC (no thermal radius) at the *lower* PPW screen (Fig. 4b). At the end of the storage stage, elevated temperatures of 60 ºC are only stored in the upper 20 m of the aquifer (Fig. 8.3e). The thermal radius at *upper* PPW depth increases slightly to a value of 48 m after 120 days in the storage stage, and then slightly reduces to 42 m after 180 days (Fig. 8.5a). This reduction of the thermal radius in the upper portion of the aquifer is due to ongoing heat loss by thermal conduction to the

ambient cooler aquifer and overlying aquitard. The production temperatures over time for the first recovery period of Case 1.ref are lower than 60 ºC, due to recovery of cooler ambient groundwater at the lower PPW (see Fig. 8.3f).

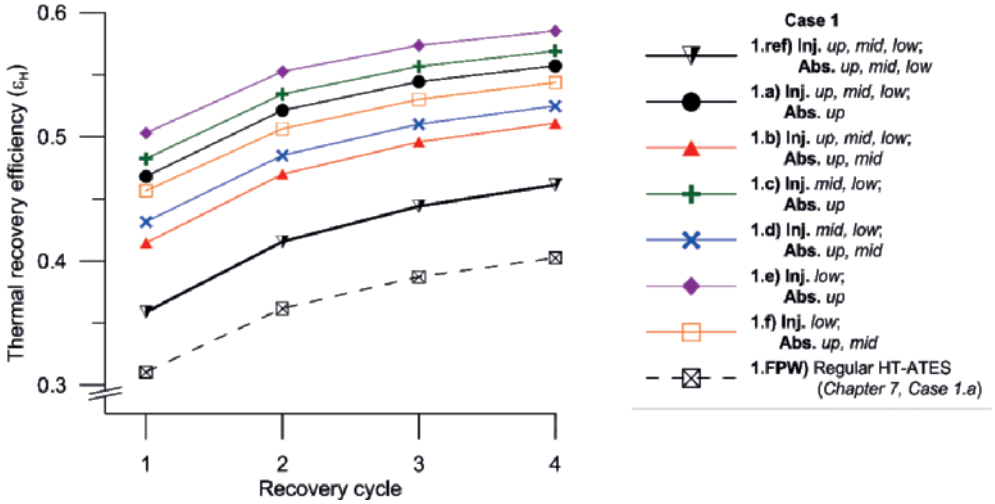

Fig. 8.4 Calculated thermal recovery efficiency per cycle for the base scenario (Case 1). Regular HT-ATES with a fully-penetrating well (1.FPW) for injection and abstraction (see Chapter 7, Case a.1) is also plotted.

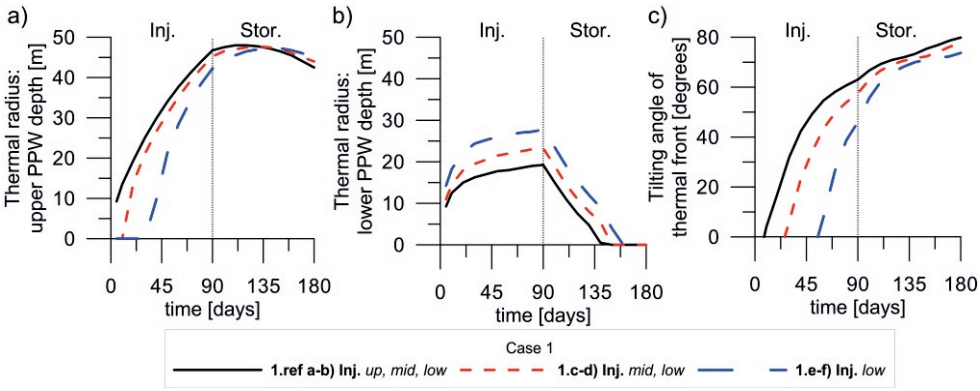

Fig. 8.5 Quantification of hot water volume spreading during injection and storage for Case 1, considering the MPPW scheme of injection in all PPWs (Cases 1.ref a-b), the lower two PPWs (Cases 1c-d) and the lower PPW (Cases 1e-f) by the thermal radius of the 60 ºC temperature contour at **a)** *upper* PPW depth (z=13.5 m) and **b)** *lower* PPW depth (z=27.5 m), as well as **c)** the thermal front tilting over time.

Cases 1.a-f show that the thermal recovery efficiency can be improved by using the different well schemes (Table 8.1) with the proposed MPPW configuration (Fig. 8.4). Overall, the scenarios with abstraction in only the upper PPW during recovery (Cases 1.a, 1.c and 1.e) resulted in the highest recovery efficiencies (Fig. 8.4), as well as the highest production temperatures over time (Fig. 8.6) for seasonal HT-ATES in the high-permeability target aquifer.

Injection in the lower PPW and abstraction in the upper PPW (Case 1.e) resulted in the largest improvement of thermal recovery efficiency. In cycle-1, ε_H is increased from 0.36 up to 0.50 (Fig. 8.4). The production temperatures over time for the first recovery period are also higher for this injection and abstraction scheme, resulting in recovery of water temperatures higher than 60 ºC for the first 40 days of recovery (Fig 8.6). Fig. 8.4 shows that the selection of an optimal MPPW scheme is also beneficial after four consecutive years of a fully-operating seasonal HT-ATES. For the most favourable well scheme (Case 1.e), the recovery efficiency increases from 0.50 up to 0.60.

In the injection stage of Cases 1.e-f, the hot water injected in the lower part of the aquifer is flowing upwards due to both free and forced thermal convection (see Fig. 8.2d-f). It takes approximately 50 days to transport the hot water volume by mixed convection over the entire thickness of the aquifer. Hence, the thermal front tilting starts at a much later stage compared to Case 1.ref (see Fig. 8.5c). Fig. 8.3c shows that the hot water volume is more compact and has a significantly smaller thermal interface with the ambient cooler groundwater and confining layers in the initial injection stage compared to Case 1.ref. The tilting angle is approximately 46º degrees after 90 days of injection for Case 1.e, while this is 63º for Case 1.ref. Hence, the hot water volume is more cylindrical for Case 1.e with heat transported over a thermal radius up to 27.75 m at *lower* PPW depth after 90 days (Fig. 8.5b), while this is only 19.25 m for Case 1.ref. At *upper* PPW depth, this is respectively 42.25 m for Case 1.e and 46.75 m for Case 1.ref. As a consequence, heat loss by thermal conduction is higher for the more cone-shaped storage of heat in Case 1.ref (see Fig. 8.3a).

Although the thermal recovery efficiency for Case 1.e (injection in the *lower* PPW, abstraction in the *upper* PPW) is improved compared to the reference scheme, the thermal recovery is still significantly lower than an optimal theoretical scenario with no free convection. A high thermal recovery difference ($\Delta\varepsilon_H$=0.21) is obtained in cycle-1, resulting in ε_H of 0.50 for Case 1.e and 0.71 for Case 1.nfc (no free convection). Significant heat loss by free thermal convection and thermal front tilting still occurs for Case 1.e after 50 days of injection during the injection and storage stage (Fig. 8.5c). Hence, a smaller time span between the initial stage of thermal front tilting and hot water abstraction should be considered in order to reduce heat loss by free thermal convection in this high-permeability target aquifer.

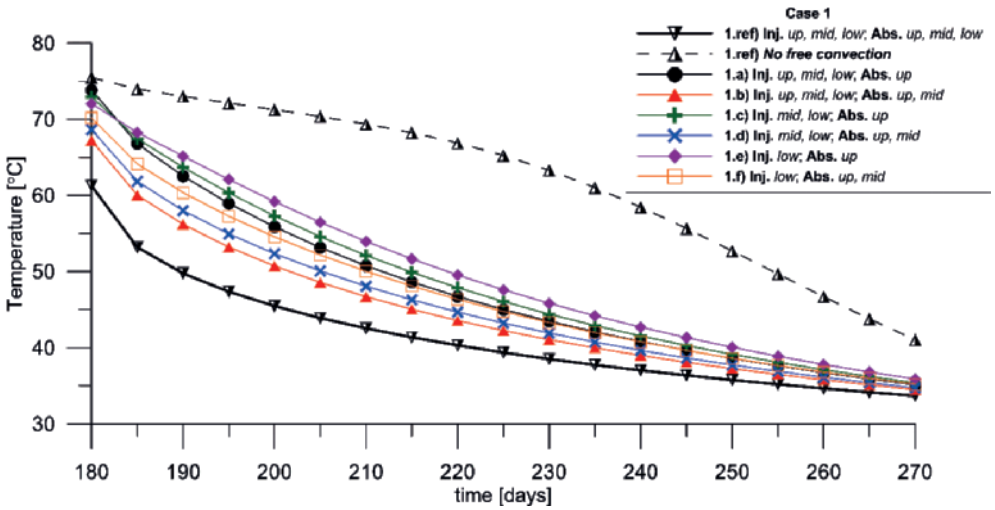

Fig. 8.6 Production temperatures over time for the first recovery period of Case 1 with the different well schemes (a-f).

8.3.2. Injection temperature (Case 2)

An injection temperature of 60 °C was considered for Case 2, to test the potential of different MPPW schemes at a lower temperature difference between hot injection water and ambient groundwater. A higher thermal recovery efficiency is achieved at a lower injection temperature (Case 2; T_i=60 °C) than for the reference scenario (Case 1; T_i=80 °C) for all MPPW schemes due to less pronounced free thermal convection (Fig. 8.8).

Again, the reference well scheme (Case 2.ref) is the least favourable configuration with a calculated thermal recovery efficiency of 0.48 for cycle-1. Similar to Case 1, the most favourable well scheme is Case 2.e with a calculated recovery efficiency increase ($\Delta\varepsilon_H$) of 0.14 compared to the reference well scheme (Case 2.ref) (see Table 8.4). Case 2.c and 2.f rank as the second-most favourable well scheme, with a calculated recovery efficiency increase ($\Delta\varepsilon_H$) of 0.11.

Hot water injected in the lower part (Case 2.d-f) of the aquifer is flowing upwards at smaller velocities due to reduced free thermal convection compared to the base case. As a consequence, the tilting of the thermal front starts at a later stage. Tilting of the thermal front starts in the storage stage after 95 days for Case 2.e-f, while this was only 60 days for Case 1.e-f (Table 8.4). The angle of tilt after storage (180 days) is in the range of 64°-70° for the tested well schemes, while more pronounced free convection in Case 1 resulted in angles of tilt in the range of 74°-80°. Due to this more compact storage of hot water at 60 °C in the aquifer, abstraction in the upper PPW resulted in improved heat recovery. Hence, in Case 2.e the recovery efficiency is closer to the theoretical case

with no free thermal convection (Case 2.nfc) with a $\Delta\varepsilon_H$ value of only 0.09 compared to Case 1 ($\Delta\varepsilon_H$=0.21, see Table 8.3). Moreover, the production temperatures over time for the first recovery period of Case 2.e are closer to the theoretical case (Case 2.nfc) compared to Case 1 (Fig. 8.7).

In cycle-1, the thermal recovery efficiency of Case 2.e (ε_H=0.61) is close to that of the storage with the density difference compensation method (see Chapter 7, ε_H=0.64).

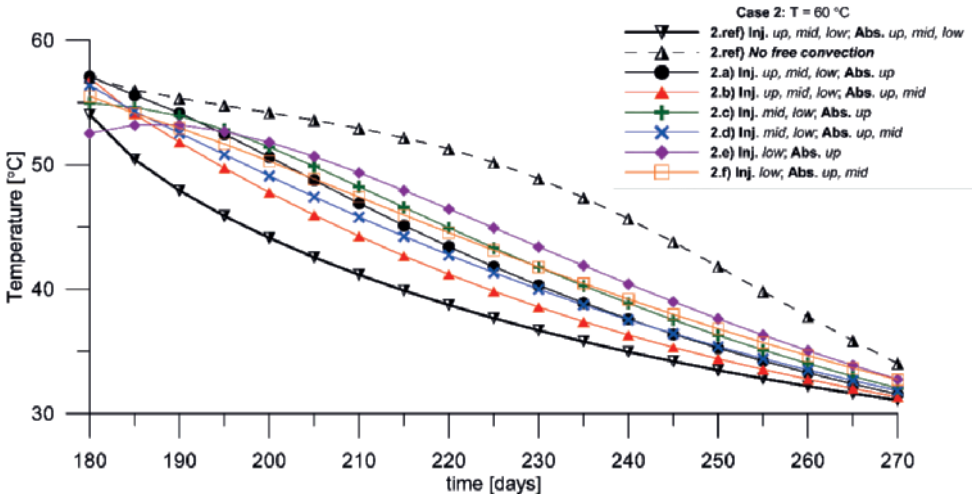

Fig. 8.7 Production temperatures over time for the first recovery period of Case 2 with the different well schemes (a-f).

	Well scheme	Inj. PPW	Abs. PPW	ε_H	$\Delta\varepsilon_H$ with reference scheme	$\Delta\varepsilon_H$ with theoretical case (nfc)
Case 1 ***Base case***	1.e	*lower*	*upper*	0.503	0.144	-0.207
Case 2 ***(T=60 °C)***	2.e	*lower*	*upper*	0.615	0.137	-0.092
Case 3 ***K_h=15 m/d*** ***K_h=1.5 m/d***	3.d	*middle, lower*	*upper, middle*	0.681	0.047	-0.029
Case 4 ***K_h=53.4 m/d*** ***K_h=1.5 m/d***	4.d	*middle, lower*	*upper, middle*	0.653	0.079	-0.053
Case 5 ***K_h=15 m/d*** ***K_h=7.7 m/d***	5.e	*lower*	*upper*	0.598	0.070	-0.114

Table 8.3 Summary of the thermal recovery efficiency for the most favourable well schemes in cycle-1.

	Injection MPPW scheme	Thermal front tilting angle		Delayed tilting of the thermal front [days]
		after 90 days	after 180 days	
Case 1 ***Base case***	**Ref, a-b**) *upper, middle and lower*	63	79.9	5
	c-d) *middle and lower*	57.5	77.7	20
	e-f) *lower*	46	73.7	50
Case 2 ***(T=60 °C)***	**Ref, a-b**) *upper, middle and lower*	52.1	69.9	5
	c-d) *middle and lower*	38.2	68.2	50
	e-f) *lower*	*no tilting*	64.4	95
Case 3 ***K_h=15 m/d*** ***K_h=1.5 m/d***	**Ref, a-b**) *upper, middle and lower*	28.2	55	5
	c-d) *middle and lower*	*no tilting*	39.4	115
	e-f) *lower*	*no tilting*	*no tilting*	*no tilting*
Case 4 ***K_h=53.4 m/d*** ***K_h=1.5 m/d***	**Ref, a-b**) *upper, middle and lower*	35.5	62.8	15
	c-d) *middle and lower*	*no tilting*	*no tilting*	*no tilting*
	e-f) *lower*	*no tilting*	*no tilting*	*no tilting*
Case 5 ***K_h=15 m/d*** ***K_h=7.7 m/d***	**Ref, a-b**) *upper, middle and lower*	50.9	67.3	5
	c-d) *middle and lower*	46.0	66.0	25
	e-f) *lower*	38.8	64.6	45

Table 8.4 Quantification of hot water volume spreading during injection and storage for the simulated cases in the sensitivity analysis, considering the MPPW scheme of injection in all PPWs (Cases ref, a-b), the lower two PPWs (Cases c-d) and the lower PPW (Cases e-f) by the thermal front tilting angle based on the 60 °C temperature contour after injection and storage stage. The start of the thermal front tilting is given in days.

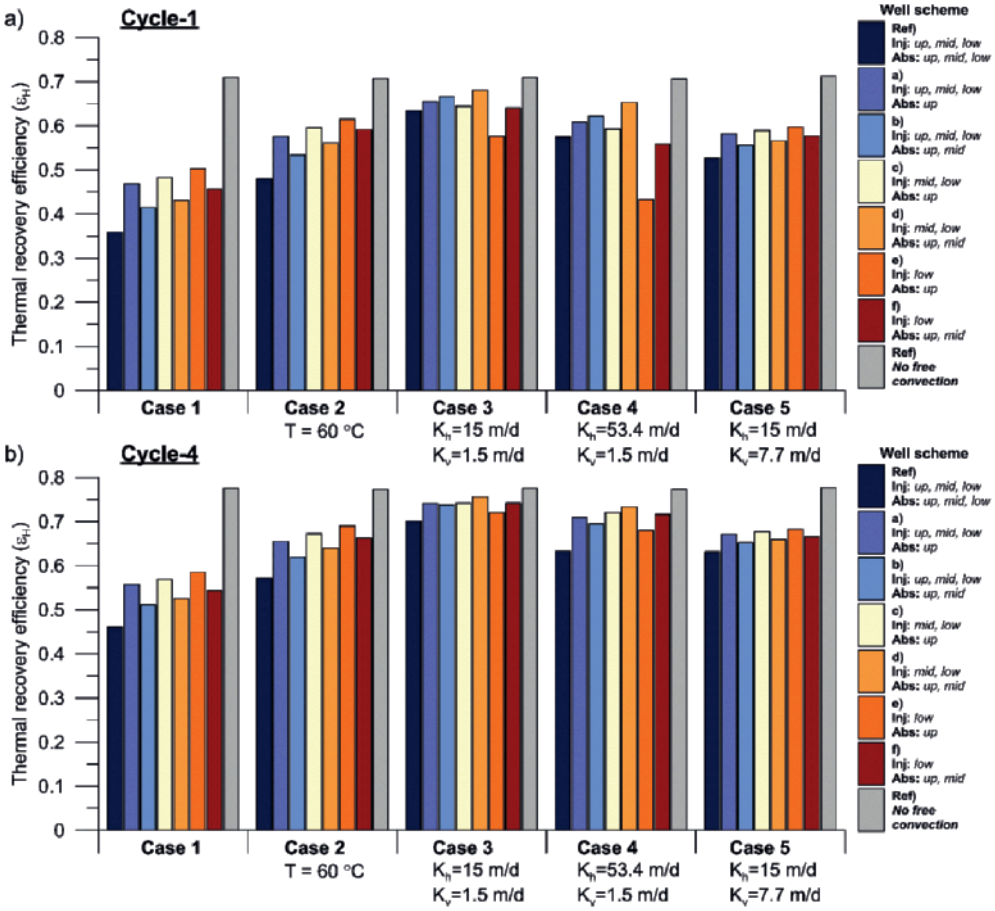

Fig. 8.8 Calculated thermal recovery efficiency for all cases and well scheme configurations **a)** of cycle-1 and **b)** cycle-4.

8.3.3 Hydraulic conductivity and anisotropy (Cases 3-5)

The aquifer characteristics by means of the horizontal and vertical hydraulic conductivity determine the extent of forced and free convection during HT-ATES with MPPW. Various aquifer systems (Cases 3-5) are tested at different anisotropy ratios. Fig. 8.8 shows that the favorability of the different MPPW well schemes differs for Cases 1 and 3-5.

Currently, low-permeability aquifers, such as in Case 3 (an aquifer with a horizontal and vertical hydraulic conductivity of 15 and 1.5 m/day) are selected for HT-ATES systems to reduce free thermal convection and to obtain sufficiently high thermal recovery efficiencies (e.g. Doughty et al. 1982; Schout et al. 2014). In the present study, the calculated thermal recovery efficiencies in the sensitivity analysis are the highest for

Case 3, with ε_H of 0.63 for Case 3.ref. The use of the MPPW configuration in such aquifers only results in a small recovery efficiency increase ($\Delta\varepsilon_H$<0.05) with respect to the reference scheme (Case 3.ref). The most favourable MPPW scheme includes injection in the lower and middle PPW and abstraction in the middle and upper PPW (Case 3.d in Table 8.3). Due to the low vertical hydraulic conductivity of 1.5 m/d, vertical flow by free convection is significantly reduced compared to Case 1. Injection in only the lower PPW (Case 3.e-f) results in no thermal front tilting in the storage stage, since the hot water volume is not transported into the upper portion of the aquifer. Hence, abstraction in the upper PPW (Case 3.e) results in a reduced thermal recovery efficiency compared to the reference scheme Case 3.ref ($\Delta\varepsilon_H$=-0.06) for cycle-1 (Fig. 8.8a).

For Case 4.e a similar trend is observed, where the difference in thermal recovery with respect to the reference well scheme Case 4.ref ($\Delta\varepsilon_H$) is -0.14 for cycle-1. The production temperatures over time for the first recovery period of Cases 4.e are significantly lower (T<50 ºC) compared to the other well schemes (see Fig. 8.9). The high horizontal hydraulic conductivity of 53.4 m/d results in pronounced forced convection in the lateral direction, while the low vertical hydraulic conductivity limits forced convection, as well as free convection in the vertical direction. Hence, the thermal radius of influence at *lower* PPW depth is 40 m after injection stage (90 days) for Cases 4.e-f, while this is only 27.75 m for Cases 1.e-f. Even for injection in both lower and middle PPWs (Case 4.c-d) preferential flow in the lateral direction during injection and limited free convection results in no thermal front tilting after the storage stage (Table 8.4). Note that aquifers with such high anisotropy ratios are used to account for strong heterogeneous layering with altering layers of very high and very low permeability. Hence, in practice, good characterization of the aquifer to account for these low permeability layers is suggested, and the implementation of PPWs might be useless for such aquifer conditions.

Case 5 considers a target aquifer with similar horizontal hydraulic conductivity as Case 3 (15 m/d) and a smaller anisotropy ratio of 1.9. Due to more pronounced free thermal recovery in Case 5, the thermal front tilting starts in early injection stage and results in significantly lower recovery efficiencies compared to Case 3 ($\Delta\varepsilon_H$=-0.11 for Case 5.ref). The differences in thermal recovery efficiencies for the different well schemes of Case 5 are small ($\Delta\varepsilon_H$=0.07) (Fig. 8.8). During injection and recovery stages, the forced convection in the vertical direction is more pronounced and enables heat transport from the upper or lower portions of the aquifer away from and towards the PPW screen. Hence, the exact screen location is less important for aquifers with a low anisotropy ratio (or relative small extent of heterogeneous layering).

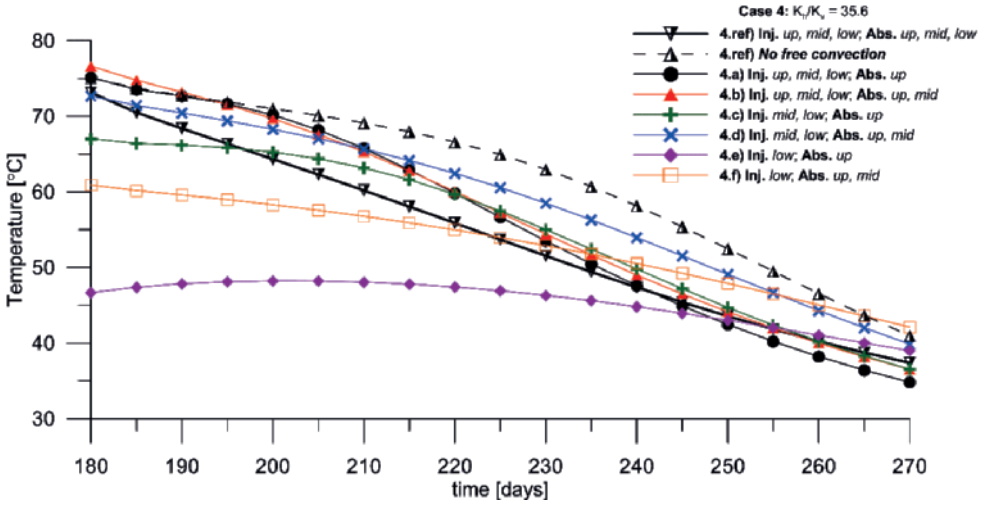

Fig. 8.9 Production temperatures over time for the first recovery period of Case 4 with the different well schemes (a-f).

8.4 Discussion

8.4.1 Further optimization of the MPPW design for HT-ATES

In this study is shown that the effects of free thermal convection during HT-ATES can be reduced using a MPPW scheme during injection and recovery. Injection in the lower part of the aquifer and abstraction in the upper part results in significant improvement of thermal recovery efficiency for seasonal HT-ATES in the high-permeability aquifer of 53.4 m/d (Case 1). However, at large temperature differences between the hot water volume and cold ambient groundwater free thermal convection during injection and storage stage still has a major impact on the thermal recovery efficiency for seasonal HT-ATES. The numerical simulations showed that the thermal front tilting can only be delayed over a limited time span by injecting water in the lower portion of the aquifer.

The sensitivity analysis in the present study assumes a conceptual well scheme for seasonal HT-ATES with equal periods of injection, storage, recovery and rest of each 90 days over a full year. Limiting the period between the start of thermal front tilting and the start of heat recovery could improve the thermal recovery efficiency drastically. However, to overcome the yearly mismatch between heat demand and supply with seasonal heat storage in aquifers of limited thickness (e.g. 20 m) at high temperature contrasts this is an impractical solution. For HT-ATES at injection temperatures of 80 ^{o}C in high-permeability aquifers (Case 1.e-f), the thermal front tilting starts within 50 days (Fig. 8.4).

The time span between heat demand and surplus could be much smaller for industries. Moreover, the efficiency of HT-ATES for the industries is largely determined by the recovered amount of usable heat. Water recovered at temperatures lower than a certain threshold are not usable for industry purposes. Consequently, recovery should be stopped at such threshold temperature. The advantage of abstraction with a MPPW scheme is that it allows for the decoupling of heat production in low-enthalpy and high-enthalpy production (e.g. for household heating and industries) in order to increase the overall efficiency of the HT-ATES system.

Moreover, more complex MPPW schemes can be used for seasonal HT-ATES to improve thermal recovery efficiency. For example, allowing vertically differentiated simultaneous abstraction and re-injection of hot water with the MPPW configuration could actively stabilize the thermal front in the injection and/or storage stage (see Fig. 8.10). Further numerical analysis is required to predict optimal thermal front stabilization at a minimum of pumping costs using this principle.

The existing knowledge in the field of ASR to maintain a stable fresh water plume and to actively limit the mixing potential in brackish aquifers during fresh water storage by a selection of an efficient injection and abstraction scheme (Zuurbier et al. 2014) could also be applied for HT-ATES systems as proposed in Fig. 8.10. A good monitoring scheme (e.g. using distributed temperature sensing with optical fibers) to monitor the thermal interface over time can be used to manage the injection and recovery stage properly and to improve the thermal recovery efficiency of the MPPW HT-ATES system. Especially if cut-off temperatures need to be taken into account, such monitoring schemes are highly recommended.

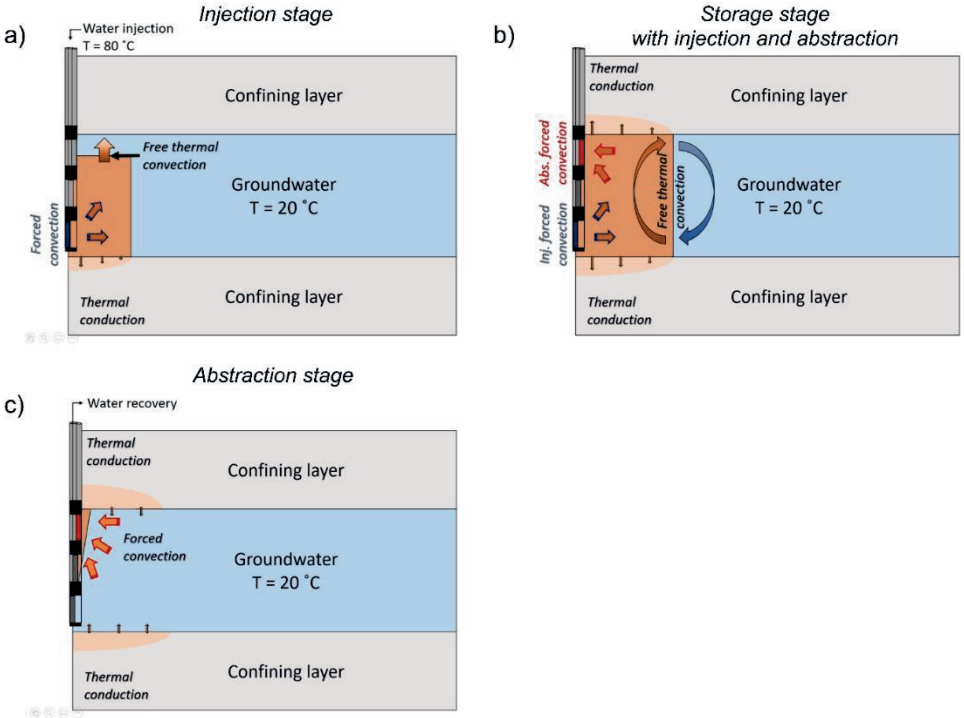

Fig. 8.10 Schematic overview of a full HT-ATES recovery cycle with an optimal MPPW injection and abstraction scheme in a confined aquifer for **a)** injection, **b)** storage and abstraction.

8.4.2 MPPW configuration and aquifer heterogeneity

In the present study, anisotropic, homogeneous aquifers are considered for the numerical simulation of the MPPW HT-ATES systems. However, in reality, aquifers are heterogeneous, and large local variations in permeability could result in erroneous numerical prediction of free and forced convection patterns during HT-ATES operation when assuming anisotropic homogeneous conditions. Proper hydraulic characterization of the aquifer allows for optimal configuration of the MPPW. Detailed information in vertical permeability variability is required to determine the favourable screen depths of the PPWs. Screening injection PPWs below low permeability lenses or layers could already hamper forced and free thermal convection to the upper portion of the aquifer and reduce the efficiency of a MPPW scheme. Moreover, completion of PPWs in low-permeability layers could reduce the well efficiency and the overall hydraulic capacity of the HT-ATES system.

8.4.3 Thermal radius of influence of hot injection water

In the present study, constant aquifer thickness and injection volume are assumed. Hence, the average thermal radius of influence for the simulated scenarios is approximately 38.8 m. Presumably, different thermal radii of influence will affect the relative enhancing effect on thermal recovery efficiency by using different MPPW schemes. For scenarios with smaller aquifer thickness, or higher injection volumes, the thermal radius will be higher than in the present study. Considering a larger thermal radius over time during injection over the entire aquifer thickness, the tilting interface of hot injection water and ambient cold groundwater is at a large radial distance from the well screens. Hence, the use of abstraction PPWs screened in upper portions of the aquifer will result in a smaller increase in thermal recovery efficiency compared to scenarios with a smaller radius of influence, since buoyancy has a lower impact on the recovery efficiency.

However, selection of an injection MPPW scheme for a given injection volume in the lower portions of the aquifer should account for the injected hot water temperature and the aquifer anisotropy (or heterogeneity). For large injection volumes in a high-permeability aquifer with a high anisotropy ratio, the contribution of forced convection in the lateral direction is predominant over combined vertical forced convection and free convection. Consequently, lateral spreading of the heated water plume in the injection stage will be significant, while the buoyancy-driven upward flow during injection and storage stage will be limited. This results in a large interfacial area between hot injection water and cooler ambient groundwater and in induced heat loss by thermal convection for such scenarios. Consequently, the thermal recovery efficiency can be drastically reduced due to picking a poor well scheme for the desired injection volume.

8.5 Conclusions

Injection and recovery with a MPPW scheme can be used to increase the thermal recovery efficiency of seasonal HT-ATES systems. For high-permeability aquifers (K_h=53.4 m/d) with relative small anisotropy ratios (K_h/K_v<7), the injection of hot water at temperatures of 80 ºC for 90 days in the lower part of the aquifer and abstraction for 90 days in the upper part resulted in a thermal recovery efficiency increase of $\Delta\varepsilon_H$ of 0.14 for cycle-1 compared to a well scheme of full injection and abstraction over the entire aquifer thickness. For the consecutive recovery cycles with a similar well scheme, similar increase in efficiency is obtained. Similar trends were observed for injection of hot water at a temperature of 60 ºC.

The use of injection PPWs in the lower part of the aquifer results in heat transport by free thermal convection in solely the vertical direction. It takes time to transport the hot water volume by both forced and free convection over the entire thickness of the aquifer. Hence, the thermal front tilting starts at a much later stage compared to scenarios that consider infiltration over the entire thickness of the aquifer. This results in the storage of more compact hot water volumes over time during injection and storage stage. The horizontal and vertical hydraulic conductivity are essential parameters to predict the start of thermal front tilting after injection in the lower part of the aquifer for a given injection volume of hot water.

In order to select the optimal well scheme for injection and recovery, thorough knowledge of the aquifer characteristics is required. The optimal well scheme for injection, as well as abstraction depends on both the horizontal and vertical hydraulic conductivity of the aquifer. The components of free and forced convection in the vertical and lateral direction determine the extent of the hot water volume during the injection, storage and recovery stage. The thermal recovery efficiency differs for each MPPW scheme in a given target aquifer. Hence, good hydraulic characterization of the aquifer is required to select the optimal well scheme and obtain the highest thermal recovery efficiency.

Chapter 9

Summary and perspectives

In this thesis, the use of partially-penetrating wells (PPWs) in heterogeneous aquifers to obtain more efficient well designs is investigated. By targeting the volumetric recharge of abstraction at a given depth or portion of the aquifer, PPWs allow for optimization of well-system processes and conditions during operation. In practice, a proper design of such well-systems requires insight in the spatial variability of the hydraulic properties of the aquifer system. Installation and completion of wells based on poor hydrogeologic characterization of the subsurface could result in less favourable conditions for the individual abstraction or injection wells, as well as for the operational processes and conditions of the entire well system.

In particular, this thesis focused at the optimization of the well design in various aquifers for the following two well applications:

- Minimize the overall hydraulic impact of construction dewatering systems with artificial recharge PPWs.
- Minimize the buoyancy impact on the thermal recovery efficiencies of seasonal high-temperature aquifer thermal energy storage (HT-ATES) systems.

9.1 Methods

In order to achieve the main research objectives, a broad range of techniques are applied, ranging from experimental fieldwork and labwork, to analytical and numerical analysis.

Groundwater flow in the vicinity of artificial recharge PPWs in heterogeneous aquifers is studied by conducting two field experiments. At first, a small scale field experiment is conducted in the Mönchengladbach area (Rheindahlen, Germany). The three-dimensional flow behavior in a sandy to gravely heterogeneous aquifer is investigated during recharge at a PPW with one meter filter length (a so-called Fast High Volume Infiltration (FHVI)-well). These wells are used by dewatering companies in the Netherlands and Germany in their construction dewatering designs for artificial recharge of abstracted groundwater. This flow behavior is compared to the flow behavior around a fully-penetrating recharge well (FPW) in the same aquifer. Based on the findings of the first experimental fieldwork, a broad fieldwork set-up is designed and realized at Utrecht Science Park area (Utrecht, the Netherlands). By using data from cone penetration tests (CPT), the hydraulic profiling tool (HPT), soil profiles of borehole logs,

aquifer tests and lab analysis of soil samples, detailed information about the aquifer heterogeneity is provided. Heat and bromide tracer tests are conducted during artificial recharge in a PPW and provided information about the flow behavior and the preferential flow paths during injection in the heterogeneous aquifer. The data of these fieldworks are analyzed numerically with the groundwater flow simulation code MODFLOW2000 (Mönchengladbach and Utrecht Science Park) and multi-species mass transport simulation code MT3DMS (Utrecht Science Park only). Moreover, the results from the fieldwork experiments are used to optimize construction dewatering well system designs with such artificial recharge PPWs by conducting a numerical sensitivity analysis.

The well hydraulics of various commonly used well-types for construction dewatering and recharge in unconsolidated soils are analyzed analytically. A broad experimental dataset on the hydraulic characteristics of uniformly-graded filter sands (used for well completion with a filter pack), as well as natural sand or gravel deposits from aquifers, is used for this analytical approach. In order to obtain the hydraulic characteristics of these sand types, packed column experiments on filter and natural sands are conducted to obtain insight in the non-linear flow behavior at high flow velocities.

To verify different optimization methods of HT-ATES systems in heterogeneous, as well as equivalent homogeneous anisotropic, aquifers, sensitivity analysis is performed. This was done by numerical simulation of seasonal HT-ATES with four consecutive recovery cycles of injection, storage, production and rest. To simulate water, heat and solute transport during the HT-ATES recovery cycles, SEAWATv4 is used, which enables simulation of density-dependent groundwater flow. The SEAWATv4 model is validated using experimental (Molz et al. 1983a) and numerical results (Buscheck et al. 1983) of a HT-ATES experiment in a heterogeneous aquifer conducted at Auburn University.

9.2 Design of construction dewatering systems with recharge PPWs

In Chapter 2 is shown that the use of artificial recharge PPWs instead of FPWs in combined construction dewatering and artificial recharge systems in a given aquifer, could significantly reduce the hydraulic impact on the dewatered excavation site. Considering a suitable recharge depth in a specific target aquifer by taking into account its heterogeneity and thickness, allows for optimal three-dimensional use of the subsurface. Consequently, the above-ground distance between the dewatered excavation site and the artificial recharge site can be reduced, while the re-pumping of recharged

water at the excavation site, as well as the overall costs of the combined dewatering and artificial recharge can be minimized. The field experiments described in Chapter 2 and 6 show the importance of detailed hydrogeological characterization of the soil. Selection of high-permeability layers in the subsurface allows infiltration at high volumetric flow rates in artificial recharge PPWs with limited well screen length. Moreover, vertical variability in hydraulic conductivity results in preferential flow paths in the lateral direction. In Chapter 6 is shown that the influence of small clay layers have a major influence on the flow paths in a heterogeneous aquifer and, hence on the transport of water in the aquifer during artificial recharge. Identifying low-permeability layers and small semi-impervious layers such as clay, peat, loam or silt in the well design stage could have a major impact on the efficiency of the well system. Chapter 6 shows that during the tracer test at the Utrecht Science Park, a small low-permeability layer can be indicated from the CPTs and borehole logs, which resulted in limited groundwater flow into the upper portion of the aquifer, and significantly delayed breakthrough of the bromide ion tracer concentration.

In practice, Dutch and German dewatering companies are using FHVI-wells (artificial recharge PPWs with a well screen length of 1 or 2 meter) to optimize their well design with the above-described method. Quick installation of such PPWs with straight-flush rotary drilling and well completion with a naturally-developed collapsed aquifer zone instead of a filter pack around the well screen have shown its advantages in construction dewatering projects. In addition, the overall well completion costs of these wells are relatively small compared to other well installation techniques and allows for economical design and installation of multiple artificial recharge PPWs. In Chapter 5 is shown that installation of wells with naturally-developed packs instead of the use of a filter pack in highly-permeability layers (K>300 m/d) does not necessarily require larger well heads during artificial recharge.

Moreover, the range of feasible well heads in PPWs during artificial recharge in deeper portions of the aquifer are larger compared to the use of FPWs in shallow aquifers. The field experiment at Utrecht Science Park show that enabling infiltration of anaerobe groundwater from the dewatering site in artificial recharge PPWs using a closed discharge piping system (e.a. maintaining sufficient hydraulic pressure throughout the system) allows for long-term artificial recharge without clogging of the filter. If the hydraulic pressure in the dewatering system is not maintained, such as during the heat tracer test, precipitation of iron-oxide occurs in the aboveground system and caused significant well clogging of the PPW. For well-systems with abstraction wells in oxic groundwater, such as in the Mönchengladbach fieldwork, one should also take into account the potential well clogging of the artificial recharge PPWs. Well clogging is an

important aspect that needs to be considered during the planning of an efficient construction dewatering design with artificial recharge PPWs.

Using PPWs with limited filter lengths always results in additional well losses due to partial penetration. However, by selection of a proper screen interval depth based on good soil characterization, additional head loss by partial penetration can be significantly minimized. For example, analytical analysis in Chapter 5 shows that the use of a PPW in a heterogeneous aquifer that screens a 2 meter thick high-permeability layer of 328 m/d, under and overlain by the non-screened permeability layers of 32.8 m/d of each 9 meter thick, results in an additional head loss by partial penetration of only 0.52 m. If this high-permeability layer is not taken into account and a simplified equivalent anisotropic homogenous aquifer is considered, the additional head loss is overestimated by a factor of 4 (2.0 m additional head loss due to partial penetration).

9.3 Non-linear flow behaviour in sand and gravel

In near-well hydraulics, increased flow velocities and Reynolds (Re) numbers in the filter pack, as well as in aquifer material, occur due to converging or diverging flow lines towards or from the well screen. Under certain flow conditions (Re>10), fluid flow through porous media starts to deviate from the linear relationship between the flow rate and hydraulic gradient. At such flow conditions, Darcy's law for laminar flow can no longer be assumed and non-linear relationships are required to predict flow in the Forchheimer regime. In Chapter 3 a dataset on non-linear flow behavior through 11 uniformly graded commercially available filter sands ($0.39<d_{50}<6.3$ mm) is provided. In order to investigate the effect of various grain size distributions, mixtures of the filter sands are used to obtain a slightly more well graded composite sand, i.e. increased C_u values by a factor of 1.19 up to 2.32, with respect to its associated reference filter sand at equal median grain size (d_{50}) and porosity. For all composite sands, the observed flow resistance is higher than in the corresponding reference sand at equal d_{50}, resulting in increased Forchheimer a coefficients by factors up to 1.68, as well as increased Forchheimer b coefficients by factors up to 1.44. A modified Ergun relationship with Ergun constants of 183.8 for A and 2.53 for B, as well as the use of d_{30} as characteristic pore length predicted the Forchheimer coefficients a and b accurately for this dataset on uniformly-graded material ($C_u<2$). In Chapter 4 we investigated the impact of variable grain size distributions on the extent of non-linear flow behavior through 18 different packed beds of natural sand and gravel deposits, as well as composite sand and gravel mixtures of filter sands within a broad range of uniformity ($2.0<C_u<17.35$) and porosity values ($0.23<n<0.36$). Increased flow resistance is observed for the sand and gravel with high C_u values and low porosity values. The present study shows that for granular

material with wider grain size distributions (C_u>2), the d_{10} instead of the average grain size (d_{50}) as characteristic pore length should be used. Ergun constants A and B with values of 63.1 and 1.72 respectively, resulted in a reasonable prediction of the Forchheimer coefficients for the investigated granular materials. This comprehensive dataset on non-linear flow behavior in sand and gravel is useful for analysing well hydraulics such as is done in Chapter 5, as well as aquifer tests.

9.4 High temperature aquifer thermal energy storage

Besides using PPWs to optimize construction dewatering systems, multiple-PPWs systems are an useful method to improve thermal recovery efficiencies during HT-ATES (T_{in}>60 °C) by limiting the heat loss due to buoyancy-driven flow. To date, the thermal recovery efficiency of small scale HT-ATES systems are low due to the buoyancy of the injected hot water and, hence fully-operational seasonal HT-ATES is barely applied in practice. In Chapter 8 is shown that injection and recovery with a multiple PPWs scheme can be used to increase the thermal recovery efficiency. Free and forced convection in the injection, storage and recovery stage is highly dependent on the hydraulic conductivity and anisotropy of the aquifer. For high-permeability aquifers (K_h=53.4 m/d) with relative small anisotropy ratios (K_h/K_v=7), the injection of hot water (T_{in}=80 ºC) for 90 days in the lower part of the aquifer and abstraction for 90 days in the upper part resulted in a thermal recovery efficiency increase of $\Delta\varepsilon_H$ of 0.14 for the first recovery cycle with respect to a well scheme of full injection and abstraction over the entire aquifer thickness. However, considering an aquifer with similar horizontal conductivity but significant anisotropy (K_h/K_v=35), i.e. an highly heterogeneous aquifer with small low permeability layers of clay, silt or peat, the well scheme of injection in the lower part and abstraction in the upper part of the aquifer is the least favorable well scheme. In this case a thermal recovery reduction of $\Delta\varepsilon_H$ of -0.06 for the first recovery cycle is obtained.

In addition, the potential to improve the thermal recovery efficiency by compensation of the density difference using increased salinity contrasts of the injected hot water for an injection-storage-recovery HT-ATES well scheme is investigated in Chapter 7. For the reference case, in which 80 °C water was injected into a high-permeability aquifer, regular HT-ATES had an efficiency of 0.40 after four consecutive recovery cycles. The density difference compensation method resulted in an efficiency of 0.69, which is close to the theoretical case of no buoyancy-driven flow (0.76). Sensitivity analysis showed that the net efficiency increase by using the density difference compensation method instead of regular HT-ATES is higher for aquifers with higher hydraulic conductivity, larger temperature difference between injection water and

ambient groundwater, smaller injection volume, and larger aquifer thickness. This means that density difference compensation allows the application of HT-ATES in thicker, more permeable aquifers, and with larger temperatures than would be considered for regular HT-ATES systems.

9.5 Perspectives

The results presented in this thesis gain insight in how PPWs can be used to improve the design of well systems in heterogeneous aquifers. For each well system it is essential to determine the site-specific hydraulic conditions and variability in the hydraulic characteristics of the subsurface in the designing stage. Assessment of the optimal well screen length, depth, as well as the mutual distance between wells itself, requires a proper consideration of anisotropy, and more-specifically, vertical variability in hydraulic conductivity in the aquifer. Detailed knowledge of these hydraulic characteristics are essential in the proper use of PPWs for optimization of well systems as proposed in this thesis.

Too often, conceptual models are considering equivalent homogenous aquifer characteristics and make use of one standard anisotropy ratio (i.e. anisotropy ratio of 2-10) to deal with aquifer heterogeneity. However, investigation of the full-potential of PPWs in order to optimize well systems should account for a much more detailed approach. For example, to date, dewatering companies often use a simplified modeling scheme to design their combined construction dewatering and artificial recharge system. The conventional approach considers artificial recharge wells that screen 10-20 meter of the aquifer. To ensure limited hydraulic impact on the dewatered excavation sites during artificial recharge, these wells need to be placed at considerable distance (in practice, easily 100 m away from the excavation site). In urban areas, selection of a proper recharge site, potential damage to underground construction and basements during artificial recharge, as well as the required amount of above-ground pipelines through public space, have significant implications for the entire well design. Accounting for aquifer heterogeneity and PPWs in predictive models while designing the construction dewatering system instead of sticking to the conventional approaches can easily solve such problems.

It is strongly recommended to have at least a rough insight of the aquifer heterogeneity prior to the design and installation of the well system. In construction dewatering systems, usually some soil characterization can already be done based on a very limited amount of data, such as CPTs and soil profiles. Analysis of such data in analytical and numerical approaches should form the basis for predicting potential well losses, as well as feasible screen depths and lengths of the PPWs.

For the feasibility of PPWs in well systems that are operative for decades, such as the proposed multiple-PPWs HT-ATES design in this thesis, a detailed hydrogeological investigation is required. The numerically simulated scenarios are assuming different equivalent homogeneous anisotropic aquifers that account for aquifer heterogeneity. These scenarios already show that the buoyancy-driven flow is highly dependent on the anisotropy. Implementation of aquifer heterogeneity is required instead of considering homogeneous aquifer conditions in numerical models to predict free and forced convection during HT-ATES operation for a specific field site to obtain reliable predictions of the thermal recovery efficiency. One needs to account for local heterogeneities of clay, peat, silt or loam layers prior to selection of the ideal well screen depths and lengths of the multiple PPWs. This also holds for the optimal abstraction and injection scheme during HT-ATES operation based on the free and forced convection patterns of the hot water volume in the heterogeneous aquifer. The simulations of the density difference compensation method using salinity contrasts for the injected hot water in the heterogeneous layered aquifer show preferential flow of hot, saline water in the high-permeability layer and complex thermo-haline convection patterns occur due to the plume segregation between the hot water and the saline water. The expenses of a detailed hydrogeological investigation could significantly outweigh the costs of a poorly developed HT-ATES well design. Especially if one wants to examine the proposed methods of multiple PPWs or density compensation by using salinity contrast for an actual scenario in the field.

Appendices

Appendix A

Volumetric recharge rate and head rise during PPW recharge test

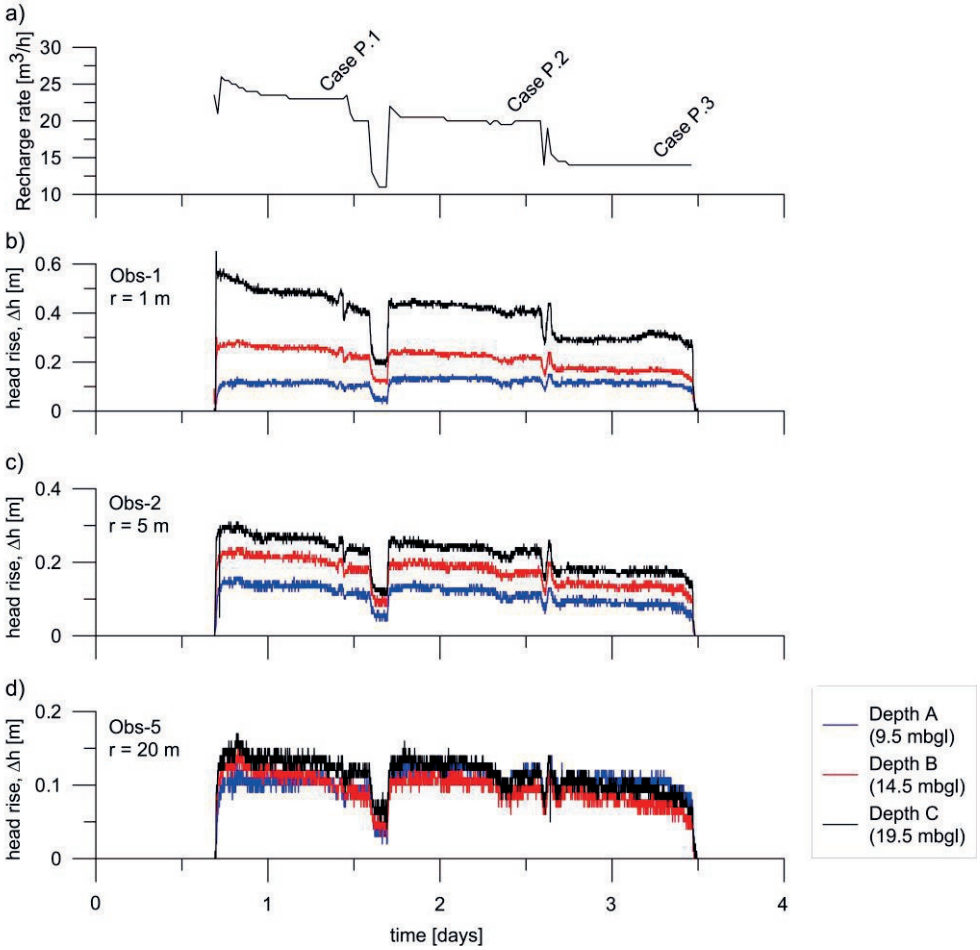

Fig. A a) The recharge rate over time, as well as the head rise, Δ*h* in **b)** Obs-1, **c)** Obs-3, **d)** Obs-1. The used values for stationary groundwater flow modelling for Case 1-3 are labelled.

Appendix B

Grain size distribution characterization of the uniformly-graded filter sands

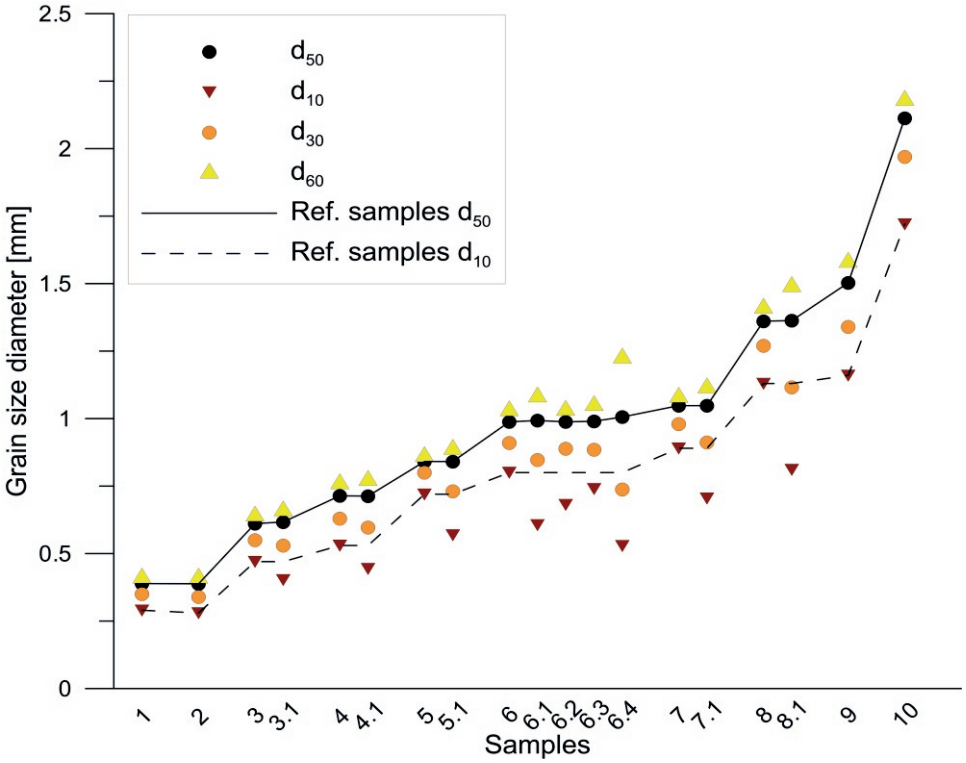

Fig. B The grain size distribution characterization (d_{10}, d_{30}, d_{50} and d_{60}) for the uniformly graded filter sands (S.1-10) and the sand mixtures (S3.1-8.1). Note that the coarse gravel (S.11 with d_{50}=6.34 mm) is not taken into account.

Appendix C

Non-linear flow behavior in the composite sands

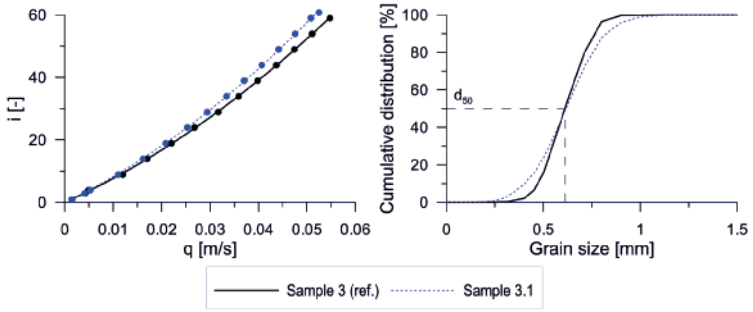

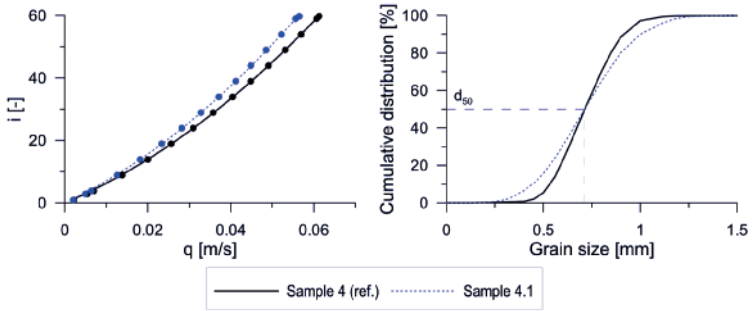

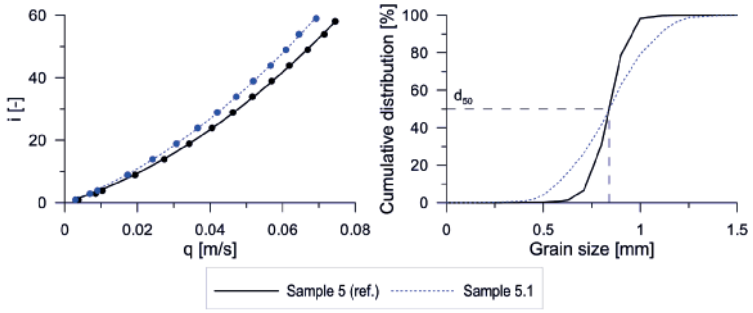

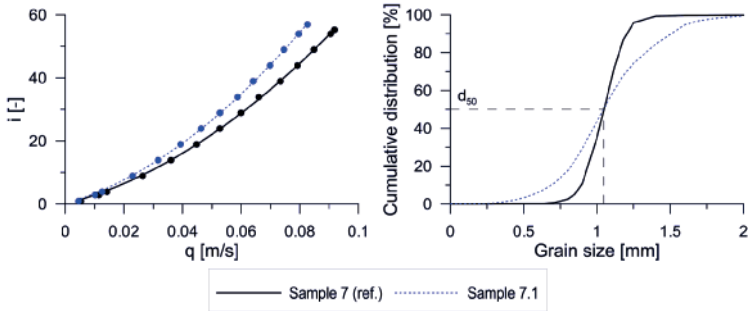

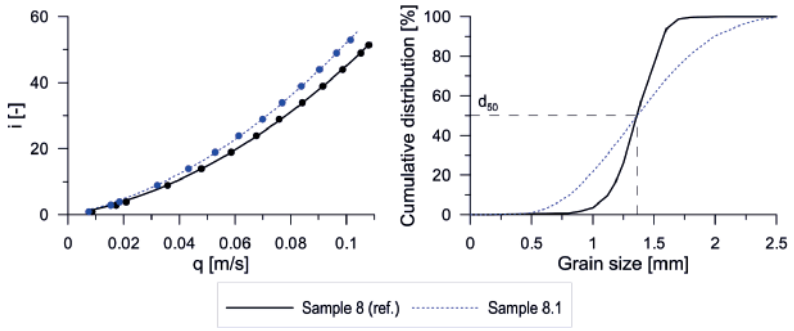

Fig. C a) The *i-q* plots for the sandy porous media S3.1-8.1 and **b)** the cumulative grain size distributions.

Appendix D

Composition of the artificial mixed filter sands

	Mass percentage of the filter sand sample												
	F.1 [0.39 mm]	**F.2 [0.39 mm]**	**F.3 0.61 mm]**	**F.4 [0.71 mm]**	**F.5 [0.84 mm]**	**F.6 [0.99 mm]**	**F.7 [1.05 mm]**	**F.8 [1.36 mm]**	**F.9 [1.50 mm]**	**F.10 [2.11 mm]**	**Gravel [3.00 mm]**	**F.11 [6.34 mm]**	**Cobbles [>9.00 mm]**
S.1	0	0	0	0	0	0	**100**	0	0	0	0	0	0
1.1	0	10	10	10	10	10	**15**	15	15	5	0	0	0
1.2	0	18	13	13	3	3	**4.5**	14.5	14.5	16.5	0	0	0
1.3	0	30	10	5	3	0	**0**	10	15	22	0	5	0
1.4	0	30	10	5	3	0	**0**	10	5	20	0	14.67	2.33
1.5	0	40	10	0	0	0	**0**	0	0	10	0	30	10
S.2	0	0	0	0	0	0	0	0	**100**	0	0	0	0
2.1	0	0	0	0	0	0	10	5	**70**	15	0	0	0
2.2	0	5	5	5	10	5	10	5	**10**	40	0	5	0
2.3	0	15	15	5	5	2.5	2.5	5	**35**	15	0	0	0
2.4	0	15	15	5	5	2.5	2.5	5	**0**	20	0	11.75	18.25
2.5	0	30	15	0	5	0	0	0	**0**	2	0	24.8	23.2
S.3	0	0	0	0	0	0	0	0	0	0	0	**100**	0
3.1	0	0	0	0	0	0	0	1	6.5	12.5	8	**42**	38
3.2	0	0	0	0	0	0	0	2	29	4	8	**14**	43
3.3	0	0	0	0	0	1	3	17	29	0	0	**0**	50

Table D Mass percentage of the uniformly-graded filter sands of the artificial mixed filter sand samples in this study. Note that the gravel (3.0 mm) and cobbles (>9 mm) are sieved and selected from the Wyenhütte gravel and sand for mixing with the filter sands to obtain a proper grain size distribution for the artificial mixed gravel samples.

Appendix E

Grain shape analysis

The grain shape properties of the filter sands that are used for the artificially mixed sands (see Appendix D), as well as for the natural sands M.1 and W.1 are determined with the CAMSIZER® P4 (Retsch, Germany). The use of the Camsizer imaging techniques enables to detect the various dimensions of irregularly shaped particles by means of the sphericity (S^{Kr}) and roundness (R^{Kr}) based on the Krumbein scale (Krumbein and Sloss 1963), sphericity (S^{QP}), symmetry (*symm*), convexity (C_x), and elongation (e) (e.g. Altuhafi et al. 2013)):

$$S^{QP} = \frac{\sqrt{4\pi A_s}}{P} \tag{E1}$$

where A_s [m²] is the surface area, and P [m] is the perimeter of the sphere.

$$symm = \frac{1}{2}[1 + \min\frac{r_1}{r_2}] \tag{E2}$$

where r_1 und r_2 [m] are the distances from the centre of the grain to the outer borders in the measuring direction. For asymmetric particles *symm* is < 1.

$$C_x = \sqrt{\frac{A_{real}}{A_{conv}}} \tag{E3}$$

where A_{real} [m²] is the real area of the particle projection and A_{conv} [m²] is the convex area of particle projection.

$$e = \frac{L}{W} \tag{E4}$$

where L [m] is the maximum grain diameter and the W [m] is minimum grain diameter.

The grain shape analysis in Table E shows that the grain characteristics of the filter sands and natural sands are similar and the granular material can be classified as subangular-subrounded sand.

Filter sand used for artificially mixed sands	S^{QP}	Symm	e	C_x	S^{Kr}	$*R^{Kr}$
F.2	0.79	0.90	1.35	0.99	0.75	0.54
F.3	0.80	0.90	1.34	0.99	0.76	0.55
F.4	0.80	0.90	1.34	0.99	0.75	0.54
F.5	0.80	0.90	1.35	0.99	0.75	0.52
F.6	0.80	0.90	1.35	0.99	0.75	0.54
F.7	0.80	0.90	1.35	0.99	0.75	0.52
F.8	0.79	0.90	1.38	0.99	0.73	0.52
F.9	0.79	0.90	1.38	0.99	0.73	0.52
Natural sand						
M.1	0.79	0.90	1.35	0.99	0.75	0.54
W.1	0.76	0.90	1.39	0.99	0.73	0.48

Table E Grain shape properties of the filter sands with a grain size smaller than 2.0 mm and the natural sand M.1 and W.1. *Note that R^{Kr} is calculated on the grain size range of 0.3-2.0 mm.

Appendix F

Comparison of the natural and variably graded granular material dataset with the literature dataset

The relationship between the average grain size d_{50} of the tested packed beds with granular material and the Forchheimer coefficients a and b is shown in Fig. F1. The dataset of the present study is compared to the entire dataset in the existing literature listed in Table 4.1. Note that for the study of Sedghi-Asl et al. (2014), the Forchheimer coefficients b given in their graphs are used instead of the values given in their table. Moreover, the packed bed experiments on unconsolidated graded aggregates (Dan et al. 2016) at the highest compaction grade are shown. Overall, the obtained relations between the Forchheimer coefficients and the average grain size for each individual experimental study on non-linear flow behaviour through packed beds of uniformly-graded granular material are good (e.g. Salahi et al. 2015; Sedghi-Asl et al. 2014; Van Lopik et al. 2017). However, fitting over the entire dataset of uniformly-graded granular material obtained much more scattering and poorer fits (Fig. F1).

For non-linear flow behaviour through packed beds of granular material with wide grain size distributions, a wide range of Forchheimer coefficients is obtained at given average grain size d_{50} and consequently, no satisfactory correlation can be found. The Forchheimer coefficients a and b for a given d_{50} are significantly higher for the samples with lower porosity values and no clear correlation can be found for the dataset with n<0.30. For example, wrongly assuming S.3.3 (d_{50}=6.33mm) as an uniformly-graded material, the fitting line predicts Forchheimer coefficients a and b of respectively 7.2 s/m and 296 s^2/m^2. However, the actual values are a factor of 40 and 30 higher.

Van Lopik et al. (2017) showed that a clear relationship can be found between Forchheimer coefficients a and b for uniformly-graded filter sands with average grain sizes ranging from 0.39 to 6.34 mm (Fig. F2). This is in agreement with the other datasets in the literature (Ranganadha et al. 1970; Venkataraman et al. 1998; Moutsopoulos et al. 2009; Sedghi-Asl et al. 2014; Salahi et al. 2015 and Li et al. 2017). In the present study, the samples with medium gradation (C_u<5 and n>0.30) the correlation between the Forchheimer coefficients a and b is in agreement with the fitting line obtained from the uniformly-graded filters sands (Van Lopik et al. (2017). However, at higher gradations (C_u>5), the Forchheimer coefficient b is significantly overestimated at a given Forchheimer coefficient a (Fig. F2). Overall, the widest grain size distributions (C_u>10) and lowest porosities (n is 0.23-0.25) resulted in the largest difference with the fitting line (see samples S1.5, S2.5, S3.3 and W.2).

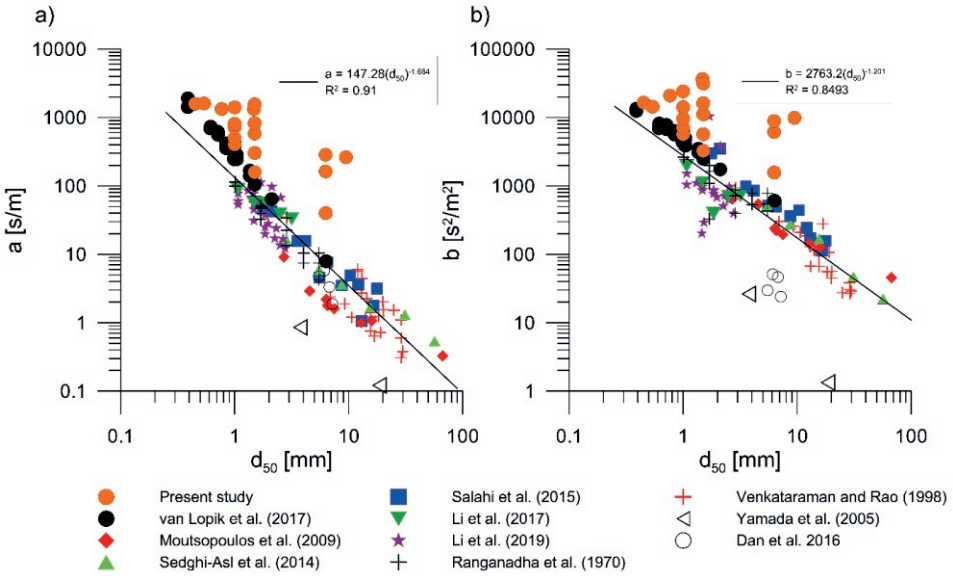

Fig. F.1 a) Relationship between the grain size d_{50} [mm] and Forchheimer coefficient *a*, **b)** as well as for Forchheimer coefficient *b.* For the fitting, the datasets with C_u>3 (the present study, Yamada et al. (2005) and Dan et al. (2016)) are not taken into account to exclude data on granular material with wide grain size distributions.

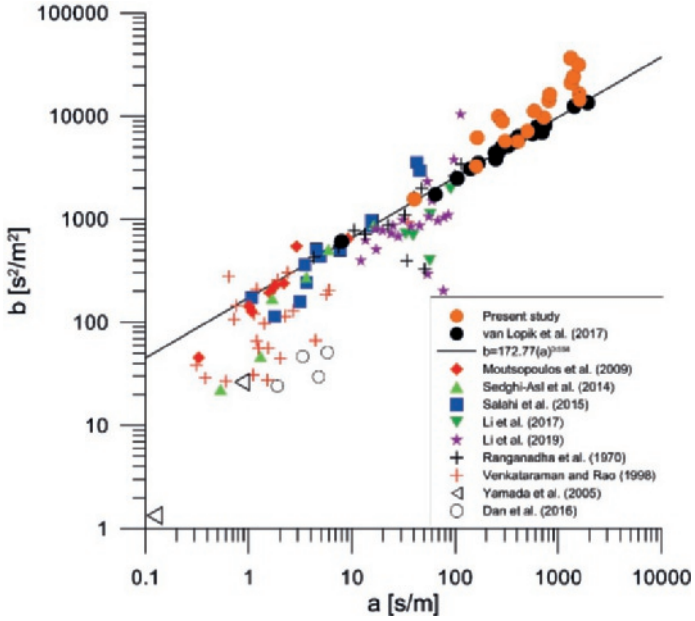

Fig. F.2 Forchheimer coefficient *b* as a function of Forchheimer coefficient *a*. The fitting line on a dataset of 20 uniformly-graded sands and gravels is provided by Van Lopik et al. (2017).

Appendix G

Assessment of the empirical relationships for the graded granular materials

In this section, the validity of the empirical relationships (Eq. 3.6-3.9) of Ergun (1952), Kovács (1981), MacDonald et al. (1979), Kadlec and Knight (1996) and Sidiropoulou et al. (2007) (see Table 3.1 in Chapter 3). The entire dataset is used for the linear regression analysis, as well as the *NOF* analysis (Tables G1 and G2). Overall, the scattering around the regression line is relatively high using the Eq. 3.5-3.9 and the d_{50} or d_{30} as characteristic pore length (R^2<0.78). Overall, the correlation between the empirical relationships (Eq. 3.5-3.9) using the average grain size (d_{50}) on the one hand and the experimental data of present study on the other hand is relatively poor, especially if compared to other studies with uniformly-graded granular material (e.g. Moutsopoulos et al. 2009; Van Lopik et al. 2017). The linear regression analysis shows that the use of the Ergun relation and that d_{10} resulted in fits with reduced scattering (R^2-coefficients of respectively 0.9 and 0.8). However, for these cases, the Forchheimer coefficient a was significantly overestimated (Table G1). Reasonable fits were obtained for Forchheimer coefficient b using d_{10} and the relationships of Ergun (1952), Kovacs (1981) and Kadlec and Knight (1998) (Eq. 3.5, 3.6 and 3.8).

	d_{10}			d_{30}			d_{50}		
	Slope	**R^2**	**NOF**	**slope**	**R^2**	**NOF**	**slope**	**R^2**	**NOF**
Ergun (1952)	2.865	0.93	2.49	1.191	0.78	0.602	0.354	0.73	0.853
Kovács (1981)	2.751	0.93	2.35	1.143	0.78	0.559	0.340	0.73	0.879
MacDonald et al. (1979)	7.358	0.90	8.46	3.088	0.73	3.15	0.884	0.78	0.436
Kadlec and Knight (1996)	16.53	0.92	20.46	6.903	0.76	8.34	2.015	0.76	1.643
Sidiropoulou et al. (2007)	0.480	0.75	0.702	0.238	0.76	0.986	0.109	0.44	1.151

Table G.1 Linear regression slope and *NOF* value for the evaluation of the empirical relationships (Eq. 3.5-3.9) for the Forchheimer coefficient *a*.

	d_{10}			d_{30}			d_{50}		
	Slope	**R^2**	**NOF**	**slope**	**R^2**	**NOF**	**slope**	**R^2**	**NOF**
Ergun (1952)	0.850	0.80	0.341	0.547	0.73	0.622	0.265	0.52	0.949
Kovács (1981)	1.166	0.80	0.441	0.750	0.73	0.448	0.363	0.52	0.834
MacDonald et al. (1979)	1.928	0.83	1.33	1.243	0.75	0.610	0.591	0,66	0.582
Kadlec and Knight (1996)	0.971	0.80	0.325	0.625	0.73	0.546	0.303	0,52	0.904
Sidiropoulou et al. (2007)	0.988	0.35	0.651	0.557	0.37	0.671	0.248	-0.08	0.995

Table G.2 Linear regression slope and *NOF* value for the evaluation of the empirical relationships (Eq. 3.5-3.9) for the Forchheimer coefficient *b*.

Appendix H

Solution for the Darcy-Forchheimer equation for converging flow in filter packs towards screen slots

Inside a filter pack, groundwater flow is affected by the presence of well screens. During abstraction, groundwater has to converge to the screen slots, which causes an additional head called Δh_{cv}. Boulton (1947) derived an equation for Δh_{cv} based on the ratio (δ_s) of slot aperture (l) and circumference of the well:

$$\delta_s = \frac{N_s l}{2\pi R} \tag{H1}$$

where N_s is the number of slots inside the circumference of a well and R is the radius of a well. The equation by Boulton (1947) is given by (as Houben, 2015):

$$\Delta h_{cv} = \frac{Q}{N_s K_{fp} L_s} \ln\left(\frac{2}{1-\cos \delta_s \pi}\right) \tag{H2}$$

where K_{fp} is the hydraulic conductivity of the gravel pack and L_s is the height of the screen opening. Unfortunately, the derivation of Boulton's equation is not given in that article and therefore the assumptions behind the equation are unknown. Therefore, a derivation of the equation for s_{cv} is given below.

The starting point of the derivation is the Darcy-Forchheimer equation, which is given by:

$$\frac{\partial h}{\partial r} = -\frac{Q}{2\pi r K_{fp} L_s N_s} - \beta\left(\frac{Q}{2\pi r K_{fp} L_s N_s}\right)^2 \tag{H3}$$

where *r* is a radial coordinate. By separating variables, we obtain:

$$\partial h = -\left(\frac{Q}{2\pi K L_s N_s}\right)\frac{1}{r}\partial r - \left[\beta\left(\frac{Q}{2\pi K L_s N_s}\right)^2\right]\frac{1}{r^2}\partial r \tag{H4}$$

The Darcy-Forchheimer equation is independent of slot aperture, therefore a geometric consideration is conducted before solving the Darcy-Forchheimer equation.

In order to obtain Boulton's equation, the distance between the well circumference and the opening (distance *D*) has to be considered constant (see Fig. H). This assumption implies that flow remains radial inside the gravel pack until the groundwater is very close

to the well. As a consequence, stagnant zones of groundwater arise between the screen slots (see Fig. H) which forces the remaining groundwater towards the screen openings. Distance *D* is defined for any circle having a radius r as such that *D* is constant (based on trigonometry) (see Fig. H):

$$D = R - H = r\left(1 - \cos\frac{\theta}{2}\right) = r(1 - \cos\pi\delta) \tag{H5}$$

Differentiating equation H5, yields:

$$\frac{1}{r}\partial r = \frac{\pi\sin\pi\delta}{1-\cos\pi\delta}\partial\delta \tag{H6}$$

Using equations H5 and H6, the Darcy-Forchheimer equation becomes:

$$\partial h = -\left(\frac{Q}{2\pi K_{fp}L_sN_s}\right)\left(\frac{\pi\sin(\pi\delta)}{1-\cos(\pi\delta)}\partial\delta\right) - \left[\frac{\beta}{D}\left(\frac{Q}{2\pi K_{fp}L_sN_s}\right)^2\right]\pi\sin(\pi\delta)\,\partial\delta \tag{H7}$$

In equation (H7), the radial coordinates are projected on δ coordinates, which represents flow perpendicular to the radius.

The boundary conditions for equation H7 are:

$$\begin{cases} h = h_{gp} & \delta = 1 \\ h = h_s & \delta = \delta_s \end{cases} \tag{H8}$$

Defining integration of equation H7 yields:

$$\int_{h=h_s}^{h_{gp}}\partial h = -\left(\frac{Q}{2\pi K_{fp}L_sN_s}\right)\int_{\delta=\delta_s}^{1}\frac{\pi\sin(\pi\delta)}{1-\cos(\pi\delta)}\partial\delta - \left[\frac{\beta}{D}\left(\frac{Q}{2\pi K_{fp}L_sN_s}\right)^2\right]\int_{\delta=\delta_s}^{1}\pi\sin(\pi\delta)\,\partial\delta \tag{H9}$$

Finally, we obtain:

$$\Delta h_{cv} = \frac{Q}{2\pi N_s K_{fp}L_s}\ln\left(\frac{2}{1-\cos\delta_s\pi}\right) + \frac{\beta}{r_s}\left(\frac{Q}{2\pi K_{fp}L_sN_s}\right)^2 \tag{H10}$$

where the Forchheimer coefficient b equals $b = \frac{\beta}{K_{fp}}$

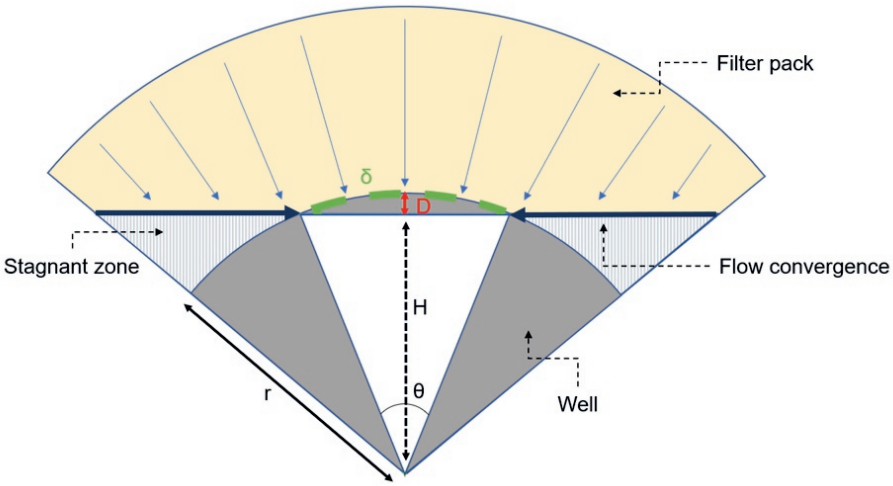

Fig. H Schematic overview of flow convergence in the filter pack (assumption by Boulton 1947).

Appendix I

Planview the tracer test field site at Utrecht Science Park

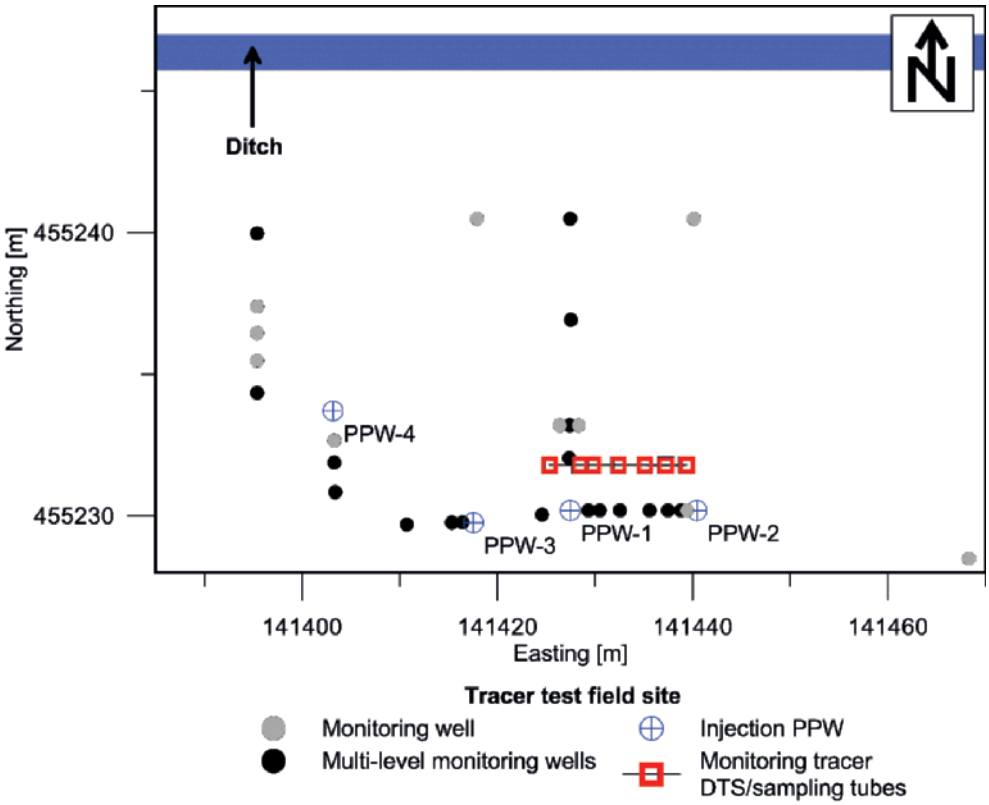

Fig. I.1 Planview of the field site with the location of four injection PPWs, where PPW-1 is screened at a depth of 11.0 to 13.0 mbsl, PPW-2 at 10.3 to 12.3 mbsl, PPW-3 at 14.8 to 16.8 mbsl and PPW-3 at 8.4 to 10.4 mbsl. Multi-level head monitoring was done during the constant rate and step rate aquifer tests on the PPWs at the shown monitoring wells with both diver and manual measurements.

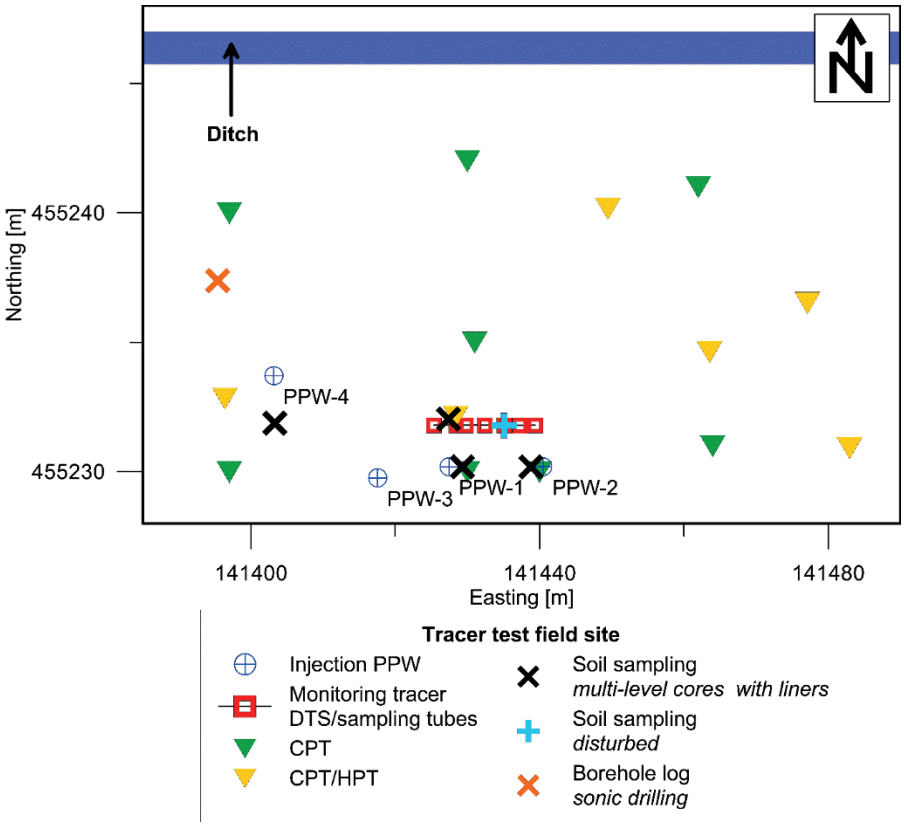

Fig. I.2 Planview of the field site with the locations of the CPTs, HPTs and soil sampling.

References

Adler, P.M., Malevich, A.E., & Mityushev, V.V. (2013). Nonlinear correction to Darcy's law for channels with wavy walls. *Acta Mechanica, 224*(8), 1823-1848.

Ahmed, N., & Sunada, D.K. (1969). Nonlinear flow in porous media. *Journal of the Hydraulics Division. Proceedings of the American Society of Civil Engineers, 95*(6), 1847–1858.

Allen, K.G., von Bäckström, T.W., & Kröger, D.G. (2013). Packed bed pressure drop dependence on particle shape, size distribution, packing arrangement and roughness. *Powder Technology, 246*, 590-600.

Altuhafi, F., O'Sullivan, C., & Cavarretta, I. (2013). Analysis of an image-based method to quantify the size and shape of sand particles. *Journal of Geotechnical and Geoenvironmental Engineering, 139*(8), 1290-1307.

Anderson, M.P. (2005). Heat as a ground water tracer. *Ground Water, 43*(6), 951-968.

Arbhabhirama, A., & Dinoy, A.A. (1973). Friction factor and Reynolds number in porous media flow. *Journal of the Hydraulics Division. Proceedings of the American Society of Civil Engineers, 99*(6), 901–911.

Aulisa, E., Ibragimov, A., Valko, P., & Walton, J. (2009). Mathematical framework of the well productivity index for fast Forchheimer (non-Darcy) flows in porous media. *Mathematical Models and Methods in Applied Sciences, 19*(8), 1241-1275.

Bağci, Ö., Dukhan, N., & Özdemir, M. (2014). Flow regimes in packed beds of spheres from pre-Darcy to turbulent. *Transport in Porous Media, 104*(3), 501-520.

Bair, E.S., & Lahm, T.D. (1996). Variations in capture-zone geometry of a partially penetrating pumping well in an unconfined aquifer. *Ground Water, 34*(5), 842-852.

Bakker, M. (2001). An analytic approximate method for modeling steady, three-dimensional flow to partially penetrating wells. *Water Resources Research, 37*(5), 1301-1308.

Banerjee, A., Pasupuleti, S., Singh, M.K., & Kumar, G.N.P. (2018). A study on the Wilkins and Forchheimer quations used in coarse granular media flow. *Acta Geophysica, 66*(1), 81-91.

Barker, J.A., & Herbert, R. (1992). A simple theory for estimating well losses: with application to test wells in Bangladesh. *Applied Hydrogeology, 0*, 20– 31.

Barrash, W., Clemo, T., Fox, J.J., & Johnson, T.C. (2006). Field, laboratory, and modeling investigations of the skin effect at wells with slotted casing, Boise Hydrogeophysical Research Site. *Journal of Hydrology, 326*(1-2), 181-198.

Barth, G.R., Illangasekare, T.H., Hill, M.C., & Rajaram, H. (2001). A new tracer-density criterion for heterogeneous porous media. *Water Resources Research, 37*(1), 21-31.

Basak, P. (1978). Analytical solutions for two-regime well flow problems. *Journal of Hydrology, 38*(1-2), 147-159.

Bayer, P., Finkel, M., & Teutsch, G. (2002). Reliability of Hydraulic Performance and Cost Estimates of Barrier-Supported Pump-and-Treat Systems in Heterogeneous Aquifers. In K. Kovar & Z. Hrkal (Eds.), *4th international conference 'Calibration and reliability in groundwater modelling'. A few steps closer to reality. ModelCARE 2002.* Prepublished proceedings of the ModelCARE 2002 conference held in Prague, Czech Republic, from 17 to 20 June 2002 (pp. 331–338). Praha: Univerzita Karlova v Praze, Nakadateství Karolinum. [IAHS-AISH Publication, 277]

Bear, J. (1988). *Dynamics of fluids in porous media* (unabridged, corr. republication). New York: Dover. [Reprint, manufactured in the US by Courier Corporation]

Bear, J. (2007). *Hydraulics of Groundwater*. New York: Dover.

Bear J., & Sun, Y. (1998). Optimization of pump-treat-injection (PTI) design for the remediation of a contaminated aquifer: multi-stage design with chance constraints. *Journal of Contaminant Hydrology, 29*, 225-244.

Bertani, R. (2016). Geothermal power generation in the world 2010–2014 update report. *Geothermics, 60*, 31-43.

Bloemendal, M., & Hartog, N. (2018). Analysis of the impact of storage conditions on the thermal recovery efficiency of low-temperature ATES systems. *Geothermics, 71*, 306-319.

Bloemendal, M., Jaxa-Rozen, M., & Olsthoorn, T. (2018). Methods for planning of ATES systems. *Applied Energy, 216*, 534-557.

Bloemendal, M., Olsthoorn, T., & Boons, F. (2014). How to achieve optimal and sustainable use of the subsurface for Aquifer Thermal Energy Storage. *Energy Policy, 66*, 104-114.

Blott, S.J., & Pye, K. (2001). GRADISTAT: a grain size distribution and statistics package for the analysis of unconsolidated sediments. *Earth Surface Processes and Landforms, 26*(11), 1237-1248.

Bodvarsson, G.S. (1982). *Mathematical modeling of the behavior of geothermal systems under exploitatio*n (Doctoral dissertation). Berkely, CA: University of California.

Bonte, M., van Breukelen, B.M., & Stuyfzand, P.J. (2013). Temperature-induced impact on groundwater quality and arsenic mobility in anoxic aquifer sediments used for both drinking water and shallow geothermal energy production. *Water Research, 47*(14), 5088-5100.

Bordier, C., & Zimmer, D. (2000). Drainage equations and non-Darcian modeling in coarse porous media or geosynthetic materials. *Journal of Hydrology, 228*(3-4) 174–187.

Boulton, N.S. (1947). Discussion of "Drawdown Test to Determine Effective Radius of Artesian Well by C. E. Jacob". *Transactions of the American Society of Civil Engineers, 112*(1), 1065-1068.

Bouwer, H. (2002). Artificial recharge of groundwater: hydrogeology and engineering. *Hydrogeology Journal, 10*(1), 121-142.

Bouwer, H., & Rice, R.C. (1976). A slug test for determining hydraulic conductivity of unconfined aquifers with completely or partially penetrating wells. *Water Resources Research, 12*(3), 423-428.

Brons H.J., Griffioen J., Appelo C.A.J., & Zehnder A.J.B. (1991). (Bio)geochemical reactions in aquifer material from a thermal energy storage site. *Water Research, 25*(6):729–736.

Brown, D.L., & Silvey, W.D. (1977). *Artificial recharge to a freshwater-sensitive brackish-water sand aquifer, Norfolk, Virginia*. Washington, DC: U.S. Government Printing Office. [Geological Survey Professional Paper, 939]

Burcharth, H.F., & Andersen, O.H. (1995). On the one-dimensional steady and unsteady porous flow equation. *Coastal Engineering 24*, 233-257.

Buscheck, T.A., Doughty, C., & Tsang, C.F. (1983). Prediction and analysis of a field experiment on a multilayered aquifer thermal energy storage system with strong buoyancy flow. *Water Resources Research, 19*(5), 1307-1315.

Butler, J.J. (2005). Hydrogeological methods. In Y. Rubin & S.S. Hubbard (Eds.), *Hydrogeophysics* (pp. 23-58). Springer: Dordrecht.

Butler, J.J., Bohling, G.C., Hyder, Z., & McElwee, C.D. (1994). The use of slug tests to describe vertical variations in hydraulic conductivity. *Journal of Hydrology, 156*, 137-162.

Butler, J.J., Dietrich, P., Wittig, V., & Christy, T., (2007). Characterizing hydraulic conductivity with the direct-push permeameter. *Ground Water, 45*(4), 409-419.

Butler, J.J., & Healey, J.M. (1998). Relationship between pumping-test and slug-test parameters: Scale effect or artifact? *Ground Water, 36*(2), 305-312.

Carman, P.C. (1937). Fluid flow through granular beds. Transactions of the Institution of Chemical Engineers, *15*, 150-166.

Carrier, W.D. (2003). Goodbye, Hazen; Hello, Kozeny-Carman. *Journal of Geotechnical and Geoenvironmental Engineering, 129*(11), 1054-1056.

Cashman, P.M., & Preene, M. (2013). *Groundwater lowering in construction: a practical guide to dewatering* (2nd ed.). Boca Raton: Taylor and Francis.

Cassiani, G., Bruno, V., Villa, A., Fusi, N., & Binley, A.M. (2006). A saline trace test monitored via time-lapse surface electrical resistivity tomography. *Journal of Applied Geophysics, 59*(3), 244-259.

Chapuis, R.P., Dallaire, V., Marcotte, D., Chouteau, M., Acevedo, N., & Gagnon F. (2005). Evaluating the hydraulic conductivity at three different scales within an unconfined sand aquifer at Lachenaie, Quebec. *Canadian Geotechnical Journal, 42*(4), 1212-1220.

Chaudhary, K., Cardenas, M.B., Den, W., & Bennett, P.C. (2013). Pore geometry effects on intrapore viscous to inertial flows and on effective hydraulic parameters. *Water Resources Research, 49*(2), 1149-1162

Chauveteau, G., & Thirriot, C. (1967). Régimes d'écoulement en milieu poreux et limite de la loi de Darcy [Regimes of flow in porous media and the limitations of the Darcy law]. *La Houille Blanche* (2, March), 141–148.

Chen, Z., Lyons, S.L., & Qin, G. (2001). Derivation of the Forchheimer Law via homogenization. *Transport in Porous Media, 44*(2), 325-335.

Chenaf, D., & Chapuis, R.P. (2007). Seepage face height, water table position, and well efficiency at steady state. *Ground Water, 45*(2), 168–177.

Cheng, A.H.-D., Halhal, D., Naji, A., & Ouazar, D. (2000). Pumping optimization in saltwater-intruded coastal aquifers. *Water Resources Research, 36*(8) 2155-2165.

Comiti, J., & Renaud, M. (1989). A new model for determining mean structure parameters of fixed beds from pressure drop measurements: application to beds packed with parallelepipepal particles. *Chemical Engineering Science, 44*(7), 1539-1545.

Comiti, J., Saribi, N.E., & Montillet, A. (2000). Experimental characterization of flow regimes in various porous media – 3: limit of Darcy's or creeping flow regime for Newtonian and purely viscous non-Newtonian fluids. *Chemical Engineering Science 55*(15), 3057-3061.

Dagan, G. (1989). *Flow and transport in porous formations*. Berlin: Springer.

Dan, H.-C., He, L.-H., & Xu, B. (2016). Experimental investigation on non-Darcian flow in unbound graded aggregate material of highway pavement. *Transport in Porous Media, 112*(1), 189-206.

Darcy, H. (1856). *Les fontaines publiques de la ville de Dyon. Exposition et application des principes à suivre et des formules à employer dans les questions de distribution d'eau. Ouvrage terminé par un appendice relatif aux fournitures d'eau de plusieurs villes au filtrage des eaux et à la fabrication des tuyaux de fonte, de plomb, de tole et de bitume*. Paris: Dalmont. [With 2nd volume: Atlas]

Das, B.M. (2008). *Advanced soil mechanics* (3rd ed.). London: Taylor & Francis.

De Glee, G.J. (1930). *Over grondwaterstroomingen bij wateronttrekking door middel van putten* (Doctoral dissertation). Delft: Technische Hoogeschool.

De Zwart, A.H. (2007). *Investigation of clogging processes in unconsolidated aquifers near water supply wells* (Doctoral dissertation). Delft: Technische Universiteit.

Dickinson, J.S., Buik, N., Matthews, M.C., & Snijders, A.L. (2009). Aquifer thermal energy storage: Theoretical and operational analysis. *Géotechnique, 59*(3), 249-260.

Dietrich, P., Butler, J.J., & Faiß, K. (2008). A rapid method for hydraulic profiling in unconsolidated formations. *Ground Water, 46*(2), 323-328.

Doughty, C., Hellström, G., Tsang, C.F., & Claesson, J. (1982). A dimensionless parameter approach to the thermal behavior of an aquifer thermal energy storage system. *Water Resources Research, 18*(3): 571-587.

Driscoll, F.G. (Ed.). (1986): *Ground water and wells* (2nd ed.). St. Paul, MN: Johnson Filtration Systems.

Du Plessis, J.P. (1994). Analytical quantification of coefficient in the Ergun equation for fluid friction in a packed bed. *Transport in Porous Media, 16*(2), 189-207.

Dybbs, A., & Edwards, R.V. (1984). A new look at porous media fluid mechanics: Darcy to turbulent. In J. Bear & Y. Corapcioglu (Eds.), *Fundamentals of transport phenomena in porous media.* Proceedings of the NATO Advanced Study Institute on Mechanics of fluids in porous media, Newark, Delaware, U.S.A., July 18-27, 1982 (pp. 199-256). Dordrecht: Nijhoff.

Engeler, I., Hendricks Fransen, H.J., Müller, R., & Stauffer, F. (2011). The importance of coupled modelling of variably saturated groundwater flow-heat transport for assessing river-aquifer interactions. *Journal of Hydrology, 397*(3-4), 295-305.

Engelund, F. (1953). *On the laminar and turbulent flow of groundwater through homogeneous sands.* København: Akademit for de Tekniske Videnskaber. [Transactions of the Danish Academy of Technical Sciences, A.T.S. 1953, 3; Technical University of Denmark. Hydraulic Laboratories. Bulletin, 4]

Erdim, E., Akgirkay, Ö, & Demir, I. (2015). A revisit of pressure drop-flow rate correlations for packed beds of spheres. *Powder Technology, 283*, 488-504.

Ergun, S. (1952). Fluid flow through packed columns. *Chemical Engineering Progress, 48*(2), 89-94.

Fand, R.M., Kim, B.Y.K., Lam, A.C.C., & Phan, R.T. (1987). Resistance to the flow of fluids through simple and complex porous media whose matrices are composed of randomly packed spheres. *Journal of Fluids Engineering, 109*(3), 268–273.

Fand, R.M., & Thinakaran, R. (1990). The influence of the wall on flow through pipes packed with spheres. *Journal of Fluids Engineering, 122*(1), 84-88.

Fang, Q., Tai, Q, Zhang, D., & Wong, L.N.Y. (2016) Ground surface settlements due to construction of closely-spaced twin tunnels with different geometric arrangements. *Tunnelling and Underground Space Technology, 51*; 144-151.

Ferdos, F., Wörman, A., & Ekström, I. (2015). Hydraulic conductivity of coarse rockfill used in hydraulic structures, *Transport in Porous Media, 108*(2), 367-391.

Ferguson, G. (2007) Heterogeneity and thermal modeling of ground water. *Ground Water, 45*(4), 485-490.

Firdaouss, M., Guermond, J.L., & Le Quéré, P. (1997). Nonlinear correction to Darcy's law at low Reynolds numbers. *Journal of Fluid Mechanics, 343*, 331–350.

Fleuchaus, P., Godschalk, B., Stober, I., & Blum, P. (2018).Worldwide application of aquifer thermal energy storage – A review. *Renewable and Sustainable Energy Reviews, 94*, 861-876.

Forchheimer, P.H. (1901). Wasserbewegung durch Boden. *Zeitschrift des Vereines Deutscher Ingenieure, 50*, 1736-1741, 1781-1788.

Forth, R. (2004).Groundwater and geotechnical aspects of deep excavations in Hong Kong. *Engineering Geology, 72*, 253–260.

Fourar, M., Radilla, G., Lenormand, R., & Moyne, C. (2004). On the non-linear behavior of a laminar single-phase flow through two and three-dimensional porous media. *Advances in Water Resources, 27*(6), 669–677.

Freyberg, D.L. (1986). A natural gradient experiment on solute transport in a sand aquifer: 2. Spatial moments and the advection and dispersion of nonreactive tracers. *Water Resources Research, 22*(13), 2031-2046.

Galeati, G, & Gambolati, G. (1988). Optimal dewatering schemes in the foundation design of an electronuclear plant. *Water Resources Research, 24*(4), 541-552.

Geertsma, J. (1974). Estimating the coefficient of inertial resistance in fluid flow through porous media. *Society of Petroleum Engineers Journal, 14*(5), 445–450.

Gelhar, L.W., Welty, C., & Rehfeldt, K.R. (1992). A critical review of data on field-scale dispersion in aquifers. *Water Resources Research, 28*(7), 1955–1974.

Gell & Partner GbR (2009) *Mönchengladbach-Rheindahlen RRB/RKB Wyenhütte: Baugrundgutachten*. Aachen: Ingenieurbüro Gell & Partner GbR, [Confidential report]

Ghanbarian, B., Hunt, A.G., Ewing, R.P., & Sahimi, M. (2013). Tortuosity in porous media. A critical review. *Soil Science Society of America Journal, 77*(5), 1461-1477.

Giambastiani, B.M.S., Colombani, N., & Mastrocicco, M. (2013). Limitation of using heat as a groundwater tracer to define aquifer properties: experiment in a large tank model. *Environmental Earth Sciences, 70* (2), 719-728.

Gianni, G., Doherty, J., & Brunner, P. (2019). Conceptualization and calibration of anisotropic alluvial systems: Pitfalls and biases. *Ground Water, 57*(3), 409-419.

Godoy, V.A., Zuquette, L.V., & Gómez-Hernández, J.J. (2018). Scale effect on hydraulic conductivity and solute transport: Small and large-scale laboratory experiments and field experiments. *Engineering Geology, 243*, 196-205.

Gorelick, S.M., Voss, C., Gill, P.E., Murray, W., Saunders, M.A., & Wright, M.H. (1984). Aquifer reclamation design: The use of contaminant transport simulation combined with nonlinear programing. *Water Resources Research, 20*(4), 415-427.

Greenly, B.T., & Joy, D.M. (1996). One-dimensional finite-element model for high flow velocities in porous media. *Journal of Geotechnical Engineering, 122*(10), 786-796.

Griffioen, J., & Appelo, C.A.J. (1993). Nature and extent of carbonate precipitation during aquifer thermal energy storage. *Applied Geochemistry, 8*(2): 161-176.

Guo, P., Stolle, D, & Guo, S.X. (2019). An equivalent spherical particle system to describe characteristics of flow in a dense packing of non-spherical particles. *Transport in Porous Media, 129*(1), 253-280.

Guo W., & Langevin CD (2002) *User's guide to SEAWAT: A computer program for simulation of three-dimensional variable-density ground-water flow*. Tallahassee, FL: USGS. [U.S. Geological Survey Techniques of Water-Resources Investigations, 6 A7]

Guo, Z., & Brusseau, M.L. (2017). The impact of well-field configuration and permeability heterogeneity on contaminant mass removal and plume persistence. *Journal of Hazardous Materials, 333*, 109-115.

Haitjema, H.M. (1985) Modeling three-dimensional flow in confined aquifers by superposition of both two-and three-dimensional analytic functions. *Water Resources Research, 21*(10):1557–1566.

Haitjema, H.M., & Kraemer, S.R. (1988). A new analytic function for modelling partially penetrating wells. *Water Resources Research, 24*(5), 683-690.

Hantush, M.S. (1961). Drawdown around a partially penetrating well. *Journal of the Hydraulics Division. Proceedings of the American Society of Civil Engineers, 87*(4), 83-98.

Hantush, M.S. (1964). Hydraulics of wells in V.T. Chow (Ed.), *Advances in hydroscience*. Vol. 1 (pp. 281–432). New York: Academic Press.

Hantush, M.S. & Jacob, C.E. (1955). Non-steady radial flow in an infinite leaky aquifer. *Transactions of the American Geophysical Union, 36*(1), 95-100.

Harbaugh, AW (2005) *MODFLOW-2005, the US geological survey modular ground-water model - the ground-water flow process*. Reston, VA: U.S. Department of the Interior, U.S. Geological Survey. [U.S. Geological Survey Techniques and Methods, 6–A16 = Chapter 16 of Book 6. Modeling techniques, Section A. Ground water]

Harbaugh, A.W., Banta, E.R., Hill, M.C., & McDonald, M.G. (2000). *MODFLOW-2000, the US Geological Survey modular ground-water model. User guide to modularization concepts and the ground-water flow process*. Reston, VA: U.S. Geological Survey. [Open-File Report 00-92]

Hartog, N., Drijver, B., Dinkla, I., & Bonte, M. (2013). Field assessment of the impacts of Aquifer Thermal Energy Storage (ATES) systems on chemical and microbial groundwater composition. [Paper presented at the European Geothermal Conference, Pisa, Italy, 3-7 June 2013: "EGC 2013. Geothermal energy towards a new horizon"]

Hassanizadeh, S.M., & Gray, W.G. (1987) High velocity flow in porous media. *Transport in Porous Media, 2*(6), 521-531.

Hellström, G., Tsang, C.F., & Claesson, J. (1979) *Heat storage in aquifers: buoyancy flow and thermal stratification problems.* Lund: Department of Mathematical Physics, Institute of Technology. [Also published as: Rep. LBL-14246, Berkeley, CA: Lawrence Berkeley Laboratory]

Hemker, K. (2000). *Groundwater flow in layered aquifer systems* (Doctoral dissertation). Amsterdam: Vrije Universiteit.

Hermans, T., Wildemeersch, S., Jamin, P., Orban, P., Brouyère, S., Dassargues, A., & Nguyen, F. (2015), Quantitative temperature monitoring of a heat tracing experiment using cross-borehole ERT. *Geothermics, 53*, 14-26.

Herrera, N.H. & Felton, G.K. (1991). Hydraulics of flow through a rockfill dam using sediment-free water. *Transactions of the American Society of Agricultural Engineers, 34*(3), 871-875.

Hidalgo, J.J., Carrera, J., & Dentz, M. (2009). Steady state heat transport in 3D heterogeneous porous media. *Advances in Water Resources, 32*(8), 1206-1212.

Hill, R.J., & Koch, D.L. (2002). The transition from steady to weakly turbulent flow in a close-packed ordered array of spheres. *Journal of Fluid Mechanics, 465*, 59–97.

Holditch, S.A., & Morse, R.A. (1976). The effects of non-Darcy flow on the behavior of hydraulically fractured gas wells. *Journal of Petroleum Technology, 28*(10), 1169-1179.

Holstenkamp, L., Meisel, M., Neidig, P., Opel, O., Steffahn, J., Strodela, N., Lauer, J.J., Vogel, M., Degenhart, H., Michalzik, D., Schomerus, T., Schönebeck, J., & Növig, T. (2017). Interdisciplinary Review of Medium-deep Aquifer Thermal Energy Storage in North Germany. *Energy Procedia, 135*, 327-336.

Holzbecher, E. (2004). The mixed convection number for porous media flow. In: D.B. Ingham D.B., A. Bejan, E. Mamut & I. Pop (Eds.), *Emerging Technologies and Techniques in Porous Media* (pp. 169-181). Dordrecht: Springer. [NATO Science Series (Series II: Mathematics, Physics and Chemistry), vol. 134]

Hopmans, J.W., Šimunek, J., & Bristow, K.L. (2002). Indirect estimation of soil thermal properties and water flux using heat pulse probe measurements: Geometry and dispersion effects. *Water Resources Research, 38*(1), WR00007 1-14.

Houben, G.J. (2003). Iron oxide incrustations in wells. Part 1: Genesis, mineralogy and geochemistry. *Applied Geochemistry, 18*(6), 927-939.

Houben, G.J. (2015a). Review: Hydraulics of water wells — flow laws and influence of geometry. *Hydrogeology Journal, 23*(8), 1633–1657.

Houben, G.J. (2015b). Review: Hydraulics of water wells — head losses of individual components. *Hydrogeology Journal, 23*(8), 1659–1675.

Houben, G.J., Halisch, M., Kaufhold, S., Weidner, C., Sand, J., & Reich, M. (2016). Analysis of Wellbore Skin Samples — Typology, Composition, and Hydraulic Properties. *Ground Water, 54*(5), 634-645.

Houben, G.J., & Hauschild S. (2011). Numerical Modeling of the Near-Field Hydraulics of Water Wells. *Ground Water, 49*(4), 570-575.

Houben. G.J., Wachenhausen, J., & Guevara Morel, C.R. (2018). Effects of ageing on the hydraulics of water wells and the influence of non-Darcy flow. *Hydrogeology Journal, 26*(4), 1285-1294.

Huang, K., Wan, J.W., Chen, C.X., He, L.Q., Mei, W.B., & Zhang, M.Y. (2013). Experimental investigation on water flow in cubic arrays of spheres. *Journal of Hydrology, 492*, 61-68.

Hyder, Z., Butler, J.J., McElwee, C.D., & Liu, W. (1994). Slug tests in partially penetrating wells. *Water Resources Research, 30*(11), 2945-2957.

Ingebritsen, S.E., Sanford, W.E., & Christopher E.N. (2006). *Groundwater in geologic processes* (2nd ed.). Cambridge: Cambridge University Press.

Irmay, S. (1958). On the theoretical derivation of Darcy and Forchheimer formulas. *Transactions of the American Geophysical Union, 39*(4), 702-707.

Irmay, S. (1964). Theoretical models of flow through porous media. In R. l'Hermite (Pres.), *Transfers de l'eau dans les milieux poreux : colloque international, Paris, avril 1964. Thème 2. Hydrodynamique des milieux poreux. Thème 3. Thermodynamique des milieux poreux*. Paris: [Réunion Internationale des Laboratoires d'Essais et de Recherches sur les Matériaux et les Constructions (RILEM)], 1965. [*Bulletin RILEM. Nouvelle série, 29* (1965), 37-43]

Isdale, JD, & Morris, R (1972). Physical properties of sea water solutions: density. *Desalination, 10*(4):329–339.

Izbash, S.V. (1931). *O filtracii v kropnozernstom materiale*. Leningrad, Izv. Nauchno-Issled. Inst. Gidro-Tekh.

Jackson, R.B., Carpenter, S.R., Dahm, C.N., McKnight D.M., Naiman, R.J., Postel S.L., & Running, S.W. (2001). Water in a changing world. *Ecological Applications, 11*(4), 1027-1045.

Jafari, A., Zamankhan, P., Mousavi, S.M., & Pietarinen, K. (2008). Modeling and CFD simulation of flow behavior and dispersivity through randomly packed bed reactors. *Chemical Engineering Journal, 144*(3), 476-482.

Janicek, J., & Katz, D. (1955). Applications of unsteady state gas flow calculations. In D.L. Katz & D. Cornell (Eds.), *Flow of natural gas from reservoirs*. Research Conference, University of Michigan, June 30 – July 1, 1955 (44 pp.). Michigan, Ann Arbor, MI: College of Engineering, University of Michigan.

Jim Yeh, T.-C., Mas-Pla, J., Williams, T.M., & McCarthy, J.F. (1995). Observation and three-dimensional simulation of chloride plumes in a sandy aquifer under forced-gradient conditions. *Water Resources Research, 31*(9); 2141-2157.

Jin, Y., Holzbecher, E., & Sauter, M. (2016). Dual-screened vertical circulation well for groundwater lowering in unconfined aquifers. *Ground Water, 54*(1), 15-22.

Johnston, C.D., Fisher, S., & Rayner, J.L. (2002) Removal of petroleum hydrocarbons from the vadose zone during multi-phase extraction at a contaminated industrial site. In S.F. Thornton & S.E. Oswald (Eds.), *Groundwater Quality. Natural and enhanced restoration of groundwater pollution.* Selected and reviewed papers presented at the Groundwater Quality 2001 Conference held in Sheffield, UK, from 18 to 21 June 2001 (pp. 287-294). Wallingford: IAHS Press. [IAHS Publication, 275]

Jolls, K.R., & Hanratty, T.J. (1966). Transition to turbulence for flow through a dumped bed of spheres. *Chemical Engineering Science, 21*(12), 1185-1190.

Juhasz, A.L., Smith, E., Smith, J., & Naidu R. (2003). In situ remediation of DDT-contaminated soil using a two-phase cosolvent flushing-fungal biosorption process. *Water, Air, & Soil Pollution, 147*(1–4), 263-274.

Jurado, A., De Gaspari, F., Vilarrasa, V., Bolster, D., Sánchez-Vila, X., Fernandez-Garcia, D., & Tartakovsky, D. (2012). Probabilistic analysis of groundwater-related risks at subsurface excavation sites. *Engineering Geology, 125*, 35-44).

Kabus, F., & Seibt, P. (2000). Aquifer thermal energy storage for the Berlin Reichstag building – new seat of the German Parliament. In E. Iglesias (Ed.), *Proceedings of the World Geothermal Congress 2000, Kyushu, Tohoku, Japan, May 28-June 10 2000* (pp. 3611-3615). N.p.: International Geothermal Association.

Kadlec, H.R., & Knight, L.R. (1996). *Treatment wetlands*. Boca Raton, FL: Lewis.

Kasenow, M. (2010). *Applied ground-water hydrology and well hydraulics* (3rd ed.). Highlands Ranch, CO: Water Resources Publications.

Khan, F.I., Husain, T., & Hejazi, R. (2004). An overview and analysis of site remediation technologies. *Journal of Environmental Management, 71*(2), 95-122.

Kim, B.-W. (2014). Effect of filter designs on hydraulic properties and well efficiency. *Ground Water, 52*(Focus issue), 175-185.

Klepikova, M.V., Le Borgne, T., Bour, O., Dentz, M., Hochreutener, R., & Lavenant, N. (2016a). Heat as a tracer for understanding transport processes in fractured media: Theory and field assessment from multiscale thermal push-pull tracer tests. *Water Resources Research, 52*(7), 5442-5457.

Klepikova, M., Wildemeersch S., Hermans, T., Jamin P., Orban, P., Nguyen F., Brouyère, S., & Dassargues A. (2016b). Heat tracer test in an alluvial aquifer: Field experiment and inverse modelling. *Journal of Hydrology, 540*, 812-823.

Köber, R., Hornbruch, G., Leven, C., Tischer, L., Großmann, J., Dietrich, P., Weiß, H., & Dahmke, A. (2009). Evaluation of combined direct-push methods used for aquifer model generation. *Ground Water, 47*(4), 536-546.

Kovács, G. (1981). *Seepage Hydraulics*. Amsterdam: Elsevier.

Kranz, S., & Frick, S. (2013). Efficient cooling energy supply with aquifer thermal energy storages. *Applied Energy, 109*, 321-327.

Krumbein, W.C., & Sloss, L.L. (1963). Stratigraphy and sedimentation (2nd ed.) San Francisco: Freeman.

Kruseman, G.P., & De Ridder, N.A. (1991). *Analysis and evaluation of pumping test data* (2nd ed.). Wageningen: International Institute for Land Reclamation and Improvement. [Reprint 2000; ILRI Publication 47]

Lage, J.L. (1998). The fundamental theory of flow through permeable media from Darcy to turbulence. In D.B. Ingham & I. Pop (Eds.), *Transport phenomena in porous media*, (pp. 1-30). New York: Pergamon.

Langevin, C.D. (2008). Modeling axisymmetric flow and transport. *Ground Water, 46*(4):579-590.

Langevin, C.D., Thorne Jr., D.T., Dausman, A.M., Sukop, M.C. , & Guo, W (2008) *SEAWAT Version 4: A computer program for simulation of multi-species solute and heat transport*. Reston, VA: U.S. Department of the Interior, U.S. Geological Survey. [U.S. Geological Survey Techniques and Methods, 6–A22 = Chapter 22 of Book 6. Modeling techniques]

Latifi, M.A., Midoux, N., & Storck, A. (1989). The use of micro-electrodes in the study of the flow regimes in a packed bed reactor with single phase liquid flow. *Chemical Engineering Science, 44*(11), 2501-2508.

Leaf, A.T., Hart, D.J., & Bahr, J.M. (2012). Active thermal tracer tests for improved hydrostratigraphic characterization. *Ground Water, 50*(5), 726-735.

Leibundgut, C., Maloszeski, P., & Külls, C. (2009). *Tracers in Hydrology*. Hoboken, NJ: Wiley.

Li, L., & Ma, W. (2011). Experimental study on the effective particle diameter of a packed bed with non-spherical particles. *Transport in Porous Media, 89*(1), 35-48.

Li, Z., Wan, J., Huang, K., Chan, W., & He, Y. (2017). Effects of particle diameter on flow characteristics in sand columns. *International Journal of Heat and Mass Transfer, 104*, 533-536.

Li, Z., Wan, J., Zhan H., Cheng, X., Chang, W., & Huang, K. (2019). Particle size distribution on Forchheimer flow and transition of flow regimes in porous media. *Journal of Hydrology, 574*, 1-11.

Liu, X., Civan, F., & Evans, R.D. (1995). Correlation of the non-Darcy flow coefficient. *Journal of Canadian Petroleum Technology, 34*(10), 50-54.

Loma González, B. de la. (2013), Clogging of deep well infiltration recharge systems in the Netherlands. In R. Martin (Ed.), *Clogging issues associated with managed aquifer recharge methods* (pp. 163-173). Australia: IAH Commission on Managing Aquifer Recharge.

Ma, H., & Ruth, D.W. (1993). The microscopic analysis of high Forchheimer number flow in porous media. *Transport in Porous Media, 13*(2), 139-160.

Ma, R., & Zheng, C. (2010). Effects of density and viscosity in modeling heat as a groundwater tracer. *Ground Water 48*(3), 380-389.

Ma, R., Zheng, C., Zachara, J.M., & Tonkin, M. (2012). Utility of bromide and heat tracers for aquifer characterization affected by highly transient flow conditions. *Water Resources Research, 48*(8), W08523.

Maas, C. (1987). Groundwater flow to a well in a layered porous medium. 1. Steady flow. *Water Resources Research, 23*(8), 1675-1681.

Macdonald, I.F., El-Sayed, M.S., Mow, K., & Dullien, F.A.L. (1979). Flow through porous media – the Ergun equation revisited. *Industrial and Engineering Chemistry Fundamentals, 18*(3), 199-208.

Macfarlane, P.A., Förster, A., Merriam, D.F., Schrötter, J., & Healey, J.M. (2002). Monitoring artificially stimulated fluid movement in the Cretaceous Dakota aquifer, western Kansas. *Hydrogeology Journal, 10*(6), 662-673.

Maliva, R.G., & Missimer, T.M. (2010). *Aquifer storage and recovery and managed aquifer recharge using wells: Planning, hydrogeology, design and operation*. Sugar Land, TX: Schlumberger.

Martin, R. (Ed.). (2013). *Clogging issues associated with managed aquifer recharge methods.* Australia: IAH Commission on Managing Aquifer Recharge.

Mas-Pla, J., Rodríguez-Florit, A., Zamarano, M., Roqué C., Menció A., & Brusi, D. (2013). Anticipating the effects of groundwater withdrawal on seawater intrusion and soil settlement in urban coastal areas. *Hydrological Processes, 27*(16), 2352-2366.

Mathey, B. (1977). Development and resorption of a thermal disturbance in a phreatic aquifer with natural convection. *Journal of Hydrology, 34*(3-4), 315-333.

Mathias, S.A., & Butler, A.P. (2007). Flow to a finite diameter well in a horizontally anisotropic aquifer with wellbore storage. *Water Resources Research, 43*(7), W07501.

Mathias, S.A., & Moutsopoulos, K.N. (2016). Approximate solutions for Forchheimer flow during water injection and water production in an unconfined aquifer. *Journal of Hydrology, 538*, 13-21.

Mathias, S.A., & Todman, L.C. (2010). Step-drawdown tests and the Forchheimer equation. *Water Resources Research, 46*(7), W07514.

McCall, W., Christy, T., Christopherson, T., & Issacs, H. (2009). Application of direct push methods to investigate uranium distribution in an alluvial aquifer. *Ground Water Monitoring and Remediation, 29*, 65–76.

McElwee, C.D., & Zenner, M.A. (1998). A nonlinear model for analysis of slug-test data. *Water Resources Research, 34*(1), 55-66.

Meyer, C.F., & Todd, D.K. (1973). Conserving energy with heat storage wells. *Environmental Science and Technology, 7*(6), 512–516.

Mijic, A., Mathias, S.A., & LaForce, T.C. (2013). Multiple well systems with non-Darcy flow. *Ground Water, 51*(4), 588-596.

Millero, F.J., & Poisson, A. (1981) International one-atmosphere equation of state of seawater. Deep Sea Research Part A, *Oceanographic Research Papers, 28*(6), 625–629.

Miotliński, K., & Dillon, P.J. (2015). Relative recovery of thermal energy and fresh water in aquifer storage and recovery systems. *Ground Water, 53*(6):877-884.

Miotliński, K., Dillon, P.J., Pavelic, P., Barry, K., & Kremer, S. (2013). Recovery of Injected Freshwater from a Brackish Aquifer with a Multiwell System. *Ground Water, 52*(4), 495-502.

Molson, J.W., Frind, E.O., & Palmer, C.D. (1992). Thermal energy storage in an unconfined aquifer 2. Model development, validation, and application. *Water Resources Research, 28*(10), 2857-2867.

Molz, F.J., Melville, J.G., Parr, A.D., King, D.A., & Hopf, M.T. (1983a). Aquifer thermal energy storage: A well doublet experiment at increased temperatures. *Water Resources Research, 19*(1), 149-160.

Molz, F.J., Melville, J.G., Güven, O., & Parr, A.D. (1983b). Aquifer thermal energy storage: An attempt to counter free thermal convection. *Water Resources Research, 19*(4), 922-930.

Molz, F.J., Parr, A.D., Andersen, P.F., Lucido, V.D., & Warman, J.C. (1979). Thermal energy storage in a confined aquifer: experimental results. *Water Resources Research, 15*(6), 1509–1514.

Molz, F.J., & Young, S.C. (1993). Development and application of borehole flowmeters for environmental assessment. *The Log Analyst, 34*(1), 13-23

Mota, M., Teixeira, J.A., Bowen, W.R., & Yelshin, A. (2001). Binary spherical particle mixed beds: Porosity and permeability relationship measurement. *Transactions of the Filtration Society, 1*(4), 101-106.

Moutsopoulos, K.N. (2007). One-dimensional unsteady inertial flow in phreatic aquifers, induced by a sudden change of the boundary head, Transport in Porous Media, *70*(1), 97-125.

Moutsopoulos, K.N., Papaspyros, I.N.E., & Tsihrintzis, V.A. (2009). Experimental investigation of inertial flow processes in porous media. *Journal of Hydrology, 374*(3-4), 242-254.

Moutsopoulos, K.N., & Tsihrintzis, V.A. (2005). Approximate analytical solutions of the Forchheimer equation. *Journal of Hydrology, 309*, 93-103.

Nield, D.A. (2000). Resolution of a paradox involving viscous dissipation and nonlinear drag in a porous medium. *Transport in Porous Media, 41*(3), 349-357.

Niemczynowicz, J. (1999). Urban hydrology and water management - present and future challenges. *Urban Water, 1*(1), 1-14.

Oldenburg, C.M., & Pruess K. (1999.) Plume separation by transient thermohaline convection in porous media. *Geophysical Research Letters, 26*(19): 2997-3000.

Olsthoorn, T.N. (1982a). *Verstopping van persputten*. Rijswijk: Keuringsdienst voor Waterleidingartikelen KIWA N.V.

Olsthoorn, T.N. (1982b). *The clogging of recharge wells, main subjects*. Rijswijk: The Netherlands Testing and Research Institute KIWA. [KIWA Communications, 72]

Oosterbaan, R.J., & Nijland, H.J. (1994). Determining the saturated hydraulic conductivity. Chapter 12 in H.P. Ritzema (Ed.), *Drainage principles and applications*. (2nd ed.). Wageningen: International Institute for Land Reclamation and Improvement. [ILRI Publication, 16]

Opel, O., Strodel, N., Werner, K.F., Geffken J., Tribel, A., & Ruck, W.K.L. (2017). Climate-neutral and sustainable campus Leuphana University of Lueneburg. *Energy, 141*, 2628-2639.

Otterpohl, R. (2002). Options for alternative types of sewerage and treatment systems directed to improvement of the overall performance. *Water Science and Technology, 45*(3), 149-158.

Paksoy, H.O., Andersson, O., Abaci, S., Evliya H., & Turgut, B. (2000), Heating and cooling of a hospital using solar energy coupled with seasonal thermal energy storage in an aquifer. *Renewable Energy, 19*(1-2), 117-122.

Palmer, C.D., Blowes, D.W., Frind, E.O., & Molson, J.W. (1992). Thermal energy storage in an unconfined aquifer 1. Field injection experiment. *Water Resources Research, 28*(10), 2845-2856.

Panfilov, M., & Fourar, M. (2006). Physical splitting of nonlinear effects in high-velocity stable flow through porous media. *Advances in Water Resources, 29*(1), 30-41.

Panfilov, M., Oltean, C., Panfilova, I., & Buès, M. (2003). Singular nature of nonlinear macroscale effects in high-rate flow through porous media. *Comptes Rendus Mecanique, 331*(1), 41-48.

Park, C.H., & Aral, M.M. (2004). Multi-objective optimization of pumping rates and well placement in coastal areas. *Journal of Hydrology, 290*, 80-99

Peltenburg, E., Colledge, S., Croft, P., Jackson, A., McCartney, C., & Murray M.A. (2000). Agro-pastoralist colonization of Cyprus in the 10th millennium BP: initial assessments. *Antiquity, 74*, 844-853

Pérez-Gonzaléz, A., Urtiaga, A.M., Ibáñez, R., & Ortiz, I. (2012). State of the art and review on the treatment technologies of water reverse osmosis concentrates. *Water Research, 46*(2):267-283.

Phien-wej, N., Giao, P.H., & Nutalaya, P. (1998). Field experiment of artificial recharge through a well with reference to land subsidence control. *Engineering Geology 50*, 187-201.

Powers, P., Corwin, A., Schmall, P., & Kaeck, W. (2007). *Construction dewatering and groundwater control* (3rd ed.). Hoboken, NJ: Wiley.

Preene, M., & Brassington, R. (2003). Potential groundwater impacts from civil-engineering works. *Water and Environment Journal, 17*(1); 59-64.

Ptak, T., Piepenbrink, M., & Martac, E. (2004). Tracer tests for the investigation of heterogeneous porous media and stochastic modelling of flow and transport—a review of some recent developments. *Journal of Hydrology, 294*, 122-163.

Pujades, E., De Simone, S., Carrera, J., Vázquez-Suñé, E., & Jurado, A. (2017). Settlements around pumping wells: analysis of influential factors and a simple calculation procedure. *Journal of Hydrology, 548*, 225–236.

Pujades, E., Vàzquez-Suñé, E., Carrera, J., & Jurado, A. (2014). Dewatering of a deep excavation undertaken in a layered soil. *Engineering Geology, 178*, 15–27.

Pyne, R.D.G. (2005). *Aquifer storage recovery. A guide to groundwater recharge through wells* (2nd ed.). Gainesville, FL: ASR Systems.

Ragab, R., Rosier, P., Dixon, A., Bromley, J., & Cooper, J.H. (2003). Experimental study of water fluxes in a residential area: 2. Road infiltration, runoff and evaporation. *Hydrological Processes, 17*(12), 2423-2437.

Ranganadha Rao, R.P., & Suresh, C. (1970). Discussion of 'Non-linear flow in porous media', by N Ahmed and DK Sunada. *Journal of the Hydraulics Division. Proceedings of the American Society of Civil Engineers, 96*(8), 1732-1734.

Rau, G.C., Andersen, M.S., & Acworth, R.I. (2012). Experimental investigation of the thermal dispersivity term and its significance in the heat transport equation for flow in sediments. *Water Resources Research, 48*(3), W03511.

Réveillère, A., Hamm, V., Lesueur, H., Cordier, E., & Goblet, P. (2013). Geothermal contribution to the energy mix of a heating network when using Aquifer Thermal Energy Storage: Modeling and application to the Paris basin. *Geothermics, 47*, 69-79.

Rietdijk, J., Schenkeveld F., Schaminée, P.E.L., Bezuijen, A. (2010). The drizzle method for sand sample preparation. In S. Springman, J. Laue & L. Seward (Eds.), *Physical modelling in geotechnics.* Proceedings of the 7th International Conference on Physical Modelling in Geotechnics (ICPMG 2010), 28th June - 1st July, Zurich, Switzerland (pp. 267-272). Leiden: CRC Press/Balkema.

Rinck-Pfeiffer, S., Ragusa, S., Sztajnbok, P., & Vandeveld, T. (2000). Interrelationships between biological, chemical, and physical processes as an analog to clogging in aquifer storage and recovery (ASR) wells. *Water Research, 34*(7), 2110-2118

Rivett, M.O., Chapman, S.W., Allen-King, R.M., Feenstra, S., & Cherry, J.A. (2006). Pump-and-treat remediation of chlorinated solvent contamination at a controlled field-experiment site. *Environmental Science and Technology, 40*(21), 6770-6781.

Robert, T., Paulus, C., Bolly, P.-Y., Lin, E.K.S., & Hermans, T. (2019). Heat as a proxy to image dynamic processes with 4D electrical resistivity tomography, *Geosciences, 9*(10), 414 (18 pp.).

Robertson, P.K. (1990). Soil classification using the cone penetration test. Canadian *Geotechnical Journal, 27*(1): 151-158.

Rode, S., Midoux, N., Latifi, M.A., Storck, A., & Saatdjian, E. (1994). Hydrodynamics of liquid flows in packed beds: an experimental study using electrochemical shear rate sensors. *Chemical Engineering Science, 49*(6), 889-900.

Roscoe Moss Company (1990). *Handbook of ground water development*. New York. Wiley.

Roy, D., & Robinson, K.E. (2009). Surface settlements at a soft soil site due to bedrock dewatering. *Engineering Geology, 107*(3), 109–117.

Ruud, N.C., & Kabala, Z.J. (1997). Response of a partially penetrating well in a heterogeneous aquifer: integrated well-face flux vs. uniform well face flux boundary conditions. *Journal of Hydrology, 194*, 76–94

Sakata, Y., Imai, T., Ikeda, R., & Nishigaki, M. (2015). Analysis of partially-penetrating slug tests in a stratified formation by altering piezometer and tube methods. *Journal of Hydrology, 528*, 385-396.

Salahi, M-B., Sedghi-Asl, M., & Parvizi, M. (2015). Nonlinear flow through a packed-column experiment. *Journal of Hydrologic Engineering 20*(9).

Sanner, B., Kabus, F., Seibt, P., & Bartels, J. (2005). Underground thermal energy storage for the German Parliament in Berlin, system concept and operational experiences. In R. Horne & E. Okadan (Eds.), *Geothermal energy, the domestic, renewable, green option*. Proceedings of the World Geothermal Congress 2005, Antalya, Turkey, 24-29 April 2005 (8 pp.). Auckland: International Geothermal Association.

Sanner, B., Karytsas, C., Mendinos, D., & Rybach, L. (2003). Current status of ground source heat pumps and underground thermal energy storage in Europe. *Geothermics, 32*(4), 579-588.

Sarris, T.S., Close, M., & Abraham, P. (2018). Using solute and heat tracers for aquifer characterization in a strongly heterogeneous alluvial aquifer. *Journal of Hydrology, 558*, 55-71.

Sauty, J.P., Gringarten, A.C., Menjoz, A., & Landel, P.A. (1982). Sensible energy storage in aquifers, 1, Theoretical study. *Water Resources Research, 18*(2), 245-252.

Scheidegger, A.E. (1974). General flow equations. Chapter 7 in *The Physics of flow through porous media* (3rd ed.), (pp. 152-187). Toronto: University of Toronto Press.

Schneebeli, G. (1955). Expériences sur la limite de validité de la loi de Darcy et l'apparition de la turbulence dans un écoulement de filtration. *La Houille Blanche* (2, March-April), 141-149.

Schout, G., Drijver, B., Gutierrez-Neri, M., & Schotting, R. (2014). Analysis of recovery efficiency in high-temperature aquifer thermal energy storage: a Rayleigh-based method. *Hydrogeology Journal, 22*(1), 281-291.

Sedghi-Asl, M., & Rahimi, H. (2011). Adoption of Manning's equation to 1D non-Darcy flow problems. *Journal of Hydraulic Research, 49*(6), 814-817.

Sedghi-Asl, M., Rahimi, H., & Salehi, R. (2014). Non-Darcy flow of water through a packed column test. *Transport in Porous Media, 101*(2), 215-227.

Seguin, D., Montillet, A., Comiti, J., & Huet, F. (1998). Experimental characterization of flow regimes in various porous media – II: Transition to turbulent regime. *Chemical Engineering Science, 53*(22), 3897-3909.

Seibert, S., Prommer, H., Siade, A., Harris, B., Trefry, M., & Martin, M. (2014). Heat and mass transport during a groundwater replenishment trial in a highly heterogeneous aquifer. *Water Resources Research, 50*(12), 9463–9483.

Sen, Z. (1989). Nonlinear flow toward wells. *Journal of Hydraulic Engineering, 115*(2), 193-209.

Shaqour, F.M., & Hasan, S.E. (2008). Groundwater control for construction purposes: A case study from Kuwait. *Environmental Geology, 53*(8), 1603-1612.

Sharqawy, M.H., Lienhard, V.J.H., & Zubair, S.M. (2010). Thermophysical properties of seawater: a review of existing correlations and data. *Desalination and Water Treatment, 16*(1-3):354-380.

Sidiropoulou, M.G., Moutsopoulos, K.N., & Tsihrintzis, V.A. (2007). Determination of Forchheimer equation coefficients a and b. *Hydrological Processes, 21*(4), 534-554.

SIKB (2017a). *BRL SIKB 12000: Beoordelingsrichtlijn: Tijdelijke grondwaterbemaling* (2nd version). Gouda: SIKB (Stichting Infrastructuur Kwaliteitsborging Bodembeheer).

SIKB (2017b). *Protocol 12010: Voorbereiden melding of vergunningaanvraag* (2nd version). Gouda: SIKB (Stichting Infrastructuur Kwaliteitsborging Bodembeheer).

Simmons, C.T., Fenstemaker, T.R., & Sharp Jr., J.M. (2001). Variable-density groundwater flow and solute transport in heterogeneous porous media: approaches, resolutions and future challenges. *Journal of Contaminant Hydrology, 52*(1-4), 245-275.

Skjetne, E., & Auriault, J.L. (1999), High velocity laminar and turbulent flow in porous media. *Transport in Porous Media, 36*(2), 131-147.

Somerville, S.H. (1986). *Control of groundwater for temporary works*. London: Construction Industry Research and Information Association, [CIRIA Report 113]

Sommer, W., Valstar, J., van Gaans, P., Grotenhuis, T., & Rijnaarts, H. (2013). The impact of aquifer heterogeneity on the performance of aquifer thermal energy storage. *Water Resources Research, 49*(12), 8128-8138.

Stephenson, D. (1979). *Rockfill in hydraulic engineering*. Elsevier, Amsterdam: Elsevier.

Steward, D.R. (1999). Three-dimenional analysis of the capture of contaminated leachate by fully penetrating, partially penetrating and horizontal wells. *Water Resources Research, 35*(2), 461-468.

Tan, Y., & Wang, D. (2013). Characteristics of a large-scale deep foundation pit excavated by the central-island technique in Shanghai soft clay. II: Top-down construction of the peripheral rectangular pit. *Journal of Geotechnical and Geoenvironmental Engineering, 139*(11), 1894-1910.

Thauvin, F., & Mohanty, K.K. (1998). Network modeling of non-Darcy flow through porous media. *Transport in Porous Media, 31*(1), 19-37.

Theis, C.V. (1935). The relation between the lowering of the Piezometric surface and the rate and duration of discharge of a well using ground-water storage. *Transactions of the American Geophysical Union 16*(2), 519-524.

Thiem, A. (1870). Die Ergiebigkeit artesischer Bohrlöcher, Schachtbrunnen und Filtergalerien. *Journal für Gasbeleuchtung und Wasserversorgung, 14*, 450–467.

Thiem, G. (1906). *Hydrologische Methoden* (Doctoral dissertation). Stuttgart: Königliche Technische Hochschule.

Timmer, H., Verdel, J.-D., & Jongmans. A.G. (2003). Well clogging by particles in Dutch well fields. *Journal of the American Water Works Association, 95*(8), 112–118.

TNO-GDN (TNO Geologische Dienst Nederland) (2019*). DINOloket: Data en Informatie van de Nederlandse Ondergrond*. Retrieved from https://www.dinoloket.nl/

Tügel, F., Houben G.J., & Graf, T. (2016). How appropriate is the Thiem equation for describing groundwater flow to actual wells? *Hydrogeology Journal, 24*(8), 2093-2101.

Tyagi, A.K., & Todd, D.K. (1970). Discussion of 'Non-linear flow in porous media', by N Ahmed and DK Sunada. *Journal of the Hydraulics Division. Proceedings of the American Society of Civil Engineers, 96*(8), 1734-1738.

Tyler, S.W., Selker, J.S., Hausner, M.B., Hatch, C.E., Torgersen, T., Thodal, C.E., & Schladow, S.G. (2009). Environmental temperature sensing using Raman spectra DTS fiber-optic methods. *Water Resources Research, 45*(4), W00D23.

Ueckert, M., & Baumann, T. (2019). Hydrochemical aspects of high-temperature aquifer storage in carbonaceous aquifers: evaluation of a field study. *Geothermal Energy*, *7*(4) (22 pp.).

Utrecht, Gemeente - Stadswerken - Stedelijk Beheer (2013). *Grondwatercontourkaart gemeente Utrecht: Contourlijnen van de gemiddelde stijghoogte in het eerste watervoerende pakket*. Retrieved from https://www.utrecht.nl/fileadmin/uploads/documenten/wonen-en-leven/duurzame-stad/waterproof/Kaart_met_gemiddelde_grondwaterstanden_in_Utrecht.pdf

Van Beek, C.G.E.M, Breedveld, R.J.M., Juhász-Holterman, M., Oosterhof, A., & Stuyfzand, P.J., (2009a). Cause and prevention of well bore clogging by particles. *Hydrogeology Journal, 17*(8), 1877-1886.

Van Beek, C.G.E.M, Breedveld, R.J.M., & Stuyfzand. P.J. (2009b). Preventing two types of well clogging. *Journal of the American Water Works Association, 101*(4), 125-134.

Van Lopik, J.H., Hartog, N., & Zaadnoordijk, W.J. (2016). The use of salinity contrast for density difference compensation to improve the thermal recovery efficiency in high-temperature aquifer thermal energy storage systems. *Hydrogeology Journal, 24* (5), 1255-1271.

Van Lopik, J.H., Hartog, N., Zaadnoordijk, W.J., Cirkel, D.G., & Raoof, A. (2015). Salinization in a stratified aquifer induced by heat transfer from well casings. *Advances in Water Resources, 86*, 32-45.

Van Lopik, J.H., Snoeijers, R., van Dooren, T.C.G.W., Raoof, A., & Schotting, R.J. (2017). The effect of grain size distribution on nonlinear flow behavior in sandy porous media. *Transport in Porous Media, 120*(1), 37–66.

Van Lopik, J.H., Zazai, L, Hartog, N., & Schotting, R.J. (2019). Nonlinear flow behavior in packed beds of natural and variably graded granular materials. *Transport in Porous Media*, (27 pp.). doi.org/10.1007/s11242-019-01373-037–66. [Published online: 10 December 2019]

Vandenbohede, A., Hermans, T., Nhuygen, F., & Lebbe, L. (2011). Shallow heat injection and storage experiment: Heat transport simulation and sensitivity analysis. *Journal of Hydrology, 409*(1-2), 262-272.

Vandenbohede, A., Louwyck, A., & Lebbe, L. (2009). Conservative solute versus heat transport in porous media during push-pull tests. *Transport in Porous Media, 76*(2), 265-287.

Vandenbohede, A., Louwyck, A., & Vlamynck, N. (2014). SEAWAT-based simulation of axisymmetric heat transport. *Ground Water, 52*(6):908-915.

Vanhoudt, D., Desmedt, J., Van Bael, J., Robeyn, N., & Hoes, H. (2011). An aquifer thermal storage system in a Belgian hospital: Long-term experimental evaluation of energy and cost savings. *Energy and Buildings, 43*(12), 3657-3665.

Venkataraman, P., & Rao, P.R.M. (1998). Darcian, transitional, and turbulent flow through porous media. *Journal of hydraulic engineering [of the American Society of Civil Engineers. Hydraulics Division], 124*(8), 840-846.

Vienken, T., & Dietrich P. (2011). Field evaluation of methods for determining hydraulic conductivity from grain size data. *Journal of Hydrology, 400*(1-2), 58-71.

Vienken, T., Huber, E., Kreck, M., Huggenberger P., & Dietrich, P. (2017). How to chase a tracer – combining conventional salt tracer testing and direct push electrical conductivity profiling for enhanced aquifer characterization. *Advances in Water Resources, 99*, 60-66.

VonHofe, F., & Helweg, O.J. (1998). Modeling well hydrodynamics. *Journal of Hydraulic Engineering 124*(12), 1198-1202.

Voss, C.I. (1984). *A finite-element simulation model for saturated-unsaturated, fluid-density-dependent ground-water flow with energy transport or chemically-reactive single-species solute transport.* Reston, VA: U.S. Geological Survey. [U.S. Geological Survey, Water Resources Investigations Report, 84-4369]

Wagner, V., Li, T., Bayer, P., Leven, C., Dietrich P., & Blum, P. (2014). Thermal tracer testing in a sedimentary aquifer: field experiment (Lauswiesen, Germany) and numerical simulation. *Hydrogeology Journal 22*(1), 175-187.

Wallis I., Prommer, H., Post V., Vandenbohede A., & Simmons C.T. (2013). Simulating MODFLOW-based reactive transport under radially symmetric flow conditions. *Ground Water, 51*(3):398-413.

Wang J., Feng B., Guo T., Wu L., Lou R., & Zhou Z. (2013). Using partial penetrating wells and curtains to lower the water level of confined aquifer of gravel. *Engineering Geology, 161*, 16-25.

Wang L., Li, Y., Zhao, G., Chen, N., & Xu, Y. (2019). Experimental investigation of flow characteristics in porous media at low Reynolds numbers (Re→0) under different constant hydraulic heads. *Water, 11*(2317) (14 pp.).

Wang, S.K., Wee, Y.P., & Ofori, G. (2002). DSSDSS: a decision support system for dewatering systems selection. *Building and Environment, 37*(6), 625–645.

Ward, J.C. (1964). Turbulent flow in porous media. *Journal of the Hydraulics Division. Proceedings of the American Society of Civil Engineers, 90*(5), 1-12.

Ward, J.D., Simmons, C.T., & Dillon, P.J. (2007). A theoretical analysis of mixed convection in aquifer storage and recovery: How important are density effects? *Journal of Hydrology, 343*(3-4), 169-186.

Ward, J.D., Simmons, C.T., & Dillon, P.J. (2008). Variable-density modelling of multiple-cycle aquifer storage and recovery (ASR): Importance of anisotropy and layered heterogeneity in brackish aquifers. *Journal of Hydrology, 356*(1-2), 93-105.

Ward, J.D., Simmons, C.T., Dillon, P.J., & Pavelic, P. (2009). Integrated assessment of lateral flow, density effects and dispersion in aquifer storage and recovery. *Journal of Hydrology, 370*(1-4), 83-99.

Welty, C., & Gelhar, L.W. (1991). Stochastic analysis of the effects of fluid density and viscosity variability on macrodispersion in heterogeneous porous media. *Water Resources Research, 27*(8), 2061-2075.

Wen, Z., Huang, G., & Zhan, H. (2011). Non-Darcian flow to a well in a leaky aquifer using the Forchheimer equation. *Hydrogeology Journal, 19*(3), 563-572.

Wen, Z., Liu, K., & Chen, X. (2013). Approximate analytical solution for non-Darcian flow toward a partially penetrating well in a confining aquifer. *Journal of Hydrology, 498*, 124-131.

Weng, Q. (2001). Modeling urban growth effects on surface runoff with the integration of remote sensing and GIS. *Environmental Management, 28*(6), 737-748.

Werner, A.D., Bakker, M., Post, V.E.A., Vandenbohede, A., Lu, C., Atai-Ashtiani, B., Simmons, C.T., & Barry, D.A. (2013). Seawater intrusion processes, investigation and management: recent advances and future challenges. *Advances in Water Resources, 51*, 3-26.

Whitaker, S. (1996). The Forchheimer equation: a theoretical development. *Transport in Porous Media, 25*(1), 27–61.

Wildemeersch, S., Jamin, P., Orban, P., Hermans, T., Klepikova, M., Nguyen, F., Brouyère, S., & Dassargues, A. (2014). Coupling heat and chemical tracer experiments for estimating heat transfer parameters in shallow alluvial aquifers. *Journal of Contaminant Hydrology, 169*, 90-99.

Winterleitner, G., Schütz, F., Wenzlaff, C., & Huenges, E. (2018). The impact of reservoir heterogeneities on high-temperature aquifer thermal energy storage systems: A case study from Northern Oman. *Geothermics, 74*, 150-162.

Woumeni R.S., &Vauclin M. (2006). A field study of the coupled effects of aquifer stratification, fluid density, and groundwater fluctuations on dispersivity assessments. *Advances in Water Resources, 29*(7), 1037-1055.

Wu, J., Yu, B., & Yun, M. (2008). A resistance model for flow through porous media. *Transport in Porous Media, 71*(3), 331-343.

Wu Y.-Y., Shen J.S, Cheng W.-C., & Hino T. (2017). Semi-analytical solution to pumping test data with barrier, wellbore storage, and partial penetration effects. *Engineering Geology 226*, 44-51.

Xiao, X., Jiang, Z., Owen, D., & Schrank, C. (2016). Numerical simulation of a high-temperature aquifer thermal energy storage system coupled with heating and cooling of a thermal plant in a cold region, China. *Energy, 112*, 443-456.

Yamada, H., Nakamura, F., Watanabe, Y., Murakami, M., & Nogami T. (2005), Measuring hydraulic permeability in a stream bed using the packer test. *Hydrological Processes, 19*(13), 2507–2524.

Yang, W., Zhou, J. Xu, W., & Zhang G. (2010). Current status of ground-source heat pumps in China. *Energy Policy, 38*(1), 323-332.

Yeh, H.D., & Chang, Y.C. (2013). Recent advances in modeling of well hydraulics. *Advances in Water Resources, 51*, 27-51.

Zech A., Attinger, S., Cvetkovic, V., Dagan, G., Dietrich, P., Fiori, A., Rubin, Y., & Teusch, G. (2015). Is unique scaling of aquifer macrodispersivity supported by field data? *Water Resources Research, 51*(9), 7662-7679.

Zeghici R.M., Oude Essink G.H.P., Hartog N., & Sommer W. (2015). Integrated assessment of variable density-viscosity flow for a high temperature mono-well aquifer thermal energy storage (HT-ATES) system in a deep geothermal reservoir. *Geothermics, 55*, 58-68.

Zeng, C.-F., Zheng, G., Xue, X.-L., & Mei, G.-X. (2019). Combined recharge: A method to prevent ground settlement induced by redevelopment of recharge wells. *Journal of Hydrology, 568*, 1-11.

Zhang Y.-G., Wang J.-H., Cheng J.-J., & Li M.-G. (2017). Numerical study on the responses of groundwater and strata to pumping and recharge in a deep confined aquifer. *Journal of Hydrology, 548*, 342-352.

Zheng C., Bianchi, M., & Gorelick, S.M. (2011). Lessons learned from 25 years of research at the MADE site. *Ground Water 49*(5), 649-662.

Zheng, C., & Gorelick, S.M. (2003). Analysis of solute transport in flow fields influenced by preferential flowpaths at the decimeter scale. *Ground Water, 41*(2), 142-155.

Zheng C., & Wang P.P. (1999) *MT3DMS. A modular three-dimensional multispecies transport model for simulation of advection, dispersion and chemical reactions of contaminant in ground-water systems. Documentation and user's guide.* Tuscaloosa, AL: Department of Geological Sciences, University of Alabama. U.S Army Corps of Engineer Research and Development Center, [Prepared for U.S. Army Corps of Engineers. Contract Report SERDP-99-1]

Zheng, G., Cao, J.R., Cheng, X.S., Ha, D., & Wang, F.J. (2018). Experimental study on the artificial recharge of semiconfined aquifers involved in deep excavation engineering. *Journal of Hydrology, 557*, 868-877.

Zeng, Z., & Grigg, R. (2006). A criterion for non-Dacry flow in porous media. *Transport in Porous Media, 63*(1), 57-69.

Zhu, Q., & Wen, Z. (2019). Combined role of leaky and non-Darcian effects on the flow to a pumping well with a non-uniform flux well-face boundary. *Journal of Hydrology,* (article in press).

Zischg, J., Rogers, B., Gunn, A., Rauch, W., & Sitzenfrei, R. (2019). Future trajectories of urban drainage systems: A simple exploratory modeling approach for assessing socio-technical transitions. *Science of the Total Environment, 651*(2), 1709-1719.

Zlotnik, V.A. (1994). Interpretation of slug and packer tests in anisotropic aquifers. *Ground Water, 32*(5), 761-766.

Zlotnik, V.A., & Zurbuchen, B.R. (2003). Field study of hydraulic conductivity in a heterogeneous aquifer: Comparison of single-borehole measurements using different instruments. *Water Resources Research, 39*(4), SBH 8-1 1-SBH 8-12.

Zuurbier, K.G., Zaadnoordijk W.J., & Stuyfzand P.J. (2014). How multiple partially penetrating wells improve the freshwater recovery of coastal aquifer storage and recovery (ASR) systems: A field and modeling study. *Journal of Hydrology, 509*, 430-441.

Samenvatting

In dit proefschrift is onderzocht hoe putsystemen efficiënter kunnen worden ingericht door gebruik te maken van onvolkomen putfilters in heterogene grondwaterpakketten. Onvolkomen putfilters maken het mogelijk om de processen en condities tijdens gebruik van het putsysteem te optimaliseren door op specifieke dieptes in het grondwaterpakket water te infiltreren of te onttrekken. Echter, in de praktijk betekent dit dat er een duidelijk inzicht nodig is van de variabiliteit in doorlatendheid van het grondwaterpakket voor een goed putsysteemontwerp met onvolkomen putfilters. Wanneer de installatie en de afwerking van putten is gebaseerd op slechte of onvoldoende karakterisering van de bodemopbouw, kan dit leiden tot minder goed werkende putten en ongunstige processen en condities tijdens het gebruik van het putsysteem. In het bijzonder richt dit proefschrift zich op de optimalisatie van twee puttoepassingen in verschillende typen grondwaterpakketten:

- Een minimale hydraulische invloed op het bemalingsveld door gebruik te maken van onvolkomen retourputten tijdens het ontwerpen van retourbemalingssystemen.
- Een minimale invloed van dichtheidsgedreven opdrijving van warm water op het terugwinrendement na opslag van thermische energie in het grondwaterpakket tijdens hoge temperatuur opslag (HTO).

Methodes

Er is een breed scala aan technieken toegepast om de belangrijkste onderzoeksdoelstellingen te bereiken, variërend van experimenteel veldwerk en labwerk tot analytische en numerieke analyse.

Door twee veldexperimenten uit te voeren is grondwaterstroming rondom onvolkomen putfilters in heterogene grondwaterpakketten onderzocht. Allereerst is er een kleinschalig veldexperiment uitgevoerd in de buurt van Mönchengladbach (Rheindahlen, Duitsland). Het driedimensionale stromingsgedrag rondom een onvolkomen retourput met een filterlengte van maar één meter is in een zandig tot grindig heterogeen grondwaterpakket onderzocht. Deze onvolkomen putfilters met een zeer beperkte filterlengte, ook wel Fast High Volume Infiltration (FHVI)-putten genoemd, worden door bemalingsbedrijven in Nederland en Duitsland toegepast om hun bemalingswater op een efficiënte manier te retourneren in het te bemalen grondwaterpakket. Het stromingsgedrag rondom een onvolkomen FHVI-put is vergeleken met het stromingsgedrag rondom een volkomen put in hetzelfde

grondwaterpakket. Op basis van de bevindingen van dit eerste veldexperiment werd er een groot veldwerk gerealiseerd op Utrecht Science Park (Utrecht, Nederland). Er is een gedetailleerd overzicht van het geohydrologisch systeem van het grondwaterpakket verkregen door gebruik te maken van de gegevens van sonderingen (CPT), de hydraulic profiling tool (HPT), bodemprofielen van boorstaten, puttesten op de onvolkomen putfilters en laboratoriumanalyse op grondmonsters. Warmte- en bromidetracertests op een onvolkomen infiltratieput gaven informatie over het stromingsgedrag en de preferentiële stroombanen in het heterogene grondwaterpakket tijdens injectie. De data van deze veldwerken zijn numeriek geanalyseerd met het grondwaterstromingsmodel MODFLOW2000 (voor zowel het Mönchengladbach als het Utrecht Science Park experiment) en het grondwatertransportmodel MT3DMS (alleen voor het Utrecht Science Park experiment). Daarnaast zijn de resultaten van de veldwerkexperimenten gebruikt in een numerieke gevoeligheidsanalyse om het ontwerp van retourbemalingssystemen met onvolkomen FHVI-retourputten te optimaliseren.

Het putverlies is voor verschillende onttrekkings- en retourputtypes die worden gebruikt voor bemalingssystemen in ongeconsolideerde grondwaterpakketten analytisch berekend. Voor de analytische berekeningen is er een brede experimentele dataset gebruikt om het putverlies te bepalen van zowel puttypes die zijn afgewerkt met een kunstmatige omstorting (filterzand met een uniforme sortering), als die zijn afgewerkt met een natuurlijke omstorting. Om inzicht te krijgen in het niet-lineaire stromingsgedrag en de resulterende hydraulische weerstand van deze kunstmatige en natuurlijke zandtypes rondom het putfilter, zijn er kolomexperimenten uitgevoerd.

Om verschillende optimalisatiemethoden voor HTO in homogeen anisotrope grondwaterpakketsystemen te verifiëren zijn er gevoeligheidsanalyses uitgevoerd. Dit is gedaan door numerieke simulatie van seizoensgebonden HTO met een jaarlijkse cyclus van injectie, opslag, productie en rust over een periode van vier jaar. Om het grondwater-, warmte- en opgeloste stoffentransport tijdens HTO te modelleren is het grondwaterstromingsmodel voor variabele dichtheden SEAWATv4 gebruikt. Het SEAWATv4-model is gevalideerd op de experimentele (Molz et al. 1983a) en de numerieke resultaten (Buscheck et al. 1983) van een HTO-experiment uitgevoerd op het terrein van Auburn University.

Ontwerp van retourbemalingssystemen met onvolkomen FHVI-retourputten

Hoofdstuk 2 laat zien dat door het gebruik van onvolkomen FHVI-retourputten in plaats van volkomen retourputten in een retourbemalingssysteem de hydraulische invloed op de bemaling tijdens het retourneren aanzienlijk kan worden verminderd. Door een geschikte doorlatende infiltratielaag aan te boren en rekening te houden met de heterogeniteit en dikte van het grondwaterpakket, maakt men optimaal gebruik van de ondergrond in zowel horizontale als verticale richting. Hierdoor kan de bovengrondse afstand tussen te bemalen locatie en retourputten worden verminderd, of het rondpompeffect van het bemalingswater bij een gegeven bovengrondse putafstand worden gereduceerd. De totale projectkosten voor een retourbemaling kunnen zo worden verminderd. De veldexperimenten die zijn beschreven in hoofdstuk 2 en 6 tonen het belang van duidelijke geohydrologische karakterisering van de bodem. De selectie van de infiltratiediepte voor de onvolkomen FHVI-retourputten in bodemlagen met een hoge doorlatendheid maakt retourneren bij hoge infiltratiedebieten en relatief gering putverlies mogelijk. Bovendien resulteert een grote verticale variabiliteit in doorlatendheid (d.w.z. een hoge anisotropie) in preferentiële stroming in de laterale richting van het grondwaterpakket. Hoofdstuk 6 laat zien dat de aanwezigheid van kleine kleilaagjes een grote invloed heeft op de grondwaterstroming en het grondwatertransport tijdens retourneren in een heterogeen grondwaterpakket. Het identificeren van kleine semi-ondoordringbare laagjes zoals klei, veen, leem of silt, of bodemlagen van fijn zand met een relatief lage permeabiliteit tijdens de putontwerpfase kan een grote invloed hebben op de efficiëntie van het bemalingssysteem. Dit kan men in de praktijk doen aan de hand van aanwezige sonderingen en bodembeschrijvingen rondom de bemalingslocatie. De tracertesten in hoofdstuk 6 laten zien dat tijdens infiltratie op de onvolkomen FHVI-retourputten beperkt grondwatertransport naar het bovenste gedeelte van het grondwaterpakket plaatsvond door de aanwezigheid van de bodemlaag met een lage doorlatendheid. Deze bodemlaag met kleifracties kon duidelijk worden aangetoond aan de hand van de sonderingen en bodembeschrijvingen die waren uitgevoerd op deze locatie.

In de praktijk gebruiken Nederlandse en Duitse bemalingsbedrijven FHVI-retourputten om hun putontwerp te optimaliseren met de hierboven beschreven methode. Door FHVI-putten te plaatsen met spoelboringen en door een natuurlijke putomstorting te genereren in heterogene doorlatende bodemlagen is een snelle installatie van meerdere FHVI-putten mogelijk. Bovendien zijn de totale kosten voor afwerken en plaatsen van deze retourputten relatief klein in vergelijking met andere putinstallatietechnieken, waardoor een economisch ontwerp van een bemalingssysteem met meerdere FHVI-retourputten mogelijk is. In hoofdstuk 5 wordt aangetoond dat de installatie van

onvolkomen putten met een natuurlijk omstorting in plaats van installatie met een filteromstorting in bodemlagen met een hoge permeabiliteit (K> 300 m/d) niet noodzakelijkerwijs tot een groter putverlies leidt.

In vergelijking met volkomen putfilters kan men hogere infiltratiedrukken gebruiken tijdens het retourneren op diepte in zandige grondwaterpakketten met onvolkomen putfilters. De veldexperimenten tonen aan dat een gesloten onttrekkings-retoursysteem (met handhaving van voldoende leidingdruk naar de FHVI-retourputten) het mogelijk maakt om anoxisch bemalingswater langdurig te retourneren zonder putverstopping van het filter. Wanneer de leidingdruk niet wordt gehandhaafd kan zowel ontgassing, als neerslag van ijzeroxidedeeltjes in de pijpleiding, bufferbak en put, leiden tot putverstopping. Voor bemaling van oxisch grondwater, zoals tijdens het veldwerk in Mönchengladbach, moet er altijd rekening worden gehouden met putverstopping van FHVI-retourputten. Het gebruik van onvolkomen putfilters met een beperkte filterlengte resulteert altijd in extra putverlies ten opzichte van volkomen putfilters. Door de keuze van een juiste diepte voor het putfilter op basis van goede bodemkarakterisering kan extra putverlies aanzienlijk worden beperkt. De analytische berekeningen in hoofdstuk 5 laat zien dat het gebruik van een onvolkomen putfilter in een heterogene doorlatende bodemlaag van 2 meter dik en een doorlatendheid van 328 m/d, met daarboven en onder zandlagen van 32,8 m/d van elke 9 meter dik, resulteert in extra putverlies van slechts 0,52 m. Wanneer de heterogeniteit niet wordt meegenomen en men een vereenvoudigd equivalent anisotroop homogeen grondwaterpakket aanneemt, wordt het extra putverlies overschat met een factor 4 (2,0 m extra putverlies).

Niet-lineair stromingsgedrag in zand en grind

Bij het bepalen van putverliezen moet rekening worden gehouden met de verhoogde stroomsnelheden (hogere Reynolds getallen) in het filterpack materiaal of natuurlijk omstortingsmateriaal, als gevolg van convergerende of divergerende stroomlijnen naar of van het putfilter. Bij hoge stroomsnelheden (Re>10) begint stroming door poreuze media af te wijken van de lineaire relatie tussen het debiet en de hydraulische gradiënt. Bij dergelijke stroomsnelheden mag de wet van Darcy voor laminaire grondwaterstroming niet langer worden aangenomen en moet men gebruik maken van niet-lineaire relaties zoals de Forchheimer vergelijking. Hoofdstuk 2 geeft een dataset voor niet-lineair stromingsgedrag in 11 uniform gesorteerde filterzanden die worden gebruikt als putomstorting (0,39<d_{50}<6,3 mm). Om het effect van verschillende korrelgrootteverdelingen bij een gegeven porositeit te onderzoeken zijn er mengsels gemaakt van de filterzanden om een iets slechter gesorteerd composietzand te verkrijgen. Ten opzichte van het referentiezand zijn de C_u-waarden licht verhoogd tot 1,19 tot 2,32 bij een gegeven gemiddelde referentiekorrelgrootte (d_{50}). Voor alle composietzanden is

de waargenomen stromingsweerstand hoger dan voor het overeenkomstige referentiezand bij een gelijke gemiddelde korrelgrootte en porositeit. Dit resulteert in verhoogde Forchheimer *a*-coëfficiënten tot een factor van 1,68 en verhoogde b-coëfficiënten tot een factor van 1,44. Voor deze dataset van relatief goed gesorteerd zand (C_u<2) werkt een alternatieve Ergun-vergelijking met Ergun-constanten van 183,8 voor A en 2,53 voor B, en het gebruik van d_{30} als karakteristieke porielengte, goed. In hoofdstuk 3 is het niet-lineair stromingsgedrag door slecht gesorteerd materiaal bij variërende korrelgrootteverdelingen (van 2,0<C_u<17,35) en porositeitswaarden (0,23<n <0,36) onderzocht. Hiervoor zijn 5 verschillende natuurlijke zand- en grindafzettingen en 13 verschillende mengsels van filterzand en -grind gebruikt. Voor het zand en grind met hoge C_u-waarden en lage porositeitswaarden wordt een sterk verhoogde stromingsweerstand waargenomen. Deze studie toont aan dat voor het slecht gesorteerde materiaal (C_u>2), de d_{10} in plaats van de gemiddelde korrelgrootte (d_{50}) als karakteristieke porielengte moet worden gebruikt in de empirische Ergun-vergelijking. Ergun-constanten A en B met waarden van respectievelijk 63,1 en 1,72 resulteren in een redelijke voorspelling van de Forchheimer-coëfficiënten voor het onderzochte slecht gesorteerde zand en grind. De uitgebreide dataset in hoofdstuk 2 en 3 over niet-lineair stromingsgedrag in zand en grind is nuttig voor het analyseren van puttesten en putverliezen rondom het putfilter zoals is gedaan in hoofdstuk 5.

Hoge temperatuur opslag

In hoofdstuk 8 is onderzocht of er met meerdere onvolkomen infiltratie- en onttrekkingsputfilters in één boorgat het terugwinrendement van thermische energie in HTO-systemen kan worden verhoogd. Door het grote temperatuurcontrast tussen het warme infiltratie/opslagwater en het koudere grondwater tijdens seizoensgebonden HTO (40<ΔT<60 °C in deze studie) vindt er dichtheidsgedreven stroming plaats tijdens infiltratie en opslag in het grondwaterpakket. Hierdoor is het terugwinrendement van de thermische energie in een doorlatend grondwaterpakket laag. Zowel natuurlijke als gedwongen convectie in de injectie-, opslag- en terugwinningsfase tijdens HTO met meerdere onvolkomen putfilters is sterk afhankelijk van de horizontale en verticale doorlatendheid van het grondwaterpakket. De injectie en opslag van warm water (T_{in}=80 ºC) in een grondwaterpakket met een hoge doorlatendheid (K_h=53,4 m/d) en een anisotropiewaarde (K_h/K_v) van 7 is aanzienlijk verbeterd met een putconfiguratie van meerdere onvolkomen putfilters. Infiltratie van warm water gedurende 90 dagen in het onderste gedeelte van het grondwaterpakket en onttrekking voor 90 dagen in het bovenste gedeelte van het grondwaterpakket resulteert in een toename van het terugwinrendement ($\Delta\varepsilon_H$=0,14) ten opzichte van HTO met een volkomen infiltratie- en onttrekkingsput. Echter, hetzelfde scenario in een grondwaterpakket met een

vergelijkbare horizontale doorlatendheid maar met een significant hogere anisotropiewaarde (K_h/K_v=35) resulteert in het minst gunstige putschema en een afname van het terugwinrendement ($\Delta\varepsilon_H$=-0,06) ten opzichte van HTO met een volkomen infiltratie- en onttrekkingsput. In sterk heterogene grondwaterpakketten is het van belang dat er naast de horizontale doorlatendheid ook een goede inschatting wordt gemaakt van de variabiliteit in de verticale doorlatendheid om tot de juiste putconfiguratie te komen indien men gebruik wilt maken van meerdere onvolkomen putfilters.

Daarnaast is onderzocht of de terugwinefficiëntie kan worden verbeterd door te compenseren voor het dichtheidsverschil tijdens HTO met behulp van een verhoogd zoutgehaltecontrast tussen het geïnjecteerde warme water en koudere grondwater (zie hoofdstuk 7). Voor een referentiescenario is een grondwaterpakket met een hoge doorlatendheid aangenomen, waarbij water van 80 °C wordt opgeslagen in een grondwaterpakket met een temperatuur van 20 °C. Dit resulteert in een terugwinrendement van 0,40 voor een conventioneel HTO-systeem zonder dichtheidscompensatie na vier opeenvolgende opslagcycli. De methode met dichtheidscompensatie resulteert in een terugwinrendement van maar liefst 0,69, hetgeen dicht in de buurt komt van het theoretische geval zonder warmteverlies door dichtheidsgedreven stroming (0,76). Gevoeligheidsanalyse toont aan dat de toename van het terugwinrendement met behulp van de dichtheidscompensatie in plaats van conventionele HTO groter is voor de scenario's met een hogere doorlatendheid van het grondwaterpakket, een groter temperatuurverschil tussen injectiewater en omgevingsgrondwater, en een kleiner injectievolume of grotere dikte van de watervoerende laag. Door gebruik te maken van dichtheidscompensatie met zout kan HTO breder worden toegepast. Op die manier is HTO ook realiseerbaar in dikkere en meer doorlatende grondwaterpakketten, bij kleinere opslagvolumes en bij hogere temperatuurcontrasten.

Utrecht University
Faculty of Geosciences
Department of Earth Sciences

ISSN 2211-4335